Title	Influence of East Asian Monsoon and El Niño Southern Oscillation (ENSO) to Holocene Hydroclimate deduced from Northwest Pacific corals
Author(s)	Garas, Kevin Lariosa
Citation	北海道大学. 博士(理学) 甲第15562号
Issue Date	2023-06-30
DOI	10.14943/doctoral.k15562
Doc URL	http://hdl.handle.net/2115/90563
Type	theses (doctoral)
File Information	Kevin_Garas.pdf

Doctoral Dissertation

Influence of East Asian Monsoon and El Niño Southern Oscillation (ENSO) to Holocene Hydroclimate deduced from Northwest Pacific corals

(完新世のサンゴ骨格記録を用いた東アジアモンスーンが ENSO に与える影響の解明)

KEVIN LARIOSA GARAS

Graduate School of Science, Hokkaido University
Department of Natural History Sciences

June 2023

TABLE OF CONTENTS

ABSTRACT

Geochemical records are important evidence of past climate and environmental changes beyond historical and instrumental records. This dissertation will focus on the interaction of East Asian monsoon (EAM) and El Niño Southern Oscillation (ENSO) in modulating the interannual and seasonal sea surface temperature (SST), sea surface salinity (SSS), and rainfall variabilities in the subtropical and tropical Northwest Pacific during the Holocene. Investigating how the interannual ENSO affects the monsoon is vital in seasonal rainfall prediction. Due to the complex teleconnections of equatorial Pacific SST anomalies (SSTA) and the East-Southeast Asian climate, few paleoclimate records could explain the mechanism of EAM-ENSO interaction in the Holocene.

This research explores the potential of corals from Kikai Island, Japan and NW Luzon Island, Philippines. There are 40 Porites colonies collected from the two study areas. A series of screening of fossil corals was done using thin section analysis, X-ray Diffraction (XRD), and Scanning Electron microscopy (SEM). Fossil corals with excellent preservation were dated using Accelerator Mass Spectrometer to measure the radiocarbon age dates. Corals were cut into 5-mm slabs, cleaned, and prepared for X-radiography, microsampling, and geochemical analysis. Coral growth parameters such as linear extension rate, skeletal density, and calcification rate were calculated from the X-ray photographs of corals. Sr/Ca ratio was measured with an Inductively Coupled Plasma-Atomic Emission Spectrometry (iCAP 6300 ICP Spectrometer). Similar coral powder samples were analyzed using Isotope Ratio Mass Spectrometer (MAT Finnigan 253) with an automated carbonate device Kiel IV for oxygen isotope analysis.

Results of thin section analysis, XRD, and SEM have shown that six fossil Porites have excellent to good fossil preservation. These samples have <1% calcite content based on phase mineral estimates from Reference Intensity Ratio (RIR) Method. Corals with excellent preservation are devoid of dissolution, fine- to medium-sized acicular aragonite and rhombohedral calcite overgrowths. Well-preserved fossil corals from Kikai Island yielded radiocarbon age dates of 3235±20 (KIKJ-20160907-II) and 5712±24 (KIST-20160518-I) years BP. Well-preserved fossil corals from NW Luzon Island yielded radiocarbon age dates of 6285±79 (CuPf-180218-1), 6144±77 (CuPf-180218-4), 4336±21 (DMT-2), and 4200±20 (DMT-1) years BP. The annual linear extension rates of modern corals from Kikai and NW Luzon islands were plotted against the annual Sr/Ca and $\delta^{18}O_{coral}$ for each coral colony to investigate the effect of growth rate on coral geochemistry. The absence of a strong linear correlation between these variables suggests that growth minimally affects the variation of these two climate proxies.

The ordinary least square (OLS) regression analysis demonstrated the dependence of coral Sr/Ca, $\delta^{18}O_{coral}$, and $\delta^{18}O_{sw}$ on SST, SSS, and rainfall. The monthly-resolved Sr/Ca records of modern corals from Kikai Island and NW Luzon Island are negatively correlated to the AVHRR SST from 1989-2015 (slope: -0.0643 mmol/mol°C^{-1}) and OISST from 2011-2017 (slope: -0.0057 mmol/mol°C^{-1}) respectively. The 5-point running average of $\delta^{18}O_{sw}$ and monthly in-situ rainfall data of Kikai Island from 2007-2015 were regressed and have shown statistically significant negative linear correlation ($r=0.55$; $p<0.000$; $n = 93$). The monthly-resolved $\delta^{18}O_{sw}$ from NW Luzon Island coral and SODAv3.3.1 SSS from 2011-2017 have statistically significant positive linear correlation ($r=0.50$; $p<0.000$; $n = 48$). The regression equations were used to interpret and quantify the hydroclimatic changes in fossil coral geochemical records.

The mean seasonal trends of all modern and fossil corals revealed the seasonality of SST, SSS, and rainfall. The changes in coral-based SST, SSS, and rainfall records of mid- to late Holocene were likely driven by the changes in the monsoon intensity. The summer, winter, and annual mean Sr/Ca-SST and $\delta^{18}O_{coral}$ records from fossil *Porites* in subtropical and tropical NW Pacific were compiled to investigate seasonal SST and SSS change in mid-Holocene to late Holocene. The lower SSS and higher rainfall in subtropical NW Pacific were coeval to the higher SSS and lower rainfall in tropical NW Pacific from 7.0 ka to 5.0 ka. The subtropical and tropical SSTA records consistently show that the period was not significantly different and warmer (+0-2°C) at times than the present. The SSS trend of subtropical NW Pacific shifted positively after 4.9 ka, while the SSS trend in tropical NW Pacific shifted negatively around 4.3 to 4.2 ka. After 5.0 ka, the summer SSTA shows a cooling trend in subtropical (-1.8°C) and tropical (-0.9°C) NW Pacific. The coral evidence supports the widely reported EASM intensification (8.2 ka to 4.7 ka) and weakening (4.7 ka to 3.0 ka) based on the stacked marine and terrestrial sediment records from NW Pacific. Moreover, the coral-derived SST and SSS datasets agree that the mean position of the intertropical convergence zone (ITCZ) migrated southwards from the mid-Holocene towards the late Holocene. The northward ITCZ migration and intensification of EASM resulted in the enhancement of summer rainfall in the subtropics, while the rainfall in tropical NW Pacific was reduced in the mid-Holocene. The southward migration of the ITCZ and weakening of the EASM resulted in the aridification of East Asia and reduced rainfall/higher SSS of subtropical NW Pacific. The southerly position of the ITCZ brought more rainfall in the tropical NW Pacific.

Aside from monsoon, the ENSO affects the rainfall pattern in NW Pacific. However, the lack of high temporal resolution records hinders the reconstruction of ENSO-driven rainfall seasonality. ENSO-related signal in coral-derived $\delta^{18}O_{sw}$ was isolated by filtering the 2-8-

year bandpass frequency. The $\delta^{18}O_{sw}$ threshold values for different ENSO intensities were determined using the statistically significant positive correlation (r=0.75; r2=0.56; p<0.000) of 2-8-year bandpass filtered $\delta^{18}O_{sw}$ data and the ERSST v4 NINO 3.4 SSTA from 1982 to 2012. The same bandpass filtering method was used to show the ENSO cycle in Holocene coral records from Kikai Island and NW Luzon Island. Using the threshold values from the regression analysis, El Niño and La Niña years were identified in each fossil coral records. The change of standard deviation of $\delta^{18}O_{sw}$ records from Kikai fossil corals revealed an 11% to 49% ENSO reduction relative to the 1989-2015 benchmark. The $\delta^{18}O_{sw}$ records from NW Luzon fossil corals revealed a 20% to 50% ENSO reduction relative to the 2011-2017 benchmark.

The distinct rainfall seasonality during neutral and El Niño phase of ENSO was evaluated using modern $\delta^{18}O_{sw}$ records. Seasonal rainfall in Kikai Island became more pronounced during El Niño of 1991-92 and 1997-98 because of the reduced rainfall during the developing year and enhanced rainfall during the following summer of the decaying year. The rainfall in NW Luzon generally decreased during the strong El Niño in 2015-2016 relative to the neutral phase. Analyses of 3.2 ka, 4.9 ka, and 5.7 ka corals from Kikai Island show increased subtropical rainfall with increasing ENSO variability. On the other hand, the 4.2 ka, 4.3 ka, and 6.1 ka corals from NW Luzon show that ENSO influenced the seasonal rainfall despite the relatively weak variance during these time-windows. However, the other prevailing climate modes could have masked the ENSO effect, as shown by the possible impact of strong EASM at 6.1 ka.

This research proposes a new way to investigate the complexity of monsoon and ENSO effects on the seasonal hydroclimate of the region. The new coral data from NW Pacific confirmed a mid-Holocene ENSO weakening as suggested by coral climate proxies (Cobb et al., 2013; Grothe et al., 2019) and paleo-ENSO model (Tian et al., 2017). However, the mechanism involving the interaction of the monsoon circulation and ENSO cycles in varying SST boundary conditions is still unclear and needs further research.

完新世のサンゴ骨格記録を用いた東アジアモンスーンが ENSO に与える影響の解明

地球化学的な記録は、歴史的な記録や計器的な記録を超えて、過去の気候や環境変化の重要な証拠となる。 本論文では、完新世の北西太平洋亜熱帯・熱帯域における海面水温（SST）、海面塩分（SSS）、降水量の経年・季節変動を変調させる東アジアモンスーン（EAM）とエルニーニョ南方振動（ENSO）の相互作用に焦点を当てたい。赤道太平洋海面水温偏差（SSTA）と東・東南アジア気候の複雑なテレコネクションのため、完新世における EAM-ENSO 相互作用のメカニズムを説明できる古気候記録はほとんどない。

本研究では、日本の喜界島とフィリピンのルソン島北部のサンゴからその可能性を探る。この 2 つの調査地からは 40 個の Porites コロニーが採集されている。化石サンゴの選別は、薄切片分析、X 線回折（XRD）、走査型電子顕微鏡（SEM）などを用いて行われました。保存状態が良好な化石サンゴは、加速器質量分析計を用いて放射性炭素年代を測定した。サンゴは 5 mm のスラブに切断され、洗浄され、X 線撮影、マイクロサンプリング、地球化学分析に備えられました。サンゴの直線伸長率、骨格密度、石灰化率などの成長パラメータは、サンゴの X 線写真から算出した。Sr/Ca 比は、誘導結合プラズマ原子発光分光分析装置（iCAP 6300 ICP Spectrometer）を用いて測定した。同様のサンゴ粉末試料は、酸素同位体分析用の自動炭酸装置 Kiel IV を備えた同位体比質量分析装置（MAT Finnigan 253）を用いて分析した。

喜界島の保存状態の良い化石サンゴは、放射性炭素年代が 3235±20 年（KIKJ-20160907-II）と 5712±24 年（KIST-20160518-I）BP となった。ルソン島北西部の保存状態の良い化石サンゴは、6285±79 年（CuPf-180218-1）、6144±77 年（CuPf-180218-4）、4336±21 年（DMT-2）、4200±20 年（DMT-1） BP の放射性炭素年代をもたらした。喜界島と NW ルソン島の現代サンゴの年間直線伸長率を、各サンゴコロニーの年間 Sr/Ca と δ18Ocoral に対してプロットし、サンゴ地球化学に対する成長速度の影響を調べた。これらの変数の間に強い線形相関がないことから、成長はこれら 2 つの気候プロキシの変動に最小限の影響を与えることが示唆された。

喜界島と北西ルソン島の現代サンゴの月別分解 Sr/Ca 記録は、1989-2015 年の AVHRR SST（傾き：-0.0643mmol/mol℃-1）と 2011-2017 年の OISST（傾き：-0.0057mmol/mol℃-1）にそれぞれ負の相関が見られた。2007 年から 2015 年の喜界島の月別原位置降水量データと δ18Osw の 5 点移動平均を回帰したところ、統計的に有意な負の線形相関（r=0.55; p<0.000; n = 93）が示されました。2011-2017 年の北西ルソン島サンゴと SODAv3.3.1 SSS の月次分解 δ18Osw は、統計的に有意な正の線形相関を示した（r=0.50; p<0.000; n=48）。回帰式は、化石サンゴの地球化学記録における水文気候の変化の解釈と定量化に使用された。

すべての現生サンゴと化石サンゴのコロニーの平均季節傾向は、SST、SSS、降雨の季節性を明らかにした。完新世中期から後期にかけてのサンゴ礁の海面水温、海面水温、降水量の記録は、モンスーン強度の変化に起因していると考えられる。亜熱帯北西太平洋の海面水温の低下と降水量の増加は、7.0ka から 5.0ka にかけての熱帯北西太平洋の海面水温の上昇と降水量の減少と同世代であることがわかった。亜熱帯と熱帯の SSTA 記録は一貫して、この時期が現在と大きく変わらず、暖かい（+0-2℃）時期があったことを示す。亜熱帯北西太平洋の SSS 傾向は 4.9ka 以降正にシフトし、熱帯北西太平洋の SSS 傾向は 4.3～4.2ka 頃に負にシ

フトしている。5.0ka 以降、夏の SSTA は亜熱帯北西太平洋（-1.8℃）と熱帯北西太平洋（-0.9℃）で冷却傾向を示していることがわかった。サンゴ由来の海面水温と海面水温のデータは、熱帯間収束帯（ITCZ）の平均位置が完新世中期から完新世後期にかけて南下したことに同意している。ITCZ の北方への移動と EASM の活発化により、亜熱帯の夏季降水量は増加したが、北西太平洋熱帯域の降水量は完新世中期には減少した。ITCZ の南下と EASM の弱まりは、東アジアの乾燥化と北西太平洋亜熱帯の降水量減少・SSS 上昇をもたらした。ITCZ の南下は、北西太平洋熱帯域の降雨量を増加させた。

サンゴ由来のδ18Osw の ENSO 関連シグナルは、2-8 年のバンドパス周波数でフィルタリングすることで分離した。1982 年から 2012 年までの 2-8 年バンドパスフィルターをかけたδ18Osw データと ERSST v4 NINO 3.4 SSTA の統計的に有意な正の相関（r=0.75; r2=0.56; p<0.000）を用いて、異なる ENSO 強度のδ18Osw 閾値を決定した。同じバンドパスフィルタリング法を用いて、喜界島とルソン島北西部の完新世のサンゴの記録にも ENSO 周期が示された。回帰分析で得られた閾値を用い、各化石サンゴ記録においてエルニーニョ年とラニーニャ年を特定した。喜界島化石サンゴのδ18Osw 記録の標準偏差の変化から、1989-2015 年のベンチマークに対して 11%から 49%の ENSO の減少が確認された。ルソン島化石サンゴのδ18Osw 記録は、2011-2017 年のベンチマークに対して、20%から 50%の ENSO の減少を示した。

ENSO の中立期とエルニーニョ期の明確な降雨の季節性を、現代のδ18Osw の記録を用いて評価した。喜界島の季節性降雨は、1991-92 年と 1997-98 年のエルニーニョ時に、発達年の降雨量が減少し、衰退年の翌夏の降雨量が増加したため、顕著になった。2015-2016 年の強いエルニーニョでは、北西ルソン島の降水量は中立期に比べて概ね減少した。喜界島の 3.2ka、4.9ka、5.7ka のサンゴの解析では、ENSO 変動の増加に伴い亜熱帯の降水量が増加した。一方、北西ルソンの 4.2 ka、4.3 ka、6.1 ka のサンゴは、これらの時間帯の変動が比較的弱いにもかかわらず、ENSO が季節降雨に影響を与えたことを示している。しかし、6.1ka の強い EASM の影響に見られるように、他の優勢な気候モードが ENSO の影響を覆い隠した可能性がある。

本研究は、モンスーンと ENSO がこの地域の季節的な水文気候に及ぼす複雑な影響を調査する新しい方法を提案するものである。北西太平洋の新しいサンゴデータは、サンゴ気候プロキシ（Cobb et al., 2013; Grothe et al., 2019）や古 ENSO モデル（Tian et al. 2017）が示唆するように、完新世半ばの ENSO 弱化を確認した。しかし、SST 境界条件の変化におけるモンスーン循環と ENSO サイクルの相互作用を含むメカニズムはまだ不明であり、さらなる研究が必要である。

Chapter 1

INTRODUCTION

1.1. The Holocene climate

Proxy-based climate archives are important evidence of past climate and environmental changes beyond historical and instrumental records. Paleoclimate archives allow us to investigate the characteristics and the natural forcings of past climate changes. The current climate change is known to be driven by anthropogenic CO_2 emissions. In contrast, geological climate changes occurred without the influence of anthropogenic factors. Natural factors such as solar insolation, sunspot activities, large-scale volcanism, magnetic pole reversals, disruption in global-scale oceanic circulation, and extraterrestrial impacts were possible drivers of past climate changes. These climate changes resulted in catastrophes leading to major extinction events and landscape reconfiguration throughout the Earth's geologic history.

The Holocene is the youngest epoch in Earth's history spanning from 11,700 years ago to present (Walker et al. 2012). The Holocene is subdivided into Early, Middle (Mid-), and Late Holocene. The 8.2 ka BP event marks the boundary between Early and Mid-Holocene while the 4.2 ka BP event is the boundary between Mid- and Late Holocene, both events are defined by a Global Stratotype Section and Point (GSSP). In the effort to understand the present and future climate change scenarios, it is crucial to understand the background climate of the Holocene. This period was primarily affected by natural climate variability rather than anthropogenic factors. Furthermore, the development of early human civilizations was also influenced by climate regime shifts in the Late Glacial Maximum extending to Holocene (Weiss and Bradley 2001; An et al. 2005; Kawahata et al. 2009; Kajita et al. 2018). Therefore, proxy- and model-based reconstructions of the Holocene climate are necessary.

The Holocene is probably the most extensively studied epoch due to abundance of geomorphological, biological, climatological, and archeological evidence (Walker et al., 2019). The transition from the Late Glacial Maximum (LGM) around 20,000 years ago to the Early Holocene/Greenlandian Stage (8,200 to 11,700 years ago) was accompanied by consistent upward trend in global temperature and sea-level. The generally warm and wet climate persisted and reached the peak during the mid-Holocene/Northgrippian Stage (4,200 to 8,200 years ago), which is often referred to as *Holocene climatic optimum*. The mid-Holocene transitioned to a relatively cooler and drier climate in the Late Holocene/Meghalayan Stage. The general climate trend in the Holocene is widely accepted because of the availability of published works throughout the decades (Fig.1). But despite the wealth of paleoclimate records, disagreements on the interpretations of various archives and uncertain controlling mechanism on these climate shifts resulted in a conundrum of Holocene climate.

The possible reasons of the diverging and contradicting results of paleoclimate research are as follows:

1. The prevailing ocean-climate systems influence the occurrence of unique climate trends in a particular area;
2. The different paleoclimate archives reflect different temporal (seasonal, interannual, decadal to centennial-scale) resolutions; and
3. The diverse sets of geomorphological, mineralogical, and geochemical evidence have varying environmental and climatic controls.

These factors may lead to challenges and confusion in understanding past climate changes as shown in the case studies below:

a) The zonal temperature trends from Northern Hemisphere (90°N to 30°N), tropics (30°N to 30°S), and Southern Hemisphere (30°S to 90°S) show regional variations in the Holocene with a generally 0.7°C cooling after 5000 years ago (Marcott et al. 2013). This global temperature anomaly reconstruction using 73 records contradicts the simulated climate models of regional and global temperature trends in Holocene (Liu et al. 2014). This model-data discrepancy is believed to be attributed to the seasonality bias of the proxy reconstructions and the climate sensitivity of the models.

b) Speleothem $\delta^{18}O$ records are extensively used to reconstruct past rainfall variability in the Asian monsoon domain. However, sediment-based paleoclimate archives do not support the rainfall interpretation of speleothem δ18O arguing that it has bias to moisture source (Maher 2008; Pausatta et al. 2011; Kaboth-Bahr et al. 2021; Dayem et al. 2010). Contrasting interpretations of paleoclimate records may lead to unresolved questions about the paleomonsoon development.

This dissertation will focus on the interaction between East Asian monsoon and El Niño Southern Oscillation in modulating the interannual and seasonal temperature, salinity, and rainfall variabilities in the subtropical and tropical Northwest Pacific during the Holocene. This dissertation reiterates that climate research should consider heterogeneity and regional perspectives as an integral part of global climate change.

The strengths and weaknesses of a particular paleoclimate archive should be carefully considered in making interpretations and reconstructions.

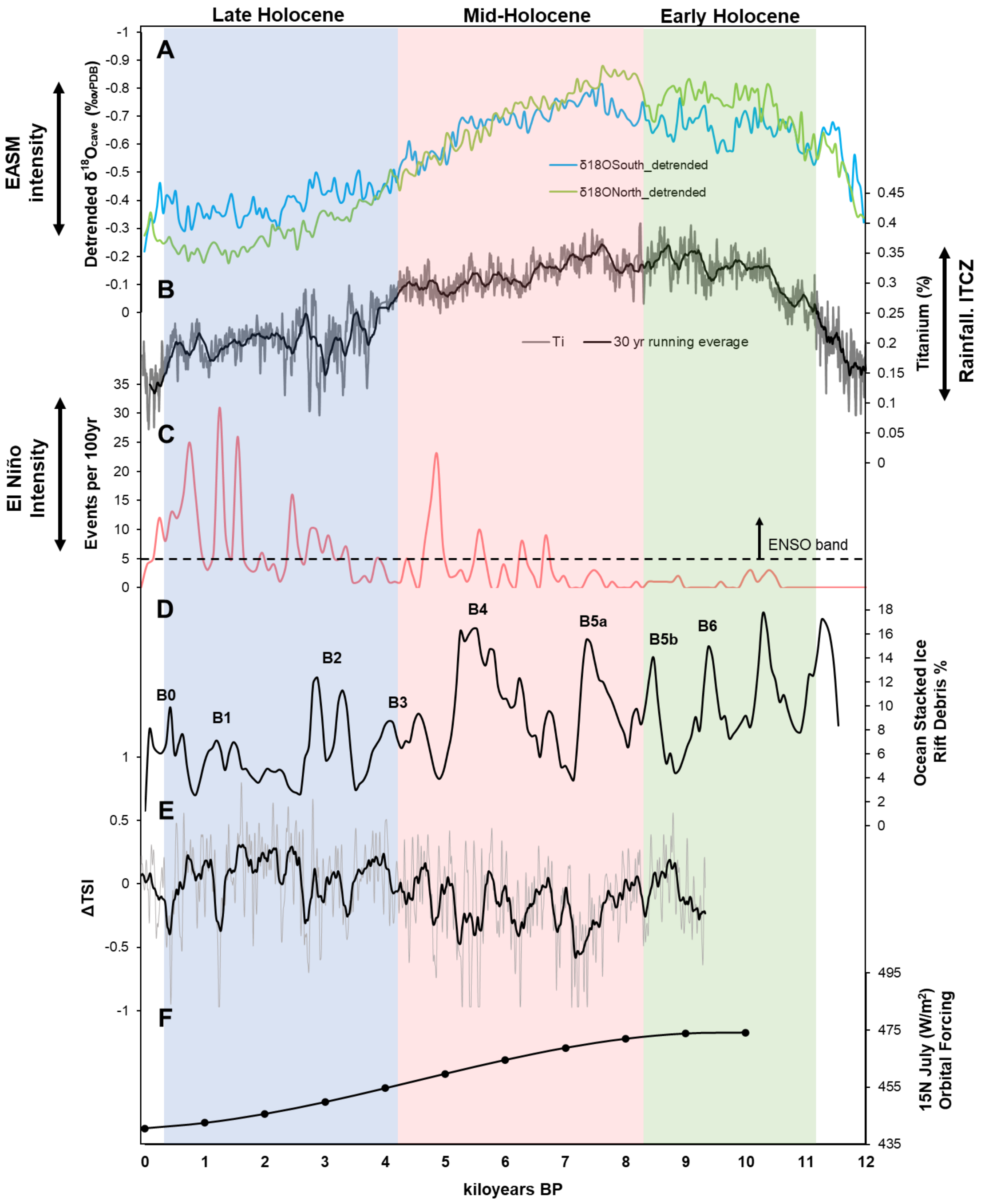

Figure 1. Paleoclimate archives and external climate forcings. A. Oxygen isotope of speleothem from Northern and Southern China *(*Dong et al. 2018; Cosford et al. 2008; Dykoski et al. 2005) B. Bulk Titanium* % of marine sediment core from Cariaco Basin, Venezuela (Haug et al. 2001) C. Event per 100yr based on the frequency of clastic laminae from Lake Pallacocha, Ecuador (Moy et al. 2002) D. Bond events from the record of ocean ice rift debris of Northern Altantic Ocean (Bond et al. 2001) E. Total Solar Irradiance (ΔTSI) record in Holocene (Steinhilber et al. 2009) F. Summer solar insolation in the tropics (Berger and Loutre 1991)

1.2. The East Asian Monsoon

East Asian Monsoon (EAM), divided into summer and winter monsoon components, influences the temperature hydrological budget (evaporation-precipitation balance) of the NW Pacific region. Climate simulations show that EAM modulates the regional water budget with high sensitivity to the current global warming condition (Rodriguez et al. 2017; Xue et al. 2018; Chevuturi et al. 2022). The response of EAM to climate regime shift from cooling to warming trends is a vital mechanism with socio-economic significance. This mechanism can disrupt societies due to impacts on hydrometeorological-related disasters, agriculture and food security, and overall social stability. Proxy- and model-based climate reconstructions revealed that the intensity of EAM has changed over the Holocene (Jiang et al. 2013; Dong et al. 2018; Kaboth-Bahr et al. 2021; Zhang et al. 2021). The Holocene (11,700 years ago to present) climatic shifts from warming to cooling conditions can provide direct evidence on the present and future scenarios of EAM. However, understanding EAM dynamics is quite challenging because of the complex forcings and limited datasets with intra-seasonal-to interannual resolution (Mohtadi et al. 2016).

To understand the paleomonsoon conditions, we will discuss the present-day mechanisms of the East Asian summer and winter monsoons. The East Asian summer monsoon (EASM) affects the rainfall distribution in the Indochina Peninsula, the Philippines, Southern and Northern China, Japan, and Korea. The wide extent of the summer monsoon rainfall is attributed to the 3-step northward seasonal march from Indochina - South China Sea (SCS) – the Philippines in early- to mid-May, then expands to the Yangtze River Basin in southern China, western and southern Japan in early- to mid-June, and finally moves further to Northern China and Korea (Yihui and Chan et al., 2005). There are external and internal forcings that affect the intensity and development of the EASM. The tropical Pacific and Indian Ocean SSTs and the Eurasian and Tibetan Plateau snow cover are critical factors in the strength of the westerlies and southwesterlies. The ocean-continent temperature forcings interact with the internal forcings from the atmospheric circulation. The anticyclonic circulation in northern Pacific modulated by the intensification or weakening of the Western Pacific Subtropical High (WPSH) is the main driver of low- level (1000 to 850 millibars/mb) tropospheric wind circulation in boreal summer (Qian et al. 2020; Yang et al. 2022). Figure 2A shows the mean sea level pressure (SLP) from June to August (JJA: boreal summer) using the National Center for Environment Prediction (NCEP) / National Center for Atmospheric Research (NCAR) reanalysis data from 1982 to 2020. The red-orange zones in the northern Pacific represent the high-pressure region located east of Japan. The SLP variation in the Pacific Ocean and the Asian continent drives the anticyclonic circulation. The 1000 mb (364 ft or 111 m) level vector wind map of the region (Fig. 2B) shows that the westward progression of the WPSH would increase the eastward and northeastward progression of the low-level westerlies and southwesterlies, respectively. This mechanism will facilitate the seasonal march of the EASM.

The seasonal march of the summer monsoon also follows the seasonal dynamics of the Indo-Pacific Warm Pool (IPWP) and intertropical convergence zone (ITCZ). Seasonal composite maps show the mean SST from JJA (Fig. 3A) and DJF (Fig. 3C) using NOAA Optimum Interpolation Sea Surface Temperature (OISST) from 1982 to 2020. The composite maps illustrate how the IPWP expands from 10°N of equator in boreal winter (DJF) to 30°N of equator in boreal summer (JJA) reaching the northernmost periphery up to southern Japan (Fig 3A). Simultaneously, the ITCZ rainbelt expands northward from 15°N of equator in boreal winter (DJF) to 35°N of equator in boreal summer (JJA). This phenomenon is shown by the composite maps of the mean rainfall from JJA (Fig. 3B) and DJF (Fig. 3D) using Global Precipitation Climatology Project (GPCP) from 1982 to 2020.

The East Asian winter monsoon primarily controls the winter SST, SSS, and rainfall in the region. The changes of winter monsoon intensity and winter temperature are affected by the changes of high latitude low-level tropospheric circulation (i.e. polar jet stream, Siberian high and Aleutian low) in boreal winter (Jhun and Lee 2004). The expansion of high latitude Eurasian snow cover and intense cooling strengthen the Siberian High-pressure region which intensifies the winter variability mode (Li et al. 2018). Not only the Siberian High, but the development of Aleutian low pressure also directly influences the wind circulation and winter climate variation over East Asia (Wu and Wang 2002; Jhun and Lee 2004). Mean SLP map during DJF from 1982 to 2020 demonstrated the occurrence of the Siberian High in the Asian continent and the Aleutian low in the North Pacific Ocean within the 40°N to 60°N latitude (Fig. 2C). The strong Aleutian low creates a cyclonic wind movement in the North Pacific Ocean above 40°N latitude. The strong Siberian high drives the southward wind circulation along the marginal northwest Pacific that converges with the southwestward wind movement in the north-central Pacific below the 30°N latitude. This winter wind circulation with respect to the Siberian high and Aleutian low is shown in Fig. 2D.

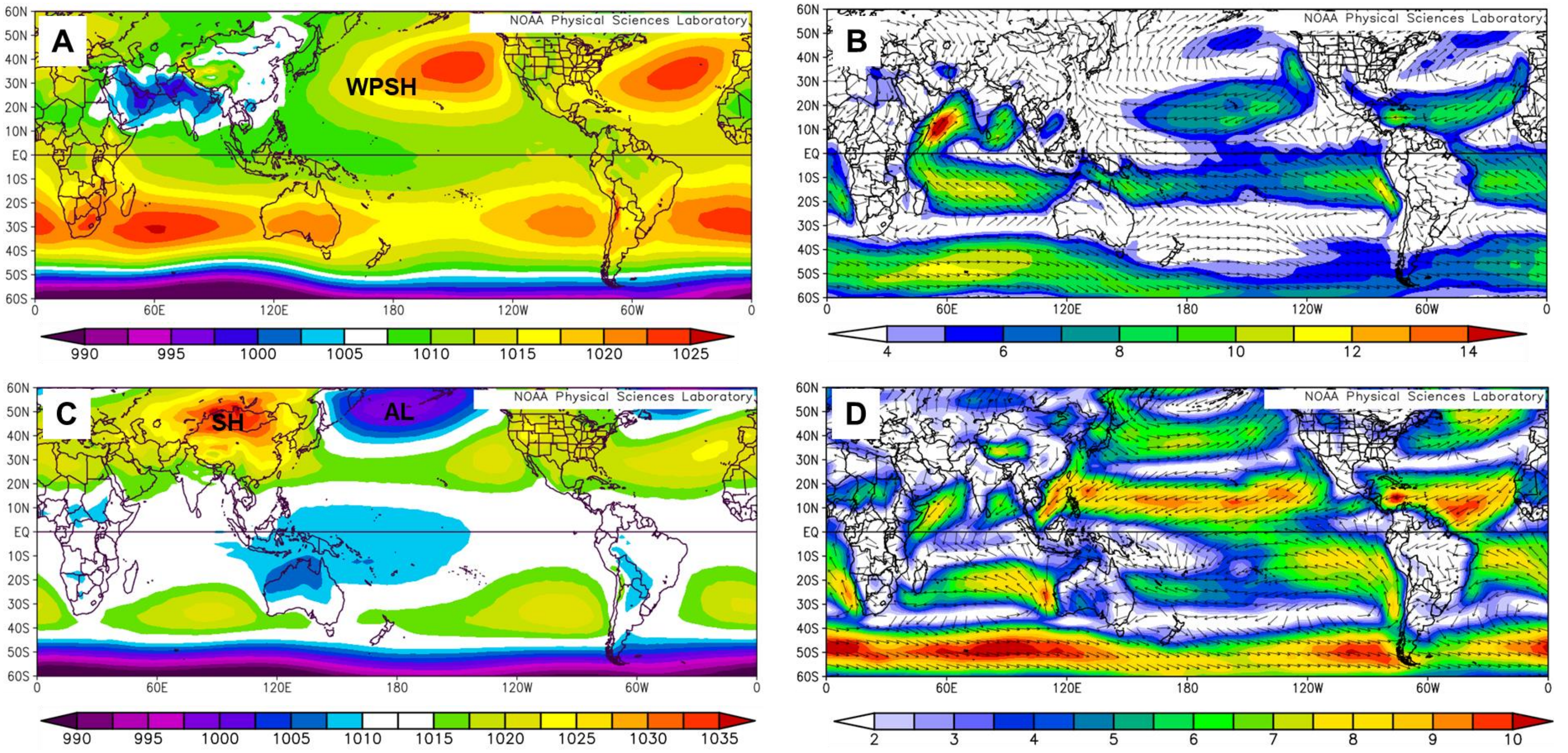

Figure 2. Composite sea-level pressure map (A) and 1000 mb vector wind map (B) from June to August (1982 – 2020) derived from NCEP/NCAR reanalysis data. The anticyclonic wind circulation around the Western Pacific Subtropical high (WPSH) is the dominant atmospheric circulation in boreal summer. Composite sea-level pressure map (C) and 1000 mb vector wind map (D) from December to February (1982 – 2020) derived from NCEP/NCAR reanalysis data. The well-developed Siberian high and Aleutian low dominate the winter variability mode in the Northern Hemisphere. Composite maps were generated in the National Ocean and Atmospheric Administration - Physical Sciences Laboratory (NOAA-PSL) Climate Plotting and Analysis Tools (https://psl.noaa.gov/data/getpage/).

The dominance of the high latitude atmospheric systems is accompanied by changes in winter SST and rainfall. Figure 3C shows winter cooling of subtropical NW Pacific from 26°C - 28°C in summer down to 16°C – 22 °C. The northern extent of IPWP contracted southwards resulted in slight cooling in SCS and the Philippine Sea. The ITCZ rainbelt also migrated southwards (10°N to 15°S). While the subtropical NW Pacific experiencing a relatively dry winter (2-3 mm/day), the eastern side of central and southern Philippines are generally wet because of the southward migration of ITCZ (Fig. 3D). The Northern Philippines is relatively drier because of the prevailing winter monsoon.

The temperature and rainfall trends in the NW Pacific have large impacts on the socio-economic stability of the region. There is a need to understand the sensitivity of the EAM system to the current global warming condition. The uncertainty of future climate trends because of global warming will disrupt the boreal winter variability mode. Earlier global warming projections using the atmosphere-ocean global climate models (AOGCMs) have shown that the Siberian high and Aleutian low will weaken triggering a weakened EAWM (Hori and Ueda 2006). However, the Siberian high recovered because of the increase in Eurasian snow cover in the past two decades (Jeong et.al. 2011). A more recent model using the Coupled Model Intercomparison Project phase 5 (CMIP5) shows large uncertainties in the EAWM's projection at +1.5°C warming but more robust changes at +2.0°C warming (Miao et al. 2020). Recent climate models are still improving to accurately predict the future scenarios. Simultaneously, paleoclimate research is also important to make necessary adjustments on the input parameters of these models. Before incorporating the anthropogenic impacts, climate modelers should understand the natural climate variability.

Paleoclimate records from the tropical and subtropical NW Pacific are vital to understand the climate variability across different latitudes. Holocene and Pleistocene climate records are often derived from higher latitude marine and terrestrial sediments. Seasonal ocean temperature and rainfall records are needed to isolate the signals from the EASM and EAWM. However, marine records with seasonal resolution are limited in Holocene and 20th century. This is one of the data gaps that can be addressed by this research.

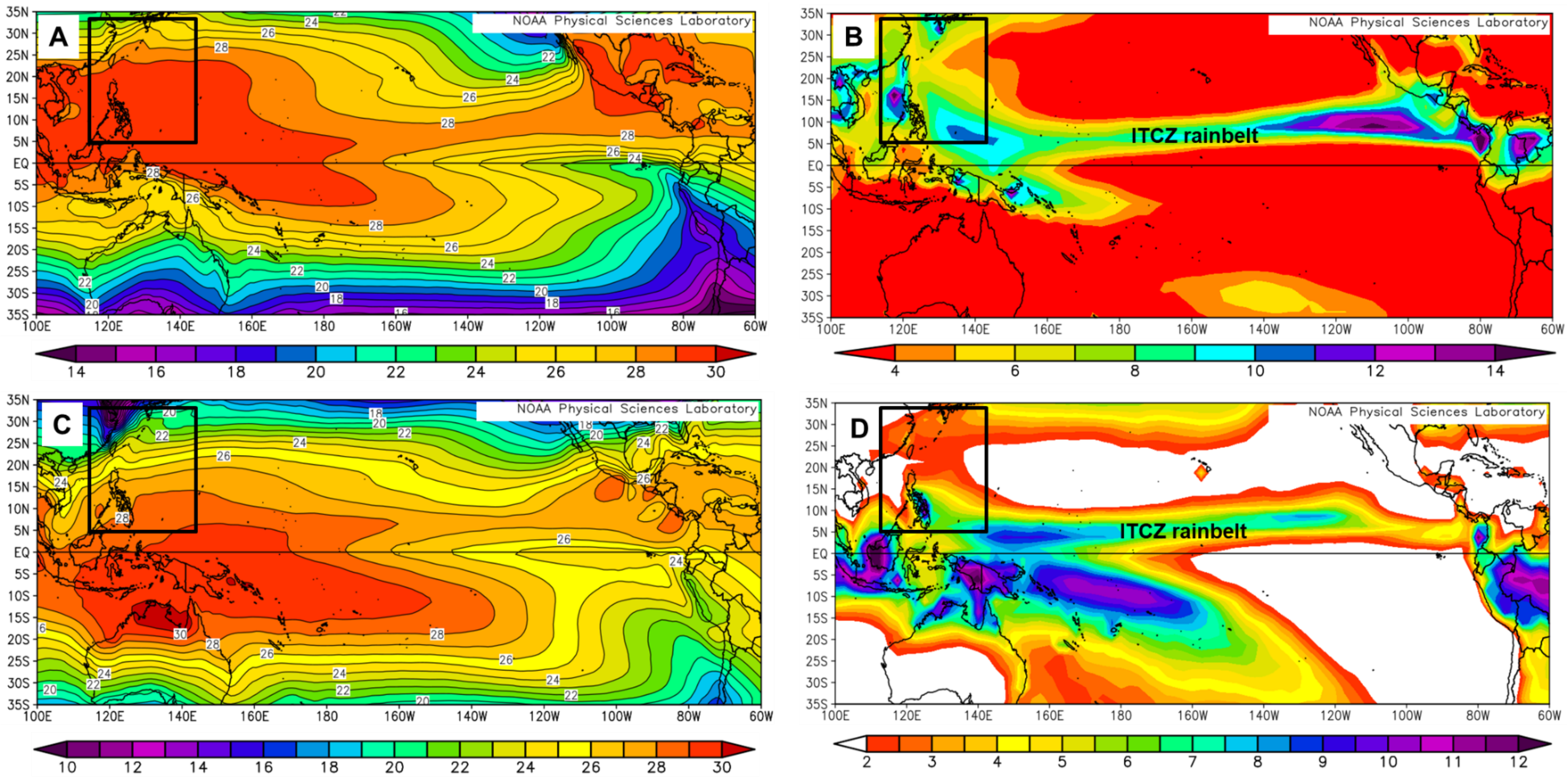

Figure 3. Composite SST map (A) and rainfall map (B) from June to August (1982 – 2020) derived from NOAA OISST and GPCP data. Composite SST map (C) and rainfall map (D) from December to February (1982 – 2020) derived from NOAA OISST and GPCP data. The seasonal shift between summer and winter monsoon corresponds to the expansion and contraction of the Indo-Pacific Warm Pool (IPWP) and the intertropical convergence zone (ITCZ) rainbelt. Black box represents the NW Pacific area. Composite maps were generated in the National Ocean and Atmospheric Administration - Physical Sciences Laboratory (NOAA-PSL) Climate Plotting and Analysis Tools (https://psl.noaa.gov/data/getpage/).

1.3. The El Niño Southern Oscillation

The El Niño Southern Oscillation (ENSO) dominates the interannual variability of the Earth's climate affecting the regional and global rainfall patterns. "Warm" and "cold" phases of ENSO are defined by the magnitude of SST anomalies (SSTA) over the Niño-3.4 region (5°S-5°N, 170-120°W) in the eastern and central equatorial Pacific (Chan et al. 1999). The "warm" phase often describes the El Niño year, and the "cold" phase described the La Niña year in a quasi-biennial oscillation. The present-day ENSO is defined by a 2-to-8-year cycle. ENSO is an ocean-atmospheric system which is closely linked with the Walker circulation in the equatorial Pacific. In neutral years, a large-scale ascent in western Pacific corresponds to low surface pressure and precipitation while a large-scale descent occurs in eastern Pacific with high surface pressure and less precipitation. During El Niño year, the Walker circulation is weakened. The central Pacific is relatively warmer and receives more precipitation than the western Pacific. This condition is opposite during La Niña year. Figure 4A shows the correlation between composite Niño-3.4 SSTA and NOAA OISST data from September to April within the period 1949 to 2012. The correlation map illustrates the warm phase of ENSO when the central and eastern equatorial Pacific are warmer than the western equatorial Pacific (160°E to 120°E). The SSTs of South China Sea and East China Sea shows weak to moderate positive correlation (r = 0.2 to 0.7) to the Niño-3.4 SSTA.

The interaction of ENSO and the East Asian monsoon system has been studied extensively in the past two decades (Webster and Yang 1992; Webster et al. 1998; Wang et al. 2000; Kim et al. 2017; Wang et al. 2020). The seasonal prediction of the East Asian precipitation has attracted attention because of its impacts on economy, and water and food security. Investigating how the interannual ENSO affects the EA monsoon is vital in seasonal prediction (Wang et al. 2020). The low-level tropospheric anticyclonic circulation in the western North Pacific is the link between the warm (cold) phase of ENSO in the Niño-3.4 region to the weak (strong) EAWM (Wang et al. 2000; Chen et al. 2013; Kim et al. 2017). The anticyclonic wind anomalies in high latitude North Pacific develop in the late fall of the El Niño developing year, indicating a weak EAWM. This anomalous anticyclone persists until the early spring to summer of the following year bringing higher rainfall in the southern China and Japan. Furthermore, the response of the EASM to the El Niño is highly dependent on the phase timing. The rainfall in China, Korea, Japan (collectively known as East Asian winter front zone (EAFZ)) tends to decrease in the El Niño developing summer but tends to increase in the El Niño decaying summer after the mature phase in winter (Wang et al. 2020). Aside from the ENSO phase timing, the ENSO amplitude fluctuations, asymmetry between El Niño and La Niña, and inherent seasonal monsoon anomalies can obscure the effect of ENSO to the EAFZ rainfall. The correlation map of the Niño-3.4 SSTA and GPCP precipitation (September to April) from 1948 to 2012 shows weak to moderate positive correlation (r = 0.2 – 0.6) in China and Southern Japan (Fig. 4B). This is consistent with the published ENSO-rainfall correlation (r = 0.61) in EAFZ (Wang et al. 2020).

The rainfall variations in mainland Southeast Asia, the Philippines, and Indonesia show robust negative correlations with ENSO. During the late fall of El Niño developing year, an anticyclone anomaly is formed in the Philippine Sea. The surface cooling and the introduction/advection of dry northerly wind further suppress the convection to the east of the anticyclone anomaly, creating a positive ocean-atmosphere feedback mechanism (Wang et al. 2020). This condition will dominate from winter to the summer of the El Niño decaying year resulting in less rainfall in mainland Southeast Asia and the Philippines. The correlation map of the Niño-3.4 SSTA and GPCP precipitation (September to April) from 1948 to 2012 shows strong negative correlation (r = -0.2 to -0.8) in mainland Southeast Asia, the Philippines, and Indonesia (Fig. 4B). This is consistent with the published ENSO-rainfall correlation (r = -0.84) in Southeast Asia (Wang et al. 2020).

Due to the complex teleconnection of equatorial Pacific SSTA and the East Asian climate, few paleoclimate records were able to explain the ENSO-EAM interaction in the past centuries and Holocene. The different response of subtropical and tropical NW Pacific climate to ENSO variability is challenging for paleoclimate reconstruction. Another challenge is the intraseasonal, seasonal, and interannual timing of the ENSO-EAM interaction, which cannot be resolved by sediment and speleothem records. This dissertation will explore the potential of modern and fossil coral records from tropical and subtropical NW Pacific to isolate the EAM and ENSO signals from coral geochemical records and to reconstruct past conditions of EAM and ENSO including the magnitude and frequency of El Niño and La Niña events. The next section will discuss the potential of coral sclerochronological and geochemical evidence to understand past environments and to detect past climate signals in reconstructed SST, salinity, and rainfall records.

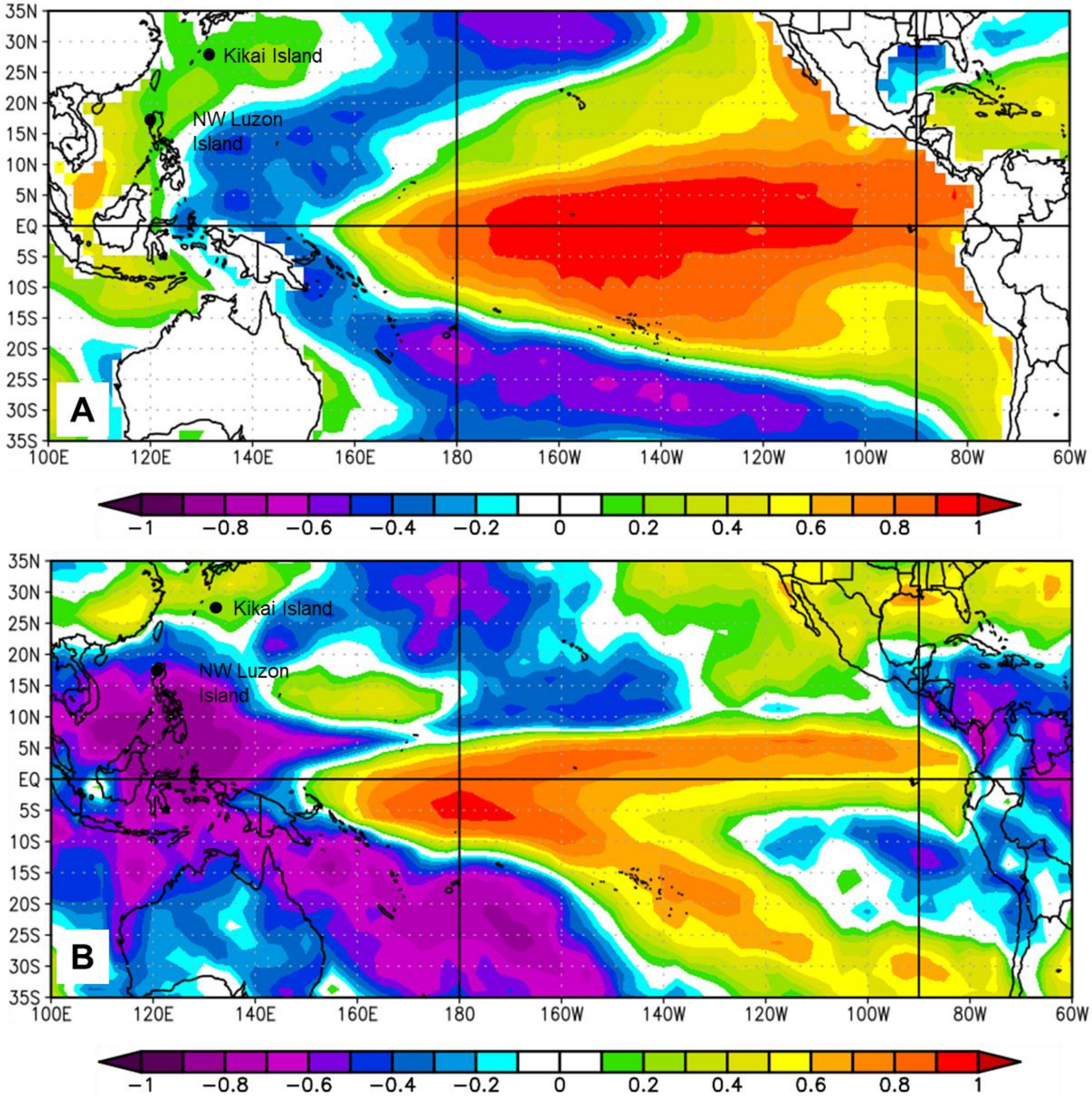

Figure 4. A. Correlation map illustrates the warm phase of ENSO when the central and eastern equatorial Pacific are warmer than the western equatorial Pacific (160°E to 120°E). The SSTs of South China Sea and East China Sea shows weak to moderate positive correlation (r = 0.2 to 0.7) to the Niño-3.4 SSTA. **B.** Correlation map of the Niño-3.4 SSTA and GPCP precipitation (September to April) from 1948 to 2012 shows weak to moderate positive correlation (r = 0.2 – 0.6) in China and Southern Japan and strong negative correlation (r = -0.2 to -0.8) in mainland Southeast Asia, the Philippines, and Indonesia**.** Correlation maps were generated in the National Ocean and Atmospheric Administration - Physical Sciences Laboratory (NOAA-PSL) Climate Plotting and Analysis Tools (https://psl.noaa.gov/data/getpage/).

1.4. Coral Growth Parameters and Geochemical Proxies

Corals are natural records of past climatic and environmental changes. The alternating high- and low-density bands (Fig. 5) reveal a strong correlation with seasonal variations in ocean conditions (Knutson et al. 1972; Barnes and Lough 1989). Spatiotemporal variables such as water depth, inshore to offshore, temperature gradients, SST variability/anomalies affect coral growth (Lough and Cooper 2011). The coral growth rate is different in coral colonies across different geographic locations and taxa. Other factors such as sedimentation, turbidity, and hydrographic conditions also affect the calcification and upward extension of coral colonies (Buddemeier et al. 1974; Scoffin et al. 1992; Cuevas et al. 2009; Lough and Cooper 2011). The linear extension rates of *Porites* corals are positively correlated with the annual changes of SST based on growth data from Hawaii, Thailand, Great Barrier Reef, Arabian Gulf, and Hong Kong (Grigg 1981; Scoffin et al. 1992; Lough and Barnes 2000; Goodkin et al. 2011). The extension rate and calcification rate are linearly correlated while the skeletal density and linear extension rate are inversely related (Scoffin et al. 1992; Lough and Barnes 2000). The correlation shows that the linear extension rate is the dominant control on calcification rates.

Modern and fossil corals from NW Pacific are sensitive to SST and SSS that are being modulated by ocean-climate systems such as Pacific Decadal Oscillation (PDO), ENSO and EASM (Morimoto et al. 2007; Kawakubo et al. 2017; Watanabe et al. 2014; Ramos et al. 2017; Ramos et al. 2019). Corals incorporates isotopes and trace elements that can be used to resolve seasonal SST, SSS, and rainfall changes. The paleothermometer coral Sr/Ca has been widely used to track SST changes (Beck et al. 1992). The partitioning of Sr and Ca in the aragonite crystal lattice of corals is dependent in 1) the Sr/Ca ratio in ocean water and 2) the Sr/Ca distribution coefficient between aragonite and seawater. Because of the long residence of Sr and Ca in the oceans thus, the Sr/Ca variability cannot be attributed to the variation of Sr and Ca ions in the seawater. Rather, the incorporation of Sr and Ca is thermodynamically dependent on the temperature of the seawater. Sr/Ca ratios of fossil corals can reconstruct the past SST changes up to seasonal timescales (Gagan et.al. 1998). The method allows paleoclimatologists to look at the annual cyclicity with clear summer and winter SST shifts using annually banded corals (Fig. 6). Precise calibration of modern coral Sr/Ca records and in situ/instrumental SST should be carefully done to avoid systematic errors in the reconstruction.

Epstein et.al. (1953) introduced the relationship of temperature and $\delta^{18}O$ relative to Cretaceous belemnite of the Pee Dee Formation. The study revealed the potential of $\delta^{18}O$ derived from marine shell-bearing animals to determine the temperature of the seawater where the organism grows. Corals and other marine carbonate organisms derived their skeleton from both seawater bicarbonate and metabolic CO^2. Earlier oxygen isotope measurements from coral aragonite reveal sea surface temperature dependency but have apparent isotopic disequilibrium (Weber and Woodhead 1992). Coral $\delta^{18}O$-SST curves are parallel or nearly parallel to the paleotemperature scale of Epstein et.al. 1953 but recorded lower values. The temperature dependency of coral $\delta^{18}O$ allows the reconstruction of past sea surface temperature in Galapagos Island (Dunbar et.al. 1994), New Caledonia (Quinn et.al. 1998), Great Barrier Reef (Gagan et.al. 1998) and Caribbean (Winter et.al. 2000; Watanabe et.al. 2001). Recent development shows that the coral oxygen isotope ($\delta^{18}O_{coral}$) is a function of both surface ocean temperature (Watanabe et al. 2001) and the $\delta^{18}O$ of the seawater ($\delta^{18}O_{sw}$) changes (Julliet-Leclerc and Schmidt 2001). The equation below shows that coral aragonite $\delta^{18}O$ is dependent on two parameters: 1) water temperature and 2) water oxygen isotopic composition (Julliet-Leclerc and Schmidt 2001).

$$\delta^{18}O_{coral}\ (‰\mathrm{VPDB}) - \delta^{18}O_{sw}(‰\mathrm{VSMOW}) = 0.45 - 0.20\ (\pm\ 0.02)\mathrm{x\ SST}(°\mathrm{C})$$

The $\delta^{18}O_{sw}$ is estimated using paired coral Sr/Ca and $\delta^{18}O_{coral}$ measurements by removing the SST component from the $\delta^{18}O_{coral}$ (Ren et al. 2003; Cahyarini et al. 2008; Nurhati et al. 2011). Because of the $\delta^{18}O_{sw}$ component, the $\delta^{18}O_{coral}$ is also sensitive to past salinity variation (Reed et al. 2022). In the Western Pacific, the $\delta^{18}O_{sw}$ contributes up to 89% of $\delta^{18}O_{coral}$ variability (Thompson et al. 2022). Sea surface salinity (SSS) is often linked to hydrological balance of evaporation and precipitation, ocean advection, and vertical mixing (Helm et al. 2010; Bingham et al. 2012). But compared to past temperature reconstruction, past salinity reconstructions are limited. Using multi-proxy geochemical approach, temperature, salinity, and rainfall changes can be reconstructed in relatively higher temporal resolutions from monthly to interannual scales. Long-term changes in the SST and rainfall driven SSS in the tropical and subtropical NW Pacific would allow us to investigate the changes in EAM and ENSO.

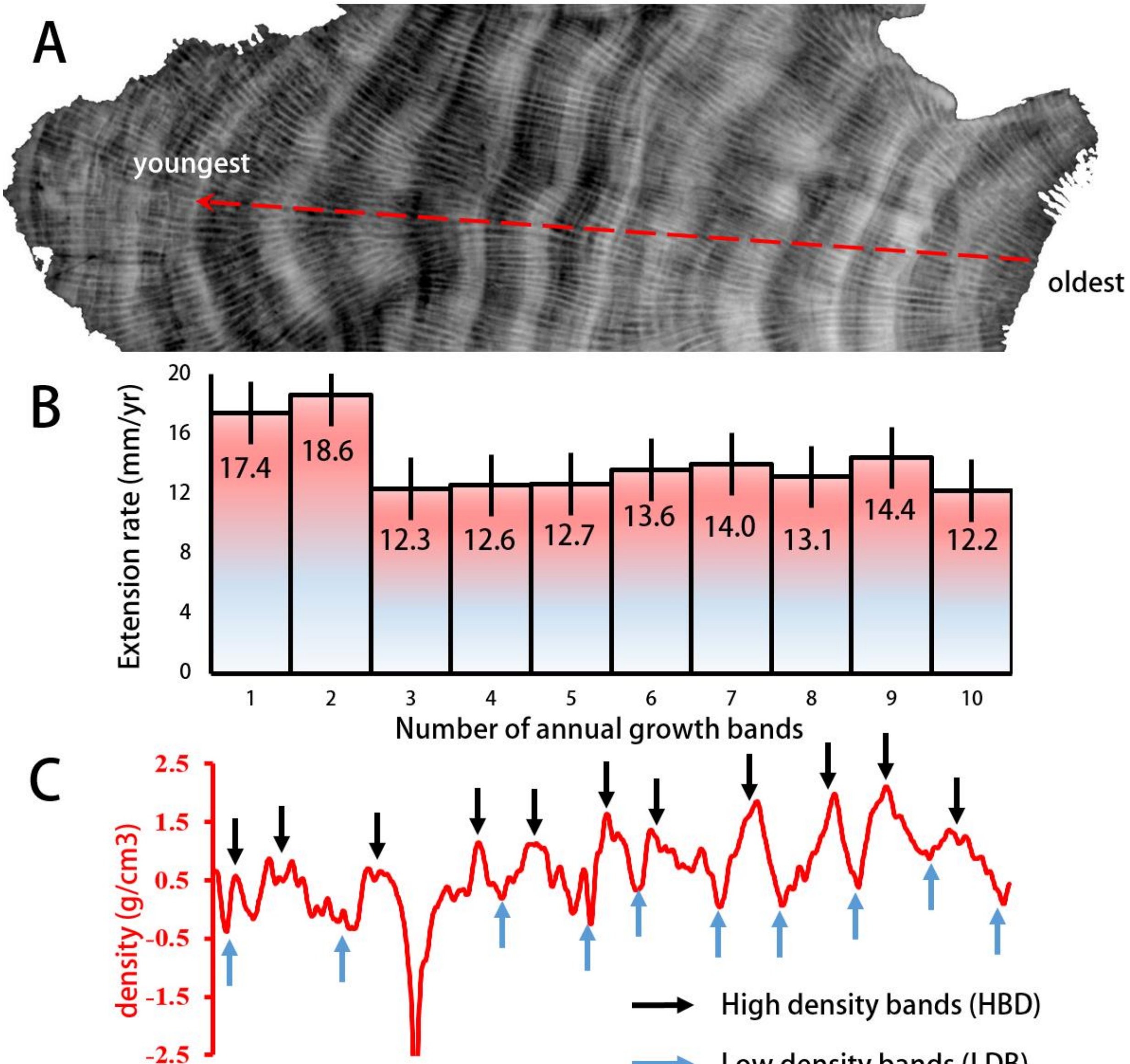

Figure 5. Growth parameters in annually banded *Porites* corals. A. The alternating light and dark bands represent seasonal cycles in annual coral growth. B. Linear extension rate is measured from the outward growth per year. C. The light and dark bands correspond to the high- and low-density bands, respectively.

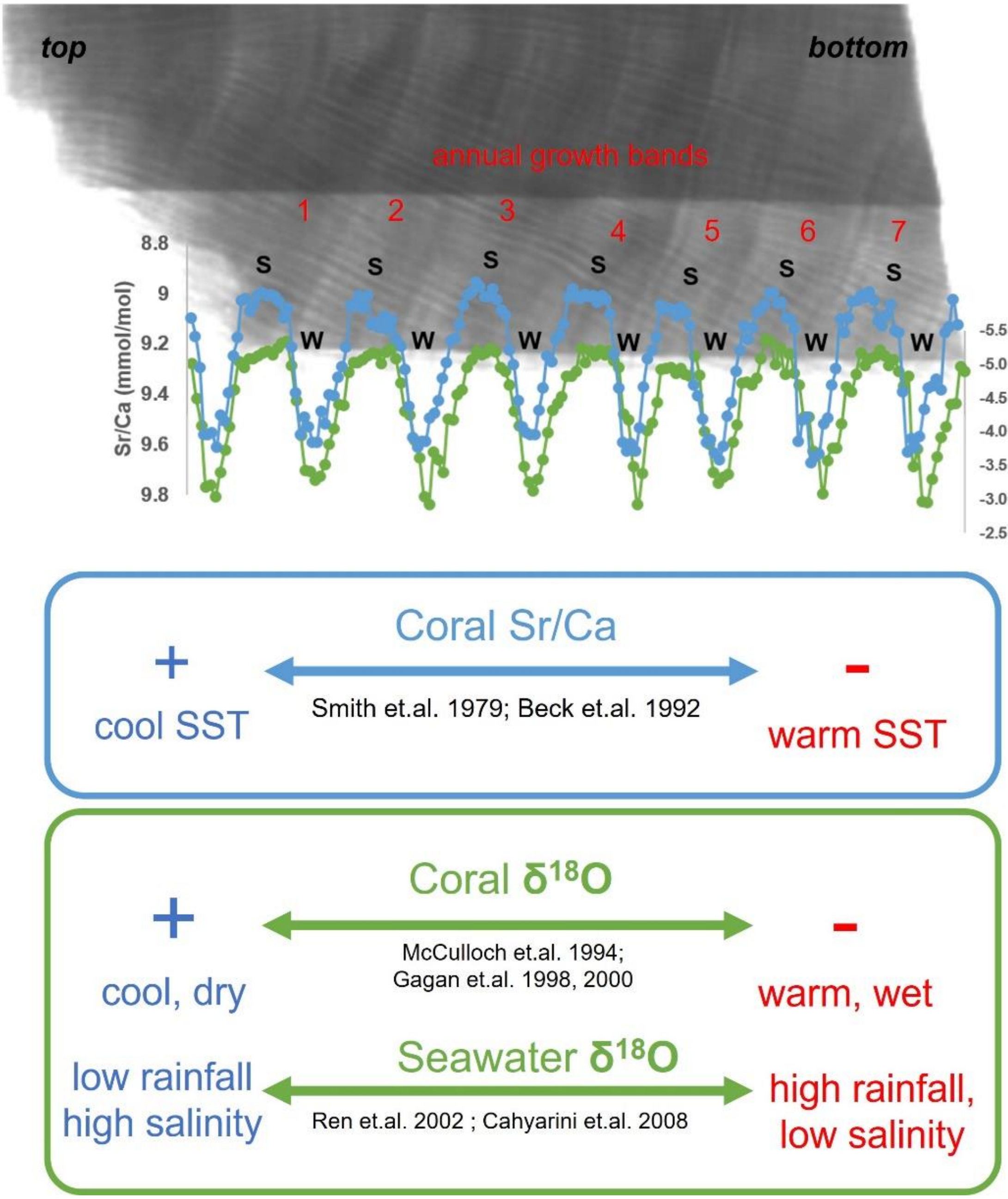

Figure 6. Coral geochemical proxies in annually banded *Porites* corals. Coral Sr/Ca is used to track changes in SST. $\delta^{18}O_{coral}$ is a function of both changes in SST and $\delta^{18}O_{sw}$ and can track changes in both SST and SSS. $\delta^{18}O_{sw}$ can potentially reconstruct changes in the hydrological processes such as evaporation and precipitation.

1.5. Geology and Climate of the Study Areas

1.5.1. Kikai Island

Geology

Kikai Island (28°16’ to 28°22’N and 129°55’ to 130°02’E) is situated in the eastern fringe of East China Sea in the northern part of Ryukyu Archipelago, Kagoshima Prefecture, Japan. The island is underlain by the Pleistocene Ryukyu Group and the Holocene marine terraces (Fig. 7; Sasaki et.al. 2004). The Holocene marine terraces are characterized by an offlap sequence of four marine terraces (Sugihara et.al. 2003). These are situated up to 13 m above mean sea level, subdivided into Terrace I (10.8–11.1 and 8.5–8.9 m), Terrace II (5.0–5.3 m), Terrace III (4.0–4.3 m) and Terrace IV (1.9–2.5 m). These Holocene terraces are part of the multi-level marine terraces dated back Late Pleistocene due to the continuous uplift over the last 100,000 years. Nine (9) fossil *Porites* samples and 1 modern coral core were collected from different locations in Kikaijima.

Emerged/uplifted marine terraces are important morpho-stratigraphic indicators of the Quaternary carbonate deposition. These terraces are formed by both sea-level fall and/or coseismic events forming the prominent staircase topography with horizontal abrasion platforms and terrace riser (Ota et.al. 1978; Sugihara et.al. 2003). The fossil *Porites* samples were collected from three marine terraces (TII, TIII and TIV). Terrace II has a wide terrace platform around 40 – 100 m in width at 4 – 5 masl. Terraces III and IV have narrower terrace platforms of ~20 m width. The highest carbonate accretion in Kikaijima occurred during the formation of TII (Ota et al. 1978). TIII and TIV represent a relatively shorter relative high stand from 4100 to 1400 years ago. There are 19 hermatypic coral genera present in the Holocene marine terraces. The most abundant genus is the branching *Acropora* (Fig. 8C-D), followed by the genus *Goniastrea*. Other genera such as *Favites* (Fig. 8B), *Cyphastrea*, *Platygyra*, *Leptoria*, *Porites* (Fig. 8E-F), *Montipora*, *Goniopora*, *Alveopora* are also present. The eastern coast of the island tends to have higher coral coverage as compared to the western coast. The eastern coast also has wider terrace platforms than the western counterpart. The horizontal accretion of the coral reef on the eastern coast was more developed based on the terrace morphology and coral coverage. The east and west coast discrepancy in coral coverage and coral reef accretion is controlled by wind-driven wave stress. The shifting monsoon intensity in the Holocene could possibly affect the wave intensity in Kikai Island.

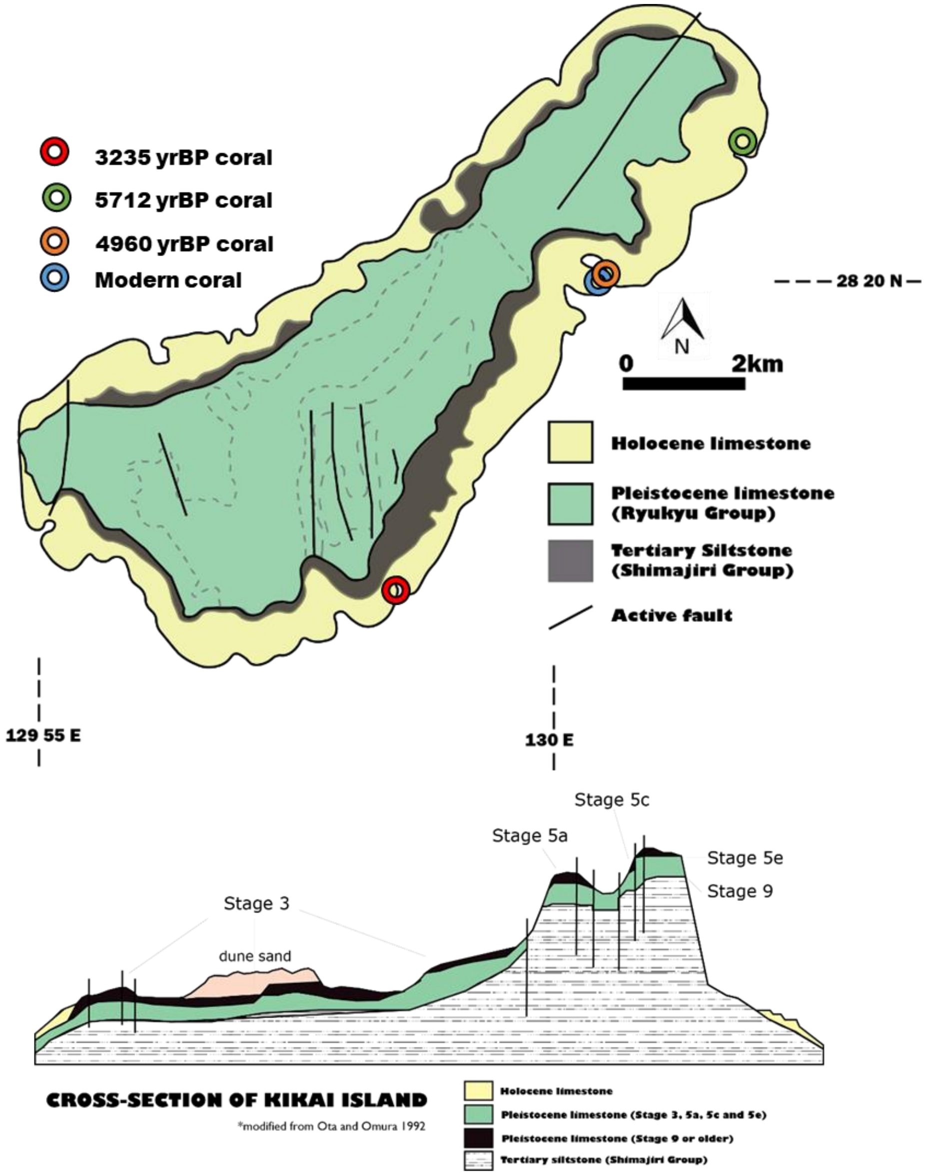

*modified from Ota and Omura 1992

Figure 7. Geologic map and cross-section of Kikai Island. The Pleistocene Ryukyu Group (green) is distributed in the interior part of the island while the Holocene uplifted terraces (yellow) are distributed along the coastal zones. The clastic-dominated Shimajiri Group is the basement unit of Kikai Island.

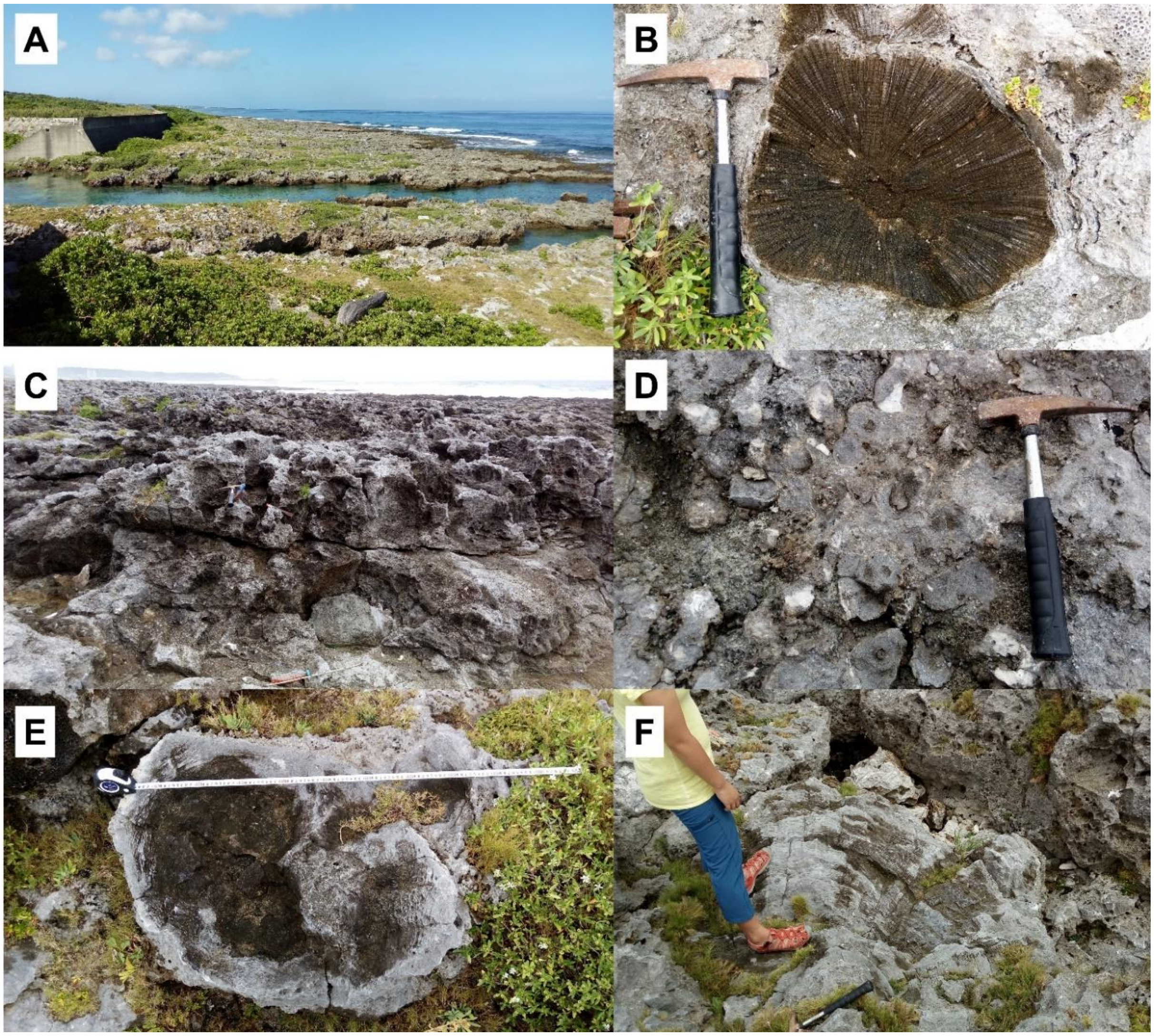

Figure 8. Carbonate sedimentological composition of the Holocene limestone in Kikai Island. A. Panoramic view of the three-level uplifted marine terraces in Kikai Island. The island is predominantly composed of reef-building hermatypic coral genera such as *Favites* (B), *Acropora* (C,D), and *Porites* (E,F).

Climate

SST from Advanced Very High-Resolution Radiometer (AVHRR) recorded maximum SST of 28.6°C to 28.7°C in July and August and minimum SST of 20.6°C in February to March from 1981 to 2015 (Fig. 9A; 9D). Reanalysis dataset from Simple Ocean Data Assimilation (http://apdrc.soest.hawaii.edu/dods/public_data/SODA/soda_3.3.1/) shows that lowest average SSS was 34.31 psu in July and highest average SSS was 34.78 psu in February from 1980 to 2015 (Fig. 9B;9E). Accumulated monthly precipitation calculated from in-situ daily measurements (Figure 9C; 9E) from Northern Kikai Island collected from 2007 to

2015 shows two peaks of high precipitation in June (ave. 248 mm) and September (ave. 175 mm) and lowest value in December (average of 72 mm). This rainfall pattern follows the “onset-break-revival” cycle of the East Asian summer monsoon (Chen et al. 2004). The rainfall peak in June corresponds to the onset of summer monsoon rainfall front in Southern Japan. The high (low) rainfall and SST months follow the dominance of the EASM (EAWM) (Fig. 9D, 9E). The monthly SSS around Kikai Island is highly influenced by the in-situ rainfall (Fig. 9E). The decrease of SSS from 34.7 psu to 34.1 psu occurs after the onset of the summer monsoon rainfall.

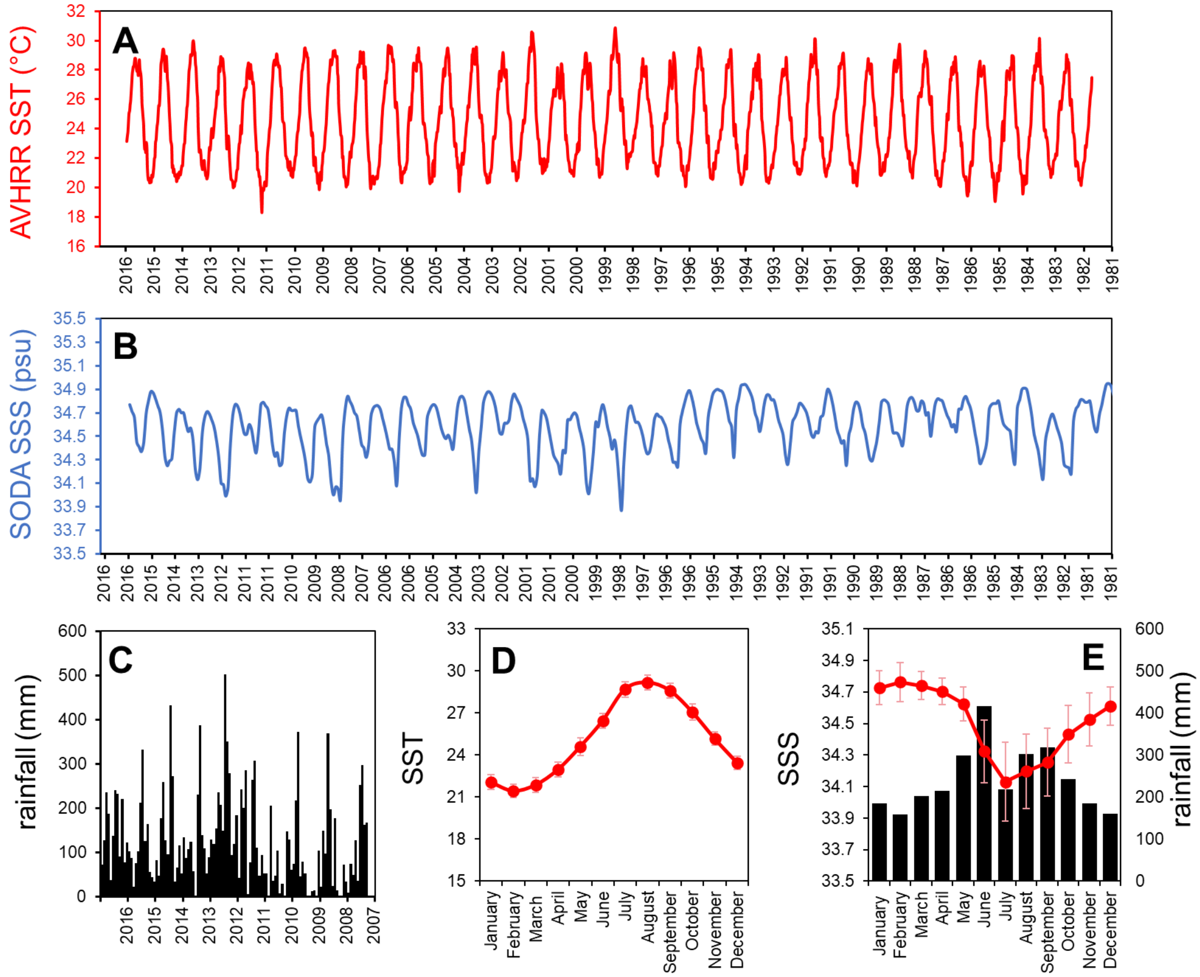

Figure 9. Hydroclimate of Kikai Island. A. Advanced Very High-Resolution Radiometer (AVHRR) SST in Kikai Island from 1981 to 2015. B. Simple Ocean Data Assimilation (SODA) reanalysis SSS in Kikai Island from 1981 to 2015. C. Monthly accumulated rainfall from in-situ daily rainfall gauge data from northern Kikai Island from 2007 to 2017. D. Mean monthly SST from AVHRR SST. E. Mean monthly SODA SSS and in-situ rainfall

1.5.2. Northwest Luzon Island

Geology

The active tectonic and geologic setting of the Luzon Island is associated with crustal plate interactions to the Philippine Mobile Belt. The Sunda Plate subducts eastward while the Philippine Sea Plate subducts westward beneath the Philippine Mobile Belt. The NW Luzon is facing the Manila Trench, a manifestation of the north-south trending subduction zone formed by the convergence of Sunda Block and the Philippine Mobile Belt (Aurelio 2000). The marine terraces in NW Luzon are attributed to the accumulated uplift by aseismic and seismic processes related to the possible earthquake generators such as Manila Trench and intraplate offshore faults (Ramos and Tsutsumi 2010; Ramos et al. 2017).

The coastal towns of La Union in NW Luzon are underlain by the Late Miocene to Early Pliocene Amlang Formation, Pliocene Cataguintingan Formation, Pleistocene Damortis Formation, and Holocene uplifted marine terraces (Fig. 10). These formations are distributed as folded sequences with major fold axis at NNW-SSE direction. Amlang Formation is composed of alternating beds of deep marine mudstones, shale, siltstone, and fine-grained sandstones with minor occurrence of conglomerate. Amlang Formation is dated late Late Miocene to Early Pliocene (Planktonic Foraminiferal NN17 - NN19 Zone) based on the first and last occurrences of *Sphaeroidinellopsis seminulina* and *Globorotalia merotumida*. Overlying the Amlang Formation, Cataguintingan Formation is described as massive to bedded volcaniclastic-dominated suite of tuffaceous sandstone and siltstone and lithic tuff, mollusk-rich sandstone strata with minor thin beds of calcareous pelagic sediments and conglomerate. The formation is dated Early Pliocene based on the first occurrence of *Globorotalia tumida*, *Globorotalia crassaformis ronda*, and *Neogloboquadrina dutertrei* and last occurrence of *Globorotalia merotumida* and *Globorotalia plesiotumida*. The Pleistocene Damortis Formation has two members: a clastic member of sandstone and siltstone and a limestone member of coralline boundstone, rudstone, floatstone, calcarenite, and calcisiltite. The Holocene uplifted marine terraces are defined by staircase topography characterized by wide platform, wave cut notches, tidal inlets, terrace risers. The limestone has main reef facies hermatypic genera of *Acropora*, *Diploria*, *Favites*, *Galaxea*, *Favia*, and *Porites*. Coral colonial morphology is often preserved but often coral skeletons are diagenetically altered.

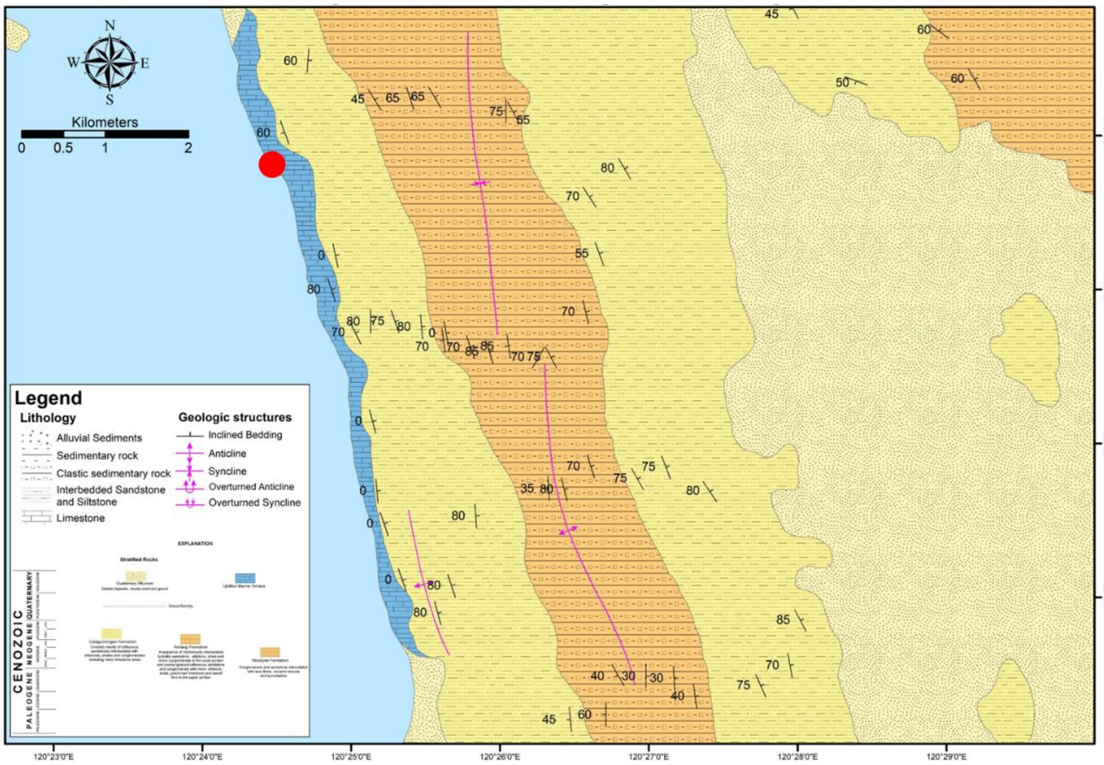

Figure 10. Geologic Map of Santo Tomas, La Union showing the Holocene uplifted marine terrace (blue) along Damortis beach. The red circle represents the sampling site. *Source: Updated MGB Geologic Map by Cenozoic Stratigraphy of the Philippines Project (2020)*

Porites colonies were exposed in the eroded terrace riser of the single terrace platform along Damortis Beach in the town of Rosario, La Union (N16°13’46.1’’ E 120°24’26.6’’). The uplifted marine terrace overlies the bedded sandstone-siltstone of Damortis Formation. The limestone is exposed by wave erosion of the terrace with maximum thickness of 2 m. The coral-dominated zone at 2-3 masl is composed of branching- and massive-type corals admixed with bivalve shells loosely bounded by carbonate-derived sand and silt. In the nearby towns of Bacnotan and Balaoan, Holocene uplifted marine terraces are also observed. There are two-level marine terraces in Bacnotan. The highest terrace (TI) is situated 2-4 m above mean sea level (amsl) while lower terrace (TII) is 1-2 m amsl. The marine platform of Terrace II is 45 m wider than the platform of the higher Terrace I. Numerous tidal inlets or creeks are cutting perpendicular to the shoreline, indicating a strong influence of wave and tidal action in the terrace morphology. In Balaoan, the uplifted reef flat is ~0.5 m amsl with higher coral rubble rampart (Immuki Island) about 2.4 m amsl (Siringan et.al. 2016). In the south, the reef flat is connected to the beach but in the northern portion, a back-reef lagoon is present. The back reef lagoon has well-preserved fossil microatolls made up of dominantly *Porites*. Microatolls are intertidal coral colonies with dead central, flat portions and living corals occur in the perimeter. The growth of coral microatolls is typically lateral, different from the vertical growth of massive coral colonies. Microatolls are used to determine the past sea level and uplift rate due to earthquakes.

The uplifted marine terraces are distributed further north of the NW Luzon coastal stretch. Stratigraphically, the Holocene terraces are situated on top of Laoag Formation. This is characterized by the occurrence of interbedded sandstone-siltstone-claystone and occasional reefal limestone and limestone breccia. The sandstones are generally well-bedded, cream to buff color and calcareous in composition. Minor conglomerate beds contain abundant molluscan shells with wood and leaf fossils. The Laoag Formation is dated late Early Pliocene to Pleistocene. In the town of Currimao, Ilocos Norte, the highest marine terrace is situated about 24 to 35 masl dated 108 ± 0.80 kyr to 198.5 ± 1.35 kyr (Maxwell et al. 2018). This terrace represents the stratigraphically younger section of Laoag Formation dated Late Pleistocene.

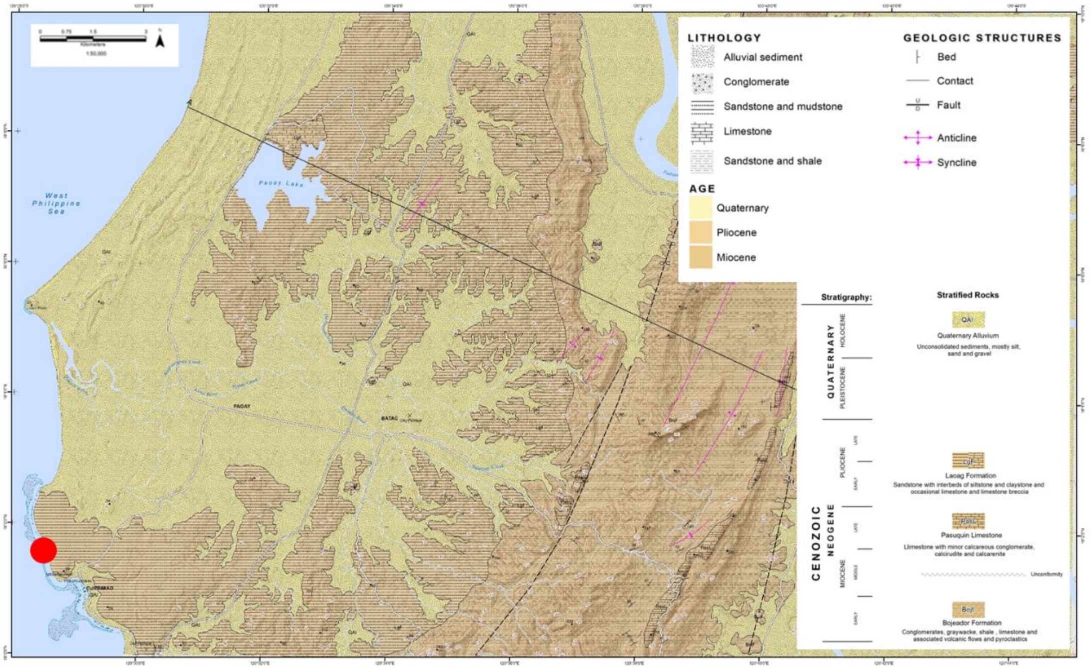

Figure 11. Geologic Map of Batac Quadrangle, Ilocos Norte where the town of Currimao is in the southwesternmost portion. The red circle represents the sampling site. *Source: MGB Region 1 (2021)*

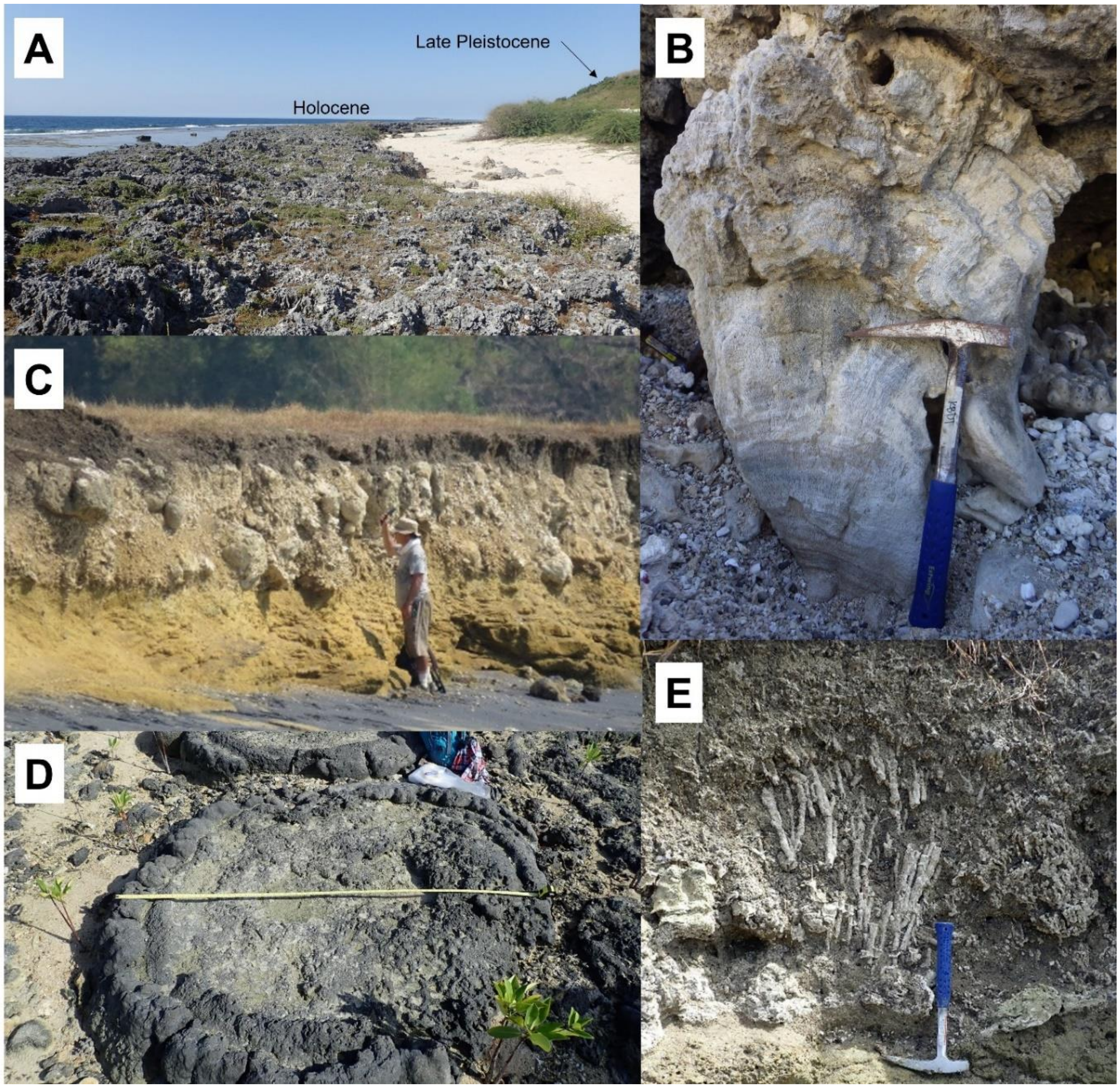

Figure 12. Carbonate sedimentological composition of the Holocene limestone in NW Luzon Island. A. Terrace I of the Holocene uplifted marine terraces in Currimao where fossil *Porites* (B) were observed. C. Photo of the single marine terrace in Damortis Beach, La Union. D. Photo of fossil microatoll in Balaoan, La Union. E. Fossil corals in Damortis Beach bounded by calcareous silt and mud.

The highest level of Holocene uplifted marine terrace of Currimao (N18°1’56.7’’ E 120°28’25.3’’) is approximately 9 m high above mean sea level. Currimao has three (3) defined marine terraces: Terrace I (TI), Terrace II (TII), and Terrace III (TIII). TI has a well-developed reef crest about 3-4 masl, characterized by the occurrence of well-preserved in-situ *Acropora*, *Heliopora*, *Pocillopora*, *Favia*, *Galaxea*, *Goniastrea*, and *Porites* that are loosely bounded by calcite cement and some coralline fragments. Borehole data revealed that the Currimao reef consisting of reef, bioclastic, clayey, and tuffaceous facies started accumulating around 9855 years ago until 6588 years ago (Shen et al. 2010). Maxwell et.al. (2018) extended the age range up to 6178 and 6163 years BP using younger ^{230}Th coral age dates, suggesting a mid-Holocene sea-level highstand in Northwest Luzon. TII and TIII have less defined terrace morphology with mostly gently sloping terrace platform. TII is composed of coral fragments and boulders loosely compacted by calcareous sandy materials. The terrace platform is mostly covered with reworked coral boulders, grassy and sandy patches. TIII is the highest terrace at 8-9 masl, mostly covered with dense vegetation. Coral fragments occur occasionally at this terrace level.

Climate

Monthly SST datasets (Fig. 13a) of Ilocos Norte and La Union from 2000 to 2021 was obtained from Integrated Global Ocean Services System (IGOSS) database (http://iridl.ldeo.columbia.edu/SOURCES/.IGOSS/.nmc/.Reyn_SmithOIv2/). The annual mean, maximum, and minimum SSTs in Ilocos Norte are 28.18°C, 29.95°C (June), and 25.89°C (February) respectively (Fig. 14a). The annual mean, maximum, and minimum SSTs in La Union are 28.56°C, 30.14°C (June), and 26.44°C (February) respectively (Fig. 14a). Monthly SSS datasets (Fig. 13b) of Ilocos Norte (2000 to 2015) and La Union (1991 to 2015) was downloaded from Simple Ocean Data Assimilation (SODA) database (http://apdrc.soest.hawaii.edu/datadoc/soda_2.2.4.php). The annual mean, maximum, and minimum SSSs in Ilocos Norte are 33.64 psu, 33.79 psu (March), and 33.45 psu (September) respectively (Fig. 14b). The annual mean, maximum, and minimum SSSs in La Union are 33.57 psu, 33.69 psu (March), and 33.38 psu (September) respectively (Fig. 14b). The 1991 – 2019 rainfall data from Laoag (Ilocos Norte) and Dagupan (La Union) stations were provided by the Climatology and Agrometeorology Division - Philippine Atmospheric, Geophysical and Astronomical Services Administration (CAD-PAGASA). The annual mean, maximum, and minimum rainfall in La Union are 2549 mm/y, 636 mm in August, and 5.8 mm in January, respectively. The annual mean, maximum, and minimum rainfall in Ilocos Norte are 2143 mm/y, 617 mm in August, and 3.1 mm in February, respectively.

The mean seasonal changes in SST, SSS, and rainfall observed in the collated datasets can be attributed to the occurrence of northeast/winter monsoon (locally known as *Amihan*) from November to February, southwest/summer monsoon (locally known as

Habagat) from May to October, and the dry season from March to May. The mean and maximum rainfall output in La Union decreased by 4% and 21% from neutral ENSO to warm ENSO (El Niño) years. The mean and maximum rainfall output in Ilocos Norte decreased by 14% and 18% from neutral ENSO to warm ENSO (El Niño) years. This suggests that the hydroclimate in NW Luzon Island in tropical Philippines is influenced by both seasonal monsoon and interannual ENSO variabilities.

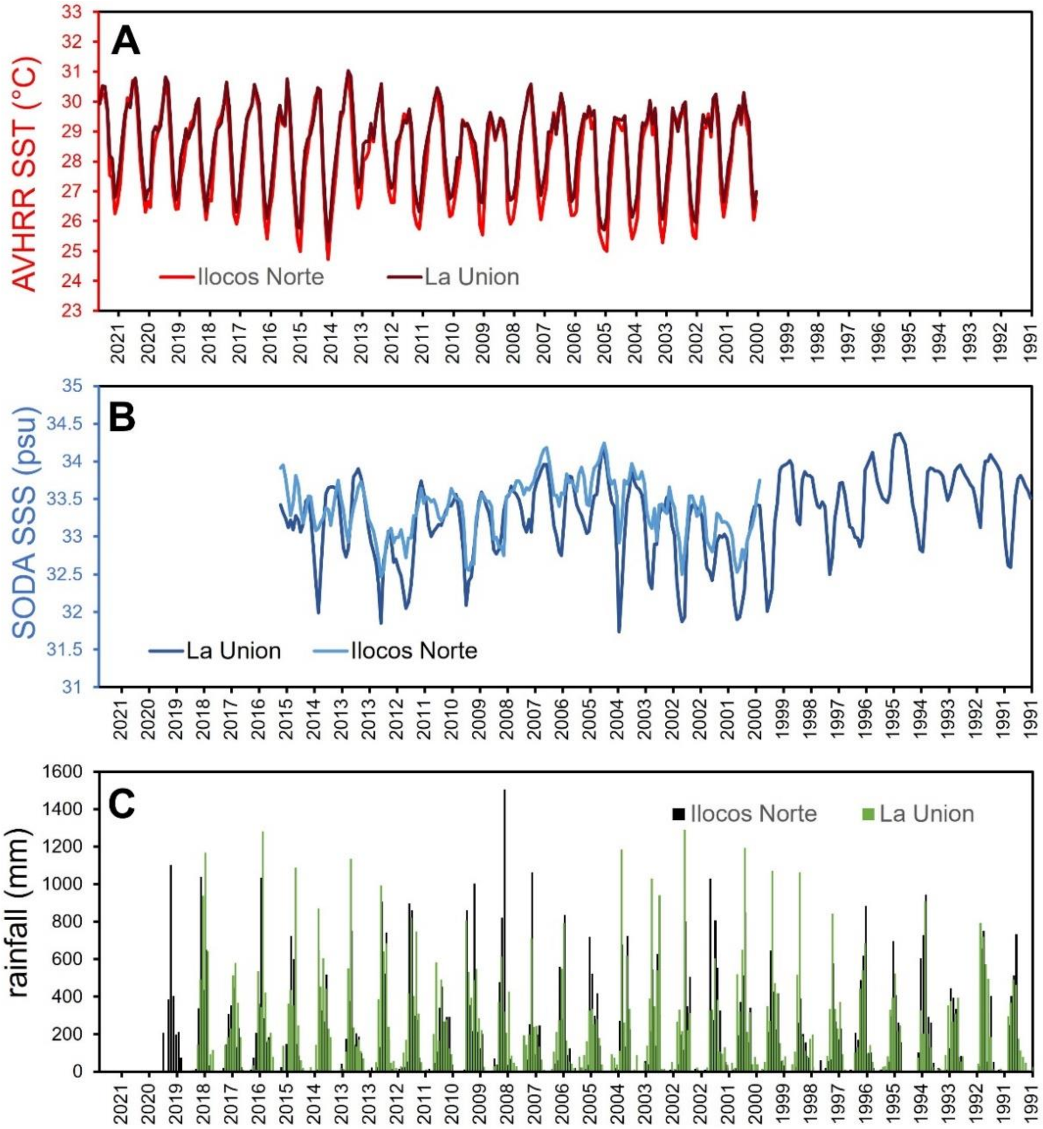

Figure 13. Hydroclimate in NW Luzon, Philippines. A. Monthly SST of Ilocos Norte and La Union from 2000 to 2021 B. Monthly SSS of Ilocos Norte (2000 to 2015) and La Union (1991 to 2015) C. The 1991 – 2019 rainfall data from Laoag (Ilocos Norte) and Dagupan (La Union) stations

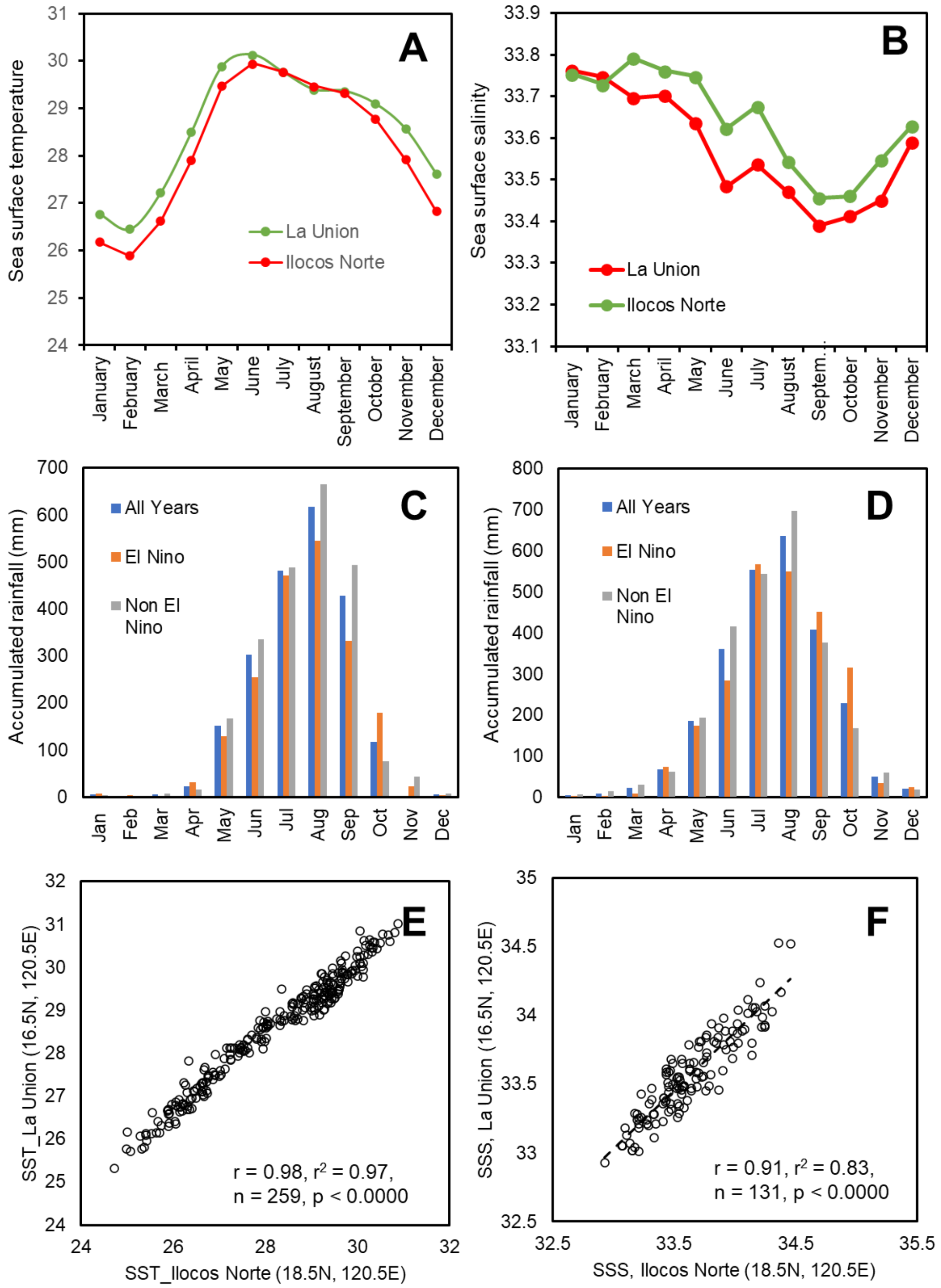

Figure 14. A. Mean seasonal change of SST in La Union and Ilocos Norte; B. Mean seasonal change of SSS in La Union and Ilocos Norte C. Mean monthly rainfall during neutral and warm (El Niño) phases of ENSO in La Union D. Mean monthly rainfall during neutral and warm (El Niño) phases of ENSO in Ilocos Norte E. Linear correlation of SST in La Union and Ilocos F. Linear correlation of SSS in La Union and Ilocos

1.6. Objectives

This dissertation aims to understand the EAM-ENSO interaction and its influence on the hydroclimatic variabilities of Northwest Pacific during the Holocene. During the conceptualization stage of the PhD thesis, two assumptions were considered:

- Climate changes in geological timescale are highly variable in terms of geographic and temporal patterns.
- Coral proxy records are controlled by both regional and local climate/environment

To validate these assumptions, the following questions will be answered in this dissertation:

- What are the paleoclimate signals of corals from subtropical Japan and tropical Philippines?
- Can fossil corals from Northwest Pacific reflect the seasonal and interannual variability of monsoon and ENSO at different Holocene time-windows?
- What are the implications of coral paleoclimate records in understanding the present and future climate?

The utility of coral geochemical records will be examined by testing the established models of geochemical proxies and hydroclimatic variables. Modern coral records from the two sites will be used to have site-specific calibrated models. Calibrated models will be applied to fossil coral records to convert the geochemical data to time-series paleoclimate data. Finally, this dissertation aims to discuss the implications of past climate mechanisms to the current global warming and future climate scenarios.

Chapter 2

MATERIALS AND METHODS

2.1. Field survey and Sampling

Several field surveys in the reported Quaternary (Holocene and Pleistocene) uplifted marine terraces were conducted in Kikai Island, Japan and NW Luzon Island, Philippines from 2016 to 2020. Fieldworks and coral sampling in Kikai Island were done in September 2016 and August 2017. A review of available geological information particularly on the geotectonic history and coral reef development in Kikai Island. Available topographic maps and geomorphologic survey profiles from previous field surveys were referred during the preparation of fieldwork. Several sites on the eastern and western coasts of Kikai Island such as Araki, Keraji, Nakaguma, Sateku, Kadon, Shiomichi, Shiitoke, and Somachi were surveyed for the occurrence of pristine fossil coral samples. A handheld Global Positioning System (GPS) receiver was used to locate and plot the geographic coordinates of the coral samples. Ten (10) fossil *Porites* samples were collected from these surveys (Table 1). Previously collected modern and fossil corals (age date: 4960 yr BP) from Shiomichi Bay were also used in this research.

Fieldworks and coral sampling in NW Luzon Island were done in February 2018 and November 2020. The field surveys were conducted together with the Department of Environment and Natural Resources - Mines and Geosciences Bureau (DENR-MGB) under the Cenozoic Stratigraphy of the Philippines Project. Topographic basemaps were prepared using 5-m resolution Interferometric Synthetic Aperture Radar-Digital Elevation Model (IfSAR-DEM) from the Department of Environment and Natural Resources - National Mapping and Resource Information Authority (DENR-NAMRIA). Geologic maps (1:50000 scale) from DENR-MGB were used during the field surveys. Reports on the occurrences of Holocene uplifted marine terraces in NW Luzon were reviewed. Several sites including Damortis Beach (Santo Tomas-Rosario), Paraoir (Balaoan), Cabarsican-Quirino (Bacnotan) in La Union, Badoc Island (Badoc), Pangil Beach (Currimao), Pasuquin, and Burgos in Ilocos Norte were surveyed. A handheld Global Positioning System (GPS) receiver was used to locate and plot the geographic coordinates of the coral samples. The height of the marine terraces and dimensions of fossil coral colonies were measured, and relatively well-preserved corals were sampled. Twenty-seven (27) fossil corals and 2 modern corals were collected from these sites (Table 2). Three (3) fossil coral cores drilled from Damortis Beach in 2009 were also used in this research.

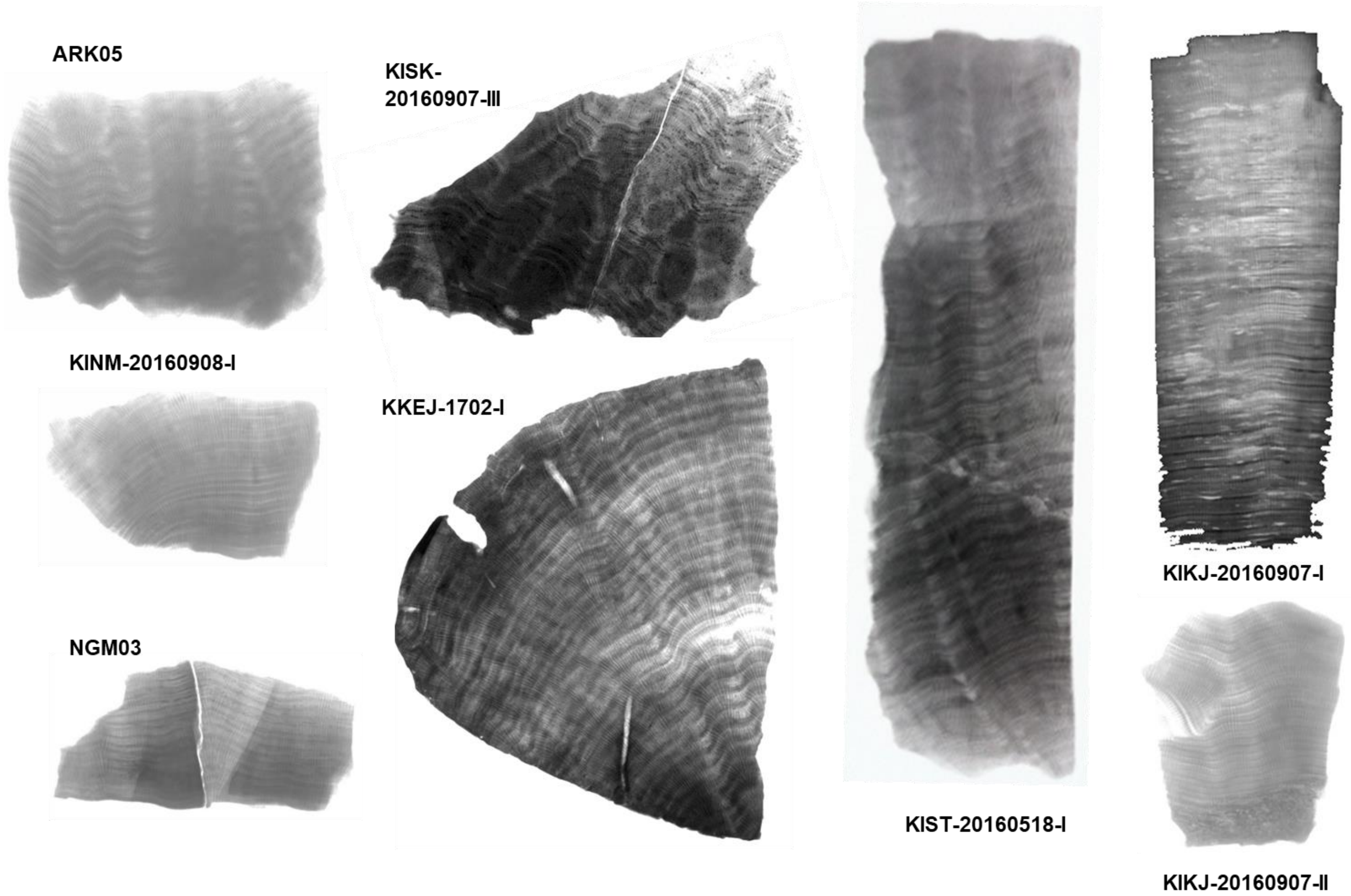

Figure 15. Selected X-ray photographs of fossil corals from Kikai Island. KINM-20160908-I and NGM03 were collected from Nakaguma; KISK-20160907-III was collected from Sateku; KIST-20160518-I was collected from Shitooke; KIKJ-20160907-I, KIKJ-20160907-II, and KKEJ-1702_I were collected from Keraji

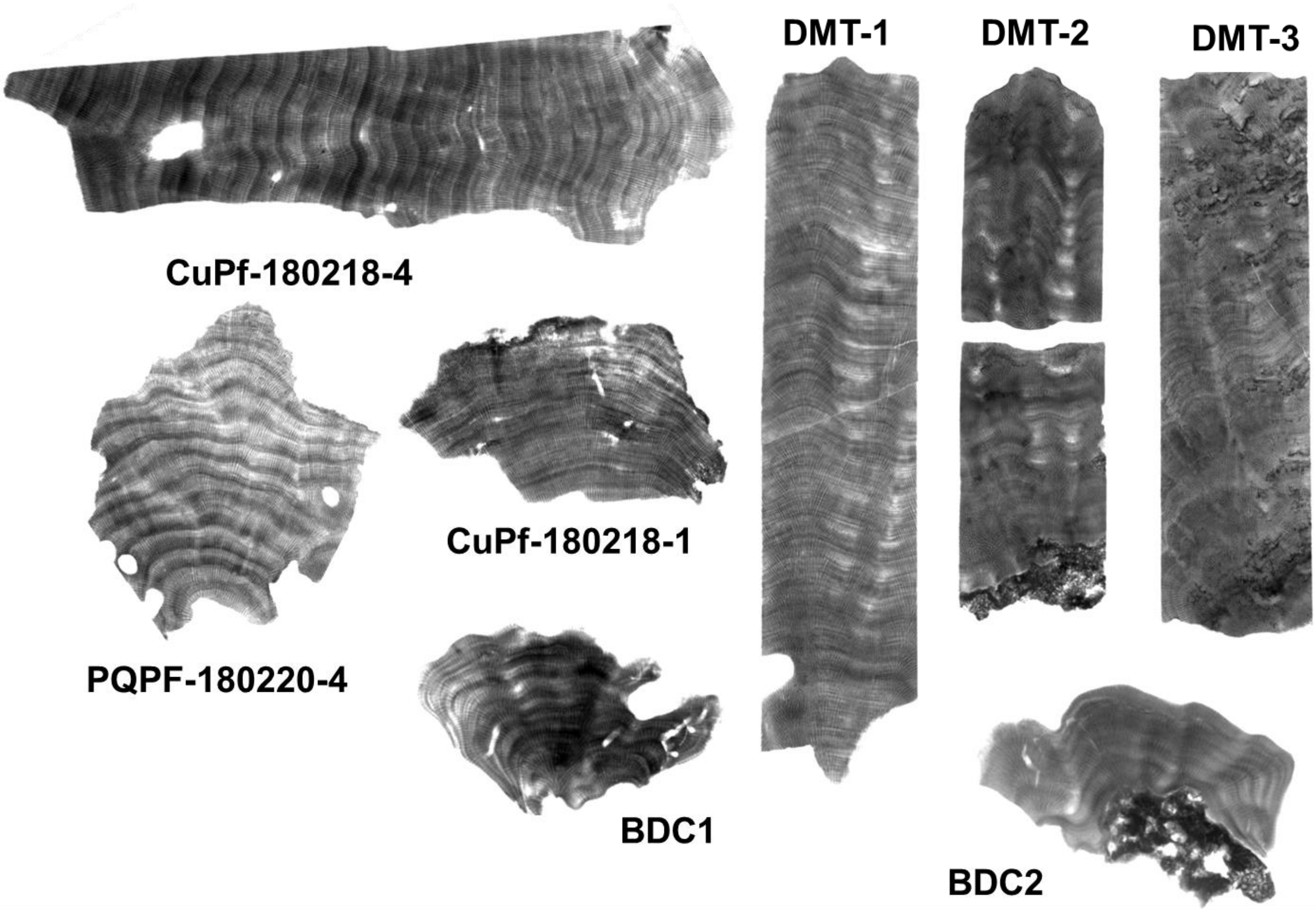

Figure 16. Selected X-ray photographs of fossil and modern corals from NW Luzon Island. CuPf-180218-1 and CuPf-180218-4 were collected from Currimao, Ilocos Norte; PQPF-180220-4 was collected from Pasuquin, Ilocos Norte; DMT-1, DMT-2, and DMT-3 were drilled from Damortis, La Union; and BDC1 and BC2 are modern corals collected from Badoc Island, Ilocos Norte

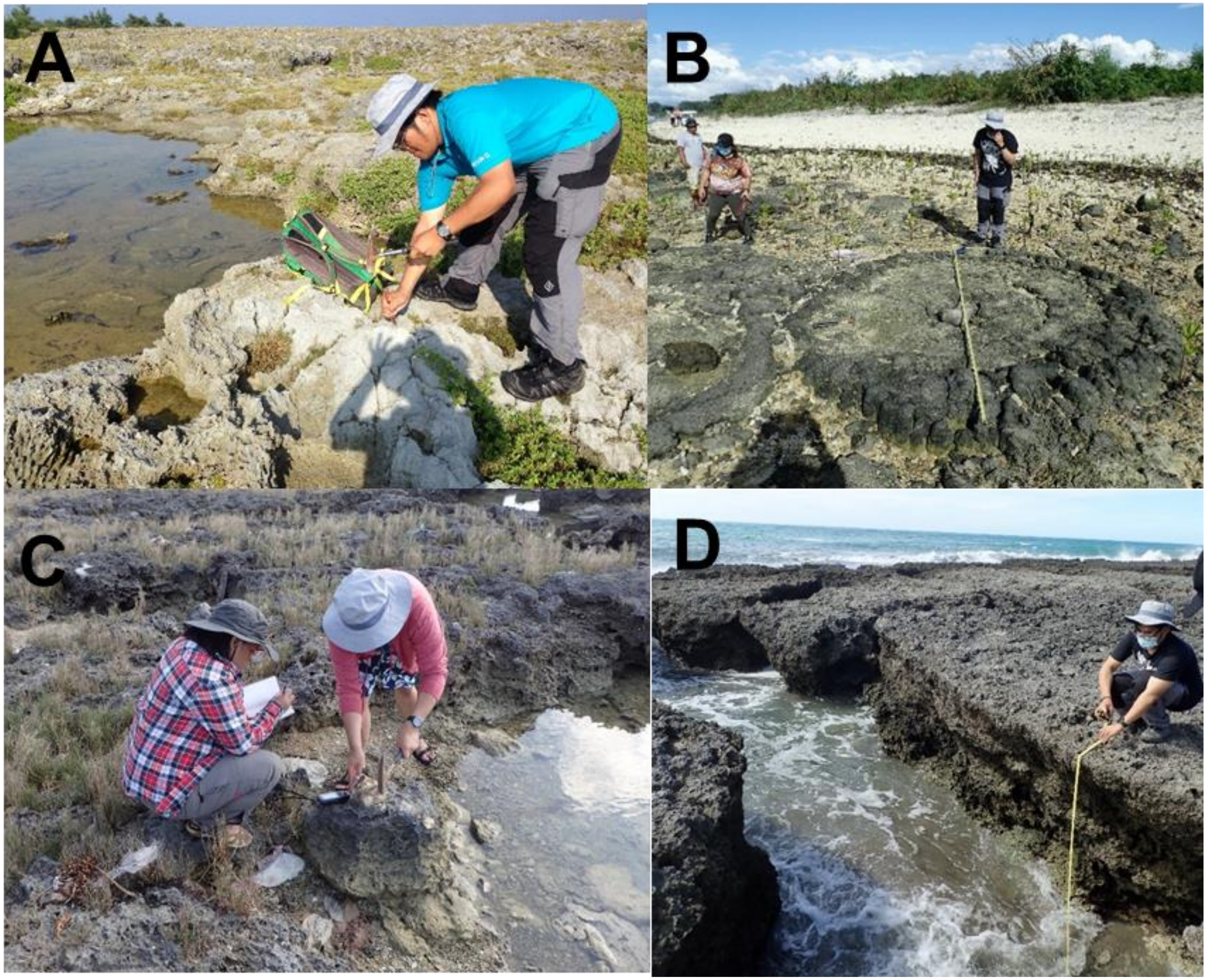

Figure 17. Fieldwork photos in Kikai Island and NW Luzon Island. A. Coral sampling in Sateku, Kikai Island. B. Measurement of fossil microatoll in Paraoir (Balaoan), La Union. C. Fossil coral sampling in Pasuquin, Ilocos Norte. D. Terrace measurement in Bacnotan, La Union

Table 1. List of coral samples from Kikai Island, Japan (blue shade = data available)

Sample Name	Location	Geographic Coordinates	Age Dating	XRD	SEM
ARK05	Araki	N 28 18.628 E 129 54.865		Y	Y
KIST-20160518-I	Shitooke		Y	Y	Y
KISK-20160907-III	Sateku	N 28.349927 E 130.02253		Y	Y
NGM03	Nakaguma	N 28 20.414 E 129 56.050		Y	Y
KIKJ-20160907-II	Keraji	N 28.28332 E 129.92451	Y	Y	Y
KINM-20160908-I	Nakaguma	N 28 20.414 E 129 56.050		Y	Y
KIKJ-20160907-I	Keraji	N 28.28774 E 129.99886		Y	Y
KKEJ-201702-1	Keraji			Y	Y
KISM-201808-1	Shiomichi				Y
KISM-201808-2	Shiomichi				Y
KSOM-201808-1	Somachi				Y
KSOM141006	Shiomichi		Y	Y	Y
Modern coral	Shiomichi				

Table 2. List of coral samples from NW Luzon Island, Philippines (blue shade = data available)

Sample Name	Location	Geographic Coordinates	Age Dating	Thin Section	XRD	SEM
CUPF-180218-1	Currimao, Ilocos Norte	N 18° 01' 56.7" E120° 28' 25.25"	Y	Y	Y	Y
CUPF-180218-2	Currimao, Ilocos Norte	N 18° 01' 56.7" E120° 28' 25.25"				
CUPF-1802118-3	Currimao, Ilocos Norte	N 18° 01' 51" E120° 28' 26.35"	Y		Y	Y
CUPF-1802118-4	Currimao, Ilocos Norte	N 18° 01' 51" E120° 28' 26.35"	Y	Y	Y	Y
CUPF-180218-5	Currimao, Ilocos Norte	N 18° 01' 50.98" E120° 28' 26.49"		Y		Y
CUF-180218-1	Currimao, Ilocos Norte	N 18° 01' 51" E120° 28' 26.35"	Y	Y		Y
PQPF-180220-1	Pasuquin, Ilocos Norte	N 18° 27' 19.22" E120° 34' 44.55"				Y
PQPF-180220-2	Pasuquin, Ilocos Norte	N 18° 27' 19.22" E120° 34' 44.55"				

PQPF-180220-3	Pasuquin, Ilocos Norte	N 18° 27' 18.99" E120° 34' 44.41"		Y		Y
PQPF-180220-4	Pasuquin, Ilocos Norte	N 18° 27' 18.51" E120° 34' 43.72"	Y	Y	Y	Y
PQPF-180220-5	Pasuquin, Ilocos Norte	N 18° 27' 19.65" E120° 34' 42.71"				
PQPF-180220-6	Pasuquin, Ilocos Norte	N 18° 27' 18.5" E120° 34' 43.55"				
PQPF-180220-7	Pasuquin, Ilocos Norte	N 18° 27' 18.9" E120° 34' 47.24"		Y		Y
BAPF-1	Badoc Island, Ilocos Norte	N 17° 55' 19.5" E120° 25' 4.4"			Y	Y
BAPF-2-1-2	Badoc Island, Ilocos Norte	N 17° 55' 19.5" E120° 25' 4.4"		Y	Y	Y
BAPF-3	Badoc Island, Ilocos Norte	N 17° 55' 20.7" E120° 25' 4.7"		Y	Y	Y
BAPF-4	Badoc Island, Ilocos Norte	N 17° 55' 24.8" E120° 25' 3.9"		Y	Y	Y
BAPF-5	Badoc Island, Ilocos Norte	N 17° 55' 24.8" E120° 25' 3.9"		Y	Y	Y
BAPF-6	Badoc Island, Ilocos Norte	N 17° 55' 25.0" E120° 25' 3.6"		Y	Y	Y
BAPF-7	Badoc Island, Ilocos Norte	N 17° 55' 25.0" E120° 25' 3.6"		Y	Y	Y
BAPF-9	Badoc Island, Ilocos Norte	N 17° 55' 25.0" E120° 25' 3.6"		Y	Y	Y
BDC-1	Badoc Island, Ilocos Norte	N 17° 55' 19.1" E120° 24' 44.0"	Modern			
BDC-2	Badoc Island, Ilocos Norte	N 17° 55' 19.1" E120° 24' 44.0"	Modern			
BLN-PAR-111320	Balaoan, La Union	N16°48’11.3’’ E120°19’26.9’’			Y	
BLN-PAR-111320-3	Balaoan, La Union	N16°48’11.3’’ E120°19’26.9’’		Y	Y	Y
BLN-PAR-111320-4	Balaoan, La Union	N16°48’11.3’’ E120°19’26.9’’		Y	Y	Y
ROS-DAM-111120-1	Rosario, La Union	N16°13’46.1’’ E 120°24’26.6’’		Y	Y	Y
DMT-P1	Rosario, La Union	N16°13’46.1’’ E 120°24’26.6’’	Y		Y	Y
DMT-P2	Rosario, La Union	N16°13’46.1’’ E 120°24’26.6’’	Y		Y	Y
DMT-P3	Rosario, La Union	N16°13’46.1’’ E 120°24’26.6’’	Y			

2.2. Screening of Diagenesis

Fossil coral samples are easily altered by secondary crystallization of abiogenic aragonite and calcite during diagenesis. Several screening tests including thin section analysis, Xray Diffraction analysis, and Scanning Electron Microscope imaging to check the mineralogical make-up and the possible diagenetic imprints in fossil corals.

A macroscopic examination of coral samples was done using physical characteristics such as density, crystal habit, fabric, and porosity. Seventeen (17) thin sections were prepared from representative portions of coral samples (Fig. 18). Thin sections were examined using an *Olympus BX53* polarizing microscope in both plane- and cross-polarized set-up at the DENR-MGB. The overall textures of the coral samples were described, and relative abundance of aragonite and calcite were reported. Simultaneously, the presence of secondary calcite was determined using X-ray Diffraction XRD) Rigaku MiniFlex II at Hokkaido University and X'Pert Pro Panalytical at the Mines and Geosciences Bureau (Fig. 19). The sample was crushed and pulverized using an agate mortar and pestle. The powdered coral sample was passed through a 125-sieve mesh and then transferred to the XRD sample holder. The sample was analyzed in an XRD unit with copper Xray tube and scanned °2θ from 3° to 70°. The abundance of aragonite and calcite was calculated in X'Pert HIGHSCORE v5.1 software using the Reference Intensity Ratio (RIR) Method.

Selected coral samples with relatively low (1-3%) calcite to 0% calcite were analyzed using the Scanning Electron Microscope (SEM; Hitachi Miniscope TM-1000) at Hokkaido University. The Miniscope TM-1000 uses backscattered electron for morphological imaging of coral skeleton. Backscattered electron images were generated for 34 samples. Four (4) samples were submitted to the Field Emission Scanning Electron Microscope (FE-SEM; Dual Beam Helios Nanolab 600i) with elemental mapping at the Department of Science and Technology – Advanced Materials Testing Laboratory (DOST-ADMATEL). The coral samples were measured under the 5.0 kV FESEM accelerating voltage with 86 pA beam current, and 15.0 kV EDS accelerating voltage with 0.69 nA beam current. Microstructures of carbonate minerals in a 1cm x 1 cm coral block were observed to identify any recrystallization overprinting in the coral skeleton. The EDX elemental maps and spectra were generated for the 4 samples. Elemental concentrations are presented in weight percentage (wt. %).

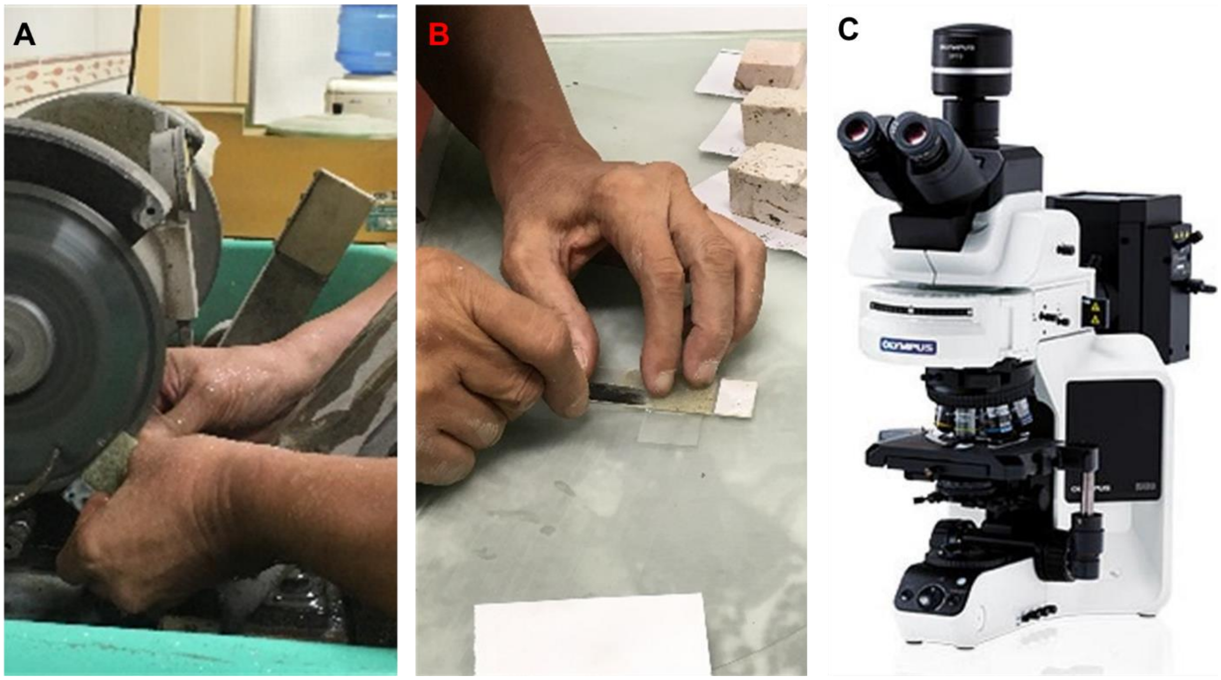

Figure 18. Thin Section Analysis. A. Cutting samples into coral blocks. B. Preparing thin sections from coral blocks. C. Petrographic analysis of corals using polarizing microscope

Figure 19. Xray diffraction (XRD) Analysis. Pulverized coral samples were analyzed in X’Pert PRO PANalytical XRD.

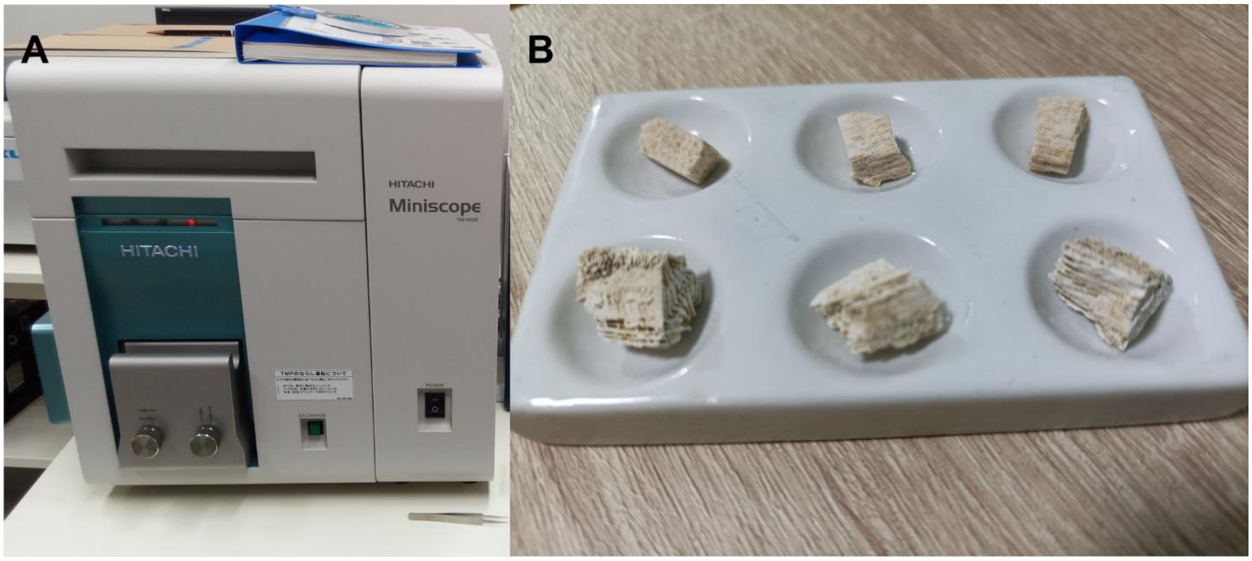

Figure 20. Scanning Electron Microscope (SEM) Analysis. Miniblocks/fragments (~1cm x 1cm) from different parts of the fossil coral colonies were analyzed using Hitachi TM-1000 Miniscope.

2.3. Radiocarbon Dating

After checking the diagenesis, candidate samples for geochemical analysis were analyzed for radiocarbon age dating. Table 3 enumerates the coral samples that were analyzed in the following Accelerator Mass Spectrometer (AMS) laboratories:

a. AMS at Paleo-Labo Co., Ltd. with 0.5MV accelerator; the average analytical error is less than ±0.3% (Kobayashi et.al. 2007);

b. AMS at Yamagata University with 0.5 MV Pelletron accelerator; the average analytical error is higher than 0.3%; the $^{14}C/^{12}C$ ratio is less than 6×10^{-16} for the reagent graphite (Moriya et.al. 2019); and

c. Micro Analysis Laboratory Tandem Accelerator (MALT) of The University of Tokyo with an ion-beam generated by a Pelletron™ 5UD tandem accelerator; only mass ^{13}C and ^{14}C are injected into the AMS, limiting the transmission of ^{12}C (Matsuzaki et.al. 2015); the average analytical error is higher than 0.5%,

The two well-preserved corals (KIKJ-20160907-II and KIST-20160518-I) from Kikaijima were analyzed for radiocarbon age dates using the AMS at Yamagata University. The five samples (PqPf-182020-4, CuPf-182018-1, CuPf-182018-4, CuPf-182018-3, CuF-182018-1) from Ilocos Norte were analyzed at the Micro Analysis Laboratory Tandem Accelerator

(MALT) of The University of Tokyo. The three samples (DMT-1, DMT-2, DMT-3) were dated at the AMS at Paleo-Labo Co., Ltd. Conventional radiocarbon age dates were corrected using the regional reservoir factor. Conventional radiocarbon age dates of fossil corals were converted into calendar age using the Marine20 datasets (Heaton et.al. 2020). Calendar ages are presented in both 1σ and 2σ calibration. The local reservoir effect (ΔR) was not yet calculated.

Table 3. Radiocarbon Age Dates of Selected Fossil Corals

Sample Name	Location	Conventional Radiocarbon Age (yr BP ±1σ)	Calendar Years	
			1σ calibrated year range	2σ calibrated year range
Kikai-jima corals				
KIKJ-20160907-II	Keraji,	3235±20[1]	1151BC (68.2%)1050BC	1193BC (95.4%)1009BC
KIST-20160518-I	Shitooke	5712±24[1]	4234BC (68.2%)4143BC	4257BC (95.4%)4063BC
Northwest Luzon corals				
PQPF-180220-4	Pasuquin, Ilocos Norte	2972±70[2]	881BC (68.3%)741 BC	973BC (95.4)609BC
DMT-1	Rosario, La Union	4200±20[3]	2400BC (68.2%)2290BC	2450BC (95.4%)2260BC
DMT-3	Rosario, La Union	4277±19[3]	2485BC (68.2%)2405BC	2540BC (95.4%)2350BC
DMT-2	Rosario, La Union	4336±21[3]	2555BC (68.2%)2475BC	2600BC (95.4%)2440BC
CuPf-180218-4	Currimao, Ilocos Norte	6144±77[2]	4714BC (68.3%)4529 BC	4808BC (95.4)4445BC
CuPf-180218-1	Currimao, Ilocos Norte	6285±79[2]	4892BC (68.3%)4699 BC	4992BC (95.4)4595BC
CuPf-180218-3	Currimao, Ilocos Norte	5979±79[2]	4521BC (68.3%)4350 BC	4648BC (95.4)4300BC
CuF-180218-1	Currimao, Ilocos Norte	5911±79[2]	4462BC (68.3%)4305 BC	4555BC (95.4)4222BC

^{14}C age calculation used AD 1950 as a base point. Libby's half-life of 5568 was used as the half-life of ^{14}C.

1 OxCal 4.21 (calibration curve data: Marine 13) was used for calendar year calibration of ^{14}C age.

2 Calib Rev7.1.0 (calibration curve data: Marine13) was used for calendar year calibration of ^{14}C age.

3 Calibration curve data: Marine 04 was used for calendar year calibration of ^{14}C age.

2.4. Sample Preparation and microsampling

Coral samples/cores were cut into 2 slabs with 5-mm thickness using a lapidary rock cutter with diamond-tipped blade along major vertical growth axis (Fig. 21). One slab was used for geochemical analysis while the second one is a duplicate sample. The slabs were washed with Milli-Q water in an ultrasonic bath for 15 minutes. Repeat the washing process thrice. Then, slabs were dried in a 40°C laboratory oven for at least 24 hours.

Figure 21. Cutting of coral samples using lapidary rock saw with diamond-tipped blade

Xray photographs of coral slabs were taken using a cabinet radiographic unit SOFTEX M60 with direct digital imaging sensor NAOMI (Fig. 22a). The NAOMI digital imaging sensor has a maximum of 192 highly sensitive monochrome CCD sensors resulting in 48.37-megapixel image quality. The X-ray unit is operating at a maximum voltage of 60 kV and maximum current of 3 mA. The aging of X-ray beam was done by gradually increasing the voltage by 10 kV every 3 minutes until it reaches the desired 50 kV setting. Samples were exposed in Xray with 50 kV and 1 mA set-up for 8-10 minutes. The standard methodology of Sowa et al. 2014 on measuring the linear extension rate, skeletal density and calcification rates was followed in this research.

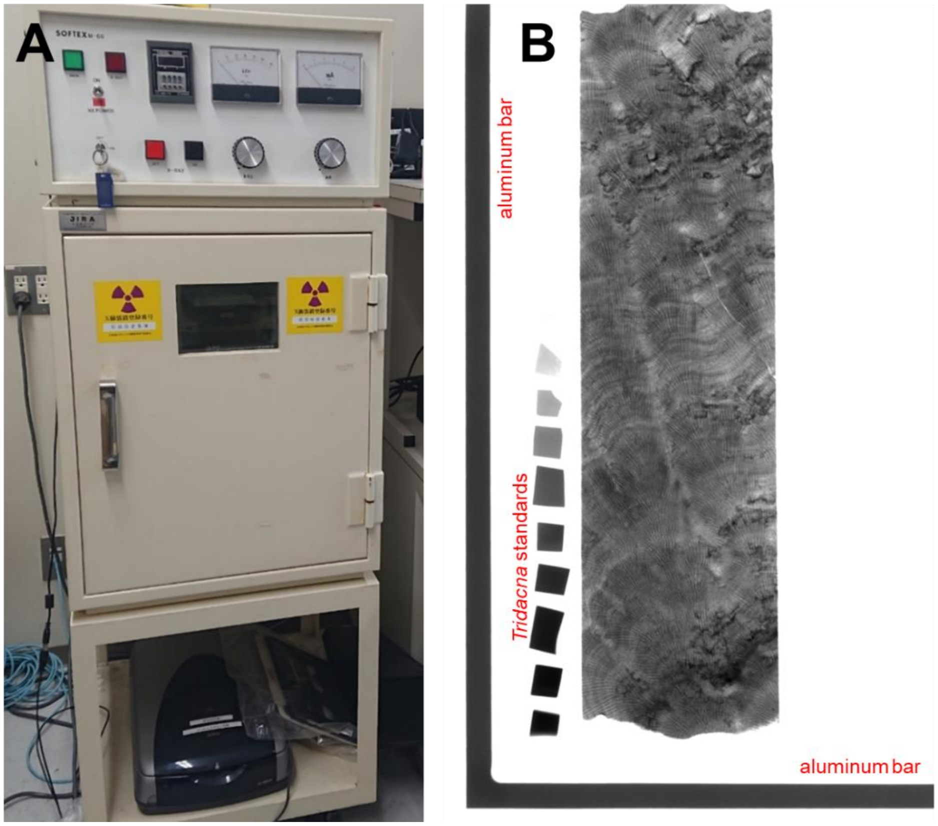

Figure 22. A. Coral slabs were X-rayed using a 2D cabinet-type radiographic unit. B. Calibration of gray values using aluminum bar and giant clam mini blocks as thickness standards

Three variables of coral growth were measured: 1) linear extension rate as the outward extension per year (mm/y); 2) the density of the coral skeleton each year (g/cm3); and 3) the product of the two previous variables expressed as calcification rate (g/cm2y). The distance between adjacent light or dark bands was measured as linear extension rate (cm/yr). The coral skeletal density as a function of thickness and optical density (gray values) was calculated. The x-y aluminum bar and the aragonitic step wedge from *Hippopus hippopus* (giant clam) blocks have assigned density and thickness. The average skeletal density of the *Hippopus hippopus* is 2.85 g/cm^3 multiplied to the thickness of the step wedge standards. The measured optical density (OD; gray values of pixels from 0-255) and the calculated skeletal density per standard block were plotted. The resulting polynomial equation was used to calibrate the OD and to correct the distance discrepancies in X-ray photo. The standard OD of aluminum bars was used to adjust the X-ray photo using the CoreCal2 software. The adjusted digital X-ray photos were used to measure the skeletal density along the maximum vertical growth axis. The OD was presented in logarithmic values for the calculation of skeletal density (g/cm^3). The average skeletal density and linear extension rate of the coral colony were multiplied to calculate the overall calcification rate. The measurement of coral growth parameters was done for 4 fossil corals (ARK05, KIKJ-20160907-I, KIKJ-20160907-II, KIST-20160518-I) from Kikai Island, Japan and 6 fossil corals (DMT-1, DMT-2, DMT-3, PQPF-180220-4, CuPf-180218-1, CuPf-180218-4) from NW Luzon Island, Philippines.

A 2.0 mm thick and 3.5 mm wide ledge was prepared along the geochemical measurement line which is parallel to the maximum coral growth axis (Fig. 23). Coral powders were milled continuously using a diamond-tipped drill bit with a constant rotation speed of 1 mm/min. The subsampling interval of KIKJ-20160907-II and KIST-20160518-I are 0.15 mm and 0.2 mm, respectively. The subsampling interval of DMT-1, DMT-2, BDC-1 is 0.2 mm. CuPf-180218-4 was subsampled at 0.35 mm milling interval. These samples were selected for geochemical analysis after the diagenesis screening and radiocarbon age dating. The subsampling interval was selected based on the linear extension rate of the annual growth bands.

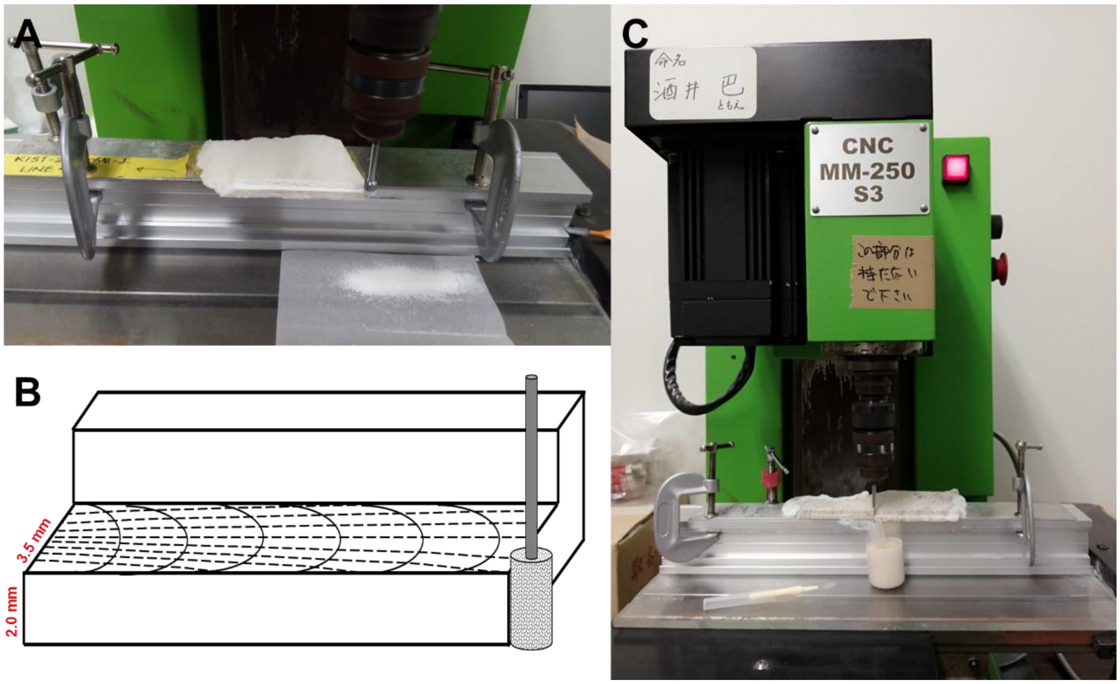

Figure 23. A. Preparation of the ledge B. Schematic diagram of the coral subsampling/micro sampling procedure C. Subsampling procedure was done using diamond-tipped drill bit with a constant rotation speed of 1 mm/min mounted in CNC MM-250 S3 milling machine

2.5. Analytical Methods

2.5.1. Sr and Ca measurements using ICP-OES

To reduce the risk contamination, a strict protocol of labware (PP or Teflon) washing was followed (Watanabe et al. 2020). Labware were soaked in four separate buckets of SCAT (1), HNO_3 (2), HCl (3), and deionized water (4) baths for 24 hours each bath. The labware were rinsed by deionized water before transferring to the next bath. After the deionized water bath, labware were rinsed with Milli-Q water (18.2 MΩ-cm at 25°C). The washed labware were transferred to a drying cabinet under a high efficiency particulate air (HEPA) filtering system.

Figure 24. The ThermoScientific iCAP 6200 Inductively-coupled Plasma-Optical Emission Spectrometer (ICP-OES) at the Hokkaido University was used to measure the Sr and Ca concentrations in coral skeleton

Sr and Ca concentrations were measured using the iCap 6200 Inductively Coupled Plasma-Optical Emission Spectrometer (ICP-OES) with CETAC ASX-260 autosampler at Hokkaido University. Coral samples approximately 80 – 100 µg, were dissolved in 25% HNO_3 solution and pre-calculated Milli-Q water to obtain 7 ppm Ca concentration solution. The solution was introduced to the glass-type spray chamber using the pneumatic pump system. Repeat measurements of every sample solution were done five times. Multiple wavelengths of Sr (421.5 nm, 407.7 nm, 346.4 nm) and Ca (315.8 nm, 370.6 nm, 373.6 nm) were analyzed in axial view.

JCp-1 was used as the reference standard solution of the trace element analysis. JCp-1 is an aragonite powder from a modern *Porites* coral colony from Ishigaki, Japan (Okai et al. 2002). The reference standard was provided by the National Institute of Advanced Industrial Science and Technology. Based on interlaboratory analyses, the Sr/Ca value of JCp-1 is 8.838 mmol/mol (Hathorne et al. 2013). A reference solution of JCp-1 was measured after every 5 samples to correct instrumental drift. The analytical precision is ±0.07%RSD (SD of ±0.006 mmol/mol) using internal standard measurements of JCp-1 solution (Watanabe et al. 2020).

2.5.2. δ^{18}O measurement using MAT 253 with Kiel IV carbonate device

Figure 25. The Finnigan MAT 253plus stable isotope ratio mass spectrometer with the Kiel IV automated carbonate device was used to measure oxygen (δ^{18}O) and carbon (δ^{13}C) isotopes in coral skeleton.

The coral samples were weighed and 20 – 40 µg were taken for oxygen and carbon isotope analysis. The samples were analyzed in a Finnigan MAT 253 stable isotope ratio mass spectrometer after the reaction with 100% H_3PO_4 at 70°C in an automated carbonate device Kiel IV. The analytical precision for $\delta^{18}O$ and $\delta^{13}C$ are ±0.07‰ and ±0.05‰ respectively, using replicate measurements of the NBS 19 (n=301). NBS 19 (TS-Limestone) was obtained from a slab of white marble that was crushed into 177 µm and 325µm (Friedman et al. 1982). The standard values of $\delta^{18}O$ and $\delta^{13}C$ are -2.20‰ and 1.95‰ in VPDB (Pee Dee Belemnite) scale.

2.5.3. Estimation of seawater δ18O

The coral oxygen isotope ($\delta^{18}O_{coral)}$ is a function of water temperature (Watanabe et al. 2001) and the $\delta^{18}O$ of the seawater ($\delta^{18}O_{sw}$) changes (Julliet-Leclerc and Schmidt 2001). Using paired coral Sr/Ca and $\delta^{18}O_{coral}$, the $\delta^{18}O_{sw}$ was estimated by removing the SST component from the $\delta^{18}O_{coral}$ (Ren et al. 2003; Cahyarini et al. 2008; Nurhati et al. 2010).

Among the different calculation methods, the centering method yielded the lowest uncertainty by omitting the intercept values in the regression slopes β and b because the intercept could be the largest source of uncertainty in the calculation (Nurhati et al. 2011). The estimation of $\delta^{18}O_{sw}$ was done by removing the $\delta^{18}O_{SST}$ component from the $\delta^{18}O_{coral}$ using the Sr/Ca-SST slope (β), $\delta^{18}O_{coral}$-SST slope (b), and the measured Sr/Ca values (Cahyarini et al. 2008) as follows:

$$\Delta\,\delta\,^{18}O_{sw-center} = \delta^{18}O_{coral} - \overline{\delta^{18}O_{coral}} - b/\beta\ x\ (Sr/Ca - \overline{Sr/Ca})$$

where Sr/Ca and $\delta^{18}O_{coral}$ are measured values, ($\overline{Sr/Ca}$, $\overline{\delta^{18}O_{coral}}$) are mean values, β is the Sr/Ca-SST slope, and b is the ($\delta^{18}O_{coral}$- $\delta^{18}O_{sw}$)-SST slope.

2.5.4. Error propagation

Analytical and slope errors should be propagated accordingly to estimate the real uncertainty of $\delta^{18}O_{sw}$ estimates (Nurhati et al. 2010). These errors were propagated in the SST and $\delta^{18}O_{sw-center}$ using the simple Monte Carlo simulation in R software (Watanabe and Pfeiffer 2022). For the slope ± error input, the Sr/Ca-SST slope of -0.0643±0.0026 mmol/mol/°C from modern Porites in Kikai Island (Kajita et al. 2017) and the ($\delta^{18}O_{coral}$-

$\delta^{18}O_{sw}$)-SST slope of -0.20±0.02‰$_{VPDB}$/°C (Julliet-Leclerc and Schmidt 2001) were used. For the analytical error, the values ±0.006 mmol/mol and ±0.07‰$_{VPDB}$ for Sr/Ca and $\delta^{18}O_{coral}$, respectively, were used. Watanabe and Pfeiffer (2022) accounted that the analytical error of $\delta^{18}O_{coral}$ measurement is the largest contributor of the error of $\delta^{18}O_{sw}$ estimates. The general flowchart of the procedure is below:

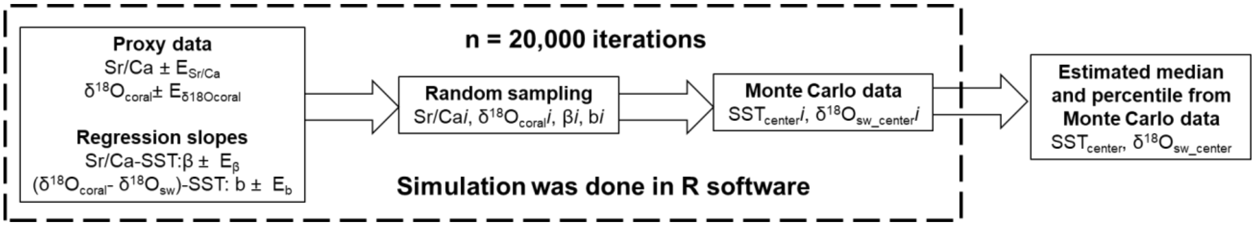

Figure 26. Flowchart of the error propagation using the simple Monte Carlo simulation in R software. The flowchart published by Watanabe and Pfeiffer (2022) was adapted.

2.6. Statistical Methods

2.6.1. Age model development and resampling

Age models of coral Sr/Ca, $\delta^{18}O_{coral}$, and $\delta^{18}O_{sw}$ were developed using AnalySeries v2.0.8 (Paillard et al. 1996) and QAnalyseries (Kotov and Paelike 2018). The mnima and maxima of modern coral Sr/Ca record was anchored to the maxima and minima of SST. In the case of NW Luzon Island, the IGOSS monthly SST shows double maxima SST in some years from 2010 to 2018. These double maxima points were also used as date anchors. For fossil corals, a date anchor dataset was prepared using the timing and value of mean maximum and minimum SST values from satellite/reanalysis data. These anchor dates were tied with the maxima and minima peaks of fossil coral Sr/Ca records. The same age model was used to $\delta^{18}O_{coral}$ and $\delta^{18}O_{sw}$ of modern and fossil corals. The Sr/Ca, $\delta^{18}O_{coral}$, and $\delta^{18}O_{sw}$ time series were resampled to monthly resolution (12 points per year) using the piecewise linear interpolation function of AnalySeries v2.0.8.

2.6.2. Bivariate Regression analysis

This analysis uses two variables to test and understand the strength of the relationship between them. The strength is often defined by the Pearson's coefficient of correlation (r), coefficient of determination (r^2), and p-value measured by student's t-test. The regression analysis was also used to see the trend between the two variables. This trend is defined by the linear regression equation. The Ordinary Least Square (OLS) method was used to generate the *best fit line* among the data points considered in the regression analysis (see the equation below). In this research, the coral geochemical records were regressed to hydroclimatic variables such as SST, SSS, rainfall. The bivariate regression analysis was also used to understand the relationship of two different geochemical records. OLS regression analysis was done in Paleontological Statistics (PAST) v4.11.

$$y_n = \sum_{i=0}^{k} \beta_i x_{n_i} + \varepsilon_n$$

x_i as independent variable y_i as dependent variable
α as y-intercept   β as slope   ε as random error

2.6.3. *Bandpass Filtering (Finite Impulse Response (FIR))*

Bandpass filtering allows the removal of all frequencies outside the pre-determined band to highlight specific climate signals with known periodicities. The bandpass filtering was performed in Paleontological Statistics (PAST) v4.11. The input data is monthly-resolved geochemical datasets. The lower filter was set at 0.01 cycle/month and the higher filter was set at 0.042 cycle/month. The 0.01 – 0.042 cycle/month band is equivalent to the 2-8-year band of the ENSO cycle. The 2–8-year band cycle was filtered from the modern and fossil coral Sr/Ca, $\delta^{18}O_{coral}$ and $\delta^{18}O_{sw}$ records from Kikai Island, Japan and NW Luzon Island, Philippines.

2.6.4. *Spectral/Frequency Analysis using REDFIT Method*

To determine the hydroclimate-related periodicities in the $\delta^{18}O_{coral}$ and $\delta^{18}O_{sw}$ time series, spectral analysis using REDFIT Method (MTM) originally proposed by Schulz and Mudelsee (2002) was used. The method allows the spectral analysis of unevenly spaced time series without the need of pre-processing such as data interpolation. The REDFIT spectral analysis was performed in Paleontological Statistics (PAST) v4.11. The power spectrum was computed with 90%, 95%, and 99% statistical significance using Monte Carlo simulations.

CHAPTER 3

PRESERVATION OF FOSSIL CORALS AND EFFECTS OF DIAGENESIS IN PALEOCLIMATE PROXIES

3.1. Diagenesis of fossil corals

Most scleractinian corals (i.e. *Porites*) secrete aragonitic skeleton. During the fossilization process, these corals undergo diagenesis after burial. Diagenesis is the overall physical and chemical alteration of the original carbonate sediments after deposition until before complete lithification. The physical and chemical changes are influenced by rock-water interaction, activities of macro- and microorganisms, and compaction. The diagenesis of the abandoned skeleton below the living coral colony starts in the submarine condition, often referred as the marine phreatic zone. The early signs of diagenesis are the occurrence of macro- and microendoliths, inorganic marine cementation, sedimentation in the pore cavities, and macroborings from other marine invertebrates. The diagenetic processes increase progressively when the corals are removed from the submarine environment into the subaerial environment. The vadose zone is located near the freshwater table which allows the partial contact of seawater-freshwater mixture to the coral carbonate. The diagenesis in the vadose zone is characterized by the dissolution of the primary aragonite with concomitant precipitation of the calcite (James 1974). The last stage is the freshwater phreatic zone which is highly influenced by the percolating freshwater. Freshwater sparry calcite cement occurs as infills of skeletal pore spaces. The skeleton exhibits moldic to large vuggy porosities. In the most advanced stage, the skeleton is completely replaced by sparry calcite forming mosaics of equant crystals.

Diagenesis is one of the sources of uncertainties of coral-based paleoclimate reconstructions (McGregor and Gagan 2003; Hendy et al. 2007; Sayani et al. 2011). Overgrowths, void infilling, and neomorphic and fabric selective replacement of calcite in primary aragonitic skeleton significantly changed the Sr/Ca, $\delta^{18}O$, and $\delta^{13}C$ values with increasing calcite vs aragonite ratio (McGregor and Gagan 2003). The average Sr/Ca and $\delta^{18}O$ have decreased from coral aragonite to calcite-replaced skeleton. The $\delta^{13}C$ values are more varied but generally reduced in diagenetically altered coral with significant amount of calcite versus pristine aragonite. Secondary aragonite during early marine diagenesis can also result in erroneous climate reconstructions. Hendy et al. 2007 demonstrated that secondary aragonite causes cool SST artifacts based on comparative values of $\delta^{18}O$-SST, Sr/Ca-SST, Mg/Ca-SST, and U/Ca-SST. The same apparent cool SST offsets are detected in modern and fossil corals from central Pacific due to dissolution and secondary aragonite (Sayani et al. 2011).

These studies recommended a stricter screening of diagenesis to avoid high uncertainties in paleoclimate proxies. Thin section analysis is one of the basic tools to investigate the textural fabric and mineralogical composition of coral skeleton (McGregor and Abram 2008). Two-dimensional Xray Diffraction (XRD) is proven effective in both identifying and quantifying the calcite and aragonite content (Smodej et al. 2015). Together with thin section and XRD analyses, detailed microscopic investigations were done using scanning electron microscope (SEM).

3.2. Thin Section Analysis of fossil corals

Seventeen (17) thin sections were analyzed using an Olympus BX53 polarizing microscope. Corals with well-preserved skeleton have no evidence of secondary mineralization of aragonite and calcite. Very fine and fibrous aragonite crystals, which appear as primary biomineralized material, are bound by the coral skeletal wall (Fig. 27a). Intraskeletal spaces are almost devoid of secondary carbonate (aragonite and calcite) infilling. Sample DMT1, CUPF-1802118-4, and BLN-PAR-111320-4 show these textural characteristics.

Early marine diagenesis was observed in coral samples. The original skeleton is completely preserved; however, fine blades of aragonite crystals occur along the outer coral walls (Fig. 27b,c). These secondary aragonite crystals are deposited after the deposition of the primary coralline aragonite even when the coral was still submerged in the water. Network of burrowing that is formed by trails/borings of microorganisms, typifies the early stage of bioerosion. Samples CUPF-0, CUPF5, BLN-PAR-111320-3, BAPF9, BAPF-1, BAPF2, and PQPF4 show these textural characteristics. Some corals show evidence of vadose zone diagenesis. These samples are altered by bladed to needle-like aragonite and minute equant calcite crystals. The primary aragonite skeleton is still intact, however, the intraskeletal pore spaces are occupied by 25% aragonite + calcite cement. Sample PQPF3 and PQPF7 have these textural descriptions.

Few samples such BAPF-6 and BAPF-7 have advanced calcite replacement. The coral skeletal structure is still apparent, albeit intense replacement of calcite in most parts (Fig. 27d). The secondary calcite has two-directional cleavage and occurs as large plates.

Some portions retain the original coralline aragonite with fine fibrous texture. Intraskeletal voids are already filled up with calcite and iron hydroxide cement.

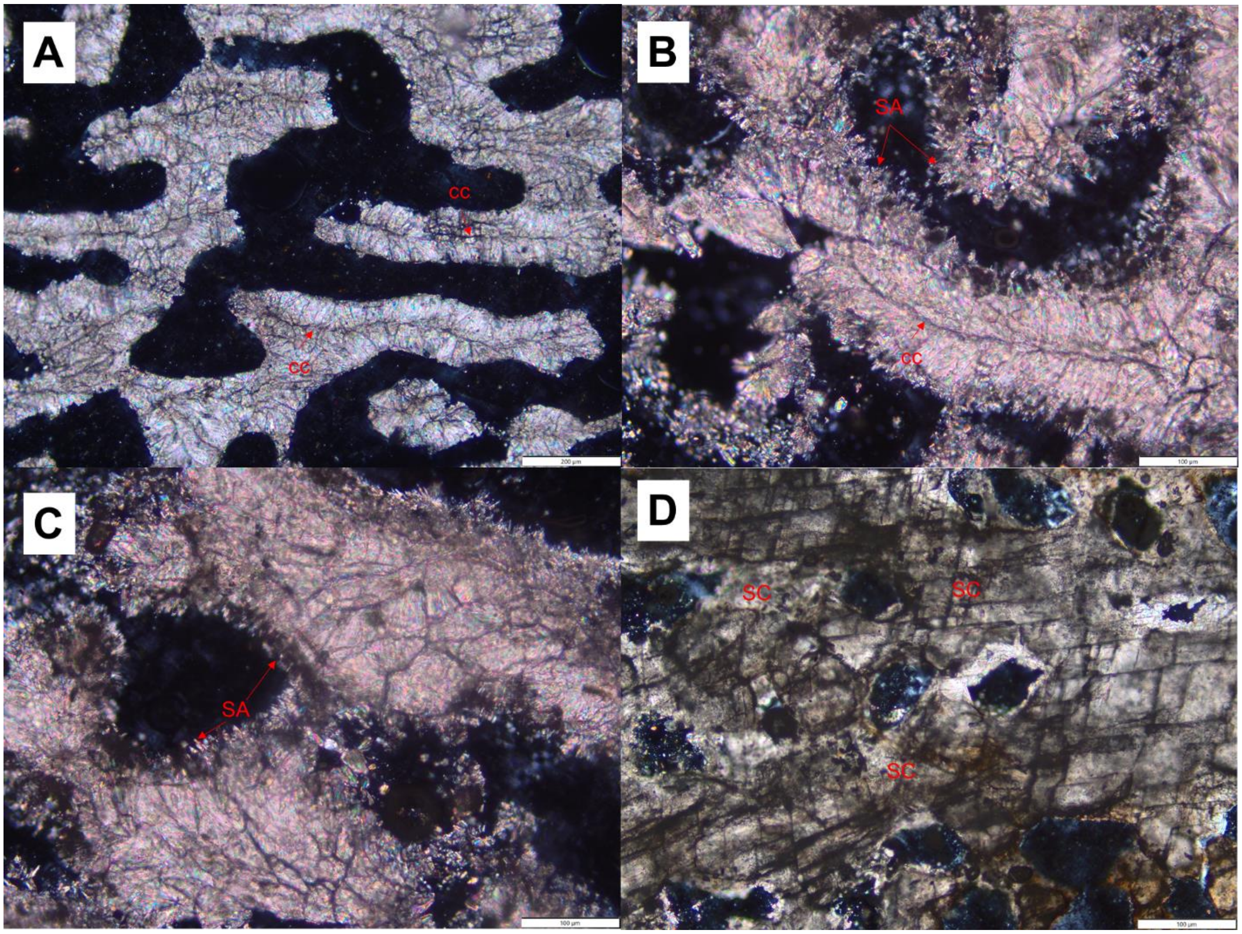

Figure 27. Diagenetic texture under thin section. A. Well-preserved coral skeleton with clear centers of calcification and no observed deposition of secondary carbonate mineral. B. The primary aragonite is still preserved but precipitation of aragonite cement is now evident. C. Aragonite cement has fine acicular fabric. D. The coral skeleton is now completely replaced by calcite.

3.3. XRD Analysis of fossil corals

Nine (9) samples from Kikai Island (Fig. 28) and 18 samples from NW Luzon Island (Fig. 29 and 30) were analyzed using XRD for mineral identification and quantification of calcite vs aragonite. Mineralogical analyses of the fossil Porites reveal that the selected samples have excellent to good preservation of aragonitic skeleton. Aragonite has diffraction peaks at a{111}, a{102}, a{201}, a{020}, a{013}, a{022}, a{122}, and a{104}. The peak with highest intensity in calcite diffraction profile is calcite {104} at $2\theta = 29.8°$ then followed by peaks at c{113}, and c{108}.

The Reference Intensity Ratio (RIR) method was used to quantify the calcite and aragonite content by measuring the intensity of the strongest peak of the mineral phase to the intensity of the strongest peak of corundum, which is considered here as the reference mineral phase (Hubbard et al. 1988). The limit of detection of the quantification of the carbonate mineral phases is $\leq$ 1%.

$$I_{ia} = \frac{k_{ia} x_a}{\rho_a \mu}$$

I_{ia} = intensity of reflection i of phase a

k_{ia} = structure, multiplicity, Lorentz-polarization, temperature, scale factors

ρ_a= density of phase a

μ= linear attenuation coefficient

x_a = weight fraction of phase a

Sample KIST-20160518-I (Fig.28a), KSOM141006 (Fig.28b), KIKJ-20160907-II (Fig.28c) from Kikai Island and DMT-1(Fig.29a), DMT2 (Fig.29b), and CUPF3 (Fig.29c) have 0% calcite content. Samples with early marine diagenetic imprints are often devoid of calcite content as shown both from thin section and XRD analyses. Samples BLN-PAR-111320-4 (Fig.29e), BAPF9 (Fig.29i), BAPF-1 (Fig.29g), and BAPF2 (Fig.29h) have 0 calcite content based on XRD mineral phase analysis. XRD analysis shows that these corals have 99% - 100% aragonite content. However, microscopic investigation revealed that some of the aragonite minerals are secondary mineralization during the early marine phreatic environment. Fossil corals from the subaerial vadose zone have 2% - 7% calcite content based on the XRD mineral phase analysis. Samples KINM-I (5%), NGM (5%), BAPF3 (3%), BAPF4 (4%), BAPF5 (2%), BAPF9-2 (4%), CUPF0 (7%), CUPF1(3%), CUPF4 (3%), CUPF5 (3%), PQPF3 (5%), and PQPF4 (2-5%) have significant calcite content (Fig. 28 and 30).

Some corals resemble diagenesis in a freshwater phreatic zone. It is characterized by the complete dissolution of the primary aragonite and subsequent replacement by secondary calcite. Samples BAPF6 and BAPF7 have 100% calcite based on XRD analysis. However, the thin section analysis shows that parts of the samples have aragonite cement approximately 20% in relative volume abundance. The possible overestimation of the RIR calculation is due to the high intensity of the calcite peaks masking the low intensity of the aragonite peaks.

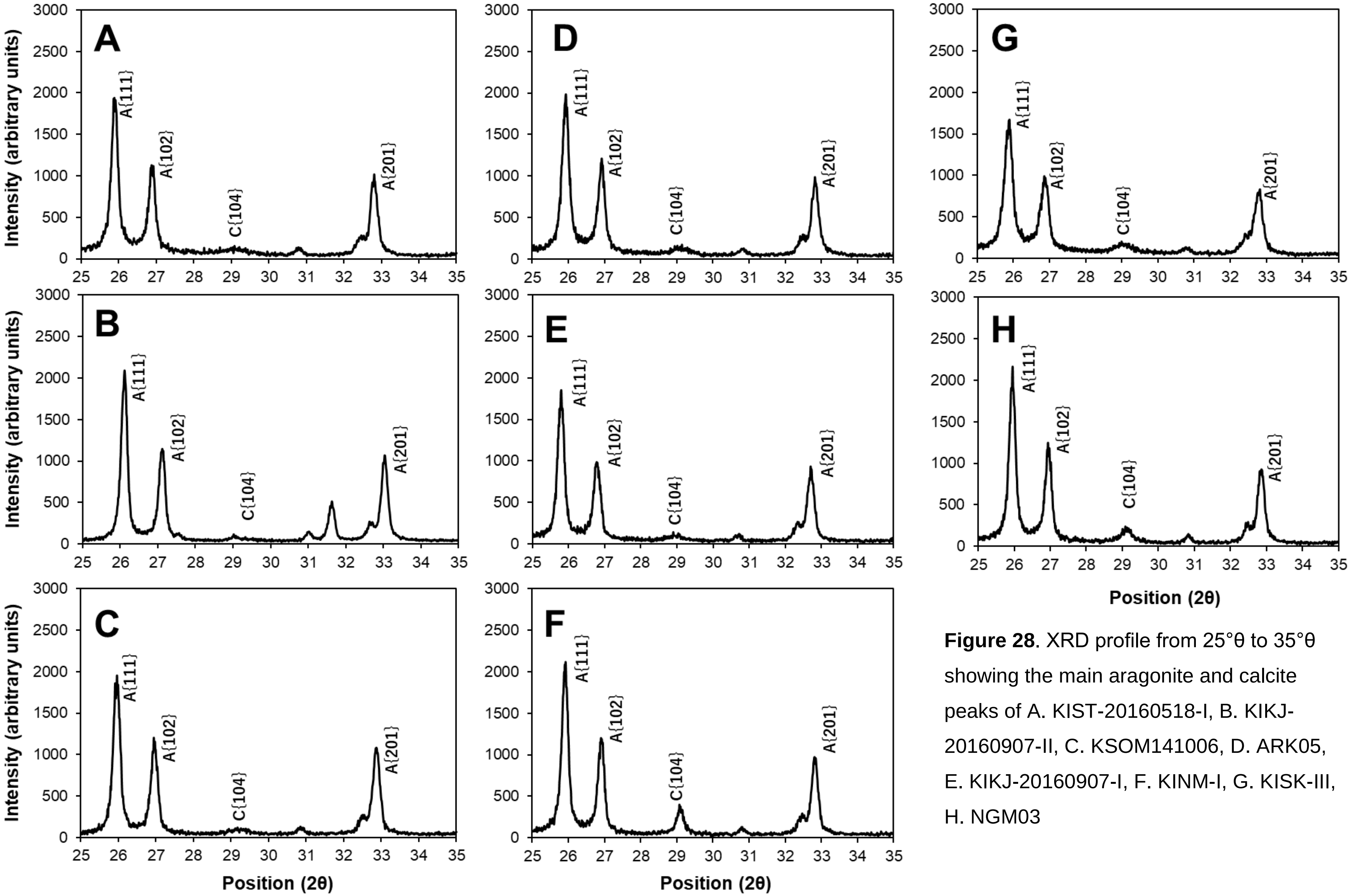

Figure 28. XRD profile from 25°θ to 35°θ showing the main aragonite and calcite peaks of A. KIST-20160518-I, B. KIKJ-20160907-II, C. KSOM141006, D. ARK05, E. KIKJ-20160907-I, F. KINM-I, G. KISK-III, H. NGM03

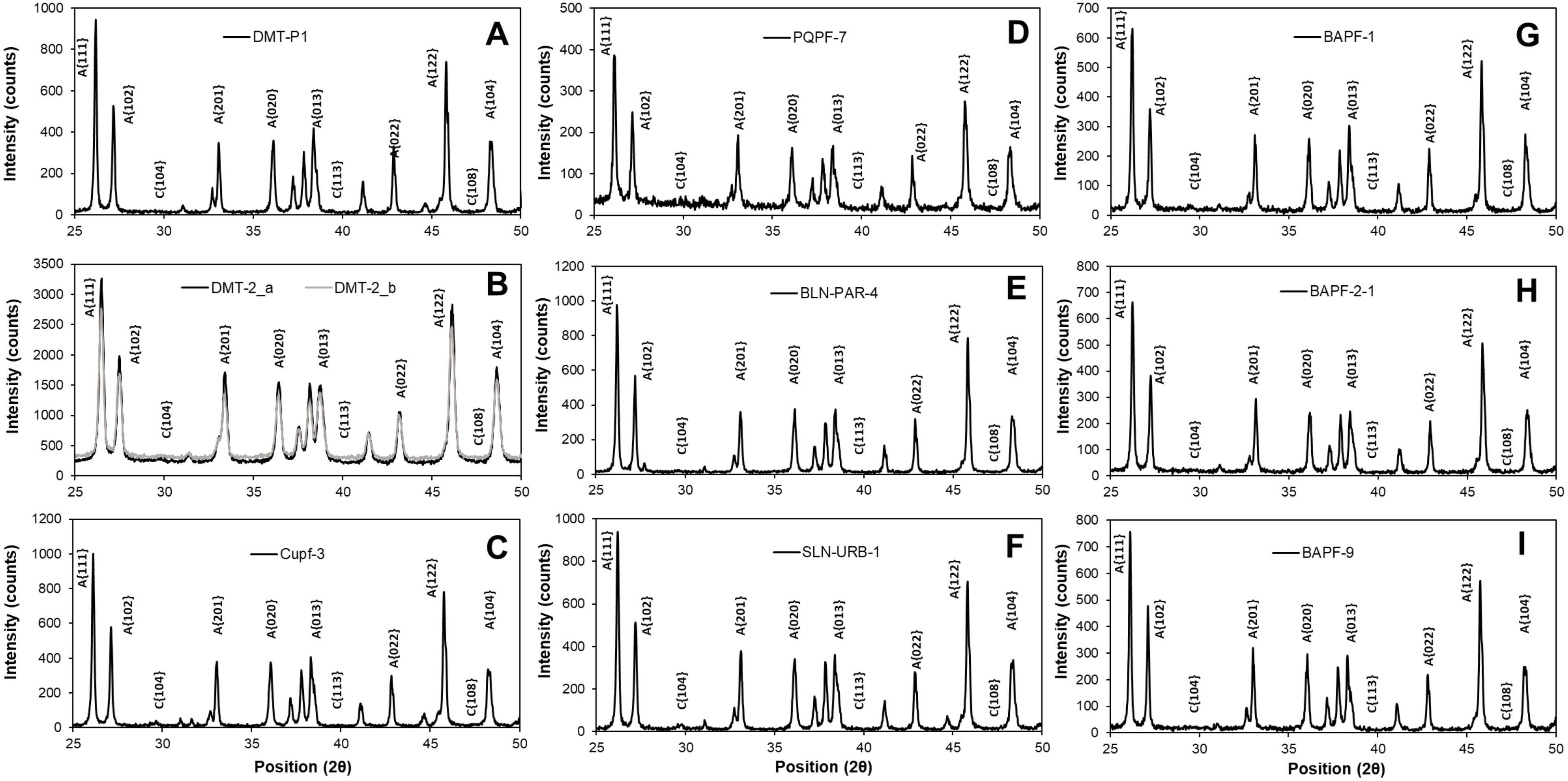

Figure 29. XRD profile from 25°θ to 50°θ showing the aragonite peaks of A. DMT1, B. DMT2, C. CUPF3, D. PQPF7, E. BLN-PAR-4, F. SLN-URB-1, G. BAPF-1, H. BAPF-2-1, I. BAPF-9. These samples have 0% calcite content.

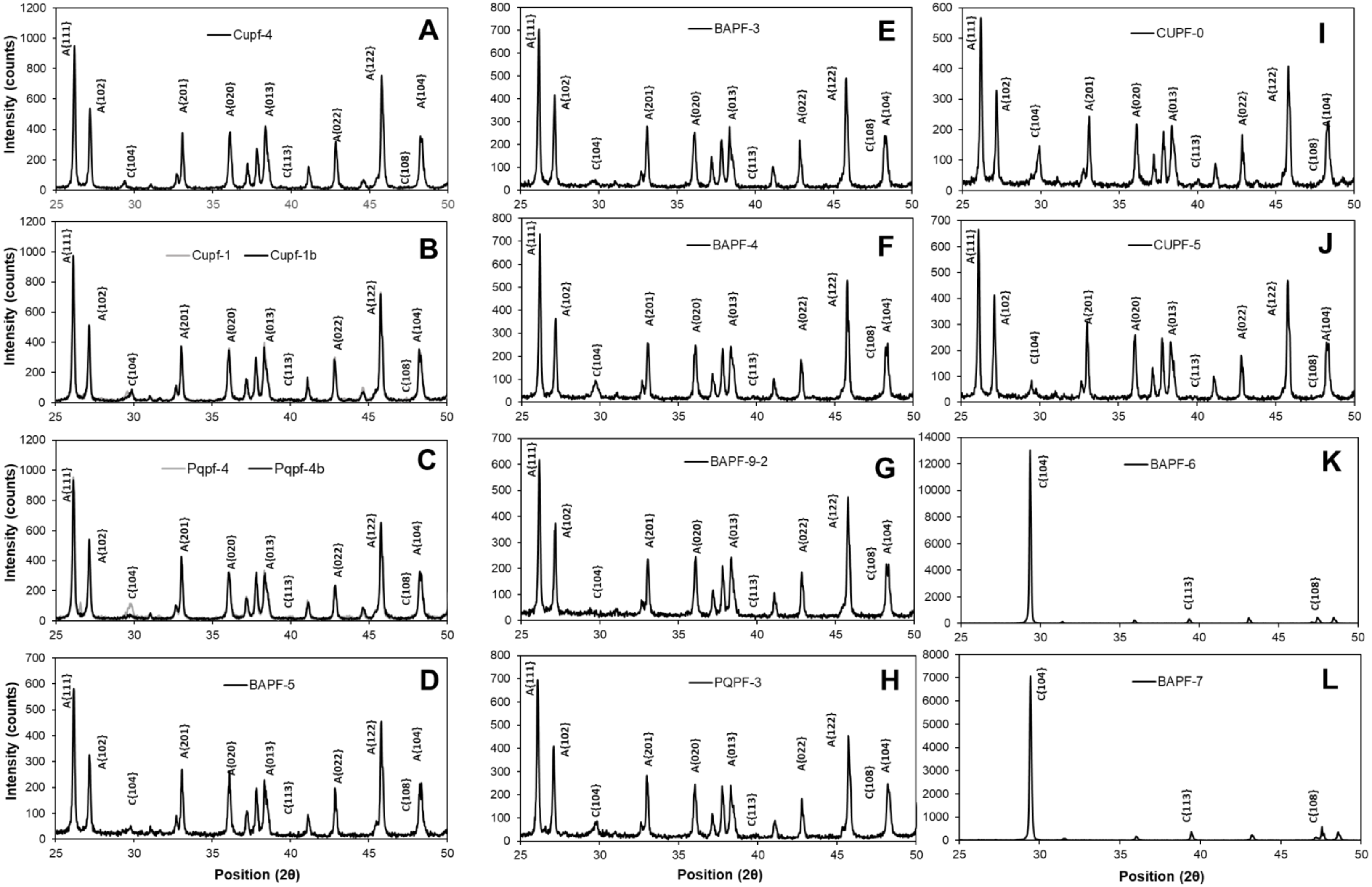

Figure 30. XRD profile from 25°θ to 50°θ showing the aragonite peaks of A. CUPF4, B. CUPF1, C. PQPF4, D. BAPF-5, E. BAPF-3, F. BAPF-9-2, G. PQPF-3, H. CUPF0, I. CUPF5, J. BAPF-6, L. BAPF7. Samples A-J have 2-7% calcite content while samples K-L have 100% calcite content.

3.4. SEM Analysis of fossil corals

Samples KIST-20160518-I, KIKJ-20160907-II, KSOM141006 from Kikai Island show good to excellent preservation of the primary aragonite skeleton (Fig. 31A-C). Similarly, the samples DMT1, DMT2, CUPF3, and CUPF4 have excellent preservation (Fig. 32). The samples are devoid of any mineralization of secondary aragonite and calcite. Aragonite cement often occurs as fine to medium-sized acicular needles that grow perpendicularly from the coral skeletal wall. The occurrence of aragonite cement and dissolution are common in early marine phreatic diagenesis. Samples ARK5 (Fig.31D), KIKJ-20160907-I (Fig.31E), and KISK-III (Fig.31H) show this type of diagenetic imprints. In XRD analysis, these samples have 0% - 1% calcite content. Samples PQPF7 (Fig. 33E) and BAPF9 (Fig. 33I) have 0% calcite content based on XRD mineral phase analysis. SEM images of these samples have acicular aragonite cement overprinting the coral skeleton. This suggests that XRD can only screen the presence of secondary calcite but not aragonite. The thin section and SEM analyses are good compliment to investigate the overall diagenetic imprints in the fossil corals.

Most of the samples have subaerial vadose zone’s diagenetic imprints. The samples are collected from the uplifted marine terraces situated a few meters above the mean sea level. Interaction with freshwater lenses and meteoric water favors the crystallization of calcite cement. The calcite content ranges from 2%-7% based on the XRD phase mineral analysis. SEM images of samples KINM-I (Fig.31F) and NGM3 (Fig.31G) from Kikai Island show that calcite and aragonite occur as carbonate cement of the coral skeleton. Calcite is commonly light colored, rhombohedral-shaped crystals as observed in backscattered electron SEM images. In sample KINM, calcite envelops the outermost surface of the coral skeleton. Blocky cement was observed in the intraskeletal spaces. Samples CUPF1 (Fig33A), CUPF5(Fig33B), PQPF3 (Fig33C), PQPF4 (Fig33D), CUPF1 (Fig33G), and BAPF3 (Fig33H) from NW Luzon have significant calcite content (2-7%).

Few samples have freshwater phreatic diagenetic imprint, which is considered as the late stage of early carbonate diagenesis. Samples BAPF 6 (Fig33F) and BAPF 7 (Fig33E) from the NW Luzon Island exhibit nearly complete replacement of the aragonite skeleton by calcite. The SEM images show extensive dissolution and neomorphic calcite fabric. Due to the interaction of the coral to freshwater, aragonite was dissolved and replaced by low-Mg calcite concomitantly. Thin section analysis shows that some parts have aragonite component. This evidence suggests that the dissolution occurred simultaneously with the mineralization of the secondary low-Mg calcite. The next part of this chapter will discuss the effect of the calcite content on the geochemical tracers in coral skeleton that are usually used as paleoclimate proxies.

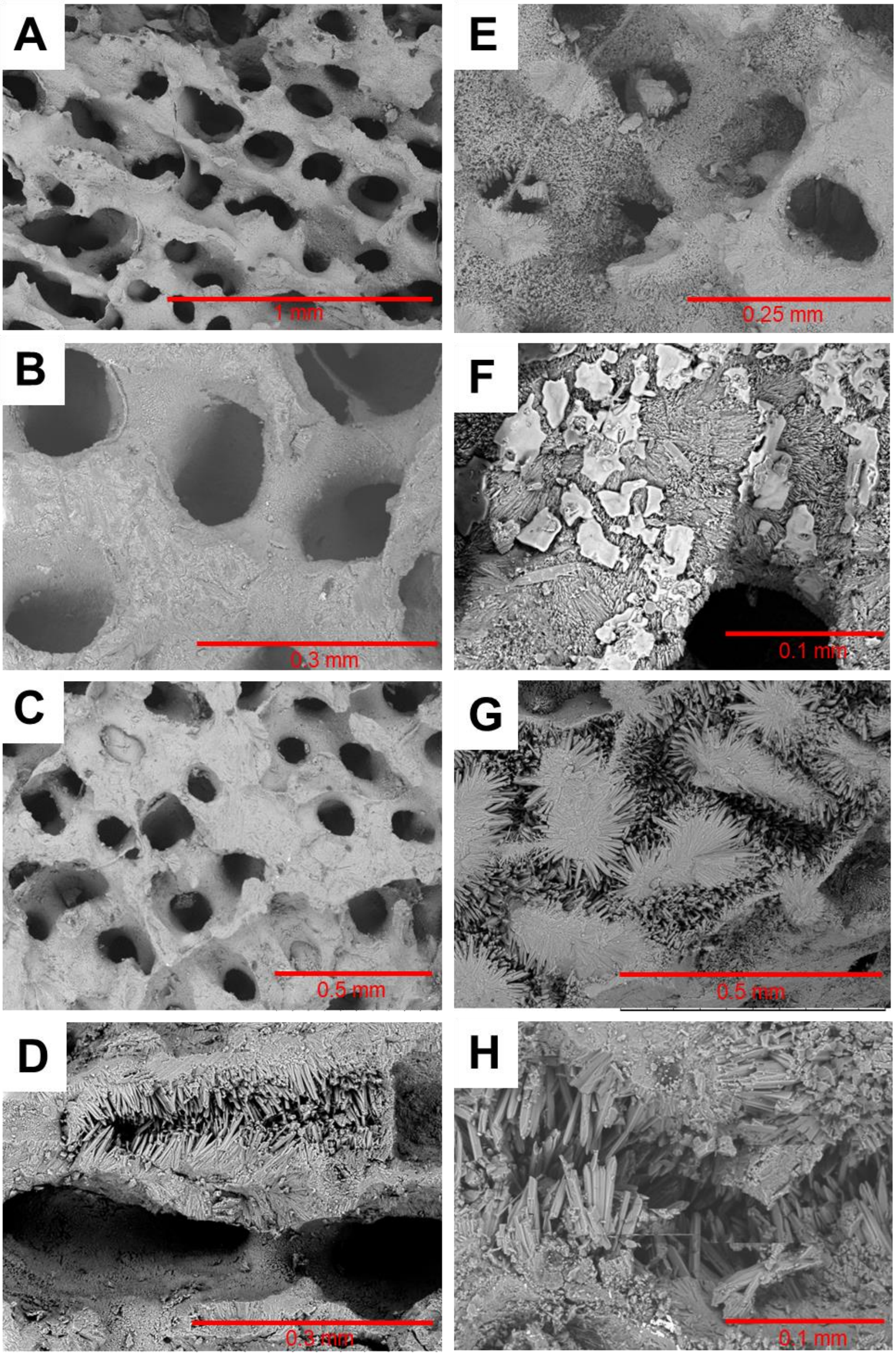

Figure 31. SEM images of A. KIST-20160518-I, B. KSOM141006, C. KIKJ-20160907-II, D. ARK05, E. KIKJ-20160907-I, F. KINM-I, G. NGM03, H. KISK-III. Samples A-C have relatively good to excellent preservation. Samples D, E, H have typical early marine phreatic diagenetic imprints while sample F-G are typical of subaerial vadose diagenesis.

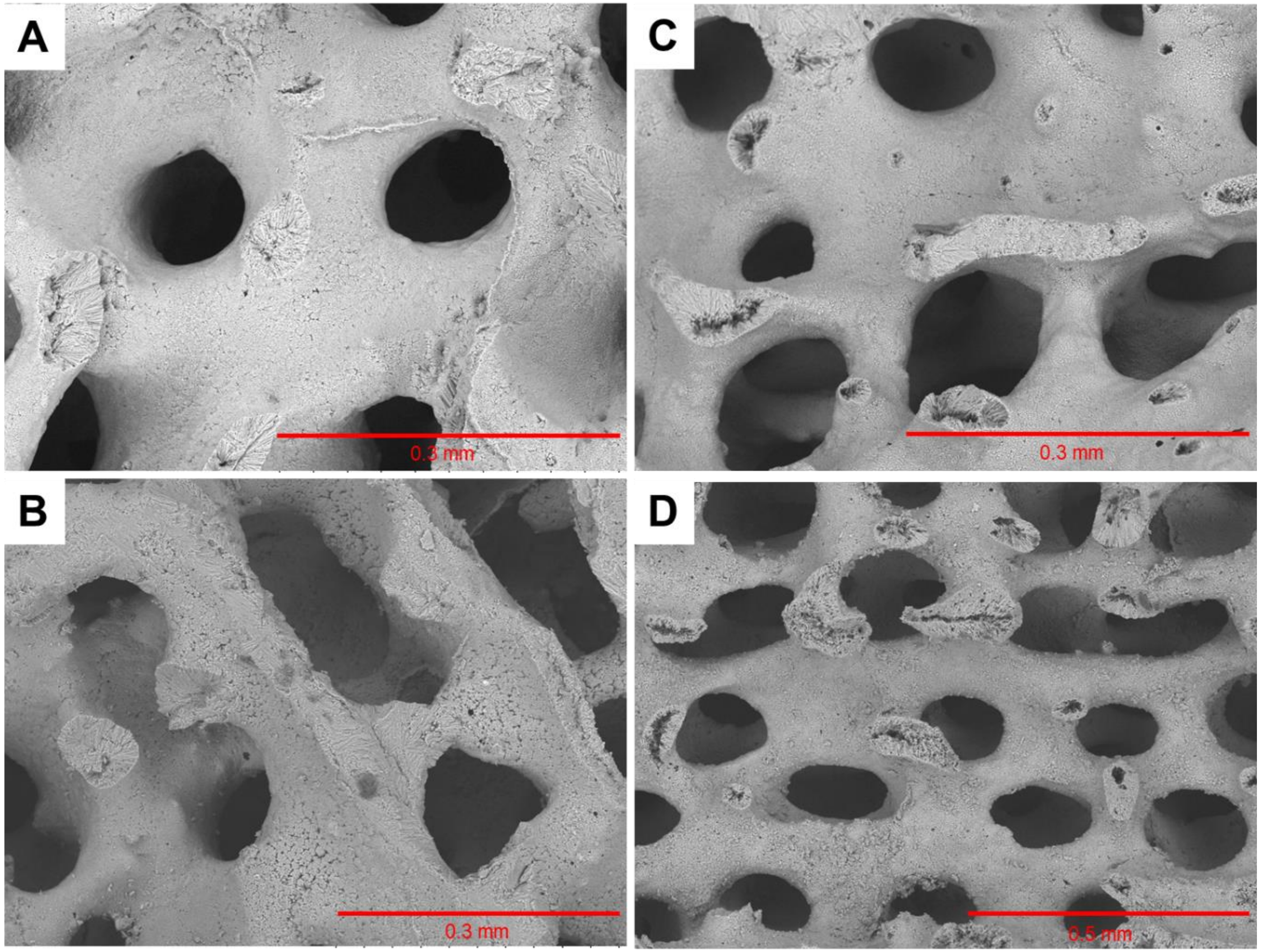

Figure 32. SEM images of A. DMT1, B. DMT2, C. CUPF-4, D. CUPF3. These samples from NW Luzon Island have good to excellent preservation of the aragonitic coral skeleton.

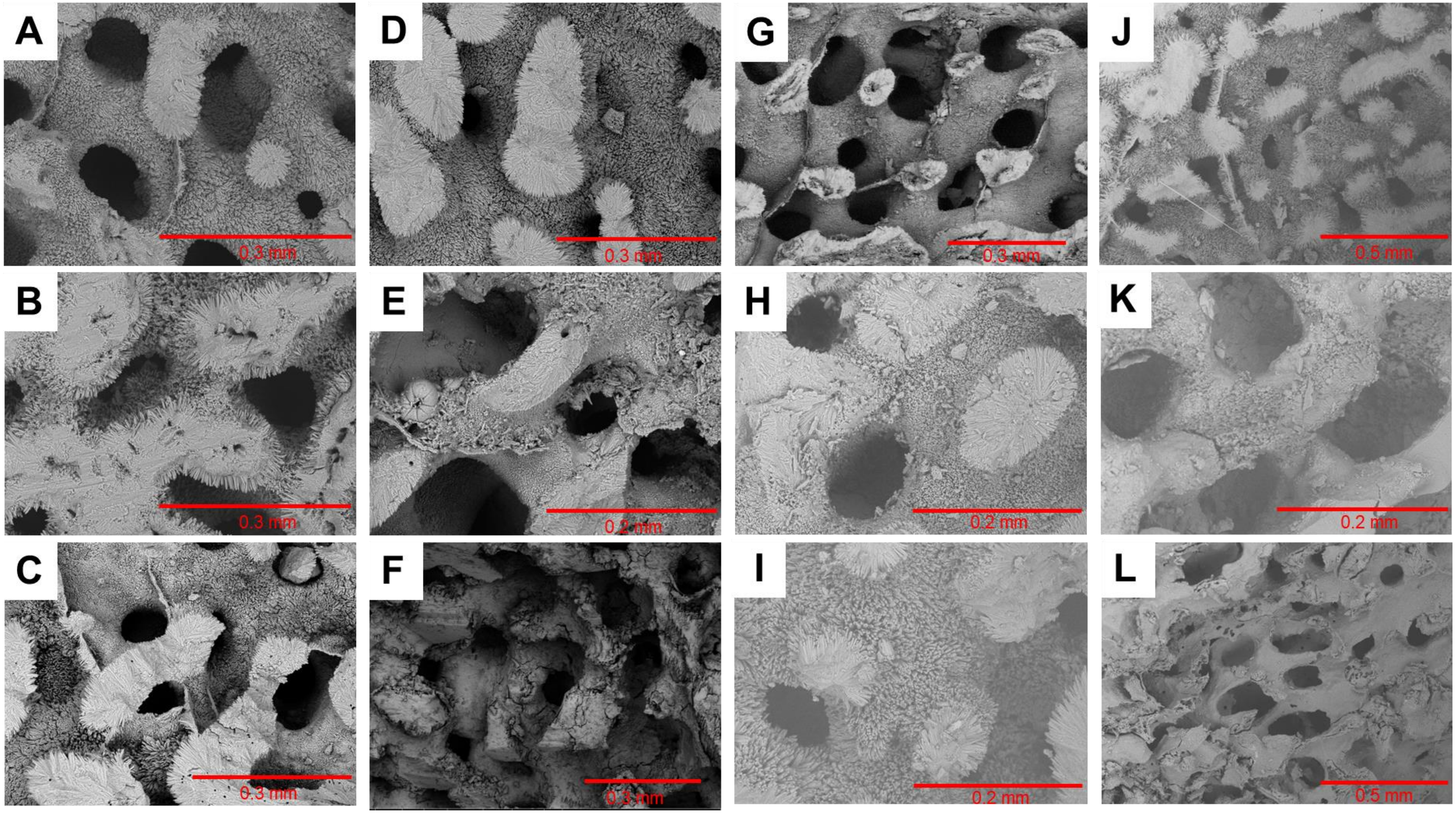

Figure 33. SEM images of A. CUPF1, B. CUPF5, C. PQPF3, D. PQPF4, E. PQPF7, F. BAPF6, G. CUPF1, H. BAPF3, I. BAPF9, J. BAPF-5, K. BAPF7, and L. ROS-DAM-1.

3.5. Effect of diagenetic calcite on coral climate proxies

To investigate the uncertainty from the diagenetic alteration of corals, a fossil coral slab from Damortis Beach, La Union in NW Luzon Island was subjected to detailed diagenetic screening using XRD and SEM analysis. Five subsampling points were identified from top to bottom of the 10-yr coral slab (Fig. 34). Bulk samples and microsamples were collected along the same measurement line.

Results of XRD analysis reveal that DMT-P1a and DMT-P1c have pristine aragonitic coral skeleton. Based on the RIR calculation, the calcite and aragonite content are 0% and 100%, respectively. SEM images of these pristine sections of the slab show the clear center of calcification along the saw-cut surfaces. The long axes of the tightly packed slender aragonite crystals are oriented nearly perpendicular to the center of calcification. In DMT-P1b, the relatively low intensity c{104} peak at 29.5° 2θ position indicates the presence of calcite in a predominantly aragonite skeleton. The calcite and aragonite content are 9% and 91% respectively. The surface of skeletal wall is relatively rough compared to P1a and P1c. Blocks of calcite cement occur in the intraskeletal pore spaces. Minor dissolution was also observed in the SEM image.

XRD results of DMT-P1d and DMT-P1e show stronger c{104} peak at 29.5° 2θ position. The calcite content is 55% in DMT-P1d and 70% in DMT-P1e. SEM analysis of DMT-P1d shows that the aragonite skeleton is still present, however, dissolution is evident. The dissolution of the skeleton has started along the center of calcification. Secondary calcite occurs as clusters of rhombohedral crystals deposited on the surface wall of the skeleton. DMT-P1e has more advanced vadose diagenetic imprints. Dissolution is more extensive resulting in the formation of the powdery texture of the unstable aragonite and microporous fabric of the skeleton. Secondary calcite is being deposited simultaneously with the dissolution process of the original aragonite skeleton.

Bulk powder samples of approximately 2.5 g were collected from points A, B, C, D, E in the coral slab (Fig. 34). Five replicate samples per point were measured for Sr, Mg, and Ca concentrations using inductively-coupled plasma optical emission spectrometer (ICP-OES). Five replicate samples per point were analyzed in isotope ratio mass spectrometer (IRMS) Finnigan MAT 253 coupled with Kiel IV carbonate device to measure the oxygen ($\delta^{18}O$) and carbon ($\delta^{13}C$) isotopes. Microsamples of approximately 250-300 µg were collected using a microdrill along the same measurement line and following a 0.2mm subsampling interval. The samples were analyzed for Sr, Mg, Ca, $\delta^{18}O$, and $\delta^{13}C$ using the same methods used for bulk samples.

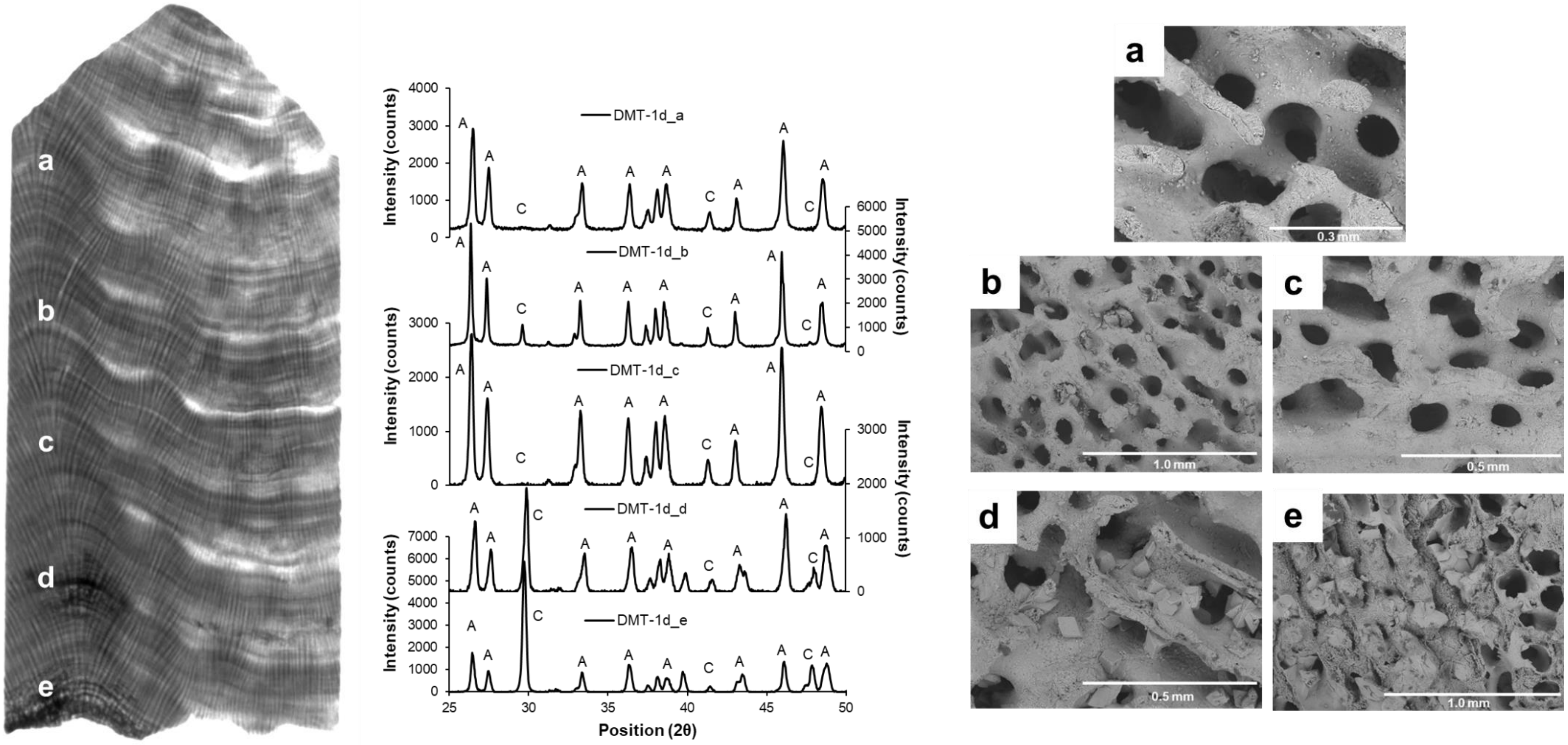

Figure 34. The Xray photo of the coral DMT-1d from Damortis Beach, La Union shows irregular, anomalously high-density sections D and E. XRD analysis shows that sections A and C have 0% calcite, section B has 9% calcite and 91% aragonite, section D has 55% calcite and section E has 70% calcite. SEM images revealed the well-preserved coral aragonite in sections A and C. Some intraskeletal spaces have been occupied by cement in section B. Rhombohedral calcite cement and minor dissolution are evident in the SEM image of Section D. In Section E, powdery unstable aragonite is formed due to the advanced dissolution and calcite crystals have been precipitated simultaneously.

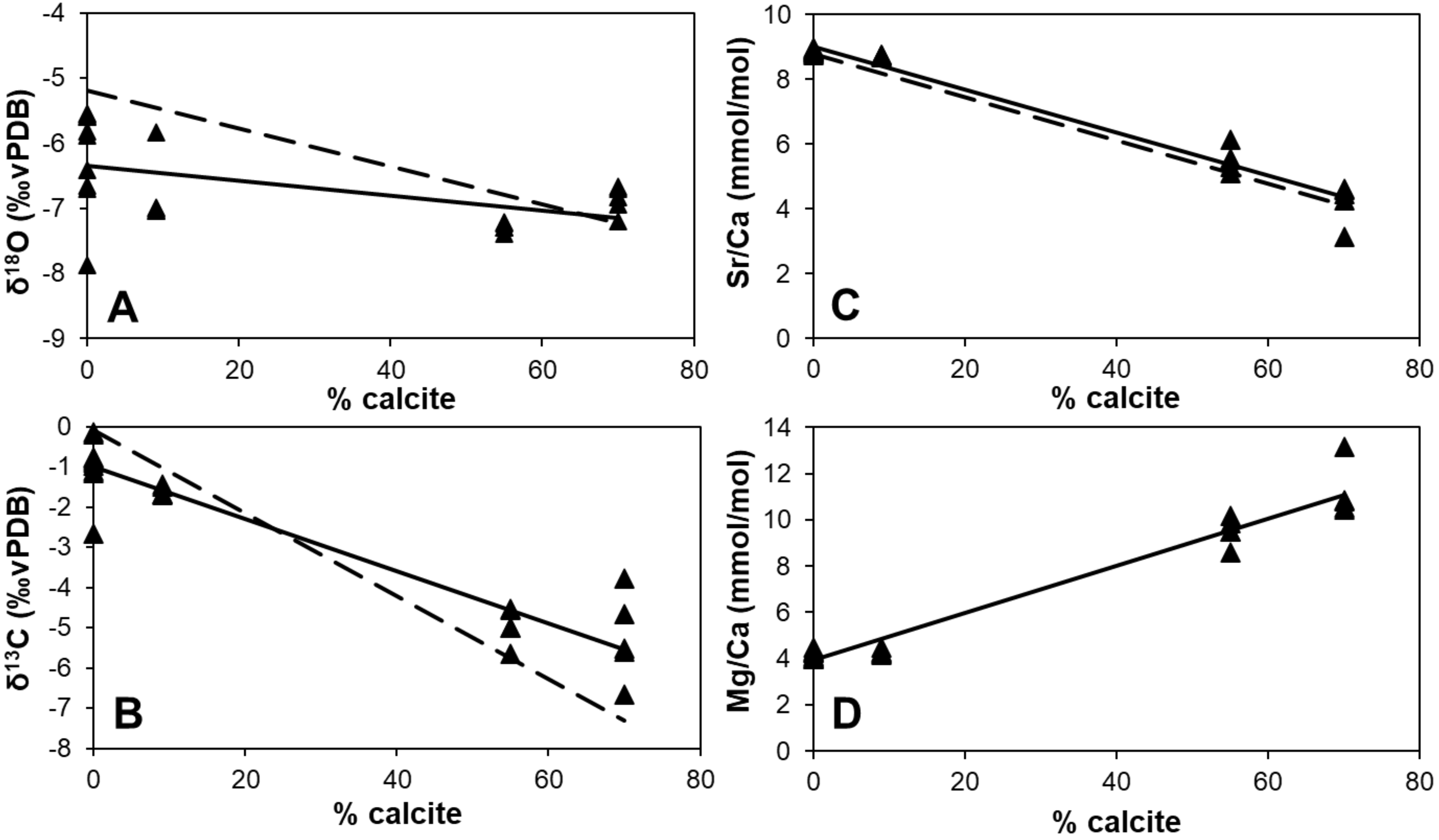

Figure 35. Cross-plots of (A) δ18O-%calcite, (B) δ13C-%calcite, (C) Sr/Ca-%calcite, and (D) Mg/Ca-%calcite. Each bulk sample from sections A, B, C, D, and E were analyzed. The δ18O, δ13C, and Sr/Ca are significantly decreased with increasing %calcite as shown by the trendline (solid black line) of the weighted mean from the 5 replicate bulk analysis for each sample. The black dashed line is the proxy-%calcite trend relationship published by McGregor and Gagan et al. 2003. The Mg/Ca is significantly increased as a function of increasing %calcite content.

The results of the 5 replicate measurements of the bulk samples were plotted against the % calcite content measured from the XRD analysis. The $\delta^{18}O$-%calcite, $\delta^{13}C$-%calcite, Sr/Ca-%calcite, and Mg/Ca-%calcite plots are presented in Figure 35A-D. The least square regression line for each plot (solid line) was established from the mean values of the 5 replicate bulk analysis. $\delta^{18}O$, $\delta^{13}C$, and Sr/Ca values of DMT-P1d decrease with the increasing %calcite content in the sample. The weight mean regression lines are defined by the following equations:

(Eq. 1) $\delta^{18}O = [-0.011\ (\pm 0.009) \times \%calcite] - 6.34(\pm 0.34)$ $r = -0.62$; $p = 0.26$

(Eq. 2) $\delta^{13}C = [-0.065\ (\pm 0.005) \times \%calcite] - 0.1\ (\pm 0.19)$ $r = -0.99$; $p = 0.00086$

(Eq. 3) $Sr/Ca = [-0.078\ (\pm 0.005) \times \%calcite] - 9.1\ (\pm 0.20)$ $r = -0.99$; $p = 0.00058$

The $\delta^{18}O$-%calcite, $\delta^{13}C$-%calcite, and Sr/Ca-%calcite slopes have similar trend to the negative correlation (dashed line) of the previously published data from Papua New Guinea (McGregor and Gagan 2003) with $\delta^{18}O$-%calcite slope of -0.029 (±0.002), $\delta^{13}C$-%calcite slopes of -0.012 (±0.007) and -0.103 (±0.007), and Sr/Ca-%calcite slope of 6.69 (±0.000193).

Mg/Ca-%calcite has opposite trend compared to the other geochemical proxies. Mg/Ca is systematically increased as a function of increasing %calcite content. The weight mean regression line is defined by the following equation:

$Mg/Ca = [0.122\ (\pm 0.009) \times \%calcite] - 3.8\ (\pm 0.35)$ $r = 0.99$; $p = 0.0008$

Figure 36 details the $\delta^{18}O$, $\delta^{13}C$, Sr/Ca, and Mg/Ca records from the microsamples collected along the same measurement line of the bulk sample analysis. The average $\delta^{18}O$ in the pristine section of the coral is -6.09‰, which is higher than -7.04‰, which is the average $\delta^{18}O$ in the diagenetically altered portion of the coral. The average $\delta^{13}C$ in the pristine section of the coral is -1.34‰, which is higher than -4.64‰, which is the average $\delta^{13}C$ in the diagenetically altered portion of the coral. Coral $\delta^{18}O$ reflects both the 1) water temperature and 2) seawater $\delta^{18}O$ (Julliet-Leclerc and Schmidt 2000). It records the temperature, salinity, and hydrological balance in the surface ocean (McCulloch et.al. 1994; Gagan et.al. 1998, 2000). The shift to more negative $\delta^{18}O$ in coral aragonite reflects warmer, less saline water conditions. However, the negative $\delta^{18}O$ shift in DMT-P1s coral as a function of replacement of aragonite by secondary calcite indicates the change of calcifying fluid rather than SST-dependent isotopic variation. The calcite in vadose zone is precipitated due to the influence of freshwater/meteoric water interaction with the fossil coral skeleton. NW Luzon Island is in the tropical western Pacific which receives high amount of rainfall annually. The freshwater aquifer is being recharged by meteoric water which infiltrates the ground. The $\delta^{18}O$ in calcite of the vadose diagenesis reflects the $\delta^{18}O$ of the meteoric water (McGregor and Gagan 2003). The $\delta^{18}O$ in precipitation (meteoric water) is enriched by lighter ^{16}O as compared to the $\delta^{18}O$ in seawater. Thus, the $\delta^{18}O$ in coral aragonite precipitated in the seawater has enriched heavier ^{18}O and higher $\delta^{18}O$ values.

Coral $\delta^{13}C$ reflects metabolic carbon consumption due to the influence of water transparency/turbidity caused by sediment discharge, upwelling, water productivity, which affects photosynthetic activity of coral (McConnaughey 1988, 1989). Photosynthesis consumes organic ^{12}C, depleting the incorporated ^{12}C in the skeleton. It increases the $\delta^{13}C$ by systematical enrichment of ^{13}C. The metabolic process of coral is dependent on light intensity. However, the negative $\delta^{13}C$ shift in altered portion of the coral slab is due to the change in mineralogy which also reflects the change in the chemistry of calcifying fluid. The $\delta^{13}C$ in vadose zone's calcite is also affected by the processes involving meteoric water. The meteoric water percolates through the soil layer before reaching the surface of the coral carbonate. The vegetation in the soil changes the $\delta^{13}C$ of the meteoric water. The uplifted reef terrace in Damortis beach where DMT-P1s was collected has a very thin soil layer with almost no vegetation. The meteoric water dissolves minimal soil-gas CO_2 in this condition. However, compared to seawater, the CO_2 gas exchange in meteoric water is higher. The increase of organic ^{12}C in meteoric water lowers $\delta^{13}C$. This explains the relatively lower $\delta^{13}C$ in calcite-dominated altered coral than the pristine aragonitic coral.

The average Sr/Ca value in the pristine sections of the coral is 8.83 – 8.87 mmol/mol. This is higher than 3.43 – 4.89 mmol/mol, which is the range of average Sr/Ca value in the diagenetically altered portion of the coral. The average Mg/Ca value in the pristine sections of the coral is 4.05 – 4.31 mmol/mol. This is lower than 10.46 – 12.54 mmol/mol, which is the range of average Mg/Ca value in the diagenetically altered portion of the coral. The data shows that the concentration of Sr^{2*} is enriched in coral aragonite while the Mg^{2+} is depleted. The change of carbonate mineralogy due to diagenesis resulted in opposite shift of the Sr/Ca and Mg/Ca values. In the calcite-dominated altered sections, the Mg^{2+} is enriched while Sr^{2+} is depleted. Sr/Ca and Mg/Ca are both SST proxies. In a pristine aragonite coral, higher Sr/Ca and lower Sr/Ca values correspond to cooler and warmer SST conditions. Mg/Ca, on the other hand, is positively correlated with SST where higher Mg/Ca reflects higher SST and vice versa. But the large shifts of the mean Sr/Ca and Mg/Ca values between well-preserved and diagenetically altered portions of the a single corals are not dependent on SST variability. The change of mineral composition and in turn, change of calcifying fluid dictates such anomalies.

McGregor and Gagan 2003 discussed that the negative shift of Sr/Ca from pristine to diagenetically altered coral is because of the difference of partitioning coefficient of calcite and aragonite. The Sr/Ca of the carbonate is a function of the partitioning coefficient (D_{Sr}) of Sr multiplied by the Sr/Ca of the seawater. The D_{Sr} of calcite varies from 0.016 to 0.14, which is significantly lower than 0.9-1.2, the D_{Sr} of aragonite (Kinsman and Holland 1969; Katz et al. 1972; Veizer 1983). The D_{Sr} for aragonite to calcite transformation is 0.05 (Katz et al. 1972). It means that the Sr/Ca of calcite is much lower than the seawater where the carbonate precipitates while the Sr/Ca of aragonite is near equilibrium with the seawater.

Mg/Ca is significantly depleted in the coral skeleton relative to the concentration of Mg/Ca in the seawater. Aragonite precipitation experiments have shown that the exchange coefficient of Mg^{2+} from seawater to coral aragonite is decreasing with respect to the increasing temperature from 5°C to 75°C (Gaetani and Cohen 2006). The predicted aragonite-seawater partitioning coefficient of Mg^{2+} (D_{Mg}) is lower than the D_{Sr} of aragonite suggesting the Sr^{2+} is strongly compatible to the aragonite crystal lattice than Mg^{2+} (Gaetani and Cohen 2006). In contrast, the distribution coefficient (λ_{Mg}) of Mg^{2+} from the calcifying solution to calcite is increasing with respect to the increasing temperature (Oomori et al. 1987). The same study explained that the changes in molar ratio between Mg^{2+}/Ca^{2+} has small effect to calcite but largely affecting the distribution coefficient (λ_{Sr}) of Sr^{2+}. These experimental data explain the diverging pattern of Sr/Ca and Mg/Ca with respect to different aragonite-calcite ratios in diagenetically altered fossil coral.

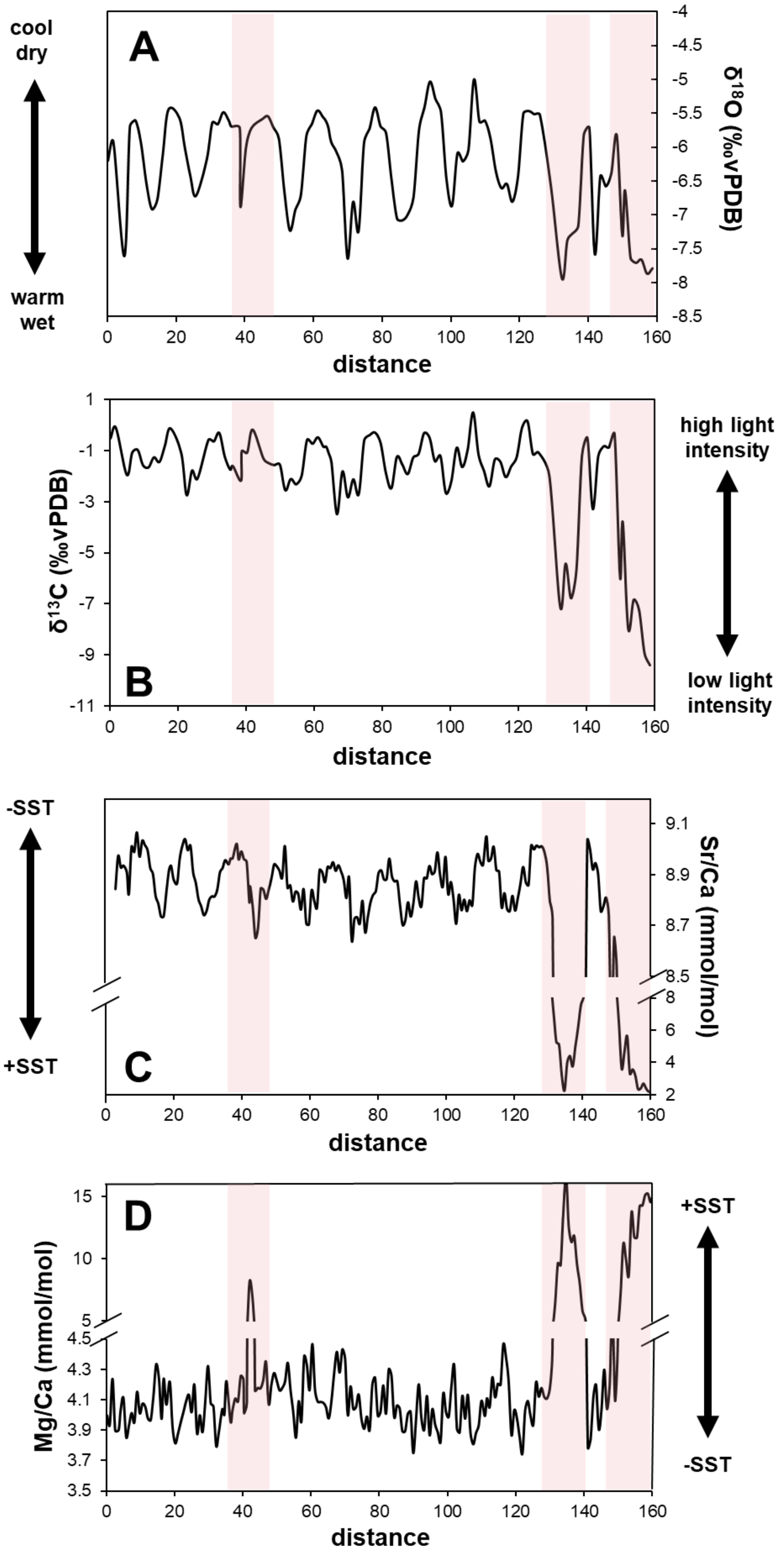

Figure 36. Ten-year record of (A) δ^{18}O, (B) δ^{13}C, (C) Sr/Ca, and (D) Mg/Ca of DMT-1d. The red-shaded sections indicate the parts where coral is diagenetically altered. The incorporation of secondary calcite significantly changes the geochemistry of the fossil coral.

Chapter 4

Growth Patterns of fossil *Porites*

4.1 Linear extension rate, skeletal density, and calcification rate

The study of coral growth variables could potentially unravel oceanographic changes and reef development in geologic timescale. Corals are sensitive to environmental changes and often used to track long-term changes in the ocean. The alternating pattern of high- and low-density bands observed in X-radiographed images of corals have a strong relationship with the seasonal variability of ocean conditions (Knutson et.al. 1972; Barnes and Lough 1989). Coral growth is influenced by water depth, distance from the shore, and SST as well as different stressors such as thermal stress, nutrients, ocean acidification, and radioactivity (Lough and Barnes 2000; Lough and Cooper 2011). High sedimentation, turbidity, and hydrographic conditions also affect the calcification and upward extension of corals (Buddemeier et.al. 1974; Scoffin et.al. 1992; Cuevas et.al. 2009; Lough and Cooper 2011).

The linear extension rate is positively correlated with the annual SST, based on the coral growth records from Hawaii, Thailand, Great Barrier Reef, Arabian Gulf and Hong Kong (Grigg 1981; Scoffin et.al. 1992; Lough and Barnes 2000; Goodkin et.al. 2011). The linear extension rate is positively correlated with calcification rate (Scoffin et.al. 1992; Lough and Barnes 2000). The change in extension rate is the dominant control on calcification rates. The skeletal density is inversely proportional to the extension rate. The slow growth rate allows coral to develop thicker and denser skeleton (Barnes and Lough, 1993). There are few studies that documented the growth variations of fossil corals in NW Pacific due to limited fossil coral sampling (Sowa et.al. 2014; Roff 2020). Lough and Cooper 2011 emphasized that coral growth variable analysis should be done for holistic interpretation of coral geochemical datasets. From here, paleoenvironmental conditions are reconstructed from growth patterns and geochemical records. This would give a better scenario of the past environmental changes and coral reef development relative to the present-day.

Linear extension rates, skeletal density and calcification rates were measured in 4 fossil corals from Kikai Island and 6 fossil corals from Northwest Luzon Island (Table 4). From the 4 samples from Kikai Island, 5.7 ka coral (Fig. 37d) recorded the fastest linear extension at 0.87 cm/yr and calcification rates at 1.56 g/cm2yr. 3.2 ka coral (Fig. 37b) has the lowest extension at 0.38 cm/yr and calcification rate at 0.70 g/cm2yr. Skeletal densities ranging from 1.71 – 1.87 g/cm3, are not largely different among the four samples.

Sample Name	Location	Conventional Radiocarbon Age (cal. yr BP)	Number of Annual Bands	Extension Rate (mm/yr)	Skeletal Density (g/cm^3)	Calcification Rate (g/cm^{2}yr)
Kikai-jima corals						
ARK05	Araki, Kikai-jima	1400*	9	7.77 ± 0.86	1.81 ± 0.14	1.39 ± 0.11
KIKJ-20160907-II	Keraji, Kikai-jima	3235±20	20	3.77 ± 0.51	1.87 ± 0.09	0.70 ± 0.09
KIKJ-20160907-I	Keraji, Kikai-jima	4100*	35	6.57 ± 0.74	1.71 ± 0.13	1.12 ± 0.16
KIST-20160518-I	Shitooke, Kikai-jima	5712±24	13	8.72 ± 1.00	1.80 ± 0.14	1.56 ± 0.15
Northwest Luzon corals						
PQPF-180220-4	Pasuquin, Ilocos Norte	2972±70	10	14.11 ± 2.09	0.66 ± 0.50	0.91 ± 0.67
DMT-1	Rosario, La Union	4200±20	22	17.6 ± 3.49	1.26 ± 0.15	2.24 ± 0.56
DMT-3	Rosario, La Union	4277±19	9	10.17 ± 1.29	1.28 ± 0.18	1.30 ± 0.24
DMT-2	Rosario, La Union	4336±21	26	12.35 ± 3.97	1.04 ± 0.37	1.27 ± 0.49
CuPf-180218-4	Currimao, Ilocos Norte	6144±77	23	12.05 ± 1.31	1.06 ± 0.40	1.26 ± 0.46
CuPf-180218-1	Currimao, Ilocos Norte	6285±79	6	16.94 ± 1.66	1.67 ± 0.16	2.81 ± 0.27

Table. 4. The measurement of the number of annual growth bands, linear extension rates, skeletal densities and calcification rate of the 10 fossil corals from Kikaijima and Northwest Luzon

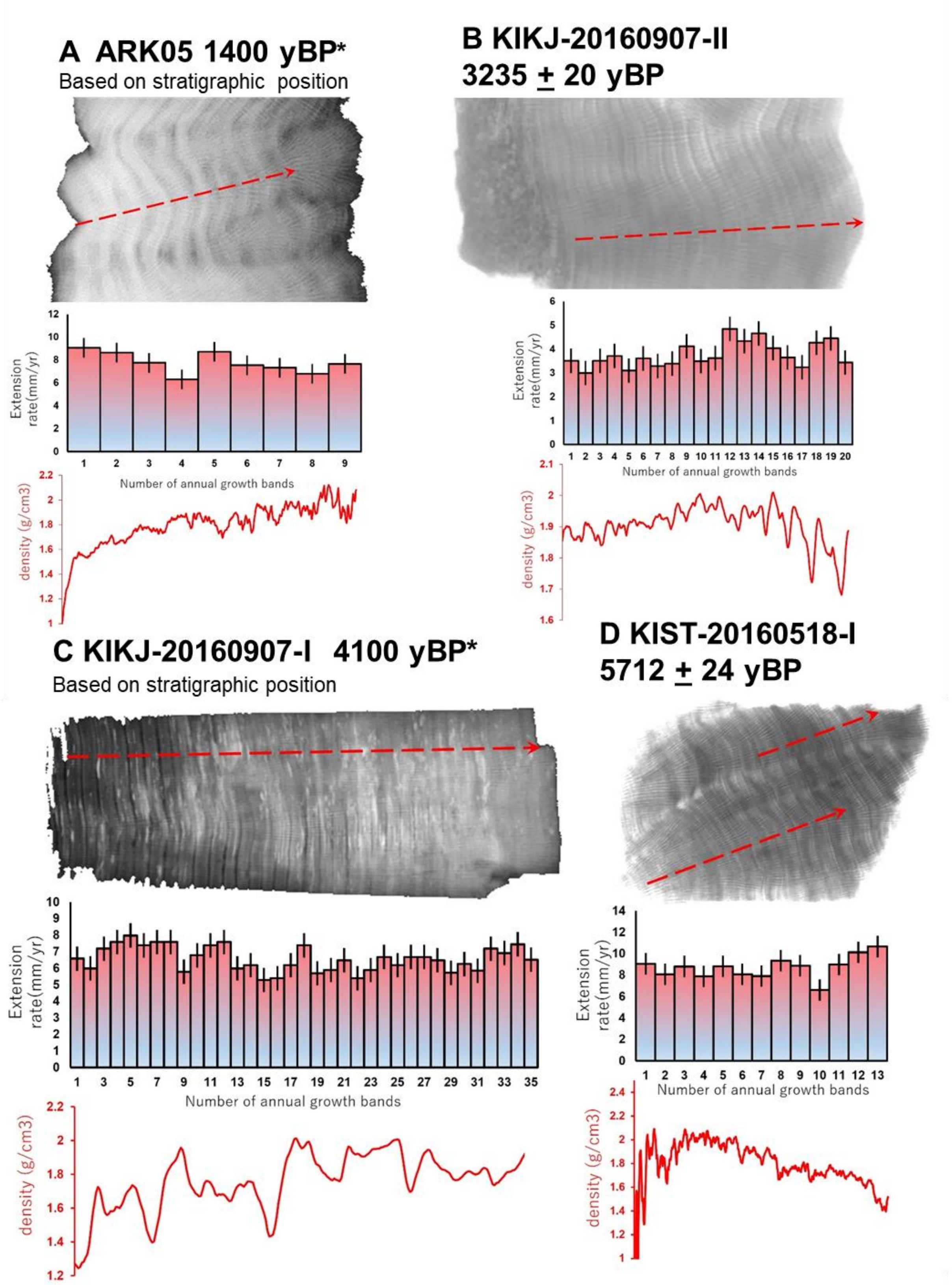

Figure 37. X-ray photographs, linear extension rate (LER) and density of the 4 fossil corals from Kikai Island: A. ARK05, B. KIKJ-20160907-II, C. KIKJ-20160907-I, D. KIST-20160518-I. Sample names and corresponding ^{14}C age dates are indicated in the figure.

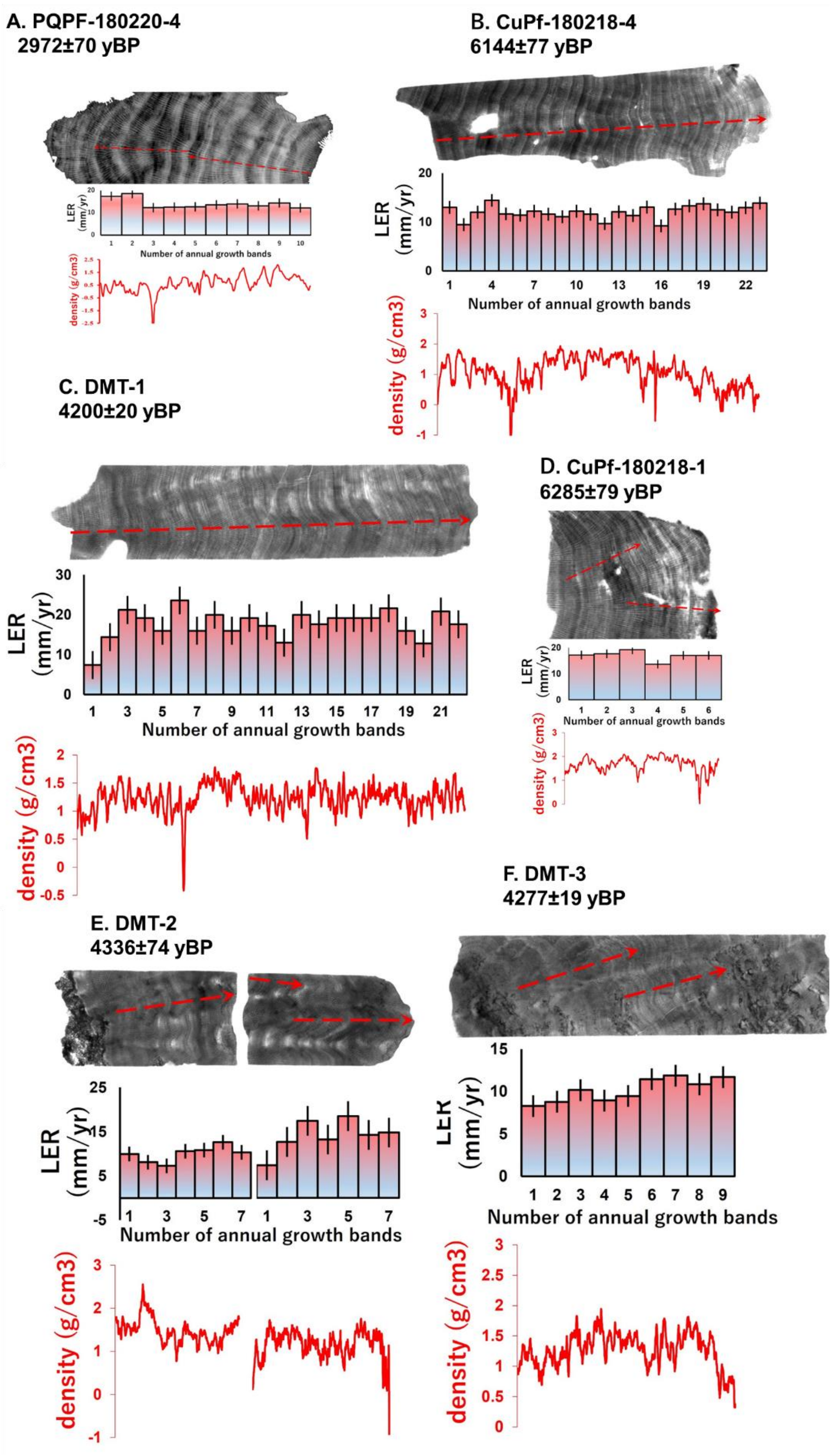

Figure 38. X-ray photographs, linear extension rate (LER) and density of the 6 fossil corals from NW Luzon Island: A. PQPF-180220-4, B. CuPf-180218-4 C. DMT-1, D. CuPf-180218-1, E. DMT-2, F. DMT-3. Sample names and corresponding ^{14}C age dates are indicated in the figure.

Linear extension (1.2 to 1.76 cm/yr) and calcification (0.91 to 2.81 g/cm2yr) rates are higher in Northwest Luzon corals compared to Kikaijima corals. DMT-1/4.2 ka coral (Fig. 38c) has the fastest growth (extension) rate at 1.76 cm/yr while DMT-3/4.27 ka coral (Fig. 38f) has the slowest growth (extension) rate at 1.02 cm/yr among the six fossil Porites from Northwest Luzon. CuPf-180218-1/6.3 ka coral (Fig. 38d) has the densest skeleton (1.67 g/cm3) and highest calcification rate (2.81 g/cm2yr). Among the 6 fossil corals, PQPF-180220-4/3.0 ka coral (Fig. 38a) is the lightest skeleton (0.66 g/cm3) and has the lowest calcification rate (0.91 g/cm2yr).

The correlation between different growth variables was tested following the analysis used in modern Porites corals (Lough and Barnes 2000). The linear extension rate is significantly and positively related to calcification rate (Fig. 39a, $r = 0.72$, $p = 0.019$, $n = 10$). The skeletal density and linear extension rates are inversely correlated with each other (Fig. 39b, $r = -0.56$, $p=0.09$, $n = 10$). The calcification rate is not significantly related to the average skeletal density (Fig. 39c, $r = 0.16$, $p = 0.66$, $n = 10$). These relationships show that the calcification rate is mostly influenced by linear extension rate. The changes in skeletal density do not reflect significantly in the changes of calcification rate.

The box plots of coral growth variables data show the variation in terms of interannual growth variability. The linear extension rate, skeletal density and calcification rate of Kikai Island corals are less varied compared to the growth patterns of Northwest Luzon Island corals (Fig. 40). The relatively large standard deviations (1σ/S.D.) of the measured values from growth bands of the Porites samples of Northwest Luzon indicate highly varied interannual variability. The 1σ of linear extension rates of Northwest Luzon coral range from 1.29 to 3.97 compared to the 0.51 to 1 of Kikai Island corals. Skeletal densities and calcification rates of individual growth bands of Northwest Luzon corals are also varied by $1\sigma = 0.15$ to 0.50 and $1\sigma = 0.24$ to 0.67, respectively. The large deviation of these values is well-presented by the difference of maxima and minima values of growth variables in the box plots of Northwest Luzon corals (Fig. 40).

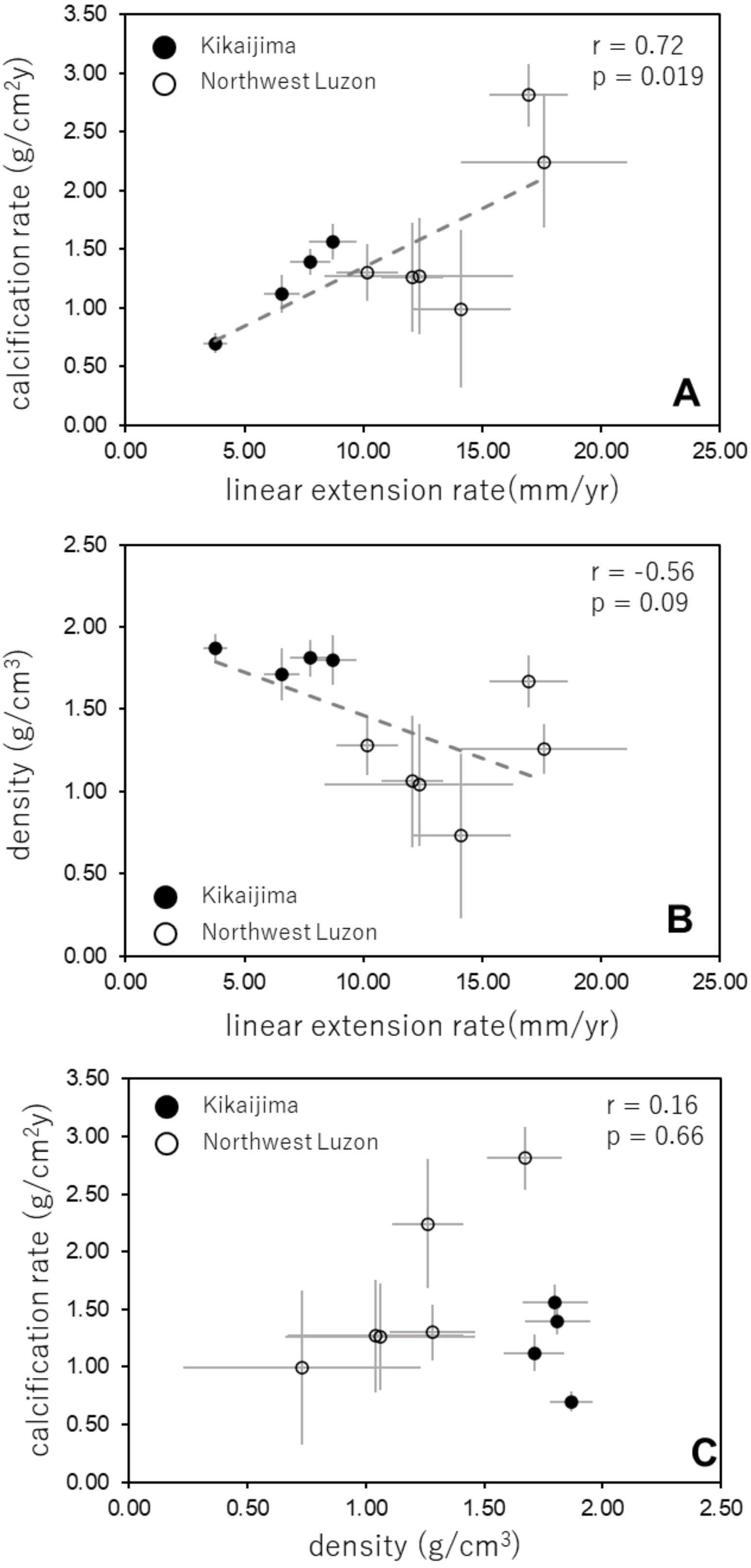

Figure 39. Relationships of coral growth variables from Kikai Island and Northwest Luzon Island. Linear extension rate was directly (r = 0.72, p = 0.019) and inversely (r = -0.56, p = 0.09) correlated with calcification rate (A) and density (B). Density was not significantly correlated with calcification rate (C; r = 0.16; p = 0.66)

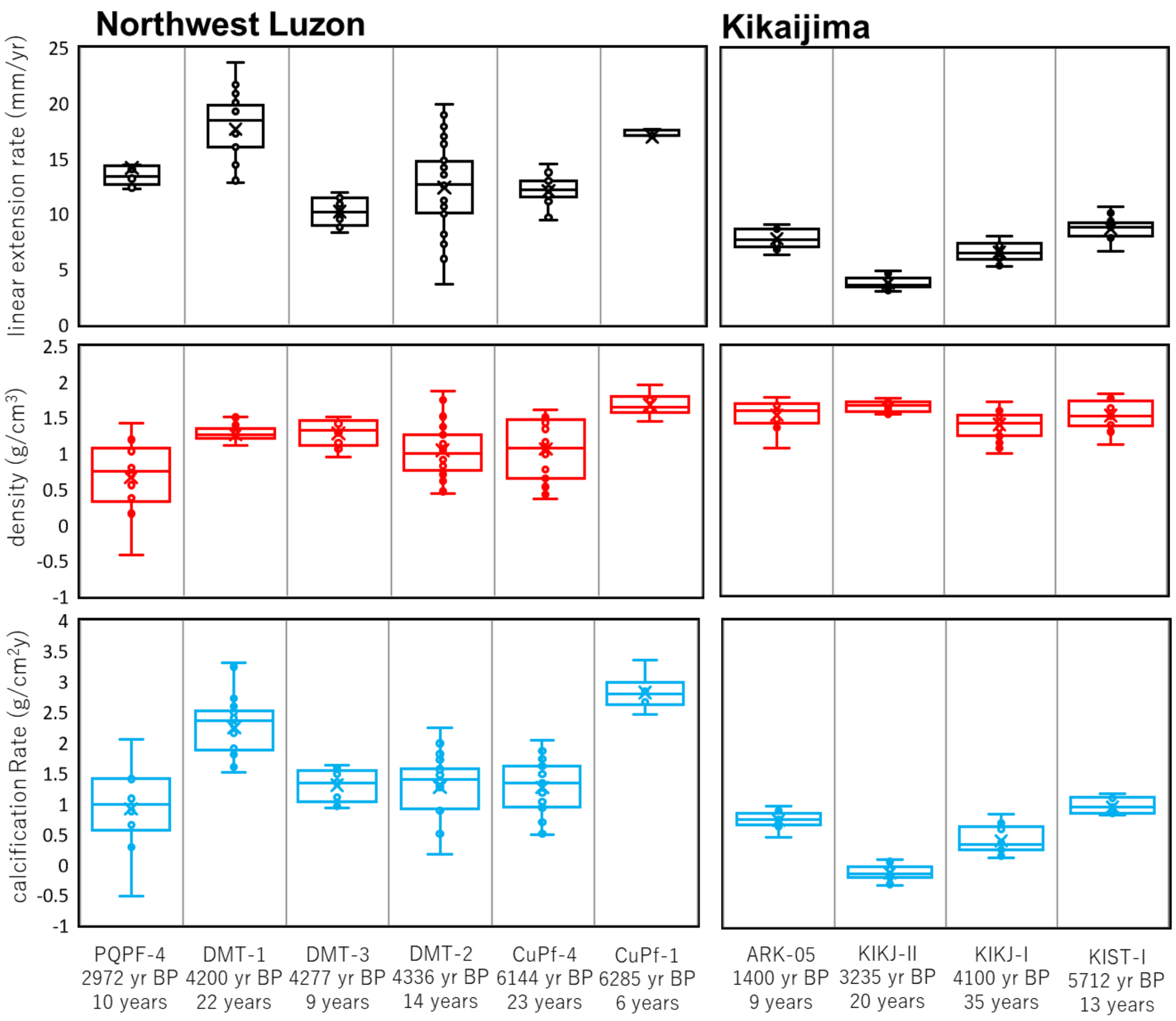

Figure 40. Box plots of the linear extension rates (black), skeletal densities (red) and calcification rates (blue) of the fossil corals from Northwest Luzon and Kikaijima. The x-axis shows the sample name, number of annual bands and radiocarbon age dates of fossil corals. Box plots show the statistical range and standard deviation of the growth variables within the internal chronology of fossil corals

4.2 Paleoenvironmental Implications of Coral Growth

The water temperature is the dominant factor influencing coral growth. The relationship of temperature and coral extension rate has been documented in the modern coral colonies in Great Barrier Reef, Hawaii and Thailand (Grigg 1981; Scoffin et.al. 1992; Lough and Barnes 2000). This correlation established that the linear extension is significantly and directly correlated with coral calcification (r = 0.96) across the 44 sites in Indo-Pacific. The skeletal density is significantly but inversely correlated with linear extension (r = -0.80) and calcification (r = -0.64) rates. The similar correlation trend between linear extension and SST was also reported in northern South China Sea for Porites lutea (Nie et.al. 1997). Other coral species from Indo-Pacific and Caribbean also recorded the same linear extension rate – SST sensitivity but have slower growth at 0.9 mm/yr/°C (Weber et.al. 1975).

From this study, linear extension rate was significantly correlated to calcification rate (r = 0.72, p = 0.019) and was inversely correlated to skeletal density (r = -0.56, p=0.09) of fossil corals from several sites in Kikai Island and Northwest Luzon Island (Fig. 39a-b). The relationships of linear extension rate to the other two growth variables from fossil corals follow the similar trend of the modern Porites growth variables from Indo-Pacific (Nie et.al. 1997; Lough and Barnes 2000). However, the calcification rate of fossil corals was not significantly and weakly correlated with skeletal density (Fig. 39c; r = 0.16, p = 0.66), which is different from the strong inverse correlation of modern Porites. This could be attributed to the limited fossil samples and geographic coverage of the sampling. Unlike the wide latitudinal coverage of the modern Porites data, fossil coral data covers the range of 16°N to 28°N. Our study covers an area with mean annual SST range is 25.1 to 28.56°C, which is smaller than the reported SST range of modern Porites (23.9 – 29.3°C) from Great Barrier Reef. Even in modern colonies, the calcification rates of Porites from sites with 25 - 28°C SST tend to scatter variedly (Lough and Barnes 2000).

Modern Porites corals from the Philippines have linear extension rates of 12.85 to 13.0 mm/yr (Patzold 1984; Dizon et.al. 2005). This is higher than the linear extension rates (7.0 to 9.5 mm/yr) of modern Porites from Southern Japan (Suzuki et.al. 2000; Mitsuguchi et.al. 2003). Our fossil data show that Northwest Luzon Island corals have higher linear extension rates (10.2-17.6 mm/yr) compared to Kikai Island corals (3.77-8.72 mm/yr), a much larger difference compared to modern Porites. Following the linear extension – SST established from modern Porites colonies (Lough and Barnes 2000), the disparity of linear extension rate of fossil corals from the two areas was probably driven by the warmer SST in Northwest Luzon Island relative to Kikai Island during mid- to late Holocene. Furthermore, the variations on growth patterns were possibly affected by the larger maximum-minimum SST difference in the subtropics than the tropics due to insolation (Liu et.al. 2003). However, the quantitative sensitivity of the linear extension rate of fossil coral to paleo-SST cannot be discussed due to the absence of reconstructed SST from coral geochemical tracers.

Light availability together with temperature, could be a limiting factor of growth of hermatypic corals and associated zooxanthellae (Kleypas et.al. 1999). Linear extension rate of Porites spp. decreases with respect to deeper water level due to low light conditions and photosynthesis-driven heterotrophy-autotrophy mechanism (Klein et.al. 1993). We can estimate the paleo-depth level of the Holocene reefs in Ryukyu Islands based on the fossil coral assemblage as discussed by Hongo and Kayanne (2010). The most dominant coral species observed in the Holocene marine terraces of Kikai Island are *Acropora digitifera* and *Acropora robusta* with relatively fewer *Porites* sp., *Favia* sp., and *Goniopora* sp. In Northwest Luzon, fossil coral coverage includes diverse species of *Acropora digitifera*, *Acropora robusta*, *Favia* sp., *Heliopora* sp., *Pocillopora* sp., *Porites* sp., *Galaxea* sp. and *Goniastrea* sp. The presence of *Acropora digitifera* and *Acropora robusta* in all sites suggests that the paleo-reef was part of the main reef crest/edge and was deposited at 0-6 m (Cabioch et.al. 1999; Hongo and Kayanne 2010). Considering that the estimated paleo-depth and paleoreef setting are relatively similar in different sampling sites, we can argue that the variation of linear extension rates of the 10 fossil coral samples was not controlled by varying water depths.

Sedimentation can also increase the water turbidity and inhibit light penetration in shallow water. The process could affect the growth pattern and coral diversity as shown by the dredging-related sedimentation in Bermuda around 1940s (Dodge and Vainys 1977). The decrease of light penetration due to sedimentation can slow down the coral growth and calcification rates, decrease coral diversity and abundance, reduce coral net productivity, increase the abundance of branching forms and reduce reef accretion (Rogers 1990; Crabbe and Smith 2005). The generally smaller linear extension and calcification rates of fossil Porites in Kikai Island were probably not driven by heavy sedimentation. No geological evidence suggests the occurrence of large river system and high terrigenous input in Kikai Island during mid- to late Holocene. In the present-day, large rivers are not observed near the sampling sites. In the contrary, the river systems of Northwest Luzon, particularly the area surrounding Lingayen Gulf have been supplying high amount of sediments to the sea since the late Holocene based on geomorphological and sedimentological investigations (Mateo and Siringan 2016). The high sedimentation in Lingayen Gulf is not indicated by the relatively large extension rates of fossil corals from Rosario, La Union (Table 4).

4.3. Coral Growth and Vital Effects

The problem of vital effects is one of the issues for the use of biogenic carbonate in paleoclimate reconstruction. One of the assumptions in coral geochemistry is that skeletal $CaCO_3$ is deposited in a thermodynamic equilibrium with $CaCO_3$ in seawater. However, the effects of growth rate, light availability, feeding mechanisms, and water chemistry can potentially alter the incorporation of trace elements and isotopic fractionation in coral skeleton (Correge 2006; Cohen and Gaetani 2010; Juillet-Leclerc et al. 2014). Experimental data from abiogenic aragonite precipitation shows that Sr/Ca is increasing with increasing growth rate, which is also observed in fast- and slow-growing corals (Cohen and Gaetani 2010).

To investigate the effect of growth rate to coral geochemistry, I calculated the annual linear extension, and annual Sr/Ca and $\delta^{18}O_{coral}$ for each coral colony. Linear extension rates of modern, 3.2 ka, 4.9 ka, and 5.7 ka corals from Kikai Island are 11.0 mm/year, 3.93 mm/year, 5.6 mm/year, and 8.7 mm/year respectively. Linear extension rates of 4.2 ka, 4.3 ka, and 6.1 ka corals from NW Luzon Island are 17.6 mm/year, 12.35 mm/year, and 12.05 mm/year respectively. Annual linear extensions of each Porites colony were compared to the annual Sr/Ca and $\delta^{18}O_{coral}$ calculated from the monthly resolved data of each year. Figure 41a and c shows that plots of annual Sr/Ca and annual linear extension of Kikai Island and NW Luzon corals are highly scattered. It indicates that the extension rate does not strongly affect the variation of Sr/Ca in coral skeleton and vice versa. Both inter- and intracolony extension rate variation do not affect the coral Sr/Ca (Hayashi et al. 2013).

The cross plot (Fig. 41b) of annual $\delta^{18}O_{coral}$ and linear extension of Kikai Island corals shows negative correlation as shown by the equation $\delta^{18}O_{coral} = 0.0105(\text{linear ext.})^2 - 0.266(\text{linear ext.}) - 3.0114$ ($r^2 = 0.7426$). This trend is not observed in the cross plot of NW Luzon corals (Fig. 41d). The cross plot of annual $\delta^{18}O_{coral}$ and linear extension of NW Luzon corals is randomly scattered. The absence of strong linear correlation of annual extension rate versus annual Sr/Ca and $\delta^{18}O_{coral}$ suggests that the linear extension is not solely affected by SST (Lough and Cooper 2011). If the linear extension is solely influenced by SST, the two variables should be directly correlated. The negative correlation of $\delta^{18}O_{coral}$ and linear extension also supports that the $\delta^{18}O_{coral}$ variation is not only affected by SST but multiple variables (e.g. SSS, $\delta^{18}O_{sw}$). Coral culture experiment results show that a large intercolony growth rate variation (2-10 mm/yr) has negligible effect to the summer $\delta^{18}O_{coral}$ but it can be affected by health-related intracolony growth rate variations (Hayashi et al. 2013). Furthermore, skeletal-density artifacts should also be considered by improving the suboptimal skeletal subsampling (Reed et al. 2021).

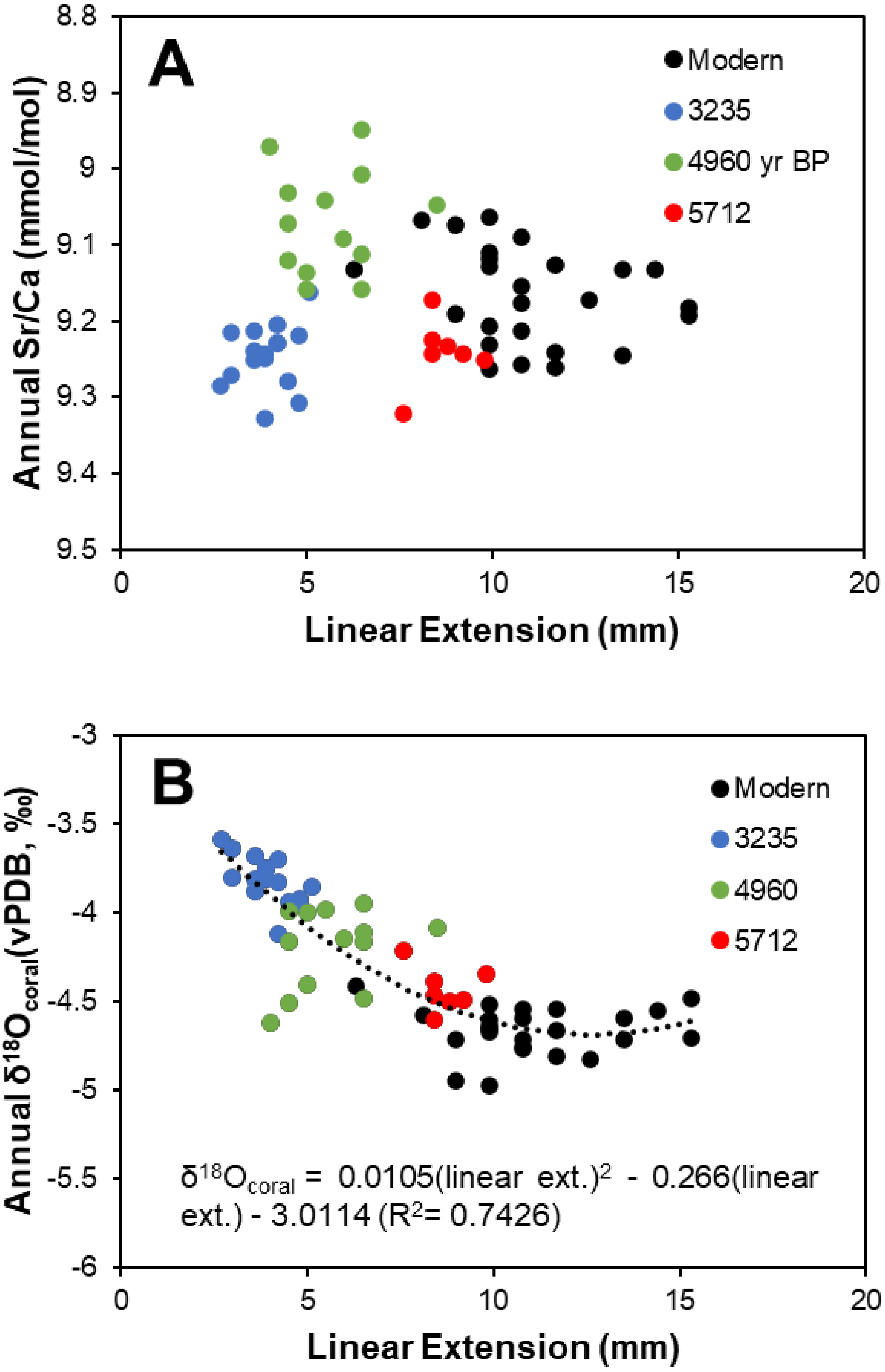
A
Annual Sr/Ca (mmol/mol)
8.8
8.9
9
9.1
9.2
9.3
9.4
9.5
0
5
10
15
20
Linear Extension (mm)
● Modern
● 3235
● 4960 yr BP
● 5712
B
Annual $\delta^{18}O_{coral}$(vPDB, ‰)
-3
-3.5
-4
-4.5
-5
-5.5
-6
0
5
10
15
20
Linear Extension (mm)
● Modern
● 3235
● 4960
● 5712
$\delta^{18}O_{coral}$ = 0.0105(linear ext.)^2 - 0.266(linear ext.) - 3.0114 (R^2= 0.7426)

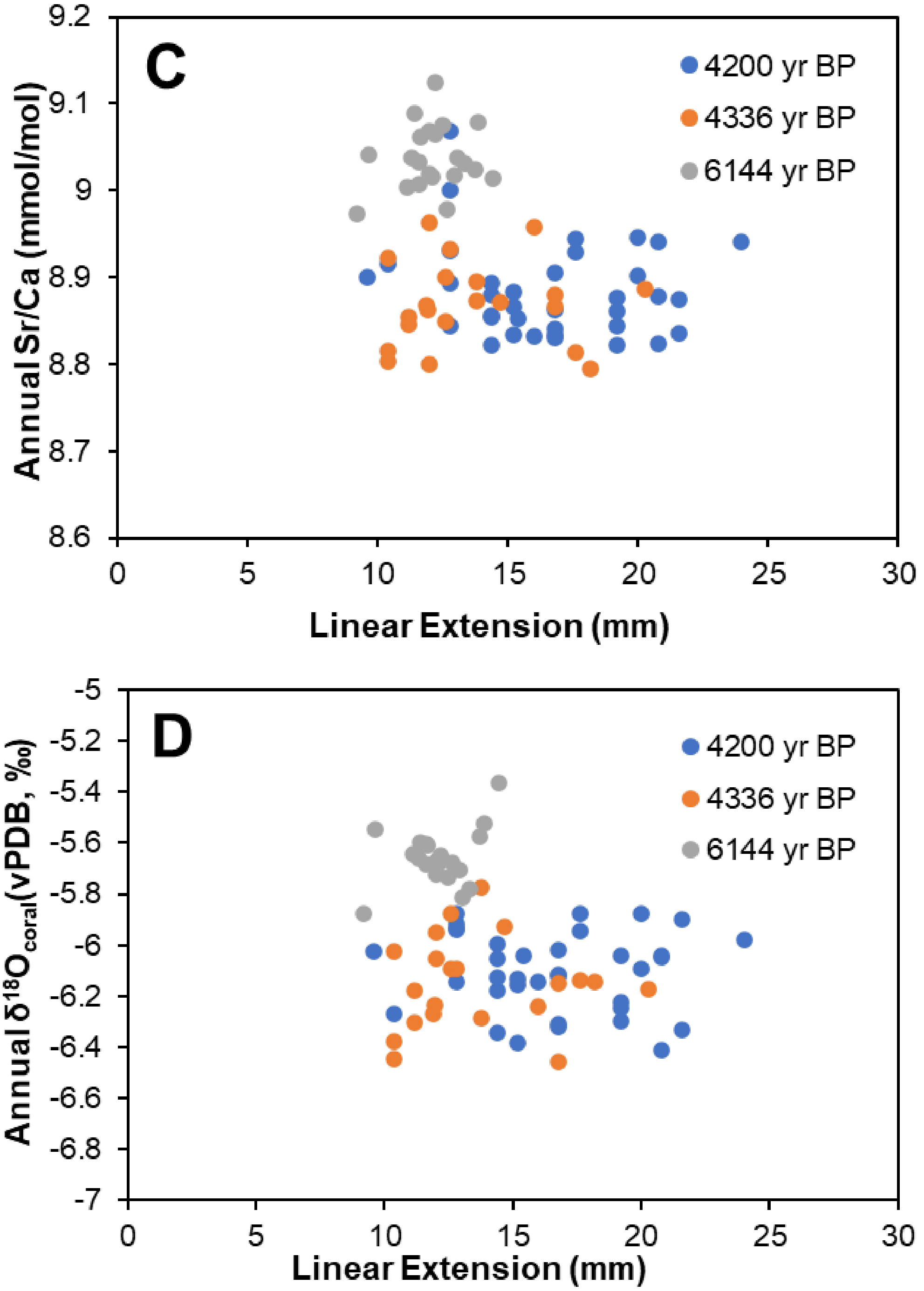

Figure 41. Scatter plots of (A) annual Sr/Ca vs linear extension and (B) $\delta^{18}O_{coral}$ vs linear extension of the modern (black), 3.2 ka (blue), 4.9 ka (green), and 5.7 ka (red) corals from Kikai Island. Fitting line of δ18Ocoral-linear extension curve is δ18Ocoral = 0.0105(linear ext.)2 - 0.266(linear ext.) - 3.0114 (R2= 0.7426). Scatter plots of (C) annual Sr/Ca vs linear extension and (D) $\delta^{18}O_{coral}$ vs linear extension of the 4.2 ka (blue), 4.3 ka (orange), and 6.1 ka (gray) corals from NW Luzon Island.

Chapter 5
Hydroclimate variability recorded by corals from Kikaijima, Japan and Northern Luzon, Philippines

5.1. Calibration of coral geochemical proxies to hydroclimatic variables

Sr/Ca – SST calibration

The Ordinary Least Square Method was used for bivariate regression analysis to show the dependence of coral Sr/Ca on sea surface temperature (SST). Temperature dependence of coral Sr/Ca ratio is shown by calibrating monthly-resolved Sr/Ca record from modern coral and corresponding SST data. The bivariate regression analysis was done in PASTv4.11.

The monthly-resolved coral Sr/Ca from Kikai Island was regressed to the SST from Advanced Very High-Resolution Radiometer (AVHRR) datasets recorded from 1981 to 2015 (Fig. 42a; Kajita et.al. 2017). The OLS regression equation is expressed as:

$$\text{Sr/Ca (mmol/mol)} = 10.80(+0.07) - 0.0643\ (+0.0026) \times \text{SST}\ (°\text{C})$$

The Sr/Ca-SST calibration (Fig. 43a) with high correlation statistics ($r^2 = 0.93$; $r = 0.96$) has slope of -0.0643 (±0.0026) mmol/mol/°C. The calibration used the maximum and minimum values of Sr/Ca regressed to the corresponding minimum and maximum SST values. This slope is within the range of previously published Sr/Ca-SST slopes (-0.053 to 0.066) from Porites corals in southern Japan (Morimoto et.al. 2007; Seki et.al. 2012; Sowa et.al. 2014; Asami et.al. 2020).

The monthly-resolved coral Sr/Ca from Badoc Island, NW Luzon was regressed to the SST from Optimum Interpolation Sea Surface Temperature (OISST) datasets recorded from 2011 to 2017 (Fig. 42b). The OLS regression equation is expressed as:

$$\text{Sr/Ca} = 10.42\ (\pm 0.16) - 0.057\ (\pm 0.006) \times \text{SST}\ (°\text{C})$$

The Sr/Ca-SST calibration (Fig. 43b) with good correlation statistics ($r^2 = 0.74$; $r = 0.86$) has slope of -0.057 (±0.006) mmol/mol/°C. The calibration used the maximum and minimum values of Sr/Ca regressed to the corresponding minimum and maximum SST values. This slope is within the range of previously published Sr/Ca-SST slopes -0.043 to -0.055 mmol/mol/°C in different localities in South China Sea (SCS) (Fig. 44; Yu et al. 2005; Sun et al. 2005; Wei et al. 2007; Mitsuguchi et al. 2008; Liu et al. 2013; Bolton et al. 2014; Ramos et al. 2017; Phan et al. 2019).

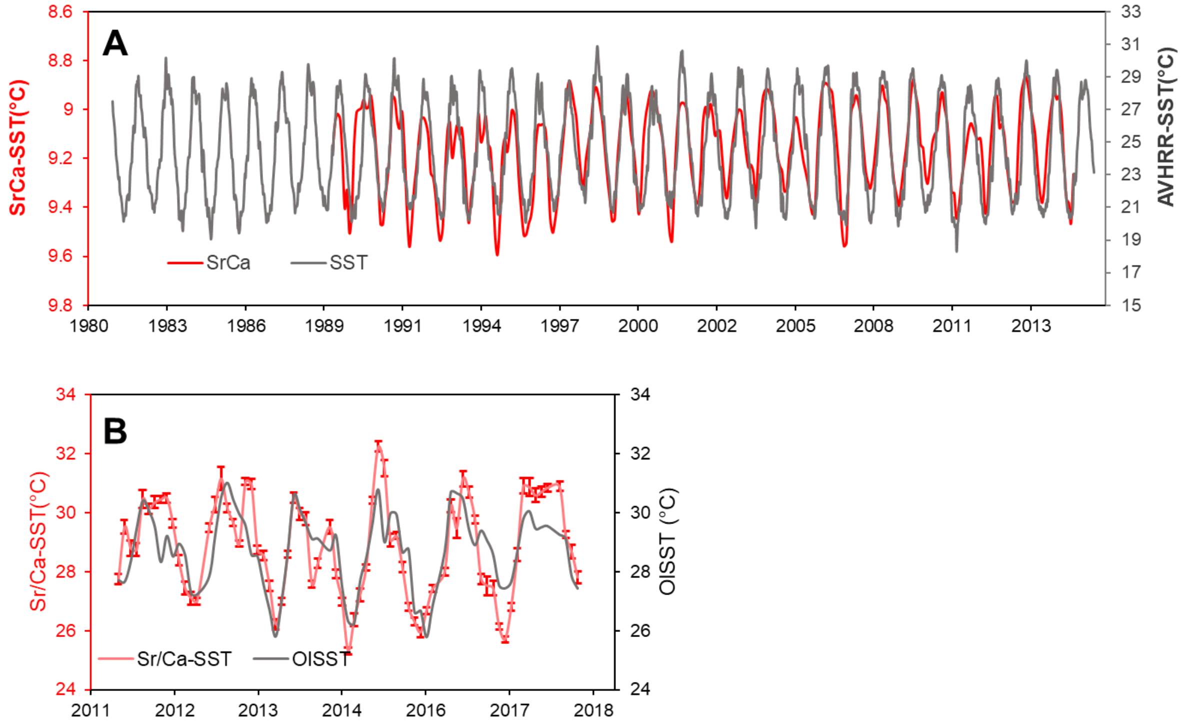

Figure 42. A. Comparison of monthly-resolved Sr/Ca (red) from Kikai Island, Japan and AVHRR SST (gray) data from 1989 to 2015. B. Comparison of monthly-resolved Sr/Ca-SST (red) from Badoc Island, NW Luzon, Philippines, and Optimum Interpolation SST (gray) data from 2011 to 2017.

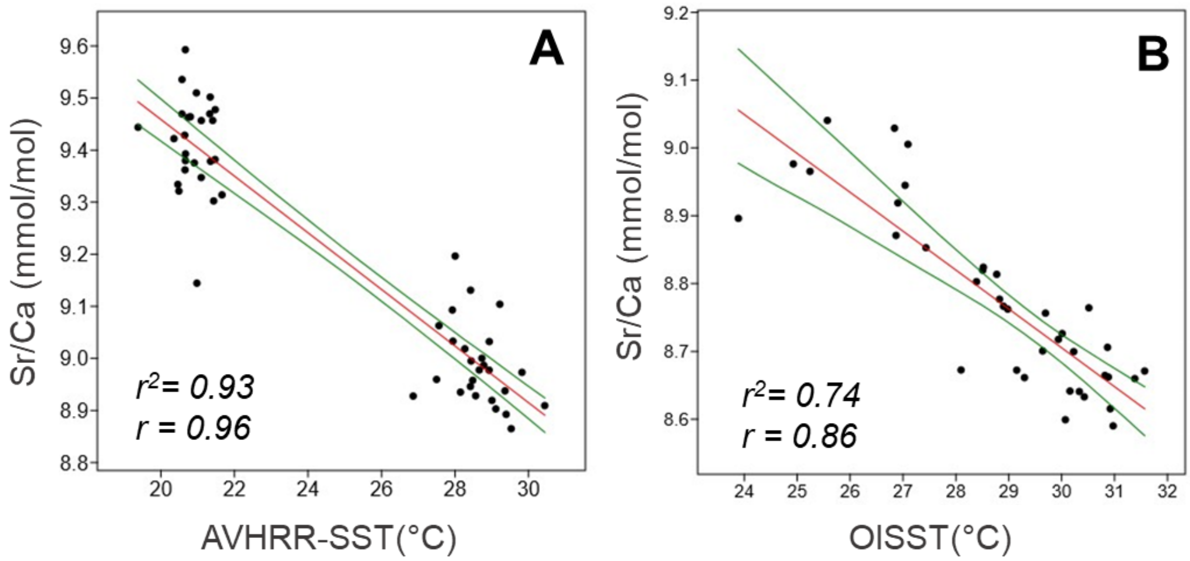

Figure 43. A. Bivariate regression analysis using the minimum and maximum Sr/Ca from Kikai Island plotted against the summer and winter SST from 1989 to 2015. B. Bivariate regression analysis using the minimum and maximum Sr/Ca from NW Luzon plotted against the summer and winter SST from 2011 to 2017. The pair of green lines indicate the 95% bootstrap confidence interval of the linear model.

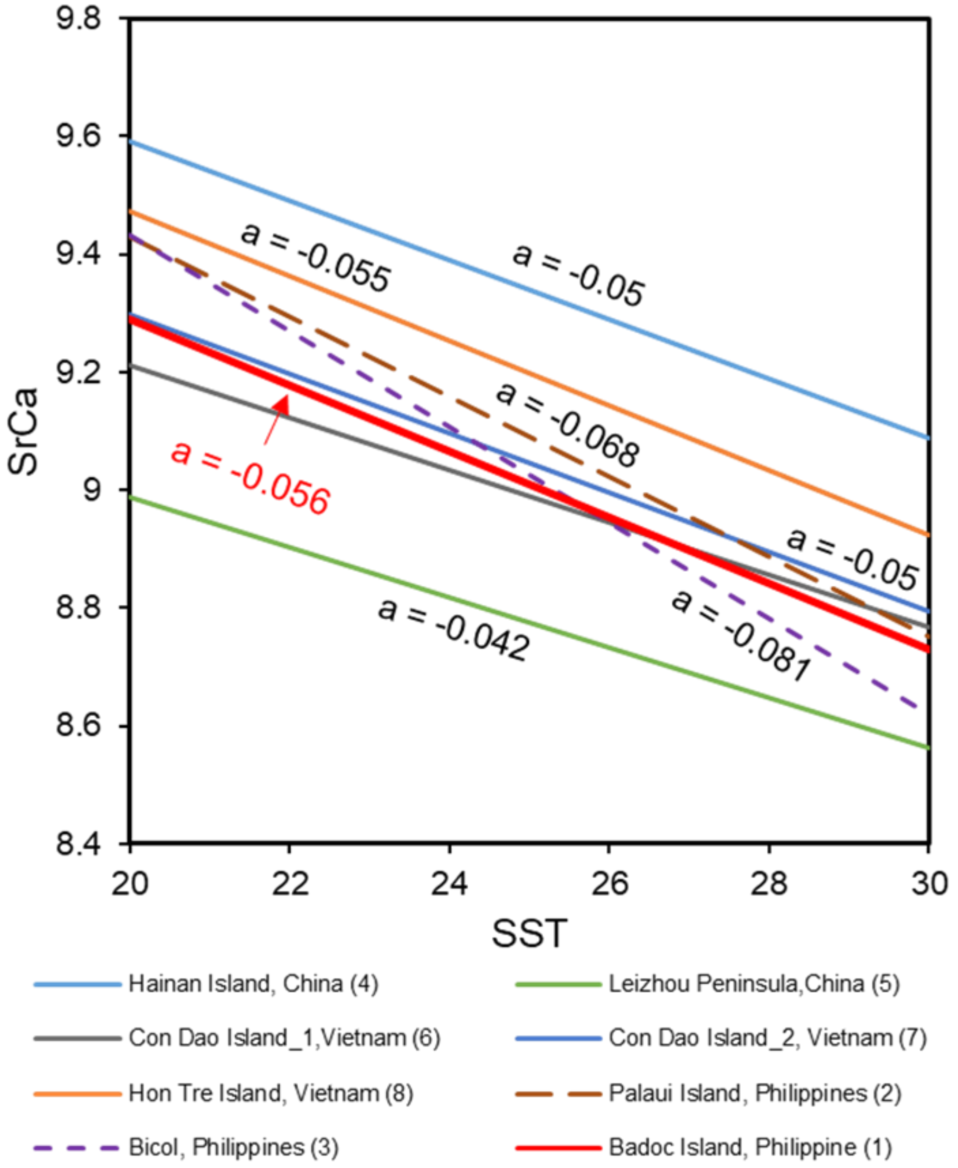

Figure 44. Plots of previously published Sr/Ca-SST slopes from several locations around South China Sea (Leizhou Peninsula, China (Yu et al. 2005); Xisha Island (Sun et al. 2005); Hainan Island, China (Wei et al. 2007); Con Dao Island, Vietnam (Mitsuguchi et al. 2008); Bicol, Philippines (Liu et al. 2013); Hon Tre Island, Vietnam (Bolton et al. 2014); Palaui Island, Philippines (Ramos et al. 2017); Con Dao Island, Vietnam (Phan et al. 2019)). These slopes were compared to the newly established Sr/Ca-SST slope from Badoc Island, NW Luzon, Philippines (red).

$\delta^{18}O_{coral}$ and SSS calibration

The Sr/Ca-SST covaries the $\delta^{18}O_{coral}$ of both Kikai Island and NW Luzon modern coral which suggests the temperature dependence of the oxygen isotopes in coral skeleton (Fig.49, 51). However, $\delta^{18}O_{coral}$ tracks both SST and oxygen isotope of seawater ($\delta^{18}O_{sw}$), thus, other oceanographic variables (i.e., sea surface salinity (SSS)) can influence the oxygen isotopic fractionation. To demonstrate the relationship of $\delta^{18}O_{coral}$ to SSS, the monthly resolved $\delta^{18}O_{coral}$ from 1989 to 2015 was regressed to the monthly SSS data of Kikai Island from SODA v3.3.1 (Fig. 45a). SSS and $\delta^{18}O_{coral}$ have statistically significant positive linear correlation ($r = 0.71$; $r^2 = 0.50$; $p < 0.000$; $n = 310$) defined by the timing of high and low SSS occurs with the high and low $\delta^{18}O_{coral}$ (Fig. 46a).

The monthly resolved $\delta^{18}O_{coral}$ measured from the NW Luzon coral from 2011 to 2017 was regressed the monthly SSS data from SODA v3.3.1 (2011 to 2015) (Fig. 45b). SSS and $\delta^{18}O_{coral}$ have statistically significant positive linear correlation ($r = 0.50$; $r^2 = 0.32$; $p < 0.000$; $n = 48$) wherein high and low SSS correspond to high and low $\delta^{18}O_{coral}$ (Fig. 46b). The seasonal cycle of $\delta^{18}O_{coral}$ is synchronous to the seasonal variation of SSS in Kikai Island and NW Luzon which is consistent with published works in tropical western Pacific (Morimoto et al. 2002, Ramos et al. 2019; Reed et al. 2022).

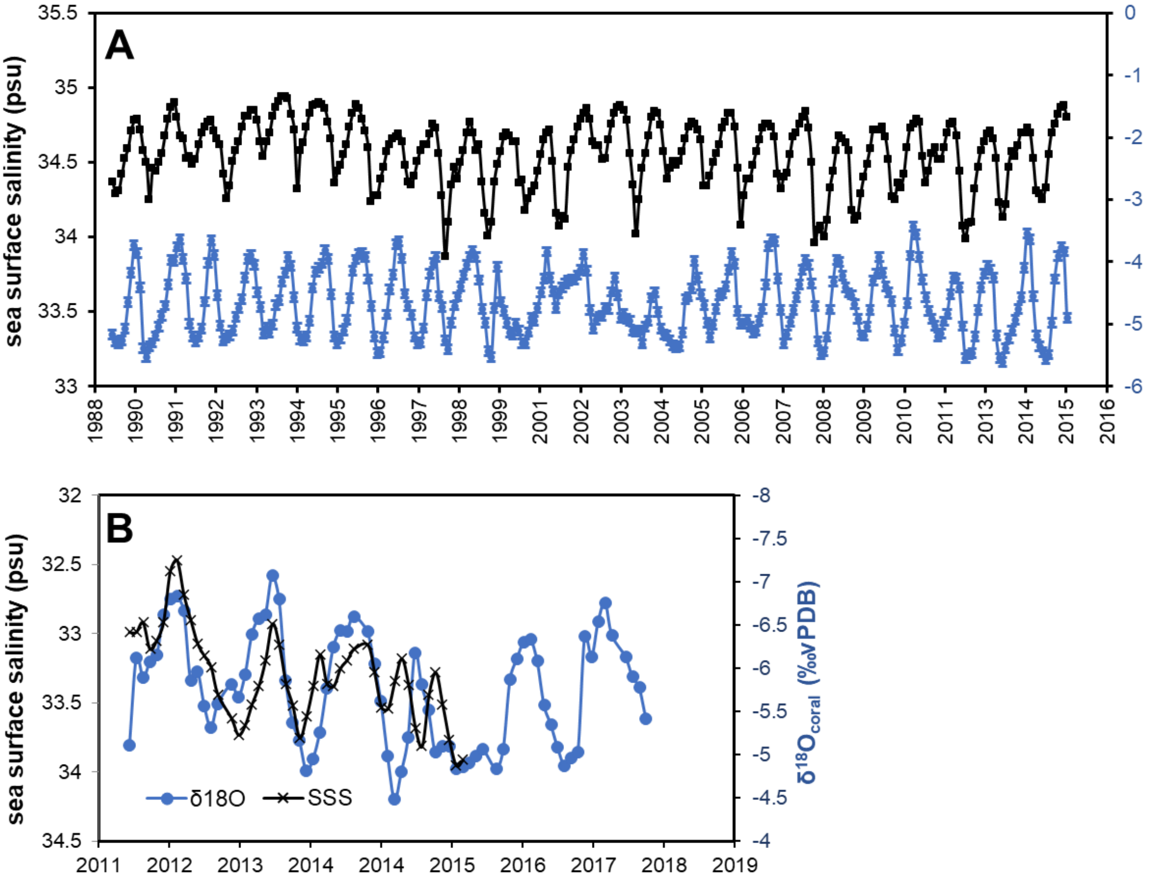

Figure 45. A. Comparison of monthly-resolved $\delta^{18}O_{coral}$ (blue) from Kikai Island, Japan and SODA v3.3.1 SSS (black) data from 1989 to 2015. B. Comparison of monthly-resolved $\delta^{18}O_{coral}$ (blue) from Badoc Island, NW Luzon, Philippines, and SODA v3.3.1 SSS from 2011 to 2015.

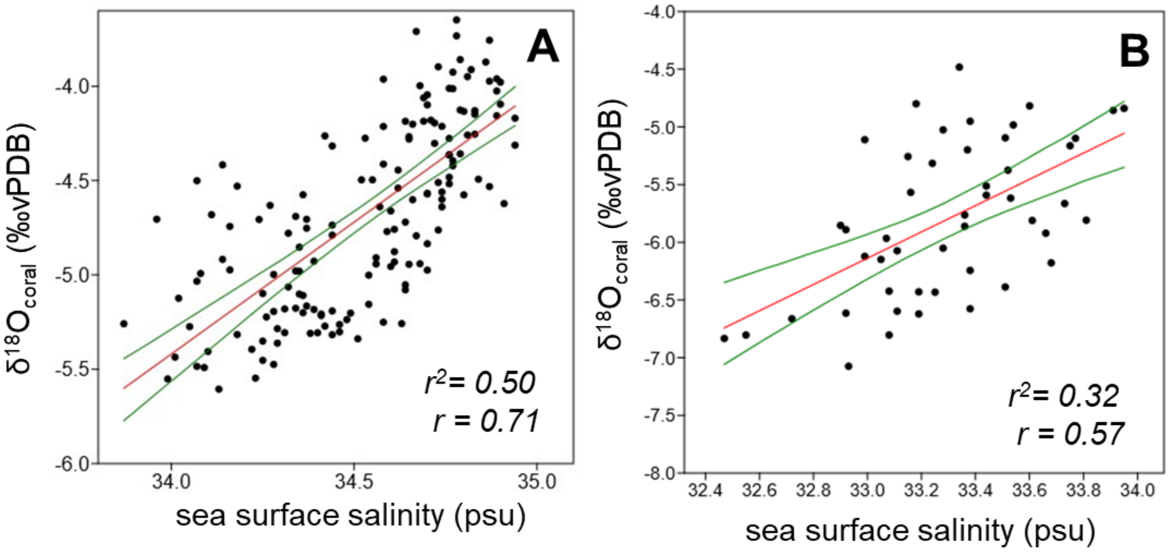

Figure 46. A. Bivariate regression analysis using the minimum and maximum $\delta^{18}O_{coral}$ from Kikai Island plotted against the minimum and maximum SSS from 1989 to 2015. B. Bivariate regression analysis using the minimum and maximum $\delta^{18}O_{coral}$ from NW Luzon plotted against the minimum and maximum SSS from 2011 to 2017. The pair of green lines indicate the 95% bootstrap confidence interval of the linear model.

$\delta^{18}O_{sw}$ (seawater $\delta^{18}O$) and SSS/rainfall calibration

The $\delta^{18}O_{sw}$ was isolated from the $\delta^{18}O_{coral}$ by removing the $\delta^{18}O_{SST}$ component using the Sr/Ca-SST slope, $\delta^{18}O_{coral}$-SST slope, and the measured Sr/Ca values following the centering method of Cahyarini et al. (2008). The $\delta^{18}O_{sw}$ from 2007-2015 was regressed to the accumulated monthly in-situ rainfall data from northern Kikai Island from the monitoring station of Kikai Town and Kagoshima Prefectural Government. The accumulated rainfall was calculated from the sum of the daily rainfall record. The 5-point moving average was applied to systematically smoothen the time series and to remove extremely high rainfall events. The smoothed (5-point moving average) rainfall and $\delta^{18}O_{sw}$ from 2007 to 2015 were plotted in Figure 47a. Cross plot of the two variables has shown a statistically significant negative linear correlation ($r = 0.55$; $r^2 = 0.30$; $p < 0.000$; $n = 93$; Fig. 48a). It shows that the low (high) $\delta^{18}O_{sw}$ months occur in high (low) rainfall month.

Monitoring rain gauge data from Badoc Island, NW Luzon is unavailable, hence, the $\delta^{18}O_{sw}$ was compared to SSS instead. The monthly resolved $\delta^{18}O_{sw}$ was regressed the monthly SSS data from SODA v3.3.1 (2011 to 2015) (Fig. 47b). SSS and $\delta^{18}O_{sw}$ have statistically significant positive linear correlation ($r = 0.50$; $r^2 = 0.32$; $p < 0.000$; $n = 48$) wherein high and low SSS correspond to high and low $\delta^{18}O_{coral}$ (Fig. 48b).

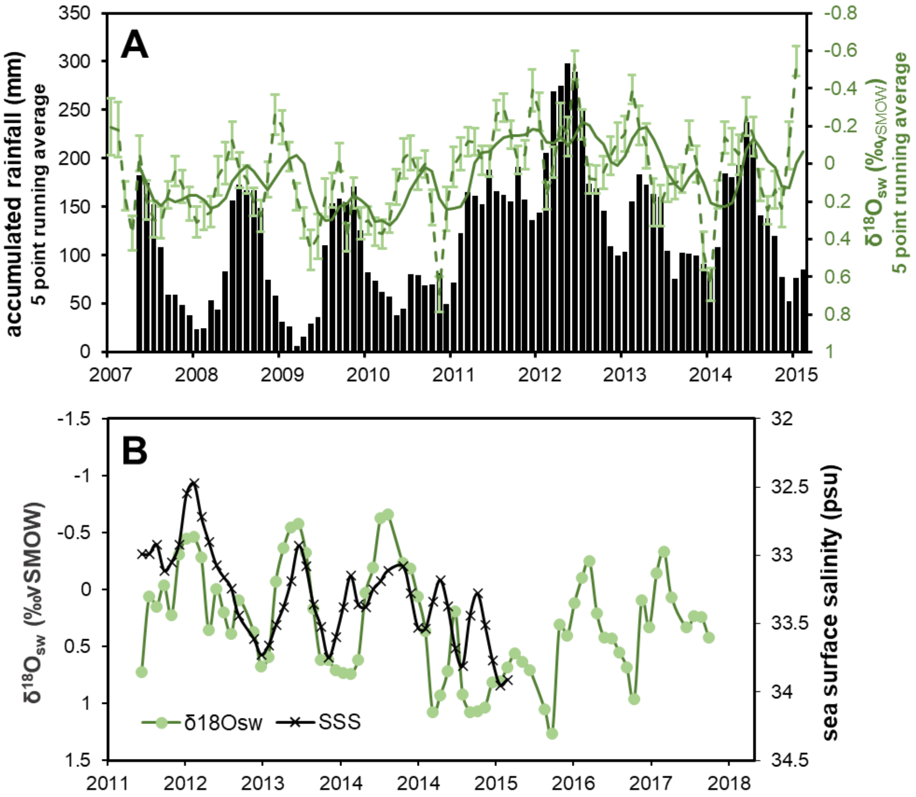

Figure 47. A. Comparison of the 5-point moving average monthly-resolved $\delta^{18}O_{sw}$ (green) and accumulated monthly rainfall data (black) from Kikai Island, Japan from 2007 to 2015. B. Comparison of monthly-resolved $\delta^{18}O_{sw}$ (green) from Badoc Island, NW Luzon, Philippines, and SODA v3.3.1 SSS from 2011 to 2015.

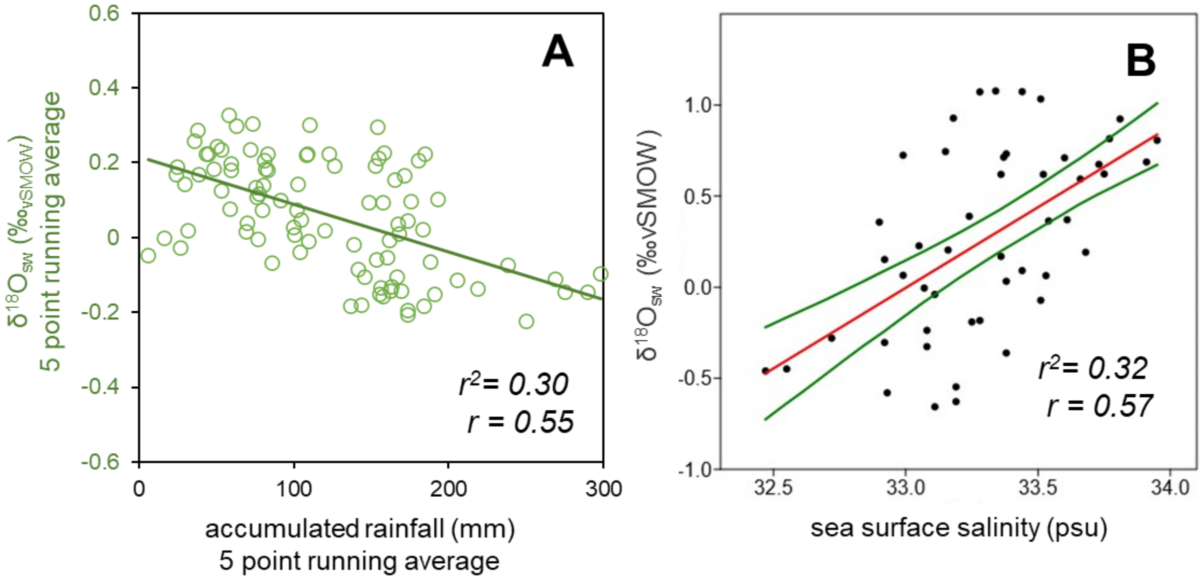

Figure 48. A. Bivariate regression analysis using the 5-point moving average monthly-resolved $\delta^{18}O_{sw}$ and accumulated monthly rainfall data from Kikai Island. B. Bivariate regression analysis using the minimum and maximum $\delta^{18}O_{sw}$ from NW Luzon plotted against the minimum and maximum SSS from 2011 to 2017. The pair of green lines indicate the 95% bootstrap confidence interval of the linear model.

5.2. Sr/Ca, $\delta^{18}O_{coral}$, and $\delta^{18}O_{sw}$ records from Kikai Island corals

Coral Sr/Ca-SST (red), centered $\delta^{18}O_{coral}$ (blue), and centered $\delta^{18}O_{seawater}$ (green) were measured from modern and three fossil Porites colonies from Kikai Island (Fig. 49). A total of 26 years was reconstructed from modern coral, 13 years from 3.2 ka coral, 13 years from 4.9 ka coral, and 7 years from 5.7 ka coral. The Sr/Ca of modern coral ranges from 8.86 to 9.59 mmol/mol (average = 9.17 mmol/mol; n=311); 3.2 ka coral ranges from 9.04 to 9.53 mmol/mol (average of 9.27 mmol/mol; n=459); 4.9 ka coral ranges 8.69 to 9.64 mmol/mol (average of 9.08 mmol/mol; n=156); and 5.7 ka coral ranges from 8.99 to 9.60 mmol/mol (average of 9.22 mmol/mol; n=334).

To invert the Sr/Ca to SST records, the ordinary least square (OLS) calibration equation published by Kajita et al. (2017) was used. The summary of the reconstructed annual mean, maximum, and minimum from Sr/Ca records of modern, 3.2 ka, 4.9 ka, and 5.7 ka corals are shown in Table 5. The reconstructed SST from 1989 – 2015 recorded 20.8°C to 28.9°C with mean SST of 25.4°C. The 1σ range error range is 0.18 to 0.57°C (median: 0.26°C). The 3.2 ka coral recorded 24.1°C, 27.7°C, and 19.9°C as annual mean, maximum, and minimum SSTs respectively. The 1σ range error range is 0.19 to 0.56°C (median: 0.26°C). The 4.9 ka coral recorded 26.7°C, 30.9°C, and 20.7°C as annual mean, maximum, and minimum SSTs respectively. The 1σ range error range is 0.19 to 0.74°C (median: 0.26°C). The 5.7 ka recorded 24.5°C, 28.0°C, and 18.5°C as annual mean, maximum, and minimum SSTs respectively. The 1σ range error range is 0.62 to 0.82°C (median: 0.66°C). The mid-Holocene 5.7 ka and 4.9 ka corals dated recorded larger $\Delta SST_{max-min}$ of 9.5°C and 10.2°C respectively. The late Holocene coral (3.2 ka) has relatively smaller $\Delta SST_{max-min}$ of 7.8°C relative to mid-Holocene corals (Fig. 50).

The $\delta^{18}O_{coral}$ ranges from -5.09‰ to -3.23‰ (average of -4.44‰, n=334) in 5.7 ka, -4.25‰ to -3.27‰ (average of -3.79‰, n=459) in 3.2 ka, -4.77‰ and -3.32‰ (average of -4.16‰, n=156) in 4.9 ka, and -5.18‰ and -4.02‰ (average of -4.66‰, n=311) in modern coral (1989-2015). Modern, 3.2 ka, 4.9 ka, and 5.7 ka corals have seasonal amplitude of 1.16±0.06‰, 0.98±0.07‰, 1.45±0.14‰, and 1.86±0.06‰ respectively. Similarly, the mid-Holocene corals, 5.7 ka and 4.9 ka reveal a larger seasonal range while the late Holocene coral shows the smallest seasonal range (Fig. 50).

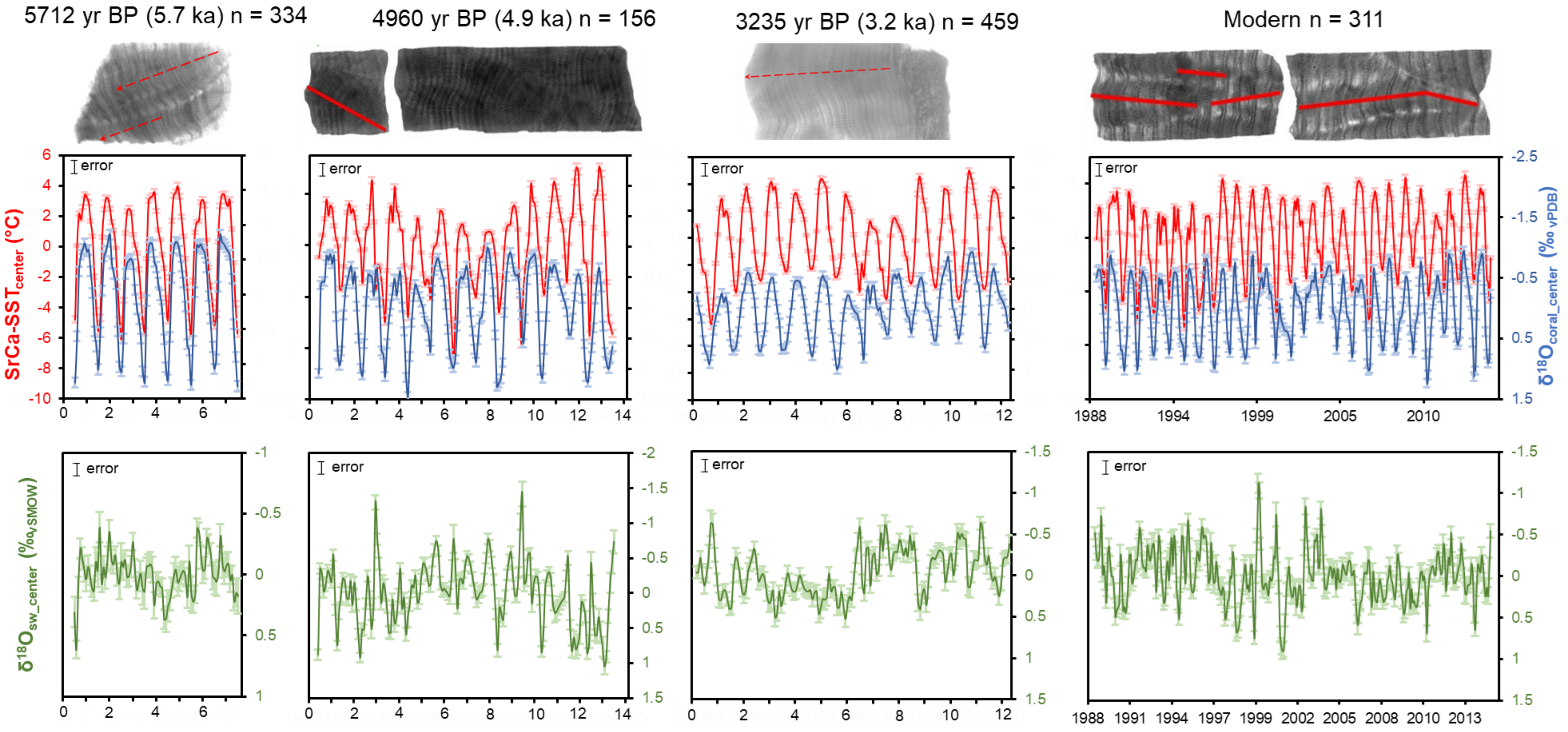

Figure 49. Centered Sr/Ca-SST anomaly (red), δ18Ocoral (blue), and estimated δ18Oseawater (green) of the modern (n = 26), 3.2 ka (n = 13), 4.9 ka (n = 13), and 5.7 ka (n = 7) corals from Kikai Island (n = no. of reconstructed years). Error bar represents the 1σ standard deviation (68% confidence interval) which shows the uncertainty estimates from analytical and calibration errors of Sr/Ca-SST and δ18Ocoral following the Monte Carlo simulation method (Watanabe and Pfeiffer 2022).

	Modern		3.2 ka		4.9 ka		5.7 ka	
	Sr/Ca-SST (°C)	$\delta^{18}O_{coral}$ (‰)	Sr/Ca-SST (°C)	$\delta^{18}O_{coral}$ (‰)	Sr/Ca-SST (°C)	$\delta^{18}O_{coral}$ (‰)	Sr/Ca-SST (°C)	$\delta^{18}O_{coral}$ (‰)
Mean	25.4	-4.66	24.1	-3.79	26.7	-4.16	24.5	-4.44
Estimated error (1σ standard deviation)	0.13	0.07	0.14	0.07	0.14	0.07	0.14	0.07
Summer	28.9	-5.18	27.7	-4.25	30.9	-4.77	28	-5.09
Estimated error (1σ standard deviation)	0.15	0.07	0.17	0.07	0.18	0.07	0.16	0.07
Winter	20.8	-4.02	19.9	-3.27	20.7	-3.32	18.5	-3.23
Estimated error (1σ standard deviation)	0.18	0.07	0.18	0.07	0.23	0.07	0.24	0.07
Seasonal difference ($\Delta_{max-min}$)	8.1	1.16	7.8	0.98	10.2	1.45	9.5	1.86

Table 5. Reconstructed annual mean, summer, and winter Sr/Ca-SST and $\delta^{18}O_{coral}$ values from the modern, 3.2 ka, 4.9 ka, and 5.7 ka corals from Kikai Island. The seasonal difference was calculated from the difference of summer and winter values. The error was estimated using the propagation method of the Watanabe and Pfeiffer (2022) considering the analytical error, slope error, and linear regression slopes of both Sr/Ca and $\delta^{18}O_{coral}$ datasets.

The higher $\delta^{18}O_{coral}$ and higher Sr/Ca in winter of 5.7 ka and 4.9 ka indicate higher SSS and cooler SST compared to the relatively warmer winter at 4.9 ka and 1989 – 2015 (Fig. 50). The 5.7 ka coral recorded the coolest winter SST among the fossil corals. The higher minimum $\delta^{18}O_{coral}$ of mid-Holocene (5.7 ka and 4.9 ka) corals indicate a wetter/less saline conditions relative to drier conditions of 3.2 ka. The 4.9 ka recorded a warmer summer SST of +2°C relative to present-day. It is the warmest summer SST record among the three fossil corals from Kikai Island. The changes in coral-based SST, SSS, and probably rainfall records in different time-windows of mid- to late Holocene were possibly driven by the changes in the monsoon intensity.

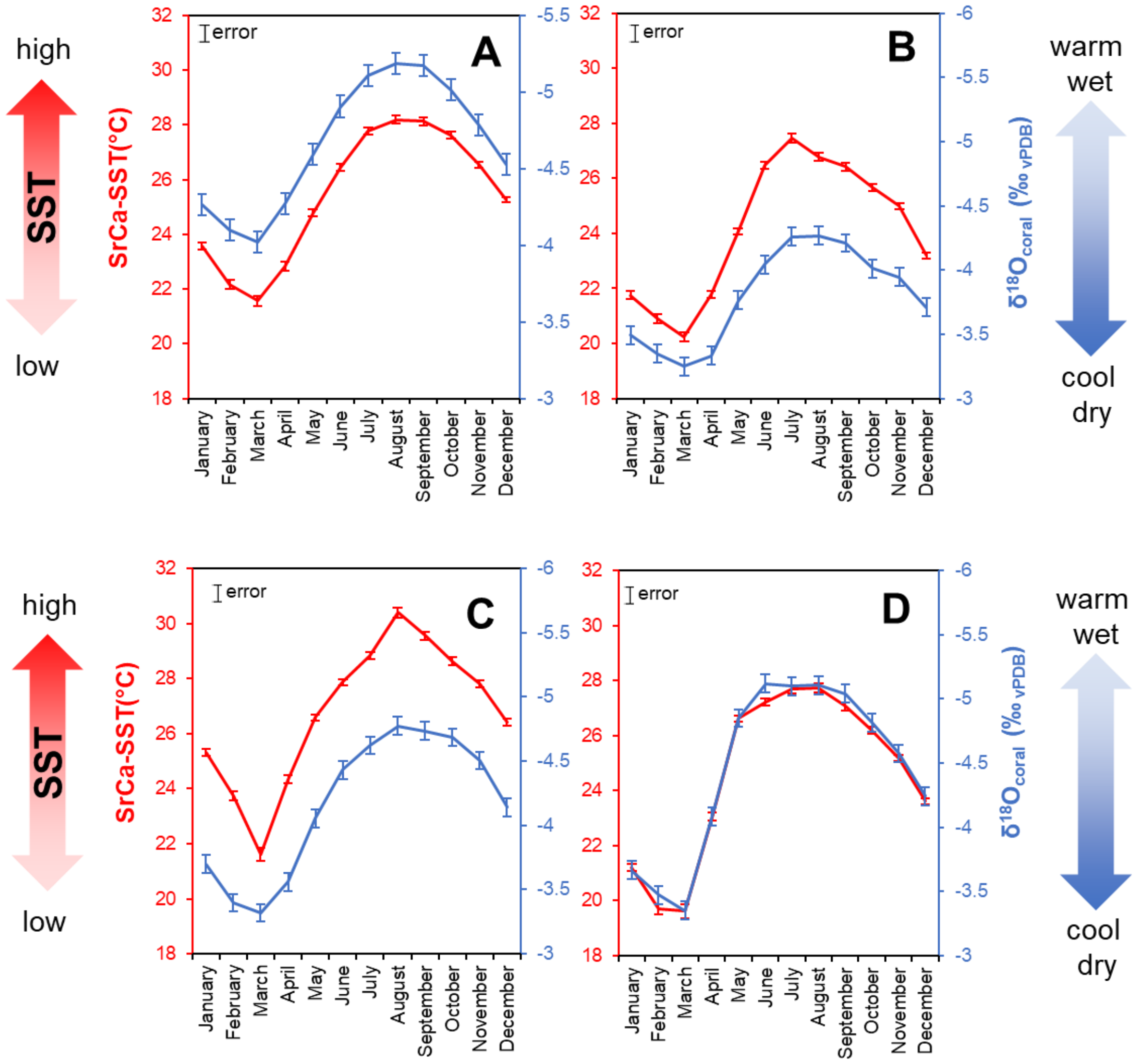

Figure 50. Mean seasonal cycles of coral Sr/Ca-SST (red) and $\delta^{18}O$ (blue) of modern (A), 3.2 ka (B), 4.9 ka (C), and 5.7 ka (D) corals from Kikai Island. Uncertainties of the monthly climatology are presented in the error bar calculated from the analytical error, calibration error, and year-to-year variability of the internal coral chronology.

5.3. Sr/Ca, $\delta^{18}O_{coral}$, and $\delta^{18}O_{sw}$ records from Northern Luzon corals

Coral Sr/Ca-SST (red), centered $\delta^{18}O_{coral}$ (blue), and centered $\delta^{18}O_{seawater}$ (green) were measured from modern and three fossil Porites colonies from NW Luzon Island (Fig. 51). A total of 7 years was reconstructed from modern coral, 44 years from 4.2 ka coral, 20 years from 4.3 ka coral, and 20 years from 6.1 ka coral. The Sr/Ca of modern coral ranges from 8.60 to 9.02 mmol/mol (average = 8.79 mmol/mol; n=90); 4.2 ka coral ranges from 8.61 to 9.36 mmol/mol (average of 8.88 mmol/mol; n=513); 4.3 ka coral ranges 8.61 to 9.15 mmol/mol (average of 8.87 mmol/mol; n=251); and 6.1 ka coral ranges from 8.83 to 9.34 mmol/mol (average of 9.04 mmol/mol; n=254).

To invert the Sr/Ca to SST records, the ordinary least square (OLS) calibration equation from the regression of coral Sr/Ca and OISST shown in Chapter 5.a. The summary of the reconstructed annual mean, maximum, and minimum from Sr/Ca records of modern, 4.2 ka, 4.3 ka, and 6.1 ka corals are shown in Table 6. The reconstructed SST from 2011-2017 recorded 26.9°C to 30.6°C with mean SST of 29.0°C. The 1σ error range is 0.18 to 0.23°C. The OISST data from 2011 to 2017 recorded maximum SST of 30.4°C in June, minimum SST of 26.8 in February and annual mean SST of 28.7°C. The comparison of reconstructed Sr/Ca-SST data and OISST record shows that corals from NW Luzon can track SST variability with good accuracy.

The 4.2 ka coral recorded 27.4°C, 29.8°C, and 25.0°C as annual mean, maximum, and minimum SSTs respectively. The 1σ error range is 0.18 to 0.25°C. The 4.3 ka coral recorded 27.5°C, 29.5°C, and 25.4°C as annual mean, maximum, and minimum SSTs respectively. The 1σ error range is 0.17 to 0.23°C. The 6.1 ka recorded 24.5°C, 25.9°C, and 23.2°C as annual mean, maximum, and minimum SSTs respectively. The 1σ error range is 0.17 to 0.18°C. The 4.2 ka (Fig.52b) and 4.3 ka (Fig.52c) corals recorded $\Delta SST_{max-min}$ of 4.8°C and 4.0° that are larger than the 3.7°C in 2011-2017. The 6.1 ka (Fig.52d) coral recorded $\Delta SST_{max-min}$ of 2.7°C that is smaller than the 3.7°C in 2011-2017.

The $\delta^{18}O_{coral}$ ranges from -6.57‰ to -4.63‰ (average of -5.65‰, n=254) in 6.1ka, -7.81‰ to -5.06‰ (average of -6.15‰, n=251) in 4.3 ka, -7.50‰ and -5.17‰ (average of -6.12‰, n=513) in 4.2 ka, and -7.07‰ and -4.48‰ (average of -5.77‰, n=90) in modern coral (2011-2017). Modern, 4.2 ka, 4.3 ka, and 6.1 ka corals have seasonal amplitude of 1.26‰, 1.02‰, 0.9‰, and 0.9‰ respectively (Fig. 52). The mid-Holocene corals (4.2 ka, 4.3 ka, and 6.1 ka) recorded reduced $\delta^{18}O_{coral}$ seasonality relative to the $\delta^{18}O_{coral}$ seasonality of 2011 to 2017.

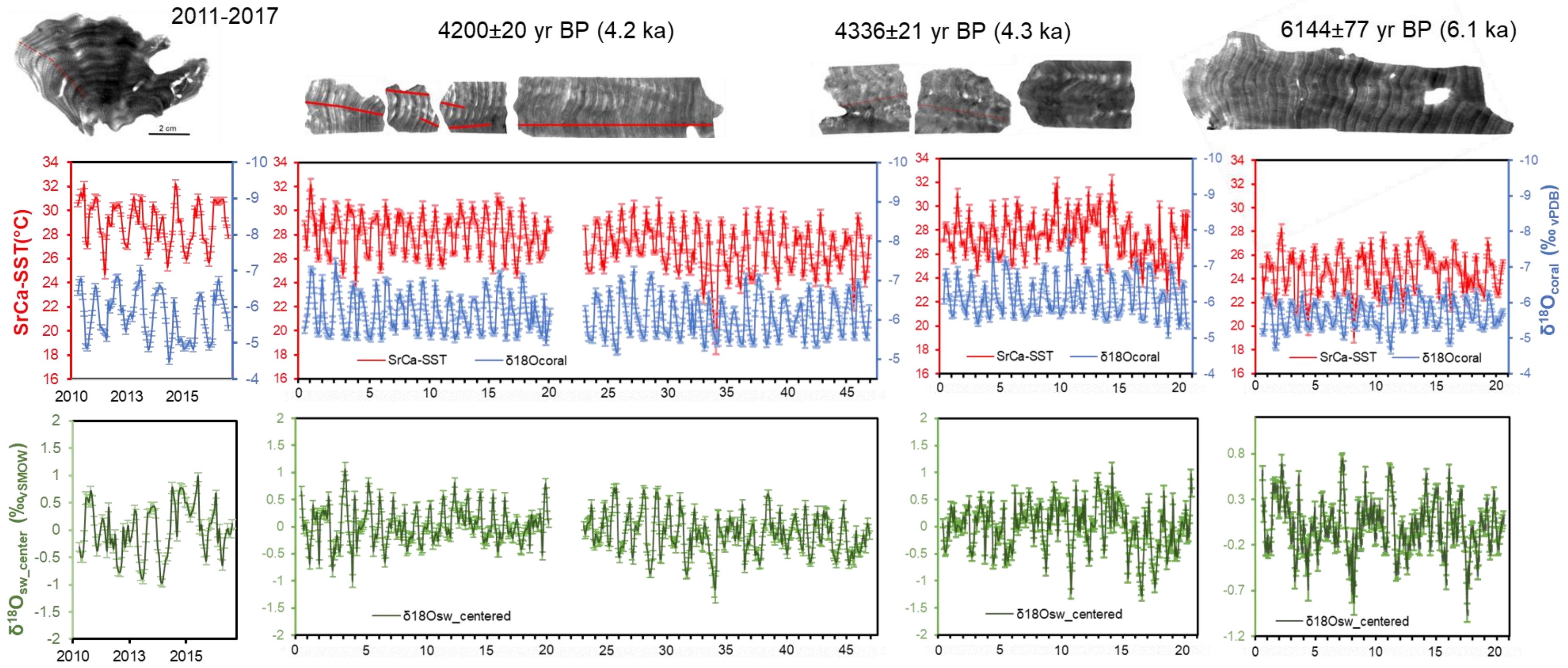

Figure 51. Centered Sr/Ca-SST anomaly (red), δ18Ocoral (blue), and estimated δ18Oseawater (green) of the modern (n = 7), 4.2 ka (n = 44), 4.3 ka (n = 20), and 6.1 ka (n = 20) corals from NW Luzon Island (n = no. of reconstructed years). Error bar represents the 1σ standard deviation (68% confidence interval) which shows the uncertainty estimates from analytical and calibration errors of Sr/Ca-SST and $\delta^{18}O_{coral}$ following the simple Monte Carlo method (Watanabe and Pfeiffer 2022).

	Modern		**4.2 ka**		**4.3 ka**		**6.1 ka**	
	Sr/Ca-SST (°C)	$\delta^{18}O_{coral}$ (‰)	Sr/Ca-SST (°C)	$\delta^{18}O_{coral}$ (‰)	Sr/Ca-SST (°C)	$\delta^{18}O_{coral}$ (‰)	Sr/Ca-SST (°C)	$\delta^{18}O_{coral}$ (‰)
Mean	28.96	-5.77	27.4	-6.12	27.51	-6.15	24.51	-5.65
Estimated error (1σ standard deviation)	0.18	0.07	0.18	0.07	0.17	0.07	0.17	0.07
Summer	30.59	-6.36	29.81	-6.63	29.46	-6.57	25.89	-6.09
Estimated error (1σ standard deviation)	0.18	0.07	0.25	0.07	0.22	0.07	0.18	0.07
Winter	26.89	-5.1	25.02	-5.61	25.45	-5.67	23.19	-5.18
Estimated error (1σ standard deviation)	0.23	0.07	0.25	0.07	0.23	0.07	0.18	0.07
Seasonal difference ($\Delta_{max-min}$)	3.7	1.26	4.79	1.02	4.01	0.9	2.7	0.91

Table 6. Reconstructed annual mean, summer, and winter Sr/Ca-SST and $\delta^{18}O_{coral}$ values from the modern, 4.2 ka, 4.3 ka, and 6.1 ka corals from NW Luzon Island. The seasonal difference was calculated from the difference of summer and winter values. The error was estimated using the propagation method of the Watanabe and Pfeiffer (2022) considering the analytical error, slope error, and linear regression slopes of both Sr/Ca and $\delta^{18}O_{coral}$ datasets.

The 4.2 ka (Fig. 52b), 4.3 ka (Fig. 52c), and 6.1 ka (Fig. 52d) corals recorded cooler SSTs based on the higher Sr/Ca values relative to 2011-2017. The 6.1 ka, 4.3 ka, and 4.2 ka were cooler by 3.7 - 4.7°C, 1.1 - 1.5°C, and 0.7 - 1.9 °C respectively. The mid-Holocene corals also reveal that the length of warm months was shorter in 4.2 ka, 4.3 ka, and 6.1 ka relative to present-day. The 6.1 ka corals recorded a more positive maximum $\delta^{18}O_{coral}$ indicating a more saline surface water conditions in "summer" relative to the present-day. The 4.2 ka and 4.3 ka corals recorded more negative maximum and minimum $\delta^{18}O_{coral}$ values which suggest less saline water conditions both in "summer" and "winter" relative to the present-day. The changes in coral-based SST and rainfall-driven SSS in different time-windows of mid-Holocene were possibly driven by the changes in the monsoon intensity.

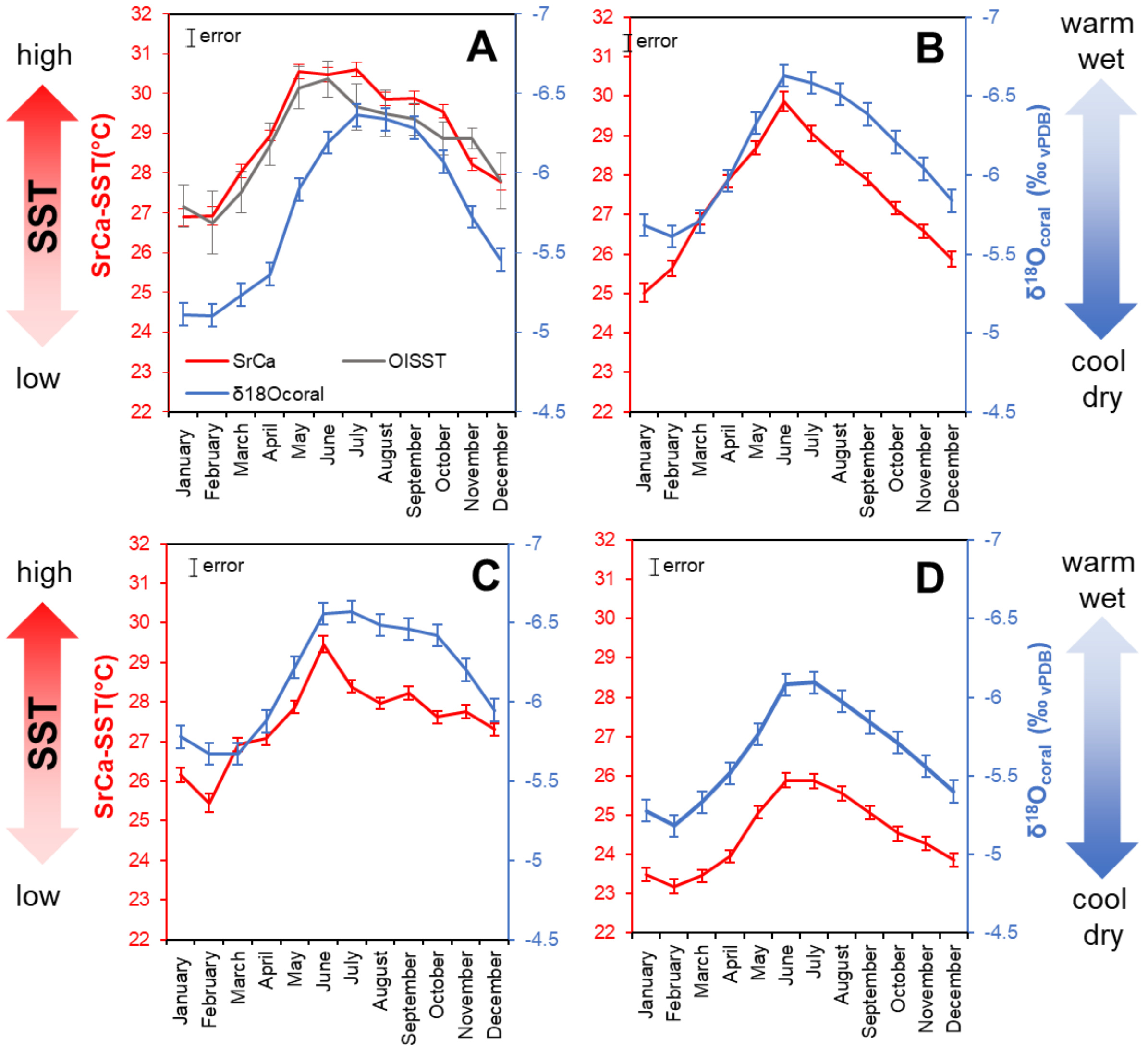

Figure 52. Mean seasonal cycles of coral Sr/Ca-SST (red) and $\delta^{18}O$ (blue) of modern (A), 4.2 ka (B), 4.3 ka (C), and 6.1 ka (D) corals from NW Luzon Island. Uncertainties of the monthly climatology are presented in the error bar calculated from the analytical error, calibration error, and year-to-year variability of the internal coral chronology.

5.4. Seasonality of hydroclimate variables reflects East Asian monsoon dynamics

EA summer monsoon in subtropical NW Pacific

The minimum, maximum, and annual mean $\delta^{18}O_{coral}$ records from fossil *Porites* in Kikai Island and Okinawa Island in Southern Japan (Fig. 53a; Kiyama et al. 2000; Abram et al. 2001; Morimoto et al. 2007; Asami et al. 2020) were compiled to investigate the seasonal SSS change in subtropical NW Pacific. There was a steady decrease of minimum (summer) and annual mean $\delta^{18}O_{coral}$ values from ~7.0 ka to ~3.5 ka centered around 5.0 ka. The average of minimum (summer) $\delta^{18}O_{coral}$ values from 5.0 ka to 7.0 ka is -5.0‰ and the average from 3.2 ka to 4.4 ka is -4.3‰. Following the $\delta^{18}O_{coral}$-SSS relationship (Fig. 46a) in Kikai, this trend suggests increasing SSS from ~7.0 ka to ~3.2 ka.

The Sr/Ca-based SST from 5.7 ka, 4.9 ka, and 3.2 ka were compiled with published coral-based SST records from Southern Japan (Fig. 53b). This includes data from Kikai Island (Morimoto et.al. 2007), Okinawa Island (Mitsuguchi et.al. 1998), Ishigaki Island (Sowa et.al. 2014) and Kume Island (Seki et.al. 2012). Summer and winter SST anomalies (SSTA) were calculated by subtracting the reconstructed SST from instrumental or modern coral-derived SST for each locality. Data are presented as SSTA to eliminate the variation in SST due to latitudinal and/or geographic location. The compiled summer SSTA (Fig. 53b) reveals that the SST from 6.0 ka to 7.0 ka was not significantly warmer/cooler than the present-day. This is consistent with the conclusion of Morimoto et al. (2007) using the Sr/Ca-SST data at 6.1 ka and 7.0 ka corals from Kikai Island. The summer SST became warmer by 2.0°C in 4.9 ka. There was a drastic change to cooler surface water conditions after 4.9 ka. The average summer SSTA from 3.2 ka to 4.9 ka is cooler by 1.8°C relative to present-day SST.

Comparing the summer SSS and SSTA from coral records, the subtropical NW Pacific was wet during warmer period around 7.0 ka to 5.0 ka, then became drier during cooler period around 3.2 ka to 5.0 ka. The summer monsoon wind circulation is driven by the strength of the Western Pacific Subtropical High (WPSH). Based on climate simulations, the WPSH is influenced by the meridional movement of heat and moisture from tropics to subtropics and the zonal gradient between North Pacific and East Asian continent (Jiang et al. 2013; Piao et al. 2020). The seasonal-scale coral Sr/Ca-SST and $\delta^{18}O_{coral}$ records from 5.7 ka ($\Delta SST_{max-min}$ = 9.5°C; $\Delta\delta^{18}O_{max-min}$ = 1.86‰) and 4.9 ka ($\Delta SST_{max-min}$ = 10.2°C; $\Delta\delta^{18}O_{max-min}$ = 1.45‰) both have larger summer-winter difference which relates to seasonal SST and SSS amplitude. The large SST amplitude indicates an enhanced surface ocean warming from early spring to summer of 5.7 ka and 4.9 ka. This could have enhanced the WPSH and in turn, increased the intensity of southwesterly summer monsoon. The stronger southwesterlies carried more rainfall in subtropical southern Japan (Fig. 55a). This is evident in the more negative SSS signal from summer $\delta^{18}O_{coral}$ record. Conversely, the 3.2 ka coral ($\Delta SST_{max\text{-}min}$ = 7.8°C; $\Delta\delta^{18}O_{max\text{-}min}$ = 0.98‰) has smaller seasonal SST and SSS amplitude. The small SST amplitude indicates a reduction in surface ocean warming from early spring to summer of 3.2 ka. This resulted in weakened WPSH and southwesterlies. This condition led to the reduced summer rainfall and positive SSS signal from summer $\delta^{18}O_{coral}$ record in 3.2 ka as a response of weakened summer monsoon (Fig. 55b).

EA winter monsoon in subtropical NW Pacific

The compiled winter $\delta^{18}O_{coral}$ (Fig. 53a) could reflect the variation of SSS during winter as a function of evaporation-precipitation balance. The winter $\delta^{18}O_{coral}$ record has more subtle shift from average value of -3.1‰ from 7.0 ka to 5.7 ka to -3.4‰ from 4.9 ka to 4.2 ka, then shifted positively back to -3.1‰ from 3.8 ka to 3.2 ka. The negative shift around 5.0 ka to 4.0 ka suggests a warmer, wetter condition. The winter $\delta^{18}O_{coral}$ was compared to the winter SSTA (Fig. 53c). The period from 7.0 ka to 5.7 ka had an average winter SSTA of -0.6°C. The 5.7 ka coral recorded a drop of -2.3°C in the winter SST relative to the present-day. The average winter SSTA of the period 4.9 ka to 4.2 ka was not significantly different from the present-day winter SST and slightly warmer than 7.0 - 5.7 ka and 3.8 - 3.2 ka. The average winter SSTA from 3.8 ka to 3.2 ka was -2.5°C. The higher winter SSS (positive $\delta^{18}O_{coral}$) and cooler winter SST indicate an intensified cold and dry northeasterlies of the winter monsoon. The lower winter SSS (negative $\delta^{18}O_{coral}$) and warmer winter SST indicate a weakened cold and dry northeasterlies of the winter monsoon.

The present-day winter SST, SSS, and rainfall in East Asia are primarily controlled by the intensity of winter monsoon. Reanalysis data and climate model simulation attributed the variation of winter monsoon intensity and winter temperature in East Asia with the changes of high latitude low-level tropospheric circulation (i.e. polar jet stream, Siberian high and Aleutian low) in boreal winter (Jhun and Lee 2004). The cold winter temperature surge in eastern China, Korea, and Japan is an indicator of strong winter monsoon intensity. The strong EAWM also enhanced the evaporation which resulted in higher SSS with increased surface ocean cooling (Fig. 56a). In contrast, the weak EAWM reduced evaporation and increased rainfall which resulted in lower SSS accompanied by decreased surface ocean cooling (Fig. 56b)

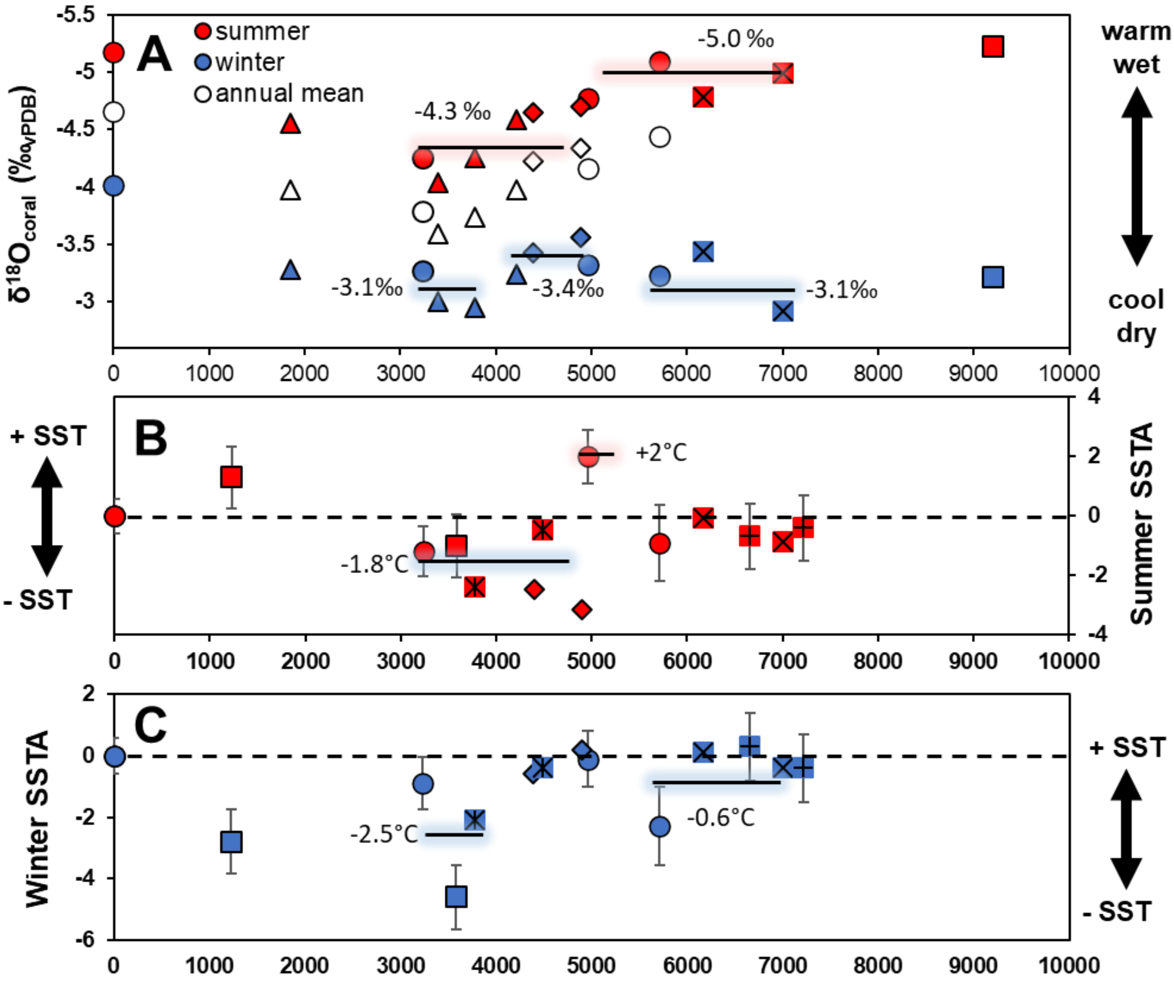

Figure 53. A. The minimum, maximum, and annual mean δ18Ocoral records from fossil Porites in Kikai Island and Okinawa Island in Southern Japan. B. Compiled summer SSTA and C. winter SSTA from Kikai Island (Morimoto et.al. 2007; Garas et al. 2023), Okinawa Island (Mitsuguchi et.al. 1998), Ishigaki Island (Sowa et.al. 2014) and Kume Island (Seki et.al. 2012).

EA summer monsoon in tropical NW Pacific

The minimum, maximum, and annual mean $\delta^{18}O_{coral}$ records from fossil *Porites* in NW Luzon Island, Philippines (This study; Yokoyama et al. 2011), Hainan Island (Wei et al. 2007; Su et al. 2010; Guo et al. 2016) and Leizhou Peninsula, China (Yu et al. 2005), and Taiwan (Shen et al. 2005) were compiled to investigate the seasonal SSS change in tropical NW Pacific. There was a negative shift in the minimum (summer) and maximum (winter) $\delta^{18}O_{coral}$ values around 5.0 ka. The average of minimum (summer) $\delta^{18}O_{coral}$ values from 6.7 ka to 4.4 ka is -6.0‰. The minimum (summer) $\delta^{18}O_{coral}$ shifted to more negative value of -6.6‰ from 4.3 ka to 4.2 ka. Following the $\delta^{18}O_{coral}$-SSS calibration (Fig. 46b), the trend indicates decreasing SSS from 6.7 ka to 4.2 ka.

To demonstrate the relationship of SST and SSS changes in Holocene, the Sr/Ca-based SST from 4.2 ka, 4.3 ka, and 6.1 ka were compiled with published coral-based SST records from northern South China See which include data from Hainan Island (Wei et al. 2007) and Leizhou Peninsula, China (Yu et al. 2005). Summer and winter SSTA from tropical SCS corals were calculated using the same data treatment used in subtropical coral records. The compiled summer SSTA (Fig. 54b) shows that the average summer SSTA from 6.7 ka to 5.0 ka was warmer by 0.45°C than the present-day. The SST became cooler by 0.9°C around 4.3 to 4.2 ka. Comparing the summer SSS and SSTA from coral records, the tropical NW Pacific was drier from 6.7 ka to 4.4 ka when the surface ocean was slightly warmer than today. The hydroclimate changed into wetter conditions around 4.3 ka to 4.2 ka when the surface ocean was cooler.

Both the subtropical (Fig. 53b) and tropical (Fig. 54b) SSTA records are consistent that the period from 5.0 ka to 7.0 ka was not significantly different and warmer at times than the present-day. Similarly, the summer SSTA records after 5.0 ka both show cooling trend in subtropical (-1.8°C) and tropical (-0.9°C) NW Pacific. However, the magnitude of SST increase varied across different locations in NW Pacific during these time-windows. In contrast, the subtropical and tropical SSS records from minimum $\delta^{18}O_{coral}$ values have diverging trends. SSS is defined by the balance between evaporation and precipitation (Helm et al. 2010; Bingham et al. 2012). The monsoon system is one of the key drivers in the overall hydrological process of NW Pacific. Proxy- and model-based paleoclimate reconstructions agreed that the EASM was intensified in mid-Holocene (Jiang et al. 2013; Piao et al. 2020; Kaboth-Bahr et al. 2021). Our data supports the interpretation of published coral data from northern SCS (Sun et al. 2005; Yokoyama et al. 2011; Guo et al. 2016). The saltier sea surface condition of mid-Holocene was caused by the interaction of EASM and ITCZ. Sun et al. (2005) interpreted that the higher SSS (positive $\delta^{18}O_{coral}$) during 4.4 ka was driven by enhanced evaporation due to the strengthened summer monsoon wind circulation. However, this interpretation is not supported by salinity observations and models of western Luzon in recent decades which indicates that the salinity is influenced by the precipitation-driven by anticyclonic wind anomaly (Yan et al. 2015). A more recent interpretation of the higher SSS in mid-Holocene is the northerly latitudinal position of the ITCZ that brought more rainfall in the subtropics and less rainfall in the tropical NW Pacific (Yokoyama et al. 2011; Guo et al. 2016). The paired Sr/Ca (SST) and $\delta^{18}O_{coral}$ (SSS) records from Ryukyu Archipelago (subtropics) and northern South China Sea (tropics) documented the north-south migration of the ITCZ coupled with strengthening/weakening of the EASM.

The ITCZ typically migrates towards a warming hemisphere as an atmospheric energy balance response to the ocean heat transport mechanism (Philander 1996; Schneider et al. 2014; Marshal et al. 2014). The mean latitudinal position of ITCZ was probably located north of the present-day location when the subtropical and tropical NW Pacific were slightly warmer from 7.0 ka to 5.0 ka. The low saline waters in Ryukyu Archipelago and high saline waters in northern SCS as indicated by low $\delta^{18}O_{coral}$ and high $\delta^{18}O_{coral}$ respectively are supported by the northerly shift of the ITCZ (Fig. 55a). The northerly ITCZ and strong EASM caused the northward extension of the summer monsoon rainfall in higher latitude during mid Holocene (Goldsmith et al. 2017). The cooling of the subtropical and tropical NW Pacific triggered the southward migration of the ITCZ. The southward migration of the ITCZ in the NW Pacific resulted in the reversal of SSS trends. The subtropical Ryukyu Archipelago was more saline while the tropical northern SCS was less saline around 4.3 to 4.2 ka (Fig. 55b). The southward shift of ITCZ increased the SSS in Ryukyu Archipelago, decreased the SSS in northern SCS and increased the rainfall in Flores, Indonesia from 5000 to 2000 years ago based on stalagmite record (Griffiths et al. 2009).

EA winter monsoon in tropical NW Pacific

The maximum $\delta^{18}O_{coral}$ records from fossil *Porites* in NW Luzon Island, Philippines (This study; Yokoyama et al. 2011), Hainan Island (Wei et al. 2007; Su et al. 2010; Guo et al. 2016) and Leizhou Peninsula, China (Yu et al. 2005), and Taiwan (Shen et al. 2005) were compiled to investigate the winter SSS change in tropical NW Pacific. The maximum (winter) $\delta^{18}O_{coral}$ values decreased from 6.7 ka to 4.2 ka. The average of maximum (winter) $\delta^{18}O_{coral}$ values from 6.7 ka to 4.4 ka is -4.1‰. The maximum (winter) $\delta^{18}O_{coral}$ shifted to more negative value of -5.6‰ from 4.3 ka to 4.2 ka.

The compiled winter SSTA (Fig. 54b) shows that the average winter SSTA from 6.7 ka to 5.0 ka was warmer by 0.7°C than the present-day. The SST became cooler by 1.7°C around 4.3 to 4.2 ka. Comparing the SSS and SSTA from coral records, the winter in tropical northern SCS was characterized by drier and warmer conditions from 6.7 ka to 4.4 ka. The lower SSS/wet conditions coincided when the region became cooler by 1.7°C after 5.0 ka relative to present-day. The cold winter SST in the East Asia is a signal of intensified northeasterlies of the EAWM (Jhun and Lee 2004). However, the SST from 6.7 ka to 4.4 ka was warmer when the EAWM was believed to be stronger. The stronger EAWM would bring less rainfall in northern SCS, which is consistent with the maximum (winter) $\delta^{18}O_{coral}$ (Fig. 56a). The cooler SST around 4.3 ka to 4.2 ka was inconsistent to the less saline/wet conditions which resembles a weak EAWM state (Fig. 56b). We can observe that the rainfall driven SSS changes of climatological winter in tropical NW Pacific were affected by the strengthening or weakening of the northeasterly EAWM. However, the SST in tropical NW Pacific did not respond to the typical EAWM intensity signals as observed in the subtropical NW Pacific. It is possible that the winter SST changes in the tropics were not greatly influenced by the EAWM intensity.

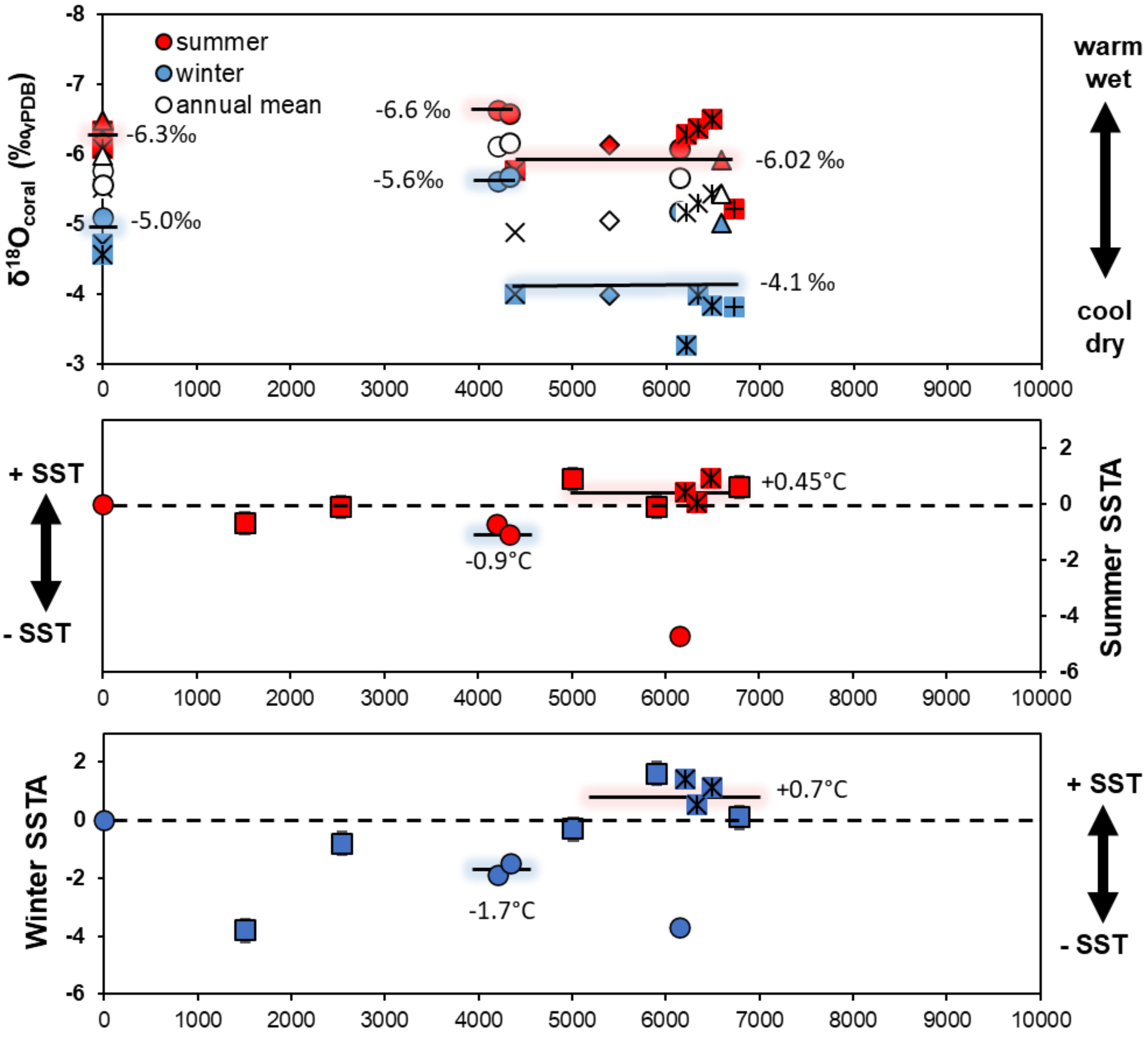

Figure 54. A. The minimum, maximum, and annual mean δ18Ocoral records from fossil Porites of NW Luzon Island, Philippines (This study; Yokoyama et al. 2011), Hainan Island (Wei et al. 2007; Su et al. 2010; Guo et al. 2016) and Leizhou Peninsula, China (Yu et al. 2005), and Taiwan (Shen et al. 2005). B. Compiled summer SSTA and C. winter SSTA from NW Luzon Island, Philippines (This study), Hainan Island (Wei et al. 2007) and Leizhou Peninsula, China (Yu et al. 2005)

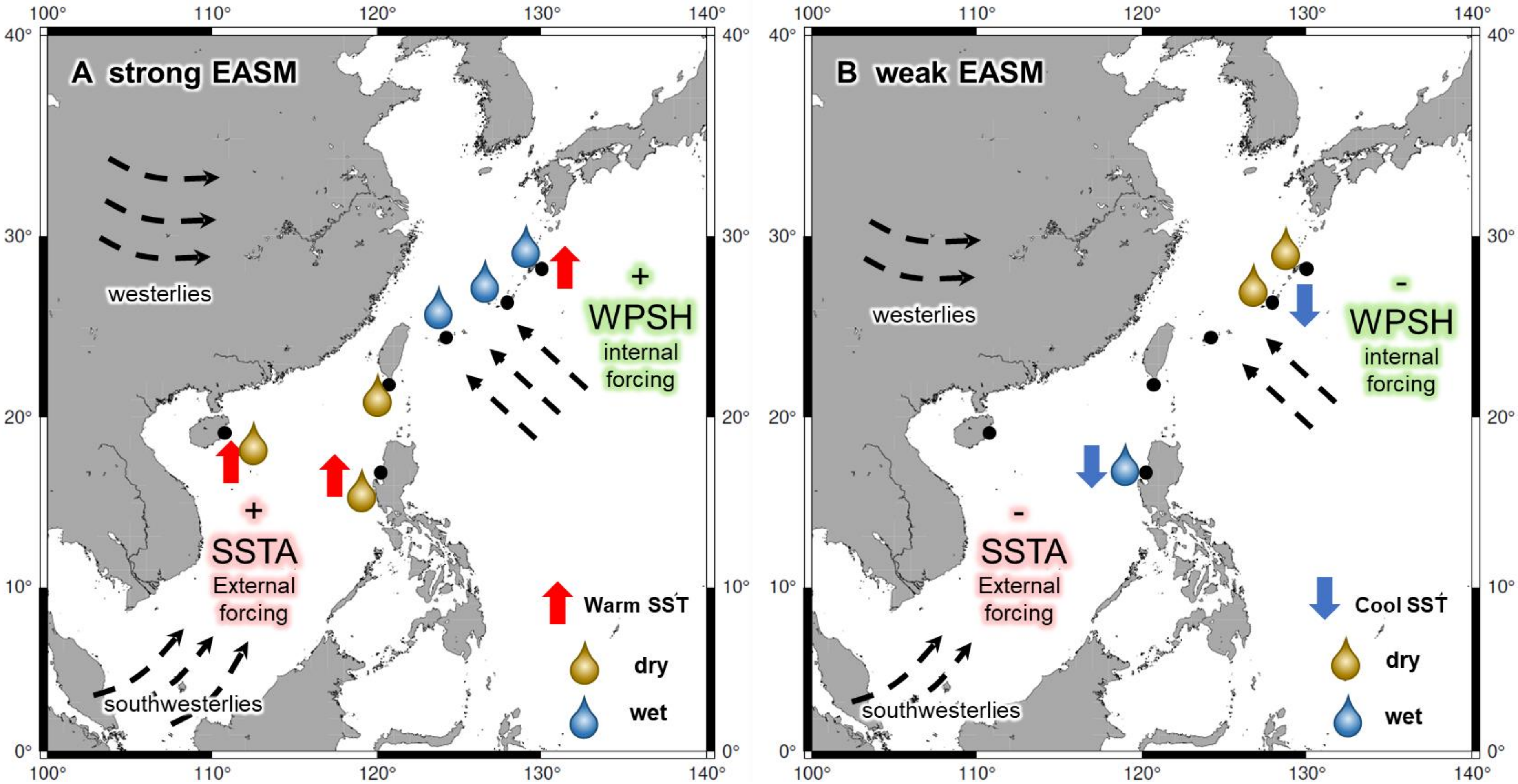

Figure 55. A. The low saline (wet) waters in Ryukyu Archipelago and high saline (dry) waters in northern SCS as indicated by low $\delta^{18}O_{coral}$ and high $\delta^{18}O_{coral}$ respectively are supported by the northerly shift of the ITCZ. B. The cooling of the subtropical and tropical NW Pacific triggered the southward migration of the ITCZ resulted in increased SSS (dry) in Ryukyu Archipelago and decreased SSS (wet) in northern SCS

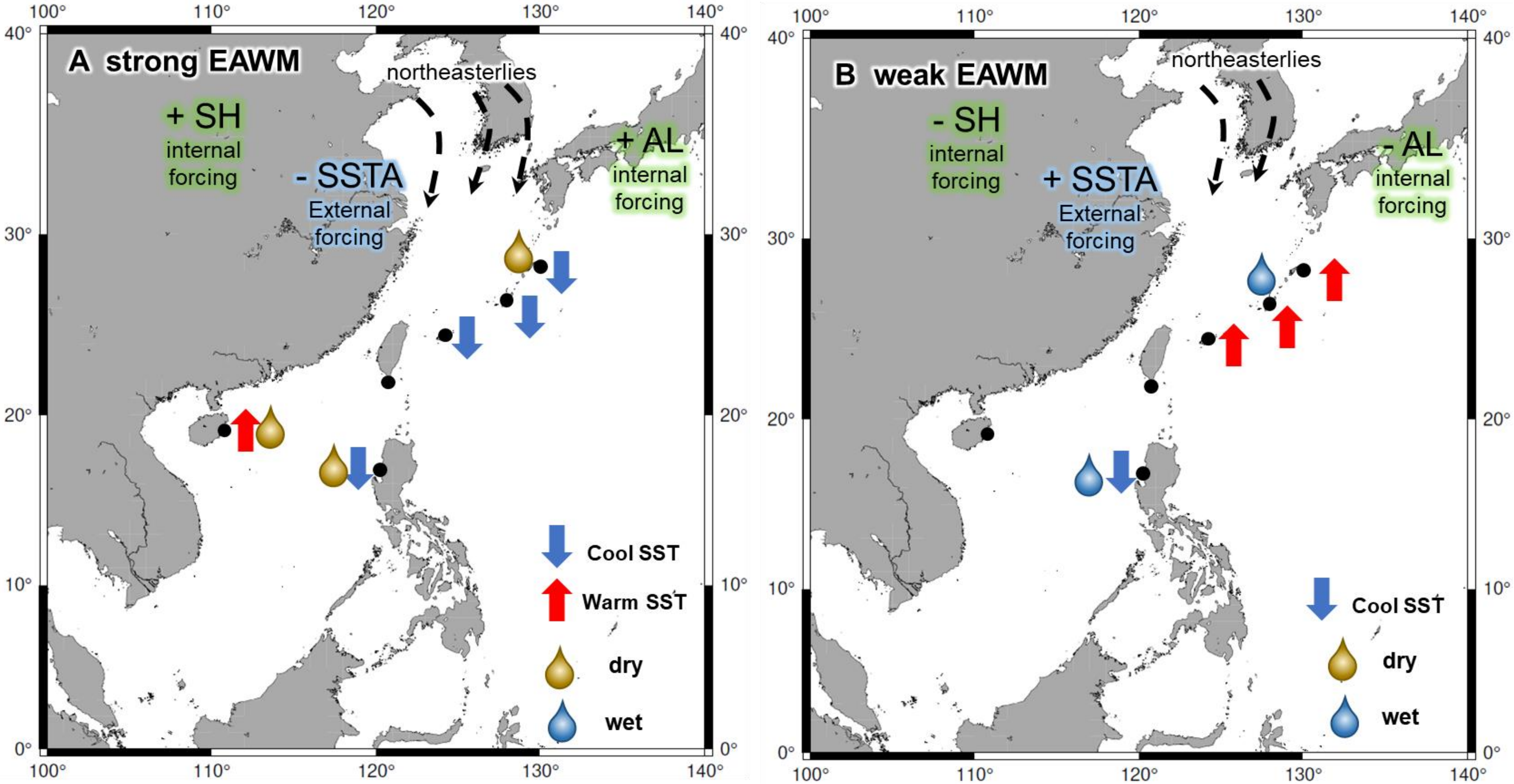

Figure 56. A. The higher winter SSS (positive $\delta^{18}O_{coral}$) and cooler winter SST indicate an intensified cold and dry northeasterlies of the winter monsoon. The lower winter SSS (positive $\delta^{18}O_{coral}$) and warmer winter SST indicate a weakened cold and dry northeasterlies of the winter monsoon. B. Winter in tropical northern SCS was characterized by dry and warm conditions from 6.7 ka to 4.4 ka and wet and cool conditions from 4.3 ka to 4.2 ka.

5.5. ENSO modulates coral-derived $\delta^{18}O_{sw}$ seasonality in NW Pacific

The influence of ENSO on the overall hydroclimate of the NW Pacific during Holocene is not yet clear. The interaction of ENSO to the prevailing climate systems such as monsoon and ITCZ is poorly understood due to the lack of high temporal resolution climate archives. Paleoclimate records from marine and lake sediments, and speleothem discuss long-term changes in the ocean and terrestrial conditions that give indicative explanation of the general trend in Holocene. But due to the absence of seasonally resolved reconstructions, these archives cannot fully discuss the mechanism and interaction governing the EAM-ENSO teleconnections. To bridge this gap in paleoclimate research, ENSO signals from coral records are being utilized. Paleo-ENSO studies using corals from Pacific have proven that geochemical proxies in coral skeleton are effective in tracking the Holocene ENSO variability (Tudhope et al. 2001; McGregor and Gagan et al. 2004; Cobb et al. 2013; McGregor et al. 2013). This chapter will discuss the possible teleconnection of ENSO to the monsoon-driven rainfall pattern in tropical and subtropical NW Pacific.

The oxygen isotope of seawater ($\delta^{18}O_{sw}$) reflects SSS change as a function of evaporation and precipitation (LeGrande and Schmidt 2011; Conroy et al. 2016; Conroy et al. 2017). Evaporation increases the $\delta^{18}O_{sw}$ and SSS while the mixing of low- $\delta^{18}O$ freshwater through precipitation and surface runoff decreases the $\delta^{18}O_{sw}$ and SSS. The $\delta^{18}O_{sw}$ contributes up to 89% of $\delta^{18}O_{coral}$ in the IPWP region (Thompson et al. 2021). Fig. 48 shows that the $\delta^{18}O_{sw}$ is negatively correlated with precipitation in Kikai Island and $\delta^{18}O_{sw}$ is positively correlated with SSS in NW Luzon Island. Furthermore, monsoon-driven rainfall plays an important role in the formation of low SSS in NW Luzon (Yan et al. 2015). In this discussion, the $\delta^{18}O_{sw}$ records from Kikai and NW Luzon islands were used to isolate the interannual signals from ENSO.

NW Luzon Island corals

The $\delta^{18}O_{sw}$ from Badoc Island, NW Luzon (Fig. 51) was calculated from paired coral Sr/Ca and $\delta^{18}O_{coral}$ from 2011 to 2017 by subtracting the SST component from the $\delta^{18}O_{coral}$ using the centering method (Cahyarini et al. 2008). The same data calculation was done to the paired coral Sr/Ca and $\delta^{18}O_{coral}$ from Palaui Island, NE Luzon covering the period of 1954 to 2012 (Ramos et al. 2017). Bandpass filtering using PAST v4.11 was employed to isolate the 2 – 8-year frequency signal from the $\delta^{18}O_{sw}$ time series data. The 2–8-year frequency band filtering was done in both NW Luzon and NE Luzon coral-derived $\delta^{18}O_{sw}$. The 2–8-year bandpass filtered $\delta^{18}O_{sw}$ was compared to the Extended Reconstructed Sea Surface Temperature (ERSST) v4 NINO3.4 SSTA from 1982 to 2022. The ERSST v4 NINO3.4 SSTA is produced on a 2°- 2° grid with spatial completeness enhanced using statistical methods (Huang et al. 2015) from the International Comprehensive Ocean-Atmosphere Dataset (ICOADS). Figure 57a shows the comparison of the 2–8-year bandpass filtered $\delta^{18}O_{sw}$ data of NE Luzon coral from 1954 to 2012 and the ERSST v4 NINO 3.4 SSTA from 1982 to 2012. Figure 57b shows the comparison of the 2–8-year bandpass filtered $\delta^{18}O_{sw}$ data of NW Luzon coral from 2011 to 2017 and the ERSST v4 NINO 3.4 SSTA from 2011 to 2017.

The $\delta^{18}O_{sw}$-SSS calibration using the NW Luzon coral from Badoc Island reveals a positive correlation between the two variables which the timing of the increase (decrease) of the SSS follows the timing of the increase (decrease) of $\delta^{18}O_{sw}$ (Fig. 48b). Historical records show that 1982 – 1983, 1987 – 1988, 1991 – 1992, and 1997 – 1998 were observed as past very strong to strong El Niño events. The El Niño years are defined by the occurrence of positive SSTA in NINO3.4 and positive $\delta^{18}O_{sw}$ values (Fig. 57). The positive $\delta^{18}O_{sw}$ values during El Niño years reflect a more saline water in both NE Luzon and NW Luzon. The increased SSS in the tropical NW Pacific was due to the relatively lower rainfall output during El Niño years. On the other hand, 1988 – 1989, 1998 – 1999, 1999 – 2000, 2007 – 2008, and 2010 – 2011 were La Niña events. The La Niña years are defined by the occurrence of negative SSTA in NINO3.4 and negative $\delta^{18}O_{sw}$ values (Fig. 57). The negative $\delta^{18}O_{sw}$ values during La Niña years reflect a less saline water in both NE Luzon and NW Luzon. The decreased SSS in the tropical NW Pacific was due to the higher rainfall output during La Niña years relative to El Niño years.

The strength of El Niño and La Niña years is defined by the value of the SSTA amplitude in the central and eastern Pacific (NINO3.4) region. The weak, moderate, strong, and very strong El Niño years have +0.5°C, +1.0°C, +1.5°C, and +2.0°C anomalies respectively. The weak, moderate, strong, and very strong La Niña years have -0.5°C, -1.0°C, -1.5°C, and -2.0°C anomalies respectively. To get the $\delta^{18}O_{sw}$ threshold values for different ENSO intensity, an OLS bivariate regression analysis was performed using the 2–8-year bandpass filtered $\delta^{18}O_{sw}$ data of NE Luzon coral from 1954 to 2012 and the ERSST v4 NINO 3.4 SSTA from 1982 to 2012 (Fig. 58). The maximum and minimum values of the filtered $\delta^{18}O_{sw}$ and NINO3.4 SSTA were correlated. The OLS regression reveals a strong statistically significant positive correlation ($r=0.75$; $r^2=0.56$; $p<0.000$) between the two variables. The weak, moderate, strong, and very strong El Niño years have $\delta^{18}O_{sw}$ threshold values of 0.092‰, 0.131‰, 0.170‰, and 0.209‰ respectively. The weak, moderate, strong, and very strong La Niña years have $\delta^{18}O_{sw}$ threshold values of 0.014‰, -0.025‰, -0.064‰, and -0.103‰ respectively.

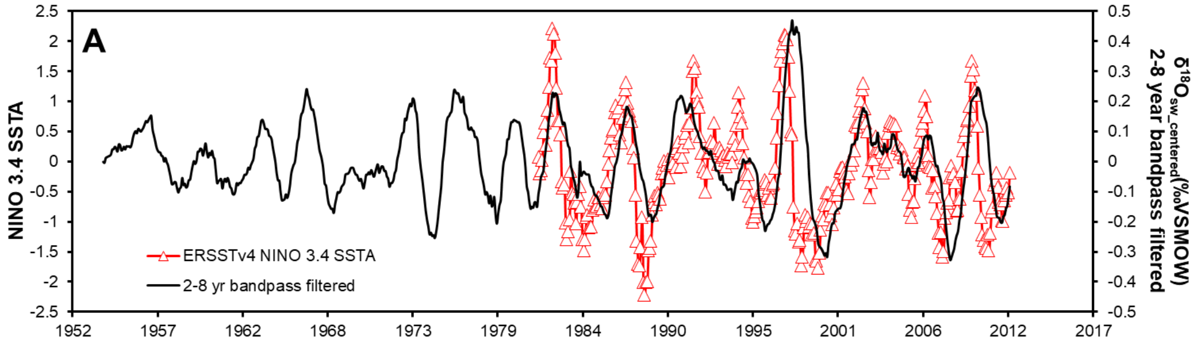

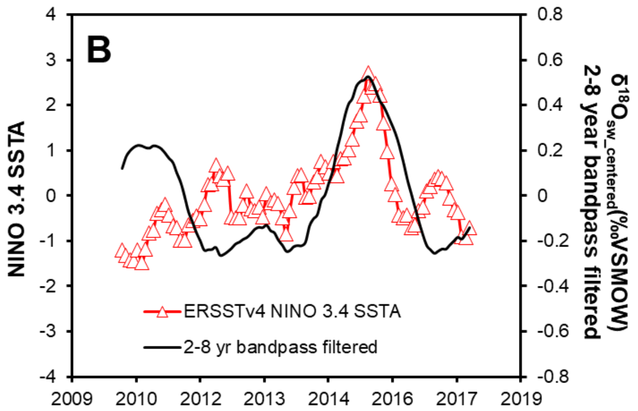

Figure 57. A. Comparison of the 2–8-year bandpass filtered δ^{18}O$_{sw}$ data from 1954 to 2012 (black) and the ERSST v4 NINO 3.4 SSTA from 1982 to 2012 (red) B. Comparison of the 2–8-year bandpass filtered δ^{18}O$_{sw}$ data from 2011 to 2017 (black) and the ERSST v4 NINO 3.4 SSTA from 2011 to 2017 (red)

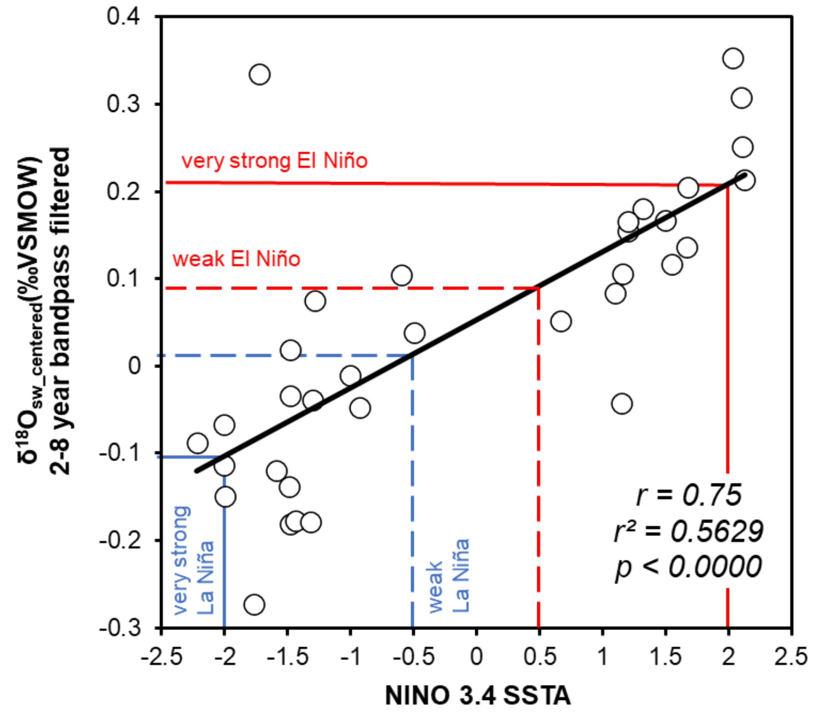

Figure 58. δ^{18}O$_{sw}$ threshold values were obtained from the OLS bivariate regression analysis of the 2–8-year bandpass filtered δ^{18}O$_{sw}$ data of NE Luzon coral and the ERSST v4 NINO 3.4 SSTA

The $\delta^{18}O_{sw}$ was also calculated from the paired coral Sr/Ca and $\delta^{18}O_{coral}$ records of 4.2 ka, 4.3 ka, and 6.1 ka fossil corals from NW Luzon Island, Philippines (Fig. 51). The reconstructed $\delta^{18}O_{sw}$ was filtered using the same frequency band of 2 – 8 year highlighted in the $\delta^{18}O_{sw}$ of modern corals from NE Luzon and NW Luzon. Figures 59 -61 show the 2 – 8-year bandpass filtered $\delta^{18}O_{sw}$ records from the 4.2 ka, 4.3 ka, and 6.1 ka corals. The positive $\delta^{18}O_{sw}$/high SSS peaks are identified as El Niño years while the negative $\delta^{18}O_{sw}$/low SSS peaks are identified as La Niña years. The $\delta^{18}O_{sw}$ threshold values from regression analysis in Fig. 58 were used to identify the ENSO intensity of the identified El Niño and La Niña years.

Spectral analysis using REDFIT method was performed to show the "red-noise" spectrum of each coral-derived $\delta^{18}O_{sw}$ record. The 1-year periodicity is the most defined cycle in annually banded corals; thus, it interferes with the spectral power of other periodicities in the coral time series. The 1-year periodicity was systematically removed from the $\delta^{18}O_{sw}$ time series. The REDFIT method is often used to analyze the red noise spectrum of unevenly spaced time series (Schulz and Mudelsee 2002). The statistical significance of 90%, 95%, and 99% percentiles were calculated using Monte Carlo simulations. The spectral analysis of the 58-year long record of NE Luzon coral shows the strong 7yr, 5yr, 3.6yr, and 2.2yr periodicities of the 2 – 8 year ENSO frequency band. A weaker 13-19yr signal is evident in the spectrum probably reflects the effect of Pacific Decadal Oscillation in the NE Luzon coral as discussed by Ramos et al. (2019). The spectral analysis of $\delta^{18}O_{sw}$ of NW Luzon coral shows a broad 4-8yr peak representing the ENSO frequency band.

The 4.2 ka coral had 8 very strong and strong, and 3 moderate El Niño events and 15 very strong and strong La Niña events in the span of 44 years (Fig. 59). The REDFIT spectral analysis shows the presence of 2.5yr and 2yr cycle exceeding 99% statistical significance, and 4yr and 3yr cycle exceeding 90% statistical significance. The 4yr and 3yr periodicities correspond to the El Niño and La Niña cycles in the $\delta^{18}O_{sw}$ time series. The 4.3 ka coral had 5 very strong and strong, and 1 moderate El Niño events and 6 very strong and strong La Niña events in the span of 20 years. The REDFIT spectral analysis shows 3yr and 2.5yr cycle exceeding 90% statistical significance. A weaker 6.6yr cycle below the 90% significance line was also noted. The 3yr and 2.5yr periodicities correspond to the ENSO cycles. The 6.1 ka coral had 4 very strong and strong, and 3 moderate El Niño events and 4 very strong and strong La Niña events in the span of 20 years. The REDFIT spectral analysis shows 5yr, 3yr, and 2.5yr cycle exceeding 99% statistical significance. A weaker 7yr cycle below the 90% significance

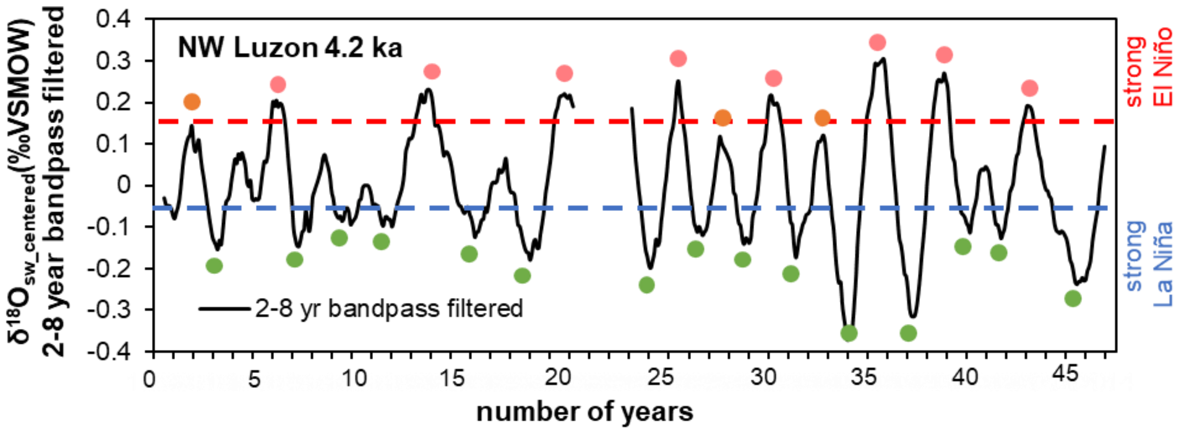

Figure 59. The bandpass filtered $\delta^{18}O_{sw}$ of 4.2 ka coral shows 8 very strong and strong (red circles), and 3 moderate (orange circles) El Niño events and 15 very strong and strong La Niña events (green circles)

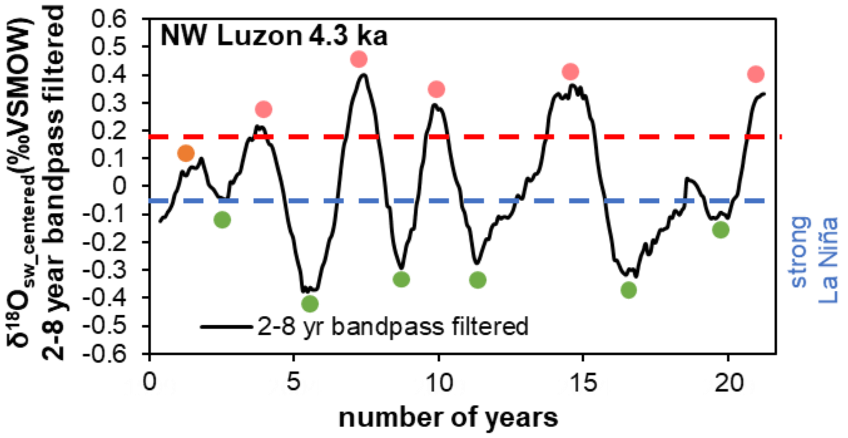

Figure 60. The bandpass filtered $\delta^{18}O_{sw}$ of 4.3 ka coral shows 5 very strong and strong (red circles), and 1 moderate (orange circles) El Niño events and 6 very strong and strong La Niña events (green circles)

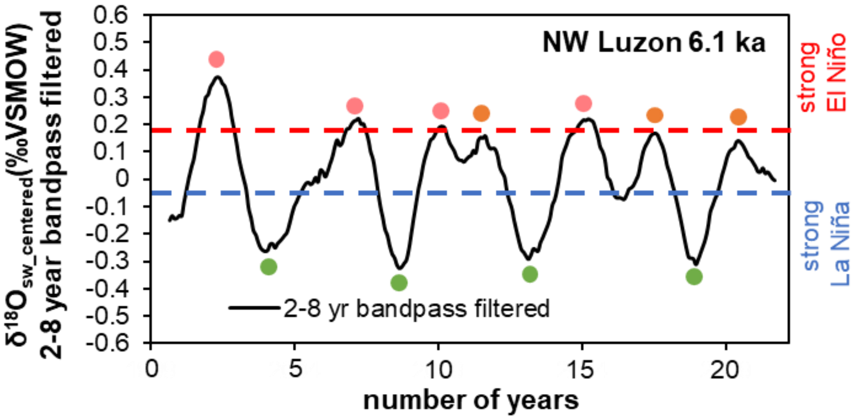

Figure 61. The bandpass filtered $\delta^{18}O_{sw}$ of 6.1 ka coral shows 4 very strong and strong (red circles), and 3 moderate (orange circles) El Niño events and 4 very strong and strong La Niña events (green circles)

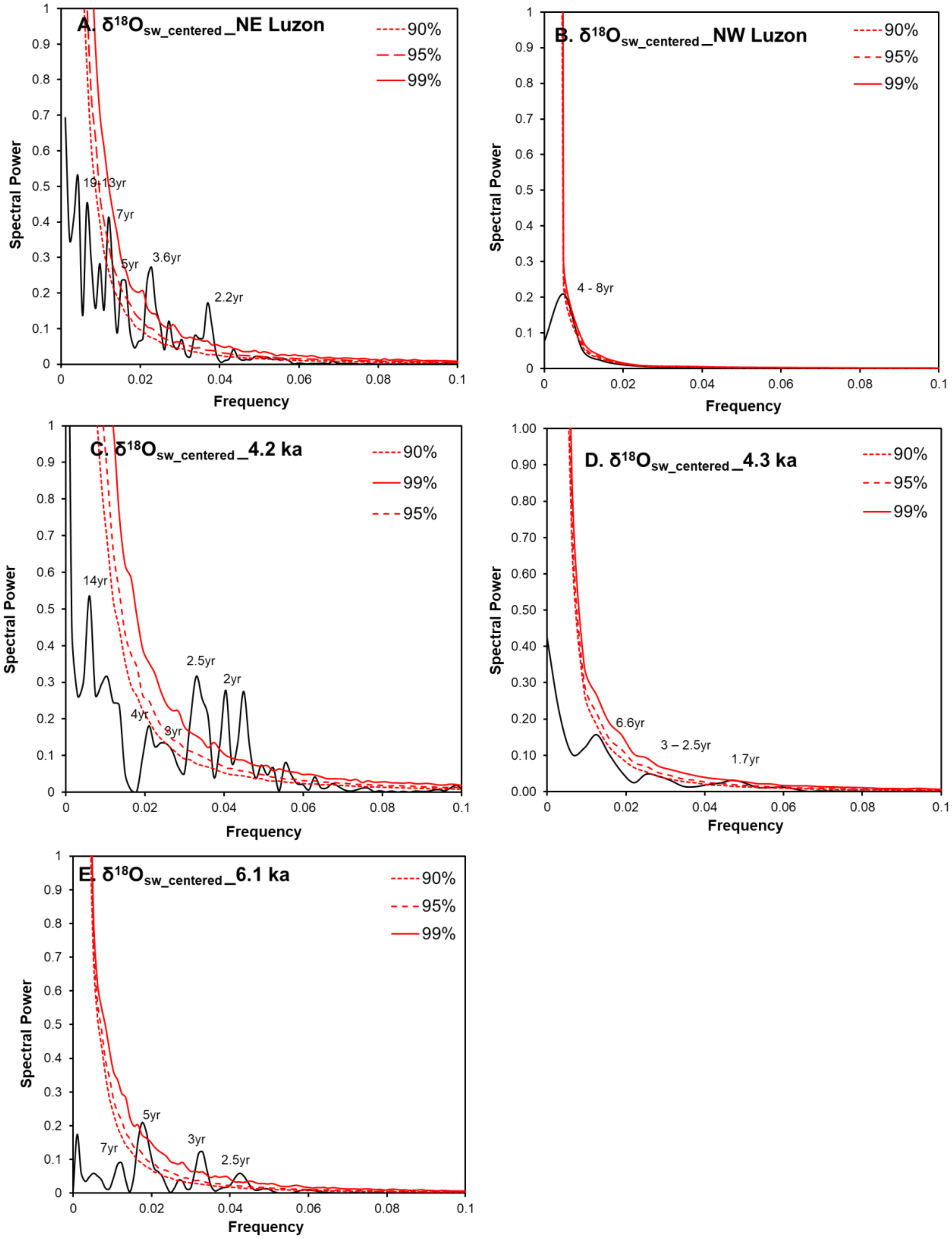

Figure 62. Spectral analysis using REDFIT method of the $\delta^{18}O_{sw}$ of (a) NE Luzon modern coral, (b) NW Luzon modern coral, (c) 4.2 ka coral, (d) 4.3 ka coral, and (e) 6.1 ka coral. The red noise spectra were tested for statistical significance of the 90%, 95%, and 99% percentiles in Monte Carlo simulation

line was also noted. The 3yr and 5yr periodicities correspond to the El Niño and La Niña cycles.

The results show that ENSO cycles were evident in 4.2 ka, 4.3 ka, and 6.1 ka time-windows in the tropical NW Pacific. However, the frequency and magnitude of the El Niño and La Niña events in different time windows were varied. The 4.2 ka experienced 4yr-interval El Niño cycles and 3yr-interval La Niña cycles and most of these events had strong to very strong intensity. The 4.3 ka coral recorded 3yr-interval El Niño cycles and 3yr-interval La Niña cycles, which had strong to very strong intensity. The frequent alternating El Niño and La Niña years during 4.2 ka and 4.3 ka was indicative of the strengthened ENSO and SSTA amplitudes in the NINO3.4 region. The 6.1 ka had 3yr-interval El Niño cycles and 5yr-interval La Niña cycles. The El Niño events were still frequent; however, half of these were moderate intensity.

The rainfall variations in mainland Southeast Asia, the Philippines, and Indonesia show robust negative correlations with El Niño based on the correlation map of the Niño-3.4 SSTA and GPCP precipitation (Fig. 4b). The development of anticyclone anomaly in the Philippine Sea during El Niño developing year has suppressed the summer monsoon wind convection which causes the decrease in rainfall in mainland Southeast Asia and the Philippines (Wang et al. 2020). Using the seasonally resolved $\delta^{18}O_{sw}$ records, the rainfall-driven SSS changes were examined during neutral and El Niño years in 20th century (1952 – 2012; 2011-2017) and mid-Holocene. The mean seasonal climatology of neutral and strong El Niño years from the 2 – 8 year bandpass filtered $\delta^{18}O_{sw}$ were calculated. The difference of $\delta^{18}O_{sw}$ of summer monsoon months (JJA-SON) during neutral and El Niño years was interpreted as the SSS difference.

The mean seasonal climatology of neutral and El Niño years from the $\delta^{18}O_{sw}$ of 1952-2012 NE Luzon coral, 2011-2017 NW Luzon, 4.2 ka, 4.3 ka, and 6.1 ka were presented in Fig. 63a-e. The summer $\delta^{18}O_{sw}$ difference ($\Delta\ \delta^{18}O_{sw}$) between neutral and El Niño years from 2011 to 2017 is 1.1‰ (Fig. 63b). The 1.1‰ difference is equivalent to an increase of 1.25 psu in summer SSS suggesting a reduced summer rainfall during El Niño. The same calculation was done in 4.2 ka, 4.3 ka, and 6.1 ka corals from NW Luzon. The 4.2 ka coral recorded a 0.34‰ $\Delta\delta^{18}O_{sw}$, which is equivalent to a 0.4 psu increase in SSS from neutral to El Niño years (Fig. 63c). The 4.3 ka coral recorded a 0.49‰ $\Delta\delta^{18}O_{sw}$, which is equivalent to a 0.56 psu increase in SSS from neutral to El Niño years (Fig. 63d). The 6.1 ka coral recorded no significant change in the summer $\delta^{18}O_{sw}$ values between neutral and El Niño years (Fig. 63e).

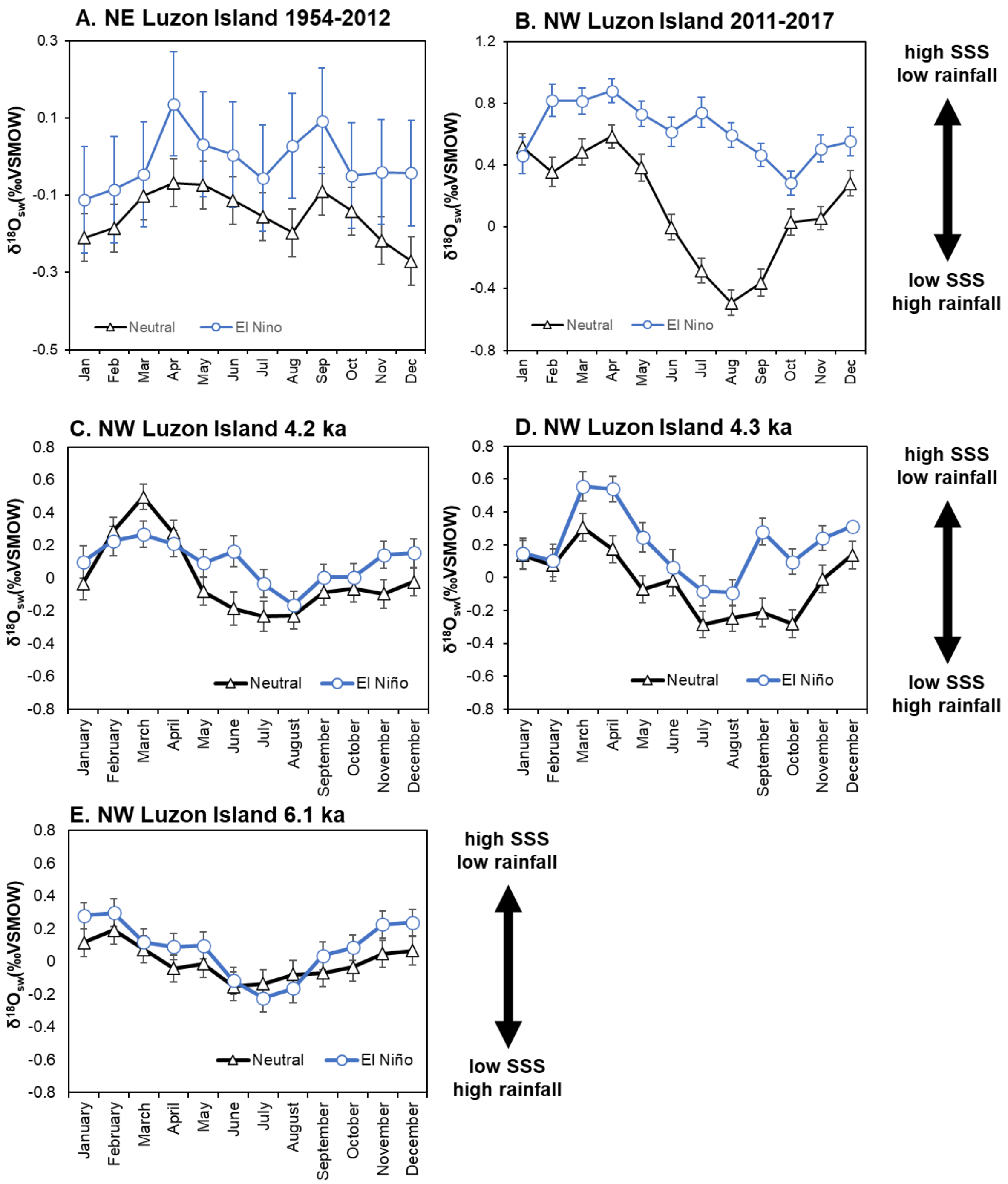

Figure 63. The mean seasonal climatology of neutral (black) and El Niño (blue) years from the 2 – 8-year bandpass filtered $\delta^{18}O_{sw}$ of (a) NE Luzon coral 1952-2012, (b) NW Luzon coral 2011-2017, (c) 4.2 ka, (d) 4.3 ka, and (e) 6.1 ka

Kikai Island corals

The $\delta^{18}O_{sw}$ from Kikai Island, Southern Japan (Fig. 49) was calculated from paired coral Sr/Ca and $\delta^{18}O_{coral}$ from 1989 to 2015 by subtracting the SST component from the $\delta^{18}O_{coral}$ using the centering method (Cahyarini et al. 2008). The same bandpass filtering was used to highlight the 2 – 8-year frequency signal from the $\delta^{18}O_{sw}$ time series data. The 2–8-year bandpass filtered $\delta^{18}O_{sw}$ of Kikai modern coral was compared to the Extended Reconstructed Sea Surface Temperature (ERSST) v4 NINO3.4 SSTA from 1982 to 2022. Figure 64 shows the comparison of the 2–8-year bandpass filtered $\delta^{18}O_{sw}$ data of Kikai coral from 1989 to 2015 and the ERSST v4 NINO 3.4 SSTA from 1989 to 2015.

The $\delta^{18}O_{sw}$-rainfall calibration using Kikai modern coral reveals a negative correlation between the two variables wherein the timing of the increase (decrease) of the SSS follows the timing of the decrease (increase) of $\delta^{18}O_{sw}$ (Fig. 48a). Historical records show that 1991 – 1992 and 1997 – 1998 were observed as past very strong to strong El Niño events. The El Niño years are defined by the occurrence of positive SSTA in NINO3.4 and positive $\delta^{18}O_{sw}$ values (Fig. 64). The positive $\delta^{18}O_{sw}$ values during El Niño years reflect a more saline water in Kikai. The negative peaks in 1998 – 1999 and 1999 – 2000 were captured in the $\delta^{18}O_{sw}$ time series as La Niña events. However, other La Niña events such as 2007 – 2008 and 2010 – 2011 were not evident. The La Niña years are defined by the occurrence of negative SSTA in NINO3.4 and negative $\delta^{18}O_{sw}$ values (Fig. 64). The negative $\delta^{18}O_{sw}$ values during La Niña years reflect a less saline water in Kikai.

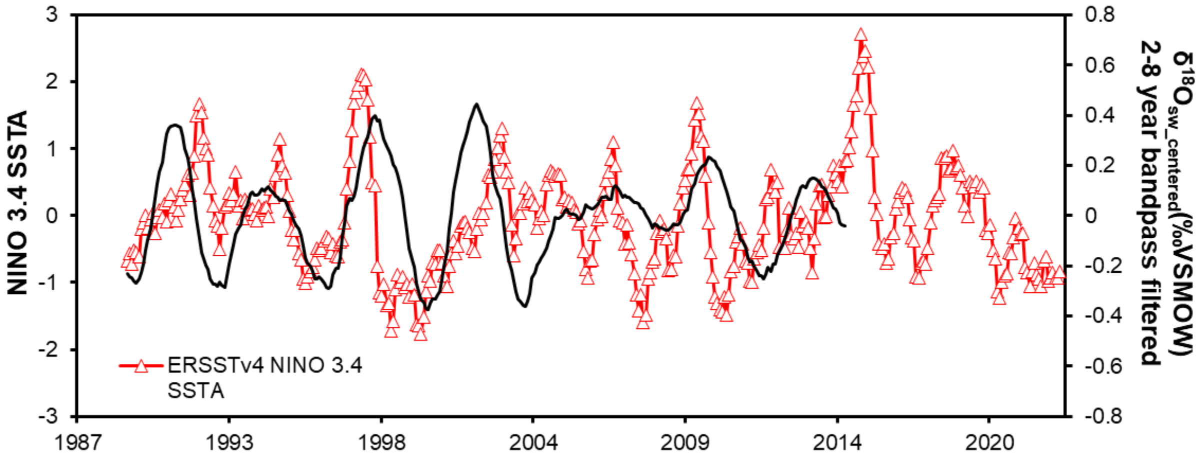

Figure 64. Comparison of the 2–8-year bandpass filtered $\delta^{18}O_{sw}$ data of Kikai modern coral from 1989 to 2015 (black) and the ERSST v4 NINO 3.4 SSTA from 1989 to 2022 (red)

The $\delta^{18}O_{sw}$ was also calculated from the paired coral Sr/Ca and $\delta^{18}O_{coral}$ records of 3.2 ka, 4.9 ka, and 5.7 ka fossil corals from Kikai Island, Southern Japan (Fig. 49). The reconstructed $\delta^{18}O_{sw}$ time series of 3.2 ka, 4.9 ka, and 5.7 ka fossil corals was filtered using the same frequency band of 2 – 8-year (Fig. 65-67). The positive $\delta^{18}O_{sw}$/high SSS peaks are identified as El Niño years while the negative $\delta^{18}O_{sw}$/low SSS peaks are identified as La Niña years. The same $\delta^{18}O_{sw}$ threshold values from regression analysis of $\delta^{18}O_{sw}$ from NE Luzon and ERSST v4 SSTA were used to identify the ENSO intensity of the identified El Niño and La Niña years (Fig. 58). Spectral analysis using REDFIT method (Schulz and Mudelsee 2002) was performed to show the “red-noise” spectrum of each coral-derived $\delta^{18}O_{sw}$ record of 3.2 ka, 4.9 ka, and 5.7 ka corals. The statistical significance of 90%, 95%, and 99% percentiles were calculated using Monte Carlo simulations.

The spectral analysis of the 26-year long record of Kikai coral shows the strong 7.7yr, 3.8yr, and 2.7yr periodicities of the 2 – 8-year ENSO frequency band. The 3.2 ka coral recorded 2 very strong and strong, and 1 moderate El Niño events and 2 very strong and strong La Niña events in the span of 13 years. The REDFIT spectral analysis shows the presence of strong 8yr exceeding 95% statistical significance, and weaker 3.4yr and 2yr cycle peaks. The 4.9 ka coral recorded 2 very strong and strong, and 2 moderate El Niño events and 2 very strong and strong La Niña events in the span of 13 years. The REDFIT spectral analysis shows the presence of weak 5.8yr and 2yr cycle peaks. The 5.7 ka coral recorded 1 moderate El Niño event and 2 very strong and strong La Niña events in the span of 7 years. The REDFIT spectral analysis shows the presence of strong 3.5yr exceeding 99% statistical significance. The results show that ENSO cycles were evident in 3.2 ka, 4.9 ka, and 5.7 ka time-windows in the subtropical NW Pacific. However, the frequency and magnitude of the El Niño and La Niña events were weaker than the present-day. The reconstructed years are also limited thus, the spectral analysis could not fully capture the real frequency of the different periodicities in the time series.

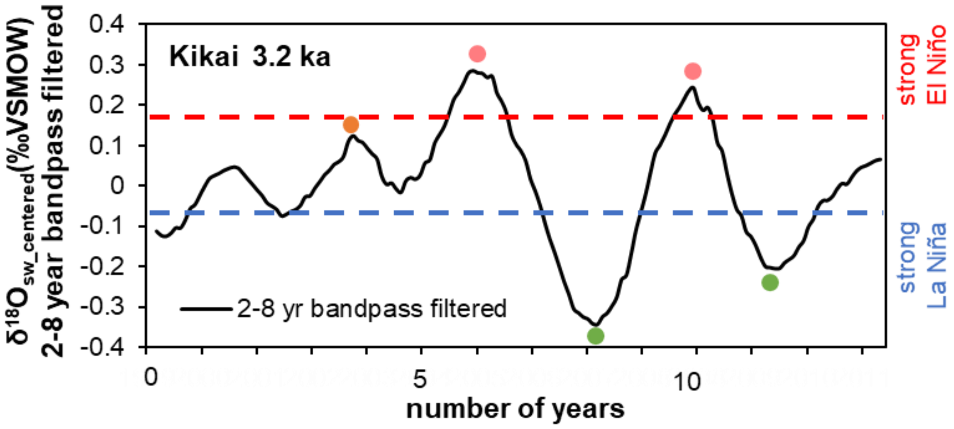

Figure 65. The bandpass filtered $\delta^{18}O_{sw}$ of 3.2 ka coral shows 2 very strong and strong (red circles), and 1 moderate (orange circles) El Niño events and 2 very strong and strong La Niña events (green circles)

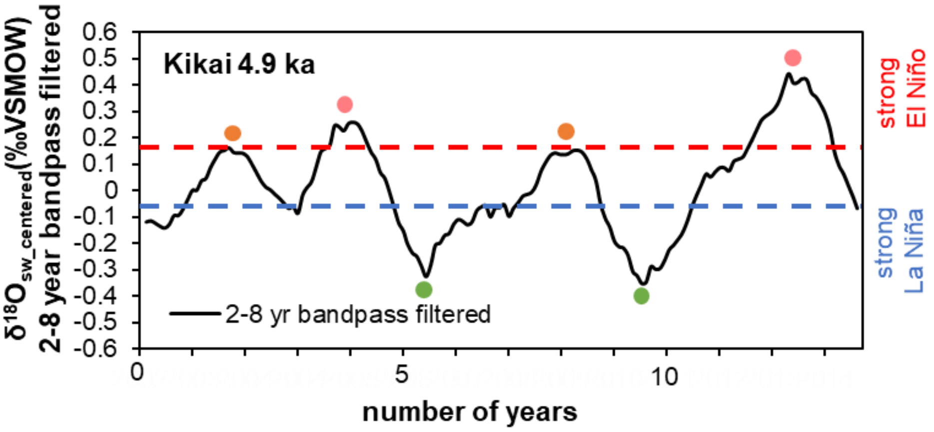

Figure 66. The bandpass filtered $\delta^{18}O_{sw}$ of 4.9 ka coral shows 2 very strong and strong (red circles), and 2 moderate (orange circles) El Niño events and 2 very strong and strong La Niña events (green circles)

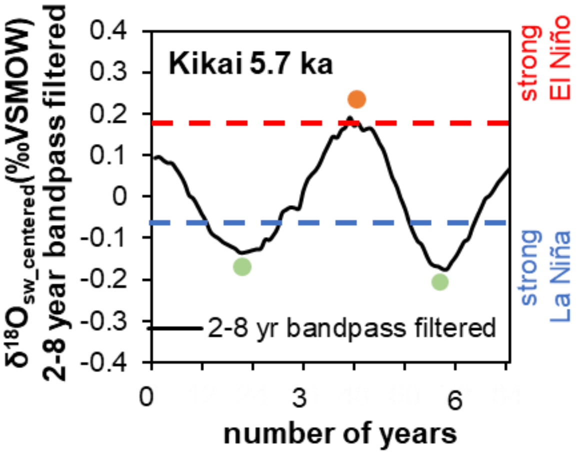

Figure 67. The bandpass filtered $\delta^{18}O_{sw}$ of 5.7 ka coral shows 1 moderate (orange circles) El Niño event and 2 very strong and strong La Niña events (green circles)

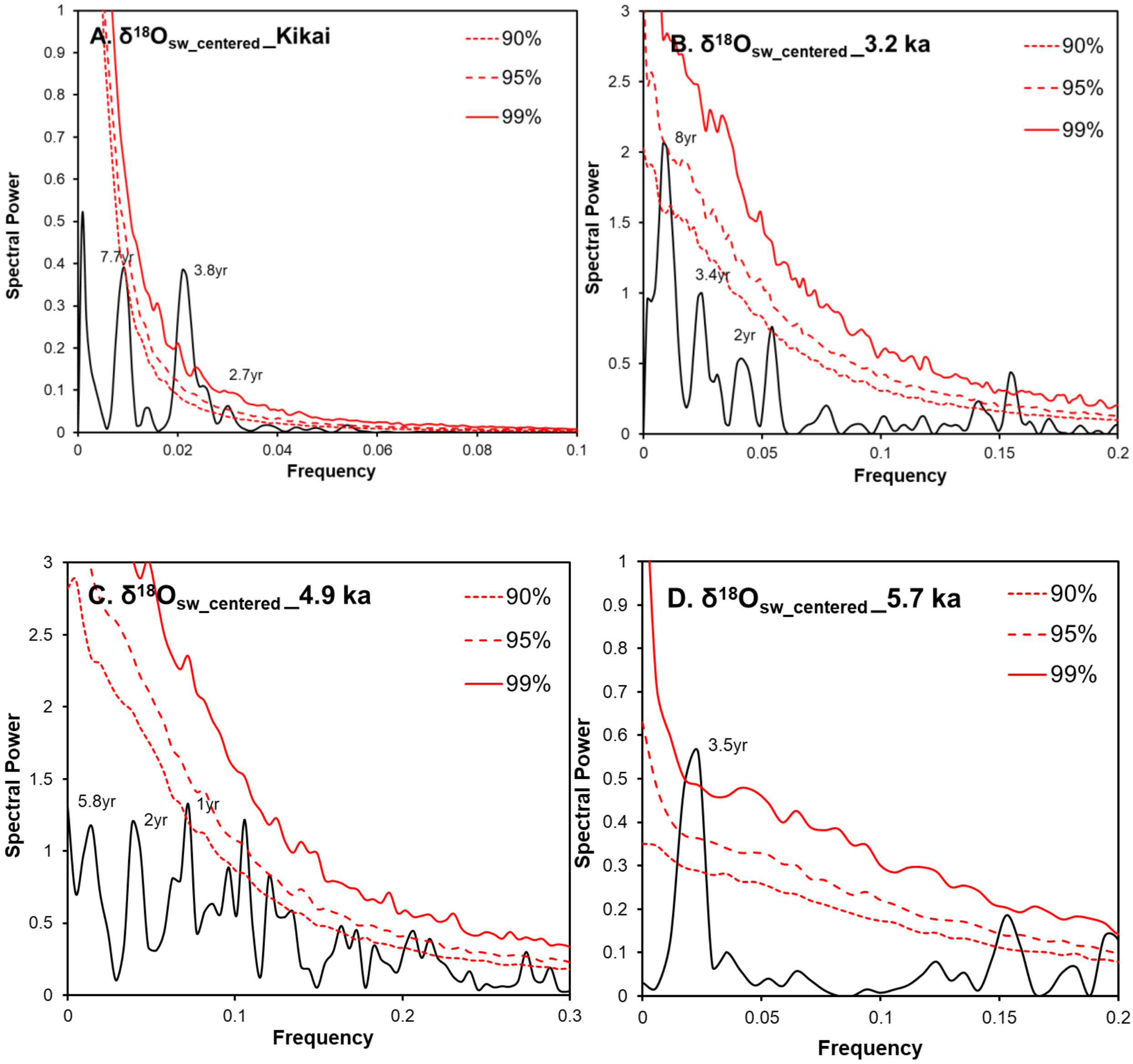

Figure 68. Spectral analysis using REDFIT method of the $\delta^{18}O_{sw}$ of (a) modern coral, (b) 3.2 ka coral, (c) 4.9 ka coral, and (d) 5.7 ka coral. The red noise spectra were tested for statistical significance of the 90%, 95%, and 99% percentiles in Monte Carlo simulations

Using the seasonally resolved $\delta^{18}O_{sw}$ records, the rainfall-driven SSS changes were examined during neutral and El Niño years in 20th century (1989 – 2015; 2011-2017) and mid-Holocene. The mean seasonal climatology of neutral and strong El Niño years from the 2 – 8-year bandpass filtered $\delta^{18}O_{sw}$ were calculated. The difference of $\delta^{18}O_{sw}$ of summer monsoon months (JJA-SON) during neutral and El Niño years was interpreted as the rainfall-driven SSS difference. The anticyclonic wind anomalies in high latitude North Pacific develop in the late fall of the El Niño developing year, resulting in a weak EAWM. This anomalous anticyclone persists until the early spring to summer of the following year bringing higher rainfall in the southern China and Japan. Furthermore, the response of the EASM to the El Niño is highly dependent on the phase timing. The rainfall in China, Korea, Japan (collectively known as East Asian winter front zone (EAFZ)) tends to decrease in the El Niño developing summer but tends to increase in the El Niño decaying summer after the mature phase in winter (Wang et al. 2020).

The mean seasonal climatology of neutral and El Niño years from the 2 – 8-year bandpass filtered $\delta^{18}O_{sw}$ of Kikai modern coral, 3.2 ka, 4.9 ka, and 5.7 ka were presented in Fig. 69a-d. The summer $\delta^{18}O_{sw}$ of the neutral years from 1989 to 2015 was 0.38‰ and the summer $\delta^{18}O_{sw}$ of the El Niño years was 0.57‰ (Fig. 69a). The increase of $\delta^{18}O_{sw}$ reflects the decrease in rainfall of the summer of decaying El Niño year. The 3.2 ka, 4.9 ka, and 5.7 ka corals show no significant difference between the summer $\delta^{18}O_{sw}$ of the neutral and El Niño years.

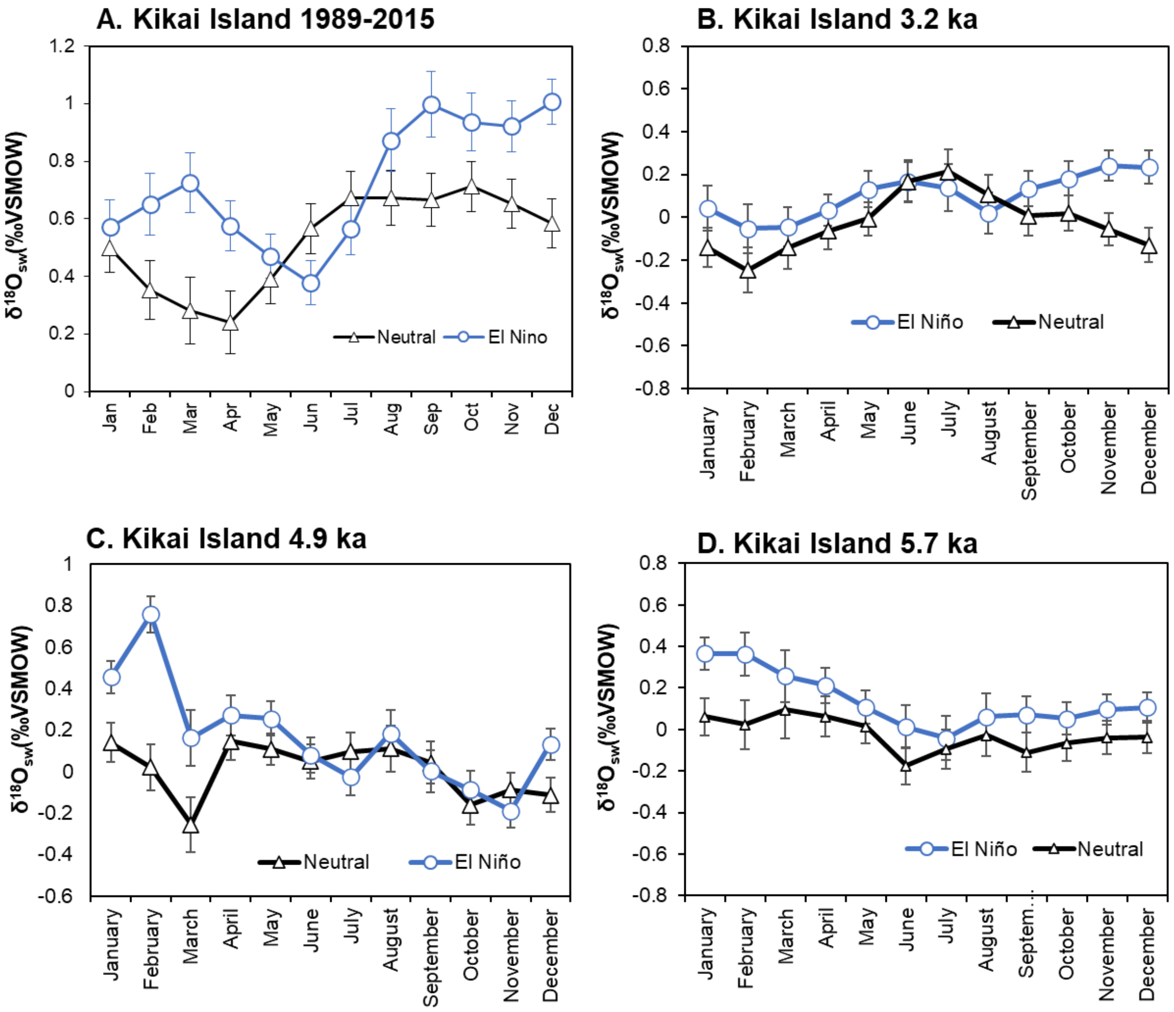

Figure 69. The mean seasonal climatology of neutral (black) and El Niño (blue) years from the 2 – 8-year bandpass filtered $\delta^{18}O_{sw}$ of (a) Kikai modern coral 1989-2015, (b) 3.2 ka, (c) 4.9 ka, and (d) 5.7 ka

The main question of this dissertation is whether modern and fossil corals from subtropical and tropical NW Pacific particularly from Southern Japan and Northern Philippines, can reconstruct the seasonal response of monsoon rainfall to the interannual variability of ENSO. Modern climate data shows that the rainfall response to El Niño phase in subtropical NW Pacific is different from tropical NW Pacific. Figure 70 demonstrates the rainfall anomaly during the 1997-1998 ENSO-El Niño phase from the 1995-1996 ENSO-neutral phase. The anomaly map shows a maximum 3mm/day precipitation increase in Taiwan, Japan, and Korea while there was a maximum 3mm/day precipitation decrease in mainland Southeast Asia, Philippines, and Indonesia. The rainfall in Southern Japan tends to increase in the El Niño decaying summer after the mature phase in winter. The anticyclonic wind anomaly in the North Pacific in winter suppresses the northeasterly winter monsoon, which increases the summer rainfall of the El Niño decaying year. In contrast, the anticyclonic wind circulation develops over the Philippine Sea weakens the southwesterly summer monsoon circulation, which decreases the summer rainfall in the Philippines.

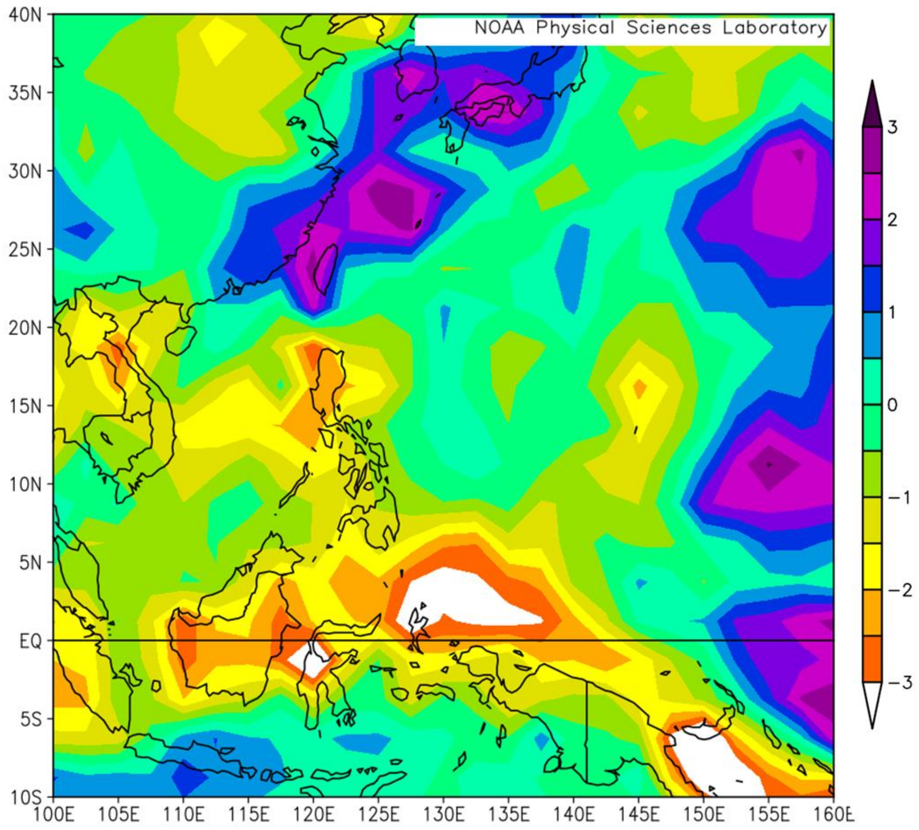

Figure 70. The rainfall anomaly map of 1997-1998 El Niño relative to the 1995-1996 neutral phase showing distinct variation in rainfall response in subtropical and tropical NW Pacific.

The coral evidence also shows that the response of geochemical proxies to ENSO-related hydroclimate variabilities is different in subtropical and tropical NW Pacific. In Figures 63a and 63b, the monthly climatology of $\delta^{18}O_{sw}$ from NE Luzon and NW Luzon corals revealed a general decrease in rainfall during El Niño relative to neutral years. In Kikai Island, seasonal rainfall becomes more pronounced during El Niño phase with reduced rainfall (more positive $\delta^{18}O_{sw}$) during the developing stage and enhanced rainfall (more negative $\delta^{18}O_{sw}$) in the succeeding summer (Fig. 69a). This is consistent with modern-day climatological observations as shown by Fig. 70.

Paleo-ENSO works using modern and fossil corals from Pacific revealed that the ENSO variability was reduced over the past 8000 years relative to the 20th century ENSO (Tudhope et al. 2001; McGregor and Gagan 2004; Cobb et al. 2013; Grothe et al. 2019). These studies used the interannual variability of $\delta^{18}O_{coral}$ to demonstrate past SST changes in ENSO-impacted localities. Interannual variance from the coral $\delta^{18}O$ from Pacific was reduced by -37% at 5.0 to 7.0 ka, -49% at 3.0 to 5.0 ka, and -30% at 0 to 2.0 ka relative at 1987-2007 benchmark. To check the ENSO impacts to the NW Pacific hydroclimate, interannual variance was also calculated from the $\delta^{18}O_{sw}$ of fossil corals. The change of standard deviation of the 2-8 yr bandpass filtered $\delta^{18}O_{sw}$ relative the modern coral record was calculated. The calculation was benchmarked from the 1989 to 2015 coral record for Kikai Island fossil corals and from the 2011 to 2017 coral record for NW Luzon fossil corals. This calculation method was adapted from Cobb et al. 2013. A modified calculation from the method of Grothe et al. 2019 was also applied. The annual climate signals were further removed from 2-8 yr bandpass filtered $\delta^{18}O_{sw}$ by applying a 13-month moving averaging. After that, the change of standard deviation was computed by benchmarking with the modern coral records of the 2 sites. The summary of the interannual variance of NW Pacific fossil corals is presented in Table 7.

Figure 69b and 69d revealed that there was no significant difference between the seasonal $\delta^{18}O_{sw}$ of El Niño and neutral phase in Kikai Island at 3.2 ka and 5.7 ka. These time windows recorded a -28% and -49% ENSO reduction. In contrast, the 4.9 ka coral shows an increase in rainfall during c considering that there was an estimated -11% ENSO reduction. We can conclude that the intensity of the ENSO variance affects the strength of ENSO impact to the subtropical rainfall. Weaker ENSO had little to no significant effect on the seasonal rainfall pattern during the last 7000 years. However, this generalization is not necessarily true for NW Luzon Island corals.

The 4.2 ka and 4.3 ka corals (Fig.63c;63d) revealed a -50% and -20% ENSO reduction based on the analysis of the interannual variance. Both fossil corals show a decrease in rainfall during El Niño relative to neutral phase. The estimated ENSO reduction at 6.1 ka was 30% relative to 2011 to 2017 benchmark. During the time window, there was no significant difference between the seasonal $\delta^{18}O_{sw}$ of El Niño and neutral phase in NW Luzon Island (Fig. 63e). What could be the reason for the different seasonality pattern of $\delta^{18}O_{sw}$ under the same reduced ENSO variance condition? We have to look at the background climate in the NW Luzon during these time windows. The 4.2 ka and 4.3 ka were periods of weak EASM monsoon which was characterized by reduced low-level tropospheric wind circulation from the tropical SCS to subtropical NW Pacific and southward migration of the ITCZ. Because the summer monsoon was weak in 4.2 ka and 4.3 ka, the ENSO effect to the seasonal rainfall was more evident, thus, significant change was reflected on the $\delta^{18}O_{sw}$ from corals. In contrast, the 6.1 ka occurred during the peak of EASM intensity, which was defined by enhanced low-level tropospheric wind circulation from the tropical SCS to subtropical NW Pacific and northward migration of the ITCZ. The effect of the stronger monsoon could have possibly masked the climatic and oceanographic effect of ENSO on the seasonal hydroclimate of NW Luzon, hence, the seasonal $\delta^{18}O_{sw}$ was not significantly different between the El Niño and neutral phase.

Table. 7. Interannual variance of $\delta^{18}O_{sw}$ records from Holocene corals of NW Pacific (Kikai Island and NW Luzon Island)

Age **(year BP)**	**$\delta^{18}O_{sw}$ variance (%)** Modified from Grothe et al. 2019	**$\delta^{18}O_{sw}$ variance (%)** Cobb et al. 2013
3235	-28.3	-27.7
4200	-50.4	-45.5
4336	-20.2	-18.2
4960	-11.1	-11.4
5712	-49.1	-48.5
6144	-31.9	-28.5

Chapter 6

Synthesis and Future Research Prospects

6.1. Coral-based Reconstruction of ITCZ Migration in Holocene

The minimum $\delta^{18}O_{coral}$ records from fossil *Porites* in Kikai Island and Okinawa Island in Southern Japan (Fig. 70a; Kiyama et al. 2000; Abram et al. 2001; Morimoto et al. 2007; Asami et al. 2020) were compiled to reconstruct the SSS change in subtropical NW Pacific from mid- to late Holocene. There was a steady decrease of minimum (summer) $\delta^{18}O_{coral}$ values from ~7.0 ka to ~3.5 ka centered around 5.0 ka suggesting an increasing SSS trend from mid- to late Holocene. The minimum $\delta^{18}O_{coral}$ records from fossil *Porites* in NW Luzon Island, Philippines (Fig. 70b; This study; Yokoyama et al. 2011), Hainan Island (Wei et al. 2007; Su et al. 2010; Guo et al. 2016) and Leizhou Peninsula, China (Yu et al. 2005), and Taiwan (Shen et al. 2005) show a negative shift in the minimum (summer) $\delta^{18}O_{coral}$ values from -6.0‰ (6.7 ka to 4.4 ka) to -6.6‰ (4.3 ka to 4.2 ka) indicating a decreasing SSS in mid Holocene in tropical NW Pacific.

The $\delta^{18}O_{coral}$ records from the subtropics follow the same increasing trend of the $\delta^{18}O$ record from Chinese speleothems (Fig. 70c; Dong et al. 2018; Cosford et al. 2008; Dykoski et al. 2005). The $\delta^{18}O$ values of spleotherm is often interpreted as the amount weighted $\delta^{18}O$ of precipitation. The increasing $\delta^{18}O$ values in spleotherm could possibly indicate the enrichment and reduction of ^{16}O in meteoric precipitaiton incorporated speleothem carbonates as a function of the increase or decrease of rainfall. However, the paleoclimate interpretation of speleothem $\delta^{18}O$ is subject to debate since this archive is often linked to moisture sourcing rather than amount-weighted $\delta^{18}O$ of precipitation (Maher 2008; Dayem et al. 2010; Pausatta et al. 2011). The reduced SSS trend in $\delta^{18}O_{coral}$ records covaries with the increased rainfall in $\delta^{18}O$ record from Chinese speleothems in mid-Holocene. The increased rainfall from 7.0 ka to 5.0 ka also correlates with paleo-lake level reconstruction and rainfall modelling in Lake Dali, Northern China (Goldsmith et al. 2017). This evidence suggests that the rainfall extent exceeded the present-day northern limit of summer rainfall about 5000 to 7000 years ago. The ITCZ primarily defines the extent of tropical rainbelt (Schneider et al. 2014). Aside from the mean latitudinal position of the ITCZ, the rainfall extent in East and Southeast Asia is also influenced by the intensity of EA summer monsoon. The lower SSS and higher rainfall in subtropical NW Pacific were coeval to the higher SSS and lower rainfall in tropical NW Pacific. The higher SSS in tropical NW Pacific is indicated by $\delta^{18}O_{coral}$ records from 6.7 ka to 4.4 ka. This is correlated with the increasing rainfall based on the decreasing $\delta^{18}O$ values of speleothem record from Northern Borneo (Fig. 70e; Partin et al. 2007).

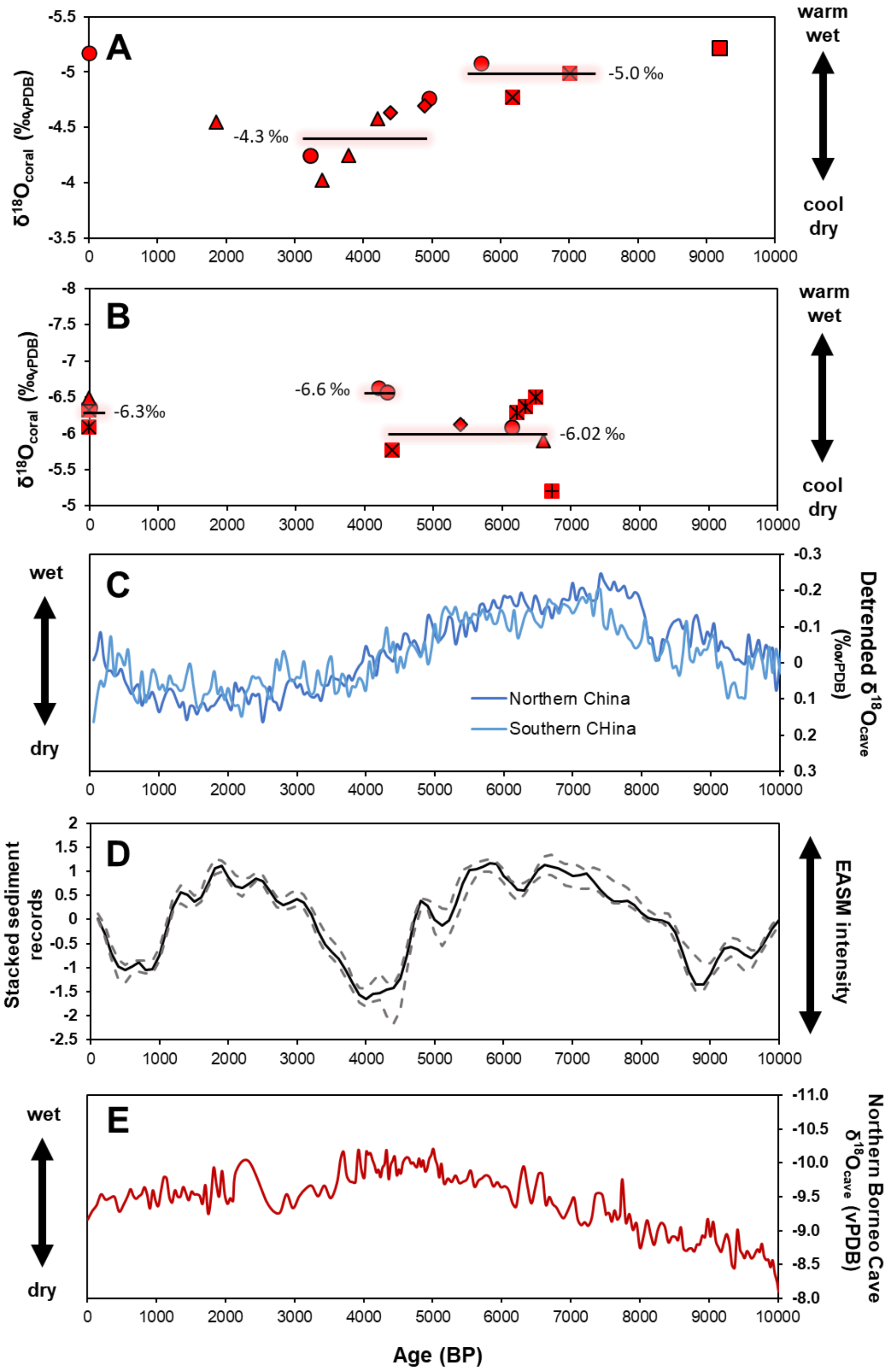

Figure 71. A. Minimum $\delta^{18}O_{coral}$ from fossil Porites in Kikai Island and Okinawa Island in Southern Japan B. Minimum $\delta^{18}O_{coral}$ from fossil Porites in NW Luzon Island, Philippines, Hainan Island and Leizhou Peninsula, China, and Taiwan C. Speleothem $\delta^{18}O$ from several stalagmite deposits from northern and southern China D. Stacked sediment records from marine and terrestrial cores showing the variation of EASM intensity in Holocene E. Speleothem $\delta^{18}O$ from northen Borneo

The SSS trend of subtropical NW Pacific shifted positively after 4.9 ka while the SSS trend in tropical NW Pacific shifted negatively around 4.3 to 4.2 ka. The rainfall trends from speleothem $\delta^{18}O$ from China and Northern Borneo follow the SSS trends of subtropical and tropical NW Pacific respectively. Our coral evidence from southern Japan supports the widely reported EASM intensification (8.2 ka to 4.7 ka) and weakening (4.7 ka to 3.0 ka) based on the stacked marine and terrestrial sediment records from NW Pacific (Fig. 70d; Kaboth-Bahr et al. 2021). This dissertation supports the north-south migration of the ITCZ previously documented by other paleoclimate/paleo-rainfall records (Haug et.al. 2001; Brocolli et. al. 2006; Sachs et.al. 2018). The northward ITCZ migration and intensification of EASM resulted in the enhancement of summer rainfall in the subtropics while the rainfall in tropical NW Pacific was reduced in mid-Holocene. The southward migration of the ITCZ and weakening of the EASM resulted in the aridification of East Asia and reduced rainfall/higher SSS of subtropical NW Pacific. The southerly position of the ITCZ brought more rainfall in tropical NW Pacific. External forcing from the tropical western Pacific SST may have influenced the weakened monsoon rainfall in the late Holocene. NCAR Community Atmospheric Model 3.5 (NCAR CAM3.5) simulation results suggest that the weak meridional land-sea thermal contrasts in western Pacific contribute to the weaker monsoon circulation in tropical and subtropical East Asian domains (Chen et.al. 2010). Reduced summer heating as indicated by seasonal-scale coral SST after the mid- to late Holocene transition could have resulted in lesser rainfall in extratropical East Asia.

6.2. East Asian Monsoon and ENSO Interaction

This dissertation proposes an alternative way to investigate ENSO impacts to rainfall and SSS changes in NW Pacific and to establish the teleconnections of Pacific/NINO3.4 SSTA and NW Pacific hydroclimate. NW Luzon and Kikai Island corals can effectively track hydroclimatic changes due to the interannual ENSO changes. ENSO variability detected in coral-derived $\delta^{18}O_{sw}$ from Kikai Island and NW Luzon Island revealed -11% to -50% reduction around 3000 to 6000 years ago. Coral records from NW Pacific were able to demonstrate the effect of the reduced ENSO variance to seasonal rainfall trend by isolating the monthly climatology of $\delta^{18}O_{sw}$ during El Niño and Neutral phase.

The new coral data from NW Pacific agree to the mid-Holocene reduction of ENSO variabilities as suggested by previous studies. A weak El Niño condition prevailed during mid-Holocene coeval to the strengthened West Pacific Subtropical High (Fig. 72). The enhanced eastward flow of Pacific equatorial trade winds resulted in the expansion of meridional scale of ENSO/NINO region, weakened the thermocline, and then the ENSO amplitude (Tian et al. 2017). However, the connection between the ENS) variability, WPSH/monsoon intensity is not yet established. Nevertheless, the different response of subtropics and tropics reconstructed from corals will help climatologists to understand the localized impact of ENSO to East Asian monsoon domain. It will further improve the input parameters in ENSO and monsoon-related climate models by considering local responses.

6.3. Future Research Prospects: ITCZ, IPWP and the East/Southeast Asian civilizations

Coral geochemical records can provide us insight on the role of ITCZ and ENSO on the overall hydroclimate of the EA monsoon domain in NW Pacific. The ITCZ typically migrates towards a warming hemisphere as an atmospheric energy balance response to the ocean heat transport mechanism. It influences the precipitation and latent heat transport in tropics and extratropics. The expansion/contraction of the Indo-Pacific Warm Pool (IPWP) in the Holocene could have been a determining factor in the past mean latitudinal position of the ITCZ. Abram et al. (2009) demonstrated the how IPWP expanded and contracted using multiple, short coral Sr/Ca-SST records from Indonesia and Papua New Guinea. The strategy is applicable to Holocene corals from NW Luzon Island, Philippines and Kikai Island to show the spatiotemporal changes in the northern limit of the IPWP during the Holocene. Quantifying the relationship of interhemispheric SST gradient and magnitude of ITCZ migration offset will improve our understanding of the mechanism over seasonal to millennial timescales.

Several archaeological studies associated the decline of East Asian civilization to past climate changes, but the mechanism is still unclear. Coral-based evidence can show the direct link of seasonal hydroclimate variations to these historical events. The retreat of EASM rainfall and southward migration of ITCZ resulted in limited water supply for rice cultivation and vegetation in East and Southeast Asia. If we can reconstruct the past position of the ITCZ, we can possibly also track past societal migration link to collapse and development of civilizations. In the present-day, fast accumulation rate of greenhouse gas could alter atmospheric energy flux while continuously warming ocean could trigger changes in ocean heat transport via ocean circulation. Therefore, the present climate change will impact the ITCZ migration in the cross-equatorial region as well as hydroclimate of different monsoon domains. Ultimately, this information can be used vis a vis socio-economic database to identify the most vulnerable communities due to climate change.

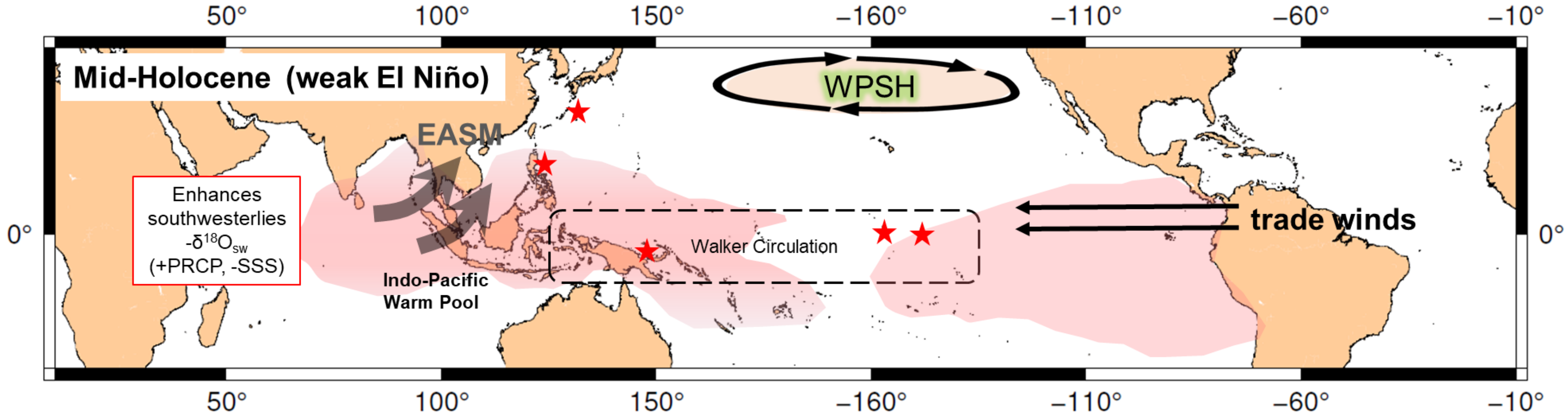

Figure 72. The strong WPSH increased the eastward flow of Pacific equatorial trade winds resulted in wide meridional scale of ENSO/NINO region, weakened the thermocline, and then reduced ENSO amplitude. This condition defines a weak El Niño phase during the mid-Holocene.

References:

1. Abram, N., Webster, J., Davies, P., & Dullo, W. (2001). Biological response of coral reefs to sea surface temperature variation: evidence from the raised Holocene reefs of Kikai-jima (Ryukyu Islands, Japan). *Coral Reefs*, *20*(3), 221-234.

2. Abram, N. J., McGregor, H. V., Gagan, M. K., Hantoro, W. S., & Suwargadi, B. W. (2009). Oscillations in the southern extent of the Indo-Pacific Warm Pool during the mid-Holocene. Quaternary Science Reviews, 28(25-26), 2794-2803.

3. An, C. B., Tang, L., Barton, L., & Chen, F. H. (2005). Climate change and cultural response around 4000 cal yr BP in the western part of Chinese Loess Plateau. Quaternary Research, 63(3), 347-352.

4. Asami, R., Yoshimura, N., Toriyabe, H., Minei, S., Shinjo, R., Hongo, C., Sakamaki, T. and Fujita, K., 2020. High-resolution evidence for middle Holocene East Asian winter and summer monsoon variations: Snapshots of fossil coral records. *Geophysical Research Letters*, *47*(16), p.e2020GL088509.

5. Aurelio, M. A. (2000). Shear partitioning in the Philippines: constraints from Philippine Fault and global positioning system data. Island Arc, 9(4), 584-597.

6. Barnes, D. J., & Lough, J. M. (1989). The nature of skeletal density banding in scleractinian corals: fine banding and seasonal patterns. Journal of Experimental Marine Biology and Ecology, 126(2), 119-134. DOI:10.1016/0022-0981(89)90084-1

7. Barnes, D. J., & Lough, J. M. (1993). On the nature and causes of density banding in massive coral skeletons. Journal of Experimental Marine Biology and Ecology, 167(1), 91-108. DOI:10.1016/0022-0981(93)90186-R

8. Beck, J.W., Edwards, R.L., Ito, E., Taylor, F.W., Recy, J., Rougerie, F., Joanot, P., Henin, C. (1992) Sea Surface Temperature from Coral Strontium/Calcium Ratios. Science Vol 257 pp 644-647

9. Bingham, F. M., Foltz, G. R., & McPhaden, M. J. (2012). Characteristics of the seasonal cycle of surface layer salinity in the global ocean. Ocean Science, 8(5), 915-929.

10. Bolton, A., Goodkin, N. F., Hughen, K., Ostermann, D. R., Vo, S. T., & Phan, H. K. (2014). Paired Porites coral Sr/Ca and δ18O from the western South China Sea: Proxy calibration of sea surface temperature and precipitation. *Palaeogeography, Palaeoclimatology, Palaeoecology*, *410*, 233-243.

11. Broccoli, A. J. Dahl, K. A. & Stouffer, R. J. Response of the ITCZ to Northern Hemisphere cooling. Geophys. Res. Lett. 33, L01702 (2006).

12. Buddemeier,R. W., Maragos, J. E., & Knutson, D. W. (1974). Radiographic studies of reef coral exoskeletons: rates and patterns of coral growth. Journal of Experimental Marine Biology and Ecology, 14(2), 179-199. DOI:10.1016/0022-0981(74)90024-0

13. Cabioch, G., Montaggioni, l. F., Faure, G., & Ribaud-Laurenti, A. (1999). Reef coralgal assemblages as recorders of paleobathymetry and sea level changes in the Indo-Pacific province. Quaternary Science Reviews, 18(14), 1681-1695. DOI: 10.1016/S0277-3791(99)00014-1

14. Cahyarini, S. Y., Pfeiffer, M., Timm, O., Dullo, W. C., & Schönberg, D. G. (2008). Reconstructing seawater δ18O from paired coral δ18O and Sr/Ca ratios: Methods, error analysis and problems, with

examples from Tahiti (French Polynesia) and Timor (Indonesia). Geochimica et Cosmochimica Acta, 72(12), 2841-2853.

15. Chen, T. C., Wang, S. Y., Huang, W. R., & Yen, M. C. (2004). Variation of the East Asian summer monsoon rainfall. Journal of Climate, 17, 744-762

16. Chen, H., Zhou, T., Neale, R. B., Wu, X., & Zhang, G. J. (2010). Performance of the new NCAR CAM3. 5 in East Asian summer monsoon simulations: Sensitivity to modifications of the convection scheme. Journal of Climate, 23(13), 3657-3675.

17. Chen, W., Feng, J., & Wu, R. (2013). Roles of ENSO and PDO in the link of the East Asian winter monsoon to the following summer monsoon. Journal of Climate, 26(2), 622-635.

18. Chevuturi, A., Klingaman, N. P., Turner, A. G., Guo, L., & Vidale, P. L. (2022). Projected changes in the East Asian hydrological cycle for different levels of future global warming. Atmosphere, 13(3), 405.

19. Cobb, K.M., Westphal, N., Sayani, H.R., Watson, J.T., Di Lorenzo, E., Cheng, H., Edwards, R.L. and Charles, C.D., 2013. Highly variable El Niño–southern oscillation throughout the Holocene. *Science*, *339*(6115), pp.67-70.

20. Cohen, A. L., & Gaetani, G. A. (2010). Ion partitioning and the geochemistry of coral skeletons: solving the mystery of the vital effect. EMU Notes Mineral, 11, 377-397.

21. Conroy, J. L., Noone, D., Cobb, K. M., Moerman, J. W., & Konecky, B. L. (2016). Paired stable isotopologues in precipitation and vapor: A case study of the amount effect within western tropical Pacific storms. *Journal of Geophysical Research: Atmospheres*, *121*(7), 3290-3303.

22. Conroy, J. L., Thompson, D. M., Cobb, K. M., Noone, D., Rea, S., & Legrande, A. N. (2017). Spatiotemporal variability in the δ18O-salinity relationship of seawater across the tropical Pacific Ocean. *Paleoceanography*, *32*(5), 484-497.

23. Corrège, T. (2006). Sea surface temperature and salinity reconstruction from coral geochemical tracers. Palaeogeography, Palaeoclimatology, Palaeoecology, 232(2-4), 408-428. DOI: 10.1016/j.palaeo.2005.10.014

24. Cosford, J., Qing, H., Eglington, B., Mattey, D., Yuan, D., Zhang, M., & Cheng, H. (2008). East Asian monsoon variability since the Mid-Holocene recorded in a high-resolution, absolute-dated aragonite speleothem from eastern China. Earth and Planetary Science Letters, 275(3-4), 296-307.

25. Crabbe, M. J. C., & Smith, D. J. (2005). Sediment impacts on growth rates of Acropora and Porites corals from fringing reefs of Sulawesi, Indonesia. Coral reefs, 24(3), 437-441. DOI: 10.1007/s00338-005-0004-6

26. Cuevas, D. N., Sherman, C. E., Ramírez, W., & Hubbard, D. K. (2009). Coral growth rates from the Holocene Cañada Honda fossil reef, Southwestern Dominican Republic: Comparisons with modern counterparts in high sedimentation settings. Caribbean Journal of Science, 45(1), 94-109. DOI:10.18475/cjos.v45i1.a13

27. Dayem, K. E., Molnar, P., Battisti, D. S., & Roe, G. H. (2010). Lessons learned from oxygen isotopes in modern precipitation applied to interpretation of speleothem records of paleoclimate from eastern Asia. Earth and Planetary Science Letters, 295(1-2), 219-230.

28. Deng, W. F., Wei, G. J., Li, X. H., Yu, K. F., Zhao, J. X., Sun, W. D., & Liu, Y. (2009). Paleoprecipitation record from coral Sr/Ca and δ18O during the mid Holocene in the northern South China Sea. The Holocene, 19(6), 811-821.

29. Dizon, R. M., & Yap, H. T. (2005). Coral responses in single-and mixed-species plots to nutrient disturbance. Marine Ecology Progress Series, 296, 165-172. DOI: 10.3354/meps296165

30. Dodge,R. E., & Vaisnys, J. R. (1977). Coral populations and growth patterns: responses to sedimentation and turbidity associated with dredging. Journal of Marine Research, 35(4), 715.

31. Dong, J., Shen, C. C., Kong, X., Wu, C. C., Hu, H. M., Ren, H., & Wang, Y. (2018). Rapid retreat of the East Asian summer monsoon in the middle Holocene and a millennial weak monsoon interval at 9 ka in northern China. Journal of Asian Earth Sciences, 151, 31-39.

32. Dunbar, R.B., Wellington, G.M., Colgan, M.W., Glynn, P.W. (1994) East Pacific sea surface temperature since 1600 AD: The δ18O record of climate variability in Galapagos Island. Paleoceanography Vol 9 No. 2 pp 291-315

33. Dykoski, C. A., Edwards, R. L., Cheng, H., Yuan, D., Cai, Y., Zhang, M., ... & Revenaugh, J. (2005). A high-resolution, absolute-dated Holocene and deglacial Asian monsoon record from Dongge Cave, China. Earth and Planetary Science Letters, 233(1-2), 71-86.

34. Epstein S. R., Buchsbaum H. A., Lowenstam H., and Urey H. C. (1951) Carbonate-water isotopic temperature scale. Bull. Geol. Soc. Am. 64, 417–426.

35. Friedman, I., O'NEIL, J., & Cebula, G. (1982). Two new carbonate stable ‐ isotope standards. Geostandards Newsletter, 6(1), 11-12.

36. Gaetani, G. A., & Cohen, A. L. (2006). Element partitioning during precipitation of aragonite from seawater: a framework for understanding paleoproxies. Geochimica et cosmochimica acta, 70(18), 4617-4634.

37. Gagan, M. K., Ayliffe, L. K., Hopley, D., Cali, J. A., Mortimer, G. E., Chappell, J., ... & Head, M. J. (1998). Temperature and surface-ocean water balance of the mid-Holocene tropical western Pacific. Science, 279(5353), 1014-1018.

38. Gagan, M. K., Ayliffe, L. K., Beck, J. W., Cole, J. E., Druffel, E. R. M., Dunbar, R. B., & Schrag, D. P. (2000). New views of tropical paleoclimates from corals. Quaternary Science Reviews, 19(1-5), 45-64.

39. Goldsmith, Y., Broecker, W.S., Xu, H., Polissar, P.J., Demenocal, P.B., Porat, N., Lan, J., Cheng, P., Zhou, W. and An, Z., (2017). Northward extent of East Asian monsoon covaries with intensity on orbital and millennial timescales, Proceedings of the National Academy of Sciences, v.114(8), pp.1817-1821, doi.org/10.1073/pnas.1616708114

40. Goodkin, N.F., Switzer, A.D., Mccorry, D., Devantier, l., True, J.D., Hughen, K.A., Angeline, N. and Yang, T.T. (2011). Coral communities of Hong Kong: long-lived corals in a marginal reef environment. Marine Ecology Progress Series, 426, 185-196. DOI:10.3354/meps09019

41. Griffiths, M. L. et. al. Increasing Australian–Indonesian monsoon rainfall linked to early Holocene sea-level rise. *Nat. Geosci.* 2, 636-639 (2009).

42. Grigg, R. W. (1981). Coral reef development at high latitudes in Hawaii. In Proc 4th Int Coral Reef Symp Vol. 1, pp. 687-693.

43. Grothe, P. R., Cobb, K. M., Liguori, G., Di Lorenzo, E., Capotondi, A., Lu, Y., t al. (2019). Enhanced El Niño Southern oscillation variability in recent decades. Geophysical Research Letters, 46, e2019GL083906. https://doi.org/10.1029/2019GL083906

44. Guo, Y., Deng, W., Chen, X., Wei, G., Yu, K., & Zhao, J. X. (2016). Saltier sea surface water conditions recorded by multiple mid-Holocene corals in the northern South China Sea. *Journal of Geophysical Research: Oceans*, *121*(8), 6323-6330.

45. Hathorne, E.C., Gagnon, A., Felis, T., Adkins, J., Asami, R., Boer, W., Caillon, N., Case, D., Cobb, K.M., Douville, E. and Demenocal, P., 2013. Interlaboratory study for coral Sr/Ca and other element/Ca ratio measurements. Geochemistry, Geophysics, Geosystems, 14(9), pp.3730-3750.

46. Haug, G. H. Hughen, K. A. Sigman, D. M. Peterson, L. C. & Röhl, U. Southward migration of the intertropical convergence zone through the Holocene. Science 293, 1304-1308 (2001).

47. Hayashi, E., Suzuki, A., Nakamura, T., Iwase, A., Ishimura, T., Iguchi, A., ... & Kawahata, H. (2013). Growth-rate influences on coral climate proxies tested by a multiple colony culture experiment. Earth and Planetary Science Letters, 362, 198-206. DOI: 0.1016/j.epsl.2012.11.046

48. Helm, K. P., Bindoff, N. L., & Church, J. A. (2010). Changes in the global hydrological-cycle inferred from ocean salinity. Geophysical Research Letters, 37(18).

49. Hendy, E. J., M. K. Gagan, J. M. Lough, Malcolm McCulloch, and P. B. DeMenocal. "Impact of skeletal dissolution and secondary aragonite on trace element and isotopic climate proxies in Porites corals." Paleoceanography 22, no. 4 (2007).

50. Hongo, C., & Kayanne, H. (2010). Holocene sea-level record from corals: Reliability of paleodepth indicators at Ishigaki Island, Ryukyu Islands, Japan. Palaeogeography, Palaeoclimatology, Palaeoecology, 287(1-4), 143-151. DOI: 10.1016/j.palaeo.2010.01.033

51. Hori, M. E., & Ueda, H. (2006). Impact of global warming on the East Asian winter monsoon as revealed by nine coupled atmosphere ‐ ocean GCMs. Geophysical Research Letters, 33(3).

52. Huang, B., Banzon, V.F., Freeman, E., Lawrimore, J., Liu, W., Peterson, T.C., Smith, T.M., Thorne, P.W., Woodruff, S.D. and Zhang, H.M., 2015. Extended reconstructed sea surface temperature version 4 (ERSST. v4). Part I: Upgrades and intercomparisons. *Journal of climate*, *28*(3), pp.911-930.

53. Huang, Z., Zhang, W., Geng, X., & Jin, F. F. (2020). Recent shift in the state of the western Pacific subtropical high due to ENSO change. Journal of Climate, 33(1), 229-241.

54. Hubbard, Camden R., and Robert L. Snyder. "RIR-measurement and use in quantitative XRD." Powder Diffraction 3, no. 2 (1988): 74-77.

55. James, N. P. (1974). Diagenesis of scleractinian corals in the subaerial vadose environment. Journal of Paleontology, 785-799.

56. Jeong, J. H., Ou, T., Linderholm, H. W., Kim, B. M., Kim, S. J., Kug, J. S., & Chen, D. (2011). Recent recovery of the Siberian High intensity. Journal of Geophysical Research: Atmospheres, 116(D23).

57. Jhun, J. G., & Lee, E. J. (2004). A new East Asian winter monsoon index and associated characteristics of the winter monsoon. Journal of Climate, 17(4), 711-726.

58. Jiang, D., Lang, X., Tian, Z., & Ju, L. (2013). Mid-Holocene East Asian summer monsoon strengthening: Insights from Paleoclimate Modeling Intercomparison Project (PMIP) simulations. Palaeogeography, Palaeoclimatology, Palaeoecology, 369, 422-429.

59. Juillet‐Leclerc, A., & Schmidt, G. (2001). A calibration of the oxygen isotope paleothermometer of coral aragonite from Porites. Geophysical Research Letters, 28(21), 4135-4138.

60. Juillet-Leclerc, A., Reynaud, S., Dissard, D., Tisserand, G., & Ferrier-Pagès, C. (2014). Light is an active contributor to the vital effects of coral skeleton proxies. Geochimica et Cosmochimica Acta, 140, 671-690. DOI: 0.1016/j.gca.2014.05.042

61. Kaboth-Bahr, S., Bahr, A., Zeeden, C., Yamoah, K.A., Lone, M.A., Chuang, C.K., Löwemark, L. and Wei, K.Y., 2021. A tale of shifting relations: East Asian summer and winter monsoon variability during the Holocene. *Scientific Reports*, *11*(1), pp.1-10.

62. Kajita, H., Yamazaki, A., Watanabe, T., Wu, C. C., Shen, C. C., & Watanabe, T. (2017). Holocene sea surface temperature variations recorded in corals from Kikai Island, Japan. *Geochemical Journal*, *51*(4), e9-e14.

63. Kajita, H., Kawahata, H., Wang, K., Zheng, H., Yang, S., Ohkouchi, N., ... & Zheng, B. (2018). Extraordinary cold episodes during the mid-Holocene in the Yangtze delta: Interruption of the earliest rice cultivating civilization. Quaternary Science Reviews, 201, 418-428.

64. Katz, A. M. I. T. A. I., Sass, E., Starinsky, A., & Holland, H. D. (1972). Strontium behavior in the aragonite-calcite transformation: An experimental study at 40–98 C. Geochimica et Cosmochimica Acta, 36(4), 481-496.

65. Kawahata, H., Yamamoto, H., Ohkushi, K. I., Yokoyama, Y., Kimoto, K., Ohshima, H., & Matsuzaki, H. (2009). Changes of environments and human activity at the Sannai-Maruyama ruins in Japan during the mid-Holocene Hypsithermal climatic interval. Quaternary Science Reviews, 28(9), 964-974.

66. Kawakubo, Y., Alibert, C., & Yokoyama, Y. (2017). A reconstruction of subtropical western North Pacific SST variability back to 1578, based on a Porites Coral Sr/Ca record from the northern Ryukyus, Japan. Paleoceanography, 32(12), 1352-1370.

67. Kim, J. W., An, S. I., Jun, S. Y., Park, H. J., & Yeh, S. W. (2017). ENSO and East Asian winter monsoon relationship modulation associated with the anomalous northwest Pacific anticyclone. Climate Dynamics, 49, 1157-1179.

68. Kiyama, O., Yamada, T., Nakamori, T., & Iryu, Y. (2000). Early Holocene coral δ18O-based sea surface temperature. *The Quaternary Research (Daiyonki-Kenkyu)*, *39*(1), 69-80.

69. Kinsman, D. J., & Holland, H. D. (1969). The co-precipitation of cations with CaCO3—IV. The co-precipitation of Sr2+ with aragonite between 16° and 96° C. Geochimica et Cosmochimica Acta, 33(1), 1-17.

70. Klein, R., Pätzold, J., Wefer, G., & Loya, Y. (1993). Depth-related timing of density band formation in Porites spp. corals from the Red Sea inferred from X-ray chronology and stable isotope composition. Marine Ecology Progress Series, 99-104. https://www.jstor.org/stable/24833602

71. Kleypas, J. A., Mcmanus, J. W., & Menez, l. A. (1999). Environmental limits to coral reef development: where do we draw the line?. American zoologist, 39(1), 146-159. DOI: 10.1093/icb/39.1.146

72. Knutson, D. W., Buddemeier, R. W., & Smith, S. V. (1972). Coral chronometers: seasonal growth bands in reef corals. Science, 177(4045), 270-272. DOI: 10.1126/science.177.4045.270

73. Kobayashi, K., Niu, E., Itoh, S., Yamagata, H., Lomtatidze, Z., Jorjoliani, I., Nakamura, K. and Fujine, H., 2007. The compact 14C AMS facility of Paleo Labo Co., Ltd., Japan. Nuclear Instruments and Methods in Physics Research Section B: Beam Interactions with Materials and Atoms, 259(1), pp.31-35.

74. Kotov, S., & Pälike, H. (2018, December). QAnalySeries-a cross-platform time series tuning and analysis tool. In AGU Fall Meeting Abstracts (Vol. 2018, pp. PP53D-1230).

75. LeGrande, A. N., & Schmidt, G. A. (2011). Water isotopologues as a quantitative paleosalinity proxy. *Paleoceanography*, *26*(3).

76. Li, D., Li, T., Jiang, H., Björck, S., Seidenkrantz, M. S., Zhao, M., ... & Knudsen, K. L. (2018). East Asian winter monsoon variations and their links to Arctic sea ice during the last millennium, inferred from sea surface temperatures in the Okinawa Trough. Paleoceanography and Paleoclimatology, 33(1), 61-75.

77. Liu, Z., Brady, E., & Lynch‐Stieglitz, J. (2003). Global ocean response to orbital forcing in the Holocene. Paleoceanography, 18(2). DOI: 10.1029/2002PA000819

78. Liu, G., Kojima, K., Yoshimura, K., Okai, T., Suzuki, A., Oki, T., Siringan, F.P., Yoneda, M. and Kawahata, H., 2013. A model-based test of accuracy of seawater oxygen isotope ratio record derived from a coral dual proxy method at southeastern Luzon Island, the Philippines. *Journal of Geophysical Research: Biogeosciences*, *118*(2), pp.853-859.

79. Liu, Z., Zhu, J., Rosenthal, Y., Zhang, X., Otto-Bliesner, B.L., Timmermann, A., Smith, R.S., Lohmann, G., Zheng, W. and Elison Timm, O., 2014. The Holocene temperature conundrum. Proceedings of the National Academy of Sciences, 111(34), pp.E3501-E3505.

80. Lough, J. M., & Barnes, D. J. (2000). Environmental controls on growth of the massive coral Porites. Journal of experimental marine biology and ecology, 245(2), 225-243. DOI:10.1016/S0022-0981(99)00168-9

81. Lough, J. M., & Cooper, T. F. (2011). New insights from coral growth band studies in an era of rapid environmental change. Earth-Science Reviews, 108(3-4), 170-184. DOI:10.1016/j.earscirev.2011.07.001

82. Maher, B. A. (2008). Holocene variability of the East Asian summer monsoon from Chinese cave records: a re-assessment. The Holocene, 18(6), 861-866.

83. Marcott, S. A., Shakun, J. D., Clark, P. U., & Mix, A. C. (2013). A reconstruction of regional and global temperature for the past 11,300 years. Science, 339, 1198-1201.

84. Marshall, J., Donohoe, A., Ferreira, D., & McGee, D. The ocean's role in setting the mean position of the Inter-Tropical Convergence Zone. *Clim. Dynam.* 42, 1967-1979 (2014).

85. Mateo, Z. R. P., & Siringan, F. P. (2016). Morphological and Sedimentological Signatures of Late Holocene Prodelta Lobes in Lingayen Gulf, Philippines. Journal of Coastal Research, 32(2), 354-364. DOI: 10.2112/JCOASTRES-D-14-00023.1

86. Matsuzaki, H., Nakano, C., Tsuchiya, Y.S., Ito, S., Morita, A., Kusuno, H., Miyake, Y., Honda, M., VII, A.T.B., Kawamoto, M. and Tokuyama, H., 2015. The status of the AMS system at MALT in its 20th

year. Nuclear Instruments and Methods in Physics Research Section B: Beam Interactions with Materials and Atoms, 361, pp.63-68.

87. Maxwell, K. V., Ramos, N. T., Tsutsumi, H., Chou, Y. C., Duan, F., & Shen, C. C. (2018). Late Quaternary uplift across northwest Luzon Island, Philippines constrained from emergent coral reef terraces. Earth Surface Processes and Landforms, 43(15), 3114-3132.

88. McConnaughey, T. (1989). 13C and 18O isotopic disequilibrium in biological carbonates: I. Patterns. Geochimica et Cosmochimica Acta, 53(1), 151-162.

89. McCulloch, M. T., Gagan, M. K., Mortimer, G. E., Chivas, A. R., & Isdale, P. J. (1994). A high-resolution Sr/Ca and δ18O coral record from the Great Barrier Reef, Australia, and the 1982–1983 El Niño. Geochimica et Cosmochimica Acta, 58(12), 2747-2754.

90. McGregor, H. V., & Gagan, M. K. (2003). Diagenesis and geochemistry of Porites corals from Papua New Guinea: Implications for paleoclimate reconstruction. Geochimica et Cosmochimica Acta, 67(12), 2147-2156.

91. McGregor, H. V., & Gagan, M. K. (2004). Western Pacific coral δ18O records of anomalous Holocene variability in the El Niño–Southern Oscillation. *Geophysical Research Letters*, *31*(11).

92. McGregor, H. V., & Abram, N. J. (2008). Images of diagenetic textures in Porites corals from Papua New Guinea and Indonesia. Geochemistry, Geophysics, Geosystems, 9(10).

93. McGregor, H. V., Fischer, M. J., Gagan, M. K., Fink, D., Phipps, S. J., Wong, H., & Woodroffe, C. D. (2013). A weak El Niño/Southern Oscillation with delayed seasonal growth around 4,300 years ago. *Nature Geoscience*, *6*(11), 949-953.

94. Mitsuguchi, T., Matsumoto, E., & Uchida, T. (2003). Mg/Ca and Sr/Ca ratios of Porites coral skeleton: Evaluation of the effect of skeletal growth rate. Coral Reefs, 22(4), 381-388. DOI: 10.1007/s00338-003-0326-1

95. Mitsuguchi, T., Dang, P. X., Kitagawa, H., Uchida, T., & Shibata, Y. (2008). Coral Sr/Ca and Mg/Ca records in Con Dao Island off the Mekong Delta: assessment of their potential for monitoring ENSO and East Asian monsoon. *Global and Planetary Change*, *63*(4), 341-352.

96. Mohtadi, M., Prange, M., Steinke, S. (2016) Paleoclimatic insights into forcing and response of monsoon rainfall. Nature Vol 533. Pp 191-199

97. Morimoto, M., Abe, O., Kayanne, H., Kurita, N., Matsumoto, F., Yoshida, N. 2002. Salinity records for the 1997–98 El Niño from Western Pacific corals. Geophysical Research Letters Vol. 29 No. 11

98. Morimoto, M., Kayanne, H., Abe, O., McCulloch, M.T. 2007. Intensified mid-Holocene Asian monsoon recorded in corals from Kikai Island, subtropical northwestern Pacific. Quaternary Research 67 pp 204-214

99. Moriya, T., Takeyama, M., Sakurai, H., Umebayashi, T., Toyoguchi, T., Shiraishi, T., Miyahara, H., Ohyama, M., Nozawa, K., Ito, S. and Itoh, S., 2019. Status of the AMS system at Yamagata University. Nuclear Instruments and Methods in Physics Research Section B: Beam Interactions with Materials and Atoms, 439, pp.94-99.

100. Nie, B., Chen, T., Liang, M., Wang, Y., Zhong, J., & Zhu, Y. (1997). Relationship between coral growth rate and sea surface temperature in the northern part of South China Sea during the past 100 a. Science in China Series D: Earth Sciences, 40(2), 173-182. DOI: 10.1007/BF02878376

101. Nurhati, I. S., Cobb, K. M., & Di Lorenzo, E. (2011). Decadal-scale SST and salinity variations in the central tropical Pacific: Signatures of natural and anthropogenic climate change. Journal of Climate, 24(13), 3294-3308.

102. Okai, T., Suzuki, A., Kawahata, H., Terashima, S., & Imai, N. (2002). Preparation of a new geological survey of Japan geochemical reference material: Coral JCp ‐ 1. Geostandards newsletter, 26(1), 95-99.

103. Oomori, T., Kaneshima, H., Maezato, Y., & Kitano, Y. (1987). Distribution coefficient of Mg2+ ions between calcite and solution at 10–50 C. Marine Chemistry, 20(4), 327-336.

104. Ota Y, Machida H, Hori N, Konishi K, Omura A. 1978. Holocene raised coral reefs of Kikai-jima (Ryukyu Islands). Geographical Review of Japan 51(2): 109–130. DOI: 10.4157/grj.51.109

105. Paillard, D., Labeyrie, L. D., & Yiou, P. (1996). AnalySeries 1.0: a Macintosh software for the analysis of geophysical time-series. Eos, 77, 379.

106. Partin, J. W., Cobb, K. M., Adkins, J. F., Clark, B., & Fernandez, D. P. (2007). Millennial-scale trends in west Pacific warm pool hydrology since the Last Glacial Maximum. Nature, 449(7161), 452-455.

107. Pätzold, J. (1984). Growth rhythms recorded in stable isotopes and density bands in the reef coral Porites lobata (Cebu, Philippines). Coral Reefs, 3(2), 87-90. DOI: 10.1007/BF00263758

108. Pausata, F. S., Battisti, D. S., Nisancioglu, K. H., & Bitz, C. M. (2011). Chinese stalagmite δ 18 O controlled by changes in the Indian monsoon during a simulated Heinrich event. Nature Geoscience, 4(7), 474.

109. Piao, J., Chen, W., Wang, L., Pausata, F. S., & Zhang, Q. (2020). Northward extension of the East Asian summer monsoon during the mid-Holocene. Global and Planetary Change, 184, 103046.

110. Phan, T. T., Yamazaki, A., Chiang, H. W., Shen, C. C., Doan, L. D., & Watanabe, T. (2019). Mekong River discharge and the East Asian monsoon recorded by a coral geochemical record from Con Dao Island, Vietnam. *Geochemical Journal*, *53*(2), e1-e7.

111. Philander, S. G. H., et.al. Why the ITCZ is mostly north of the equator. *J. Clim.*, 9, 2958-2972. (1996)

112. Qian, Q., Liang, P., Qi, L., Ding, Y., & He, J. (2020). Sub-Seasonal Variability of Meridional Activity of Western Pacific Subtropical High in Boreal Late Summer. Frontiers in Earth Science, 8, 597969.

113. Ramos NT, Tsutsumi H. 2010. Evidence of large prehistoric offshore earthquakes deduced from uplifted Holocene marine terraces in Pangasinan Province, Luzon Island, Philippines. Tectonophysics 495(3–4): 145–158. DOI:10.1016/j.tecto.2010.08.007

114. Ramos, N. T., Maxwell, K. V., Tsutsumi, H., Chou, Y. C., Duan, F., Shen, C. C., & Satake, K. (2017). Occurrence of 1 ka-old corals on an uplifted reef terrace in west Luzon, Philippines: Implications for a prehistoric extreme wave event in the South China Sea region. Geoscience Letters, 4, 1-13.

115. Ramos, R. D., Goodkin, N. F., Siringan, F. P., & Hughen, K. A. (2017). Diploastrea heliopora Sr/Ca and δ18O records from northeast Luzon, Philippines: An assessment of interspecies coral proxy calibrations and climate controls of sea surface temperature and salinity. *Paleoceanography*, *32*(4), 424-438.

116. Ramos, R. D., Goodkin, N. F., Siringan, F. P., & Hughen, K. A. (2019). Coral records of temperature and salinity in the Tropical Western Pacific reveal influence of the Pacific Decadal Oscillation since the late nineteenth century. Paleoceanography and Paleoclimatology, 34(8), 1344-1358.

117. Reed, E. V., Thompson, D. M., Cole, J. E., Lough, J. M., Cantin, N. E., Cheung, A. H., ... & Edwards, R. L. (2021). Impacts of coral growth on geochemistry: Lessons from the Galápagos Islands. Paleoceanography and Paleoclimatology, 36(4), e2020PA004051. DOI: 10.1029/2020PA004051

118. Reed, E. V., Thompson, D. M., & Anchukaitis, K. J. (2022). Coral-Based Sea Surface Salinity Reconstructions and the Role of Observational Uncertainties in Inferred Variability and Trends. Paleoceanography and Paleoclimatology, 37(6), e2021PA004371.

119. Ren, L., Linsley, B. K., Wellington, G. M., Schrag, D. P., & Hoegh-Guldberg, O. (2003). Deconvolving the δ18O seawater component from subseasonal coral δ18O and Sr/Ca at Rarotonga in the southwestern subtropical Pacific for the period 1726 to 1997. Geochimica et Cosmochimica Acta, 67(9), 1609-1621.

120. Rodríguez, J. M., Milton, S. F., & Marzin, C. (2017). The East Asian atmospheric water cycle and monsoon circulation in the Met Office Unified Model. Journal of Geophysical Research: Atmospheres, 122(19), 10-246.

121. Roff, G. (2020). Reef accretion and coral growth rates are decoupled in Holocene reef frameworks. Marine Geology, 419, 106065. DOI:10.1016/j.margeo.2019.106065

122. Rogers, C. S. (1990). Responses of coral reefs and reef organisms to sedimentation. Marine ecology progress series. Oldendorf, 62(1), 185-202.

123. Sachs, J. P., Blois, J. L., McGee, T., Wolhowe, M., Haberle, S., Clark, G., & Atahan, P. Southward Shift of the Pacific ITCZ During the Holocene. Paleoceanography and Paleoclimatology, 33, 1383-1395 (2018).

124. Sasaki, K., Omura, A., Murakami, K., Sagawa, N., & Nakamori, T. (2004). Interstadial coral reef terraces and relative sea-level changes during marine oxygen isotope stages 3–4, Kikai Island, central Ryukyus, Japan. Quaternary International, 120(1), 51-64.

125. Sayani, H. R., Cobb, K. M., Cohen, A. L., Elliott, W. C., Nurhati, I. S., Dunbar, R. B., ... & Zaunbrecher, L. K. (2011). Effects of diagenesis on paleoclimate reconstructions from modern and young fossil corals. Geochimica et Cosmochimica Acta, 75(21), 6361-6373.

126. Schneider, T., Bischoff, T., & Haug, G. H. Migrations and dynamics of the intertropical convergence zone. *Nature*, 513, 45-53 (2014).

127. Schulz, M., & Mudelsee, M. (2002). REDFIT: estimating red-noise spectra directly from unevenly spaced paleoclimatic time series. *Computers & Geosciences*, *28*(3), 421-426.

128. Scoffin, T. P., Tudhope, A. W., Brown, B. E., Chansang, H., & Cheeney, R. F. (1992). Patterns and possible environmental controls of skeletogenesis of Porites lutea, South Thailand. Coral Reefs, 11(1), 1-11. DOI:10.1007/BF00291929

129. Seki, A. er.al. Mid-Holocene sea-surface temperature reconstruction using fossil corals from Kume Island, Ryukyu, Japan. *Geochem. J.* 46, 27-32 (2012).

130. Shen, C.C., Lee, T., Liu, K.K., Hsu, H.H., Edwards, R.L., Wang, C.H., Lee, M.Y., Chen, Y.G., Lee, H.J. and Sun, H.T., 2005. An evaluation of quantitative reconstruction of past precipitation records

using coral skeletal Sr/Ca and δ18O data. *Earth and Planetary Science Letters*, *237*(3-4), pp.370-386.

131. Siringan, F. P., Shen, C. C., Lin, K., Abigania, M. I. T., & Gong, S. Y. (2016). Coral-based Holocene sea level of Paraoir, western Luzon, Philippines. Journal of Asian Earth Sciences, 123, 61-66. DOI: 10.1016/j.jseaes.2016.03.022

132. Smodej, J., Reuning, L., Wollenberg, U., Zinke, J., Pfeiffer, M., & Kukla, P. A. (2015). Two‐dimensional X‐ray diffraction as a tool for the rapid, nondestructive detection of low calcite quantities in aragonitic corals. Geochemistry, Geophysics, Geosystems, 16(10), 3778-3788.

133. Sowa, K., Watanabe, T., Kan, H., & Yamano, H. (2014). Influence of land development on Holocene Porites coral calcification at Nagura bay, Ishigaki island, Japan. *PloS one*, *9*(2), e88790.

134. Su, R., Sun, D., Chen, H., Chen, X., & Li, Z. (2010). Evolution of Asian monsoon variability revealed by oxygen isotopic record of middle Holocene massive coral in the northern South China Sea. *Quaternary International*, *213*(1-2), 56-68.

135. Sugihara, K., Nakamori, T., Iryu, Y., Sasaki, K., & Blanchon, P. (2003). Holocene sea-level change and tectonic uplift deduced from raised reef terraces, Kikai-jima, Ryukyu Islands, Japan. Sedimentary Geology, 159(1-2), 5-25.

136. Sun, D., Gagan, M.K., Cheng, H., Scott-Gagan, H., Dykoski, C.A., Edwards, R.L., Su, R. 2005. Seasonal and interannual variability of the Mid-Holocene East Asian monsoon in coral d18O records from the South China Sea. Earth and Planetary Science Letters 237 pp 69–84

137. Suzuki, A., Kawahata, H., Tanimoto, Y., Tsukamoto, H., & Yukino, I. (2000). Skeletal isotopic record of a Porites coral during the 1998 mass bleaching event. Geochemical Journal, 34(4), 321-329. DOI: 10.2343/geochemj.34.321

138. Tian, Z., Li, T., Jiang, D., & Chen, L. (2017). Causes of ENSO weakening during the Mid-Holocene. Journal of Climate, 30(17), 7049-7070.

139. Tudhope, A.W., Chilcott, C.P., McCulloch, M.T., Cook, E.R., Chappell, J., Ellam, R.M., Lea, D.W., Lough, J.M. and Shimmield, G.B., 2001. Variability in the El Niño-Southern Oscillation through a glacial-interglacial cycle. *Science*, *291*(5508), pp.1511-1517.

140. Thompson, D.M., Conroy, J.L., Konecky, B.L., Stevenson, S., DeLong, K.L., McKay, N., Reed, E., Jonkers, L. and Carré, M. (2022). Identifying hydro-sensitive coral δ18O records for improved high-resolution temperature and salinity reconstructions. Geophysical Research Letters, e2021GL096153.

141. Veizer, J. (1983). Chemical diagenesis of carbonates: theory and application of trace element technique.

142. Walker, M.J.C., Berkelhammer, M., Bjorck, S., Cwynar, L.C., Fisher, D.A., Long, A.J., Lowe, J.J., Newham, R.M., Rasussen, S.O., Weiss, H. 2012. Formal subdivision of the Holocene Series/Epoch: a Discussion Paper by a Working Group of INTIMATE (Integration of ice-core, marine and terrestrial records) and the Subcommission on Quaternary Stratigraphy (International Commission on Stratigraphy). Journal of Quaternary Science 27 pp 649-659

143. Wang, B., Wu, R., & Fu, X. (2000). Pacific–East Asian teleconnection: how does ENSO affect East Asian climate?. Journal of Climate, 13(9), 1517-1536.

144. Wang, B., Luo, X., & Liu, J. (2020). How robust is the Asian precipitation–ENSO relationship during the industrial warming period (1901–2017)?. *Journal of Climate*, *33*(7), 2779-2792.

145. Watanabe, T., Winter, A., Oba, T. (2001) Seasonal changes in sea surface temperature and salinity during the Little Ice Age in the Caribbean Sea deduced from Mg/Ca and 18O/16O ratios in corals. Marine Geology 173 pp 21-35

146. Watanabe, T., Kawamura, T., Yamazaki, A., Murayama, M., & Yamano, H. (2014). A 106 year monthly coral record reveals that the East Asian summer monsoon modulates winter PDO variability. Geophysical Research Letters, 41(10), 3609-3614.

147. Watanabe, T. K., Watanabe, T., Ohmori, K., & Yamazaki, A. (2020). Improving analytical method of Sr/Ca ratios in coral skeletons for paleo‐SST reconstructions using ICP‐OES. Limnology and Oceanography: Methods, 18(6), 297-310.

148. Watanabe, T. K., & Pfeiffer, M. (2022). A simple Monte Carlo approach to estimate the uncertainties of SST and δ18Osw inferred from coral proxies. Geochemistry, Geophysics, Geosystems, 23(3), e2021GC009813.

149. Weber, J. N., White, E. W., & Weber, P. H. (1975). Correlation of density banding in reef coral skeletons with environmental parameters: the basis for interpretation of chronological records preserved in the coralla of corals. Paleobiology, 1(2), 137-149. DOI: 10.1017/S0094837300002335

150. Weber J. N. and Woodhead P. M. J. (1972) Temperature dependence of oxygen-18 concentration in reef coral carbonates. J. Geophys. Res. 77, 463–473

151. Webster, P. J., & Yang, S. (1992). Monsoon and ENSO: Selectively interactive systems. Quarterly Journal of the Royal Meteorological Society, 118(507), 877-926.

152. Webster, P. J., Magana, V. O., Palmer, T. N., Shukla, J., Tomas, R. A., Yanai, M. U., & Yasunari, T. (1998). Monsoons: Processes, predictability, and the prospects for prediction. Journal of Geophysical Research: Oceans, 103(C7), 14451-14510.

153. Wei, G., Deng, W., Yu, K., Li, X. H., Sun, W., & Zhao, J. X. Sea surface temperature records in the northern South China Sea from mid-Holocene coral Sr/Ca atios. *Paleoceanography* 22, PA3206 (2007).

154. Weiss, H., & Bradley, R. S. (2001). What drives societal collapse?. Science, 291(5504), 609-610.

155. Winter, A., Ishioroshi, H., Watanabe, T., Oba, T., & Christy, J. (2000). Caribbean sea surface temperatures: Two‐to‐three degrees cooler than present during the Little Ice Age. Geophysical Research Letters, 27(20), 3365-3368.

156. Wu, B., & Wang, J. (2002). Winter Arctic oscillation, Siberian high and East Asian winter monsoon. Geophysical research letters, 29(19), 3-1.

157. Xue, D., Lu, J., Leung, L. R., & Zhang, Y. (2018). Response of the hydrological cycle in Asian monsoon systems to global warming through the lens of water vapor wave activity analysis. Geophysical Research Letters, 45(21), 11-904.

158. Yan, H., Wei, W., Soon, W., An, Z., Zhou, W., Liu, Z., Wang, Y. and Carter, R.M., 2015. Dynamics of the intertropical convergence zone over the western Pacific during the Little Ice Age. *Nature Geoscience*, *8*(4), pp.315-320.

159. Yang, K., Cai, W., Huang, G., Hu, K., Ng, B., & Wang, G. (2022). Increased variability of the western Pacific subtropical high under greenhouse warming. Proceedings of the National Academy of Sciences, 119(23), e2120335119.

160. Yihui, D., & Chan, J. C. (2005). The East Asian summer monsoon: an overview. Meteorology and Atmospheric Physics, 89(1-4), 117-142.

161. Yokoyama, Y., Suzuki, A., Siringan, F., Maeda, Y., Abe-Ouchi, A., Ohgaito, R., Kawahata, H. and Matsuzaki, H., 2011. Mid-Holocene palaeoceanography of the northern South China Sea using coupled fossil-modern coral and atmosphere-ocean GCM model. *Geophysical Research Letters*, *38*(8).

162. Yu, K. F. et.al. δ18O, Sr/Ca and Mg/Ca records of Porites lutea corals from Leizhou Peninsula, northern South China Sea, and their applicability as paleoclimatic indicators. *Palaeogeogr. Palaeoclimatol. Palaeoecol.* 218, 57-73 (2005).

163. Zhang, H., Zhang, X., Cai, Y., Sinha, A., Spoetl, C., Baker, J., Kathayat, G., Liu, Z., Tian, Y., Lu, J. and Wang, Z., 2021. A data-model comparison pinpoints Holocene spatiotemporal pattern of East Asian summer monsoon. Quaternary Science Reviews, 261, p.106911.

APPENDIX 1. Publications

Philippine Journal of Science
151 (1): 317-332, February 2022
ISSN 0031 - 7683
Date Received: 21 July 2021

Growth Patterns and AMS-^{14}C Age Dates of Fossil Corals from Northwest Pacific

Kevin L. Garas[1,3]*, Tsuyoshi Watanabe[1], Atsuko Yamazaki[2],
Angel T. Bautista VII[4], and Hiroyuki Matsuzaki[5]

[1]Hokkaido University, Sapporo 060-0810 Japan
[2]Kyushu University, Fukuoka 819-0395 Japan
[3]Department of Environment and Natural Resources–Mines and Geosciences
Bureau (DENR-MGB), North Avenue, Diliman, Quezon City 1128 Philippines
[4]Department of Science and Technology–Philippine Nuclear Research Institute (DOST-PNRI),
Commonwealth Avenue, Diliman, Quezon City 1101 Philippines
[5]Micro Analysis Laboratory, Tandem Accelerator (MALT),
The University Museum The University of Tokyo 113-8654 Japan

This study aims to evaluate the controlling factor/s of coral growth in the northwest Pacific during the Holocene. Here, we present newly acquired growth data and radiocarbon age dates of fossil *Porites* corals collected from Holocene uplifted marine terraces in Kikaijima, southern Japan and northwest Luzon, Philippines. Carbonate mineral identification using X-ray diffraction (XRD) and scanning electron microscope (SEM) was conducted to screen for any diagenetic alteration in the fossil corals. We used accelerator mass spectrometer (AMS) – ^{14}C dating to determine the absolute age dates of the fossil corals. Well-preserved fossil corals yielded radiocarbon age dates of 3235 ± 20 and 5712 ± 24 cal. yr BP for Kikaijima and 6285 ± 79, 6144 ± 77, 4336 ± 21, 4277 ± 19, 4200 ± 20, and 2972 ± 70 cal. yr BP for northwest Luzon. X-ray imaging of a 5-mm thick coral slab was utilized to measure growth variables. Linear extension rate, skeletal density, and calcification rate of Kikaijima corals are 3.77–8.72 mm/yr, 1.71–1.87 g/cm^3, and 0.70–1.56 g/cm^{2}yr, respectively. Linear extension rate, skeletal density, and calcification rate from northwest Luzon corals are 10.17–17.6 mm/yr, 0.66–1.67 g/cm^3, and 0.91–2.81 g/cm^{2}yr, respectively. Average linear extension rate from both sites was significantly and positively related to average calcification rate ($r = 0.72$, $p = 0.019$, $n = 10$). Skeletal density and linear extension rate measured from both sites were inversely related with each other ($r = –0.56$, $p = 0.09$, $n = 10$). Our data suggest that the variations in linear extension rates of fossil corals were influenced by the sea surface temperature (SST) difference between the study sites. However, data from modern corals are still needed to establish the local linear extension rate-SST relationship and to quantitatively evaluate how coral growth changes with respect to SST. Geomorphological, sedimentological, and geochronological studies of Holocene uplifted marine terraces should be conducted to provide the timing of emergence and coral reef development during Holocene.

Keywords: fossil corals, growth pattern, Japan, Philippines, radiocarbon

---

*Corresponding Author: kgaras91@gmail.com

INTRODUCTION

The geologic record reflects past environmental, climatic, and tectonic changes that may serve as analogs to future scenarios. The Holocene is the youngest geologic epoch of the Cenozoic era that covers the time interval from 11,700 yr ago until the present day (Walker *et al.* 2012). It is characterized by warming (4200–8200 yr BP) and cooling (~ 4000–4200 and ~ 8000–8600 yr BP) periods that are interesting time windows to evaluate coral reef responses to such climate shifts. Holocene coral records are well-preserved in the uplifted marine terraces that are widely distributed in the northwest Pacific, including southern Japan and the Philippines (Sugihara *et al.* 2003; Sasaki *et al.* 2004; Maeda and Siringan 2004; Ramos and Tsutsumi 2010). Scleractinian corals are major reef-building fossils of uplifted marine terraces in tropical and subtropical oceans. Well-preserved fossil corals are excellent materials for radiometric age dating and sclerochronological studies that can be used to determine the exact timing of the carbonate rock formation, paleoenvironmental conditions, and geologic events such as tectonic uplift and sea-level rise/fall. Aragonitic ($CaCO_3$) corals are utilized for ^{14}C measurements and can give an absolute age date of up to 55,000 yr ago (van der Plicht *et al.* 2020).

The growth assessment of precisely dated fossil corals can potentially unravel oceanographic changes and reef development in deep geologic time. Due to their environmental sensitivity, living corals are being studied across different reef sites to track the response of these organisms to environmental and oceanic changes. With the use of X-radiography, the alternating pattern of high- and low-density bands reveals a strong correlation with seasonal shifts of ocean conditions (Knutson *et al.* 1972; Barnes and Lough 1989). Coral growth is mainly influenced by spatial (depth, inshore to offshore, temperature gradients) and temporal (SST variability, temperature anomalies) aspects (Lough and Cooper 2011). The overall growth rate is significantly varied among several coral colonies across different geographic locations and taxa. Multi-species coral studies have emphasized that coral growth is affected by water temperature, salinity, light availability, and sea level (Lough and Barnes 2000; Lough and Cooper 2011). Other factors such as sedimentation, turbidity, and hydrographic conditions also affect the calcification and upward extension of coral exoskeletons (Buddemeier *et al.* 1974; Scoffin *et al.* 1992; Cuevas *et al.* 2009; Lough and Cooper 2011). The linear extension rates of living corals are positively correlated with the annual changes of SST, as suggested by coral records from Hawaii, Thailand, Great Barrier Reef, Arabian Gulf, and Hong Kong (Grigg 1981; Scoffin *et al.* 1992; Lough and Barnes 2000; Goodkin *et al.* 2011). In living *Porites* corals, the extension rate and calcification rate are linearly correlated (Scoffin *et al.* 1992; Lough and Barnes 2000). The change in linear extension rate is the dominant control on calcification rates. Skeletal density and linear extension rate are inversely related such that slower growth allows for the deposition of thicker and denser skeletons (Barnes and Lough 1993).

Fossil and living corals from the Caribbean have shown smaller linear extension rates compared to the corals from the western and eastern Pacific (Johnson and Pérez 2006). The discrepancy is due to the 1) varying environmental conditions between the sampling sites and 2) inherent difference of growth rates among various coral genera. Linear extension is the primary driver of coral calcification for *Porites* sp. and these growth variables are influenced by physico-chemical changes of the ocean as well as other environmental stressors (Lough and Cooper 2011). This study aims to evaluate the paleoenvironmental implications of coral growth patterns and how the past environment influenced the Holocene coral reefs in the northwest Pacific, which may provide a better understanding of past environmental changes relative to the present day. The global and regional temperature conditions during the Holocene are still subject to debate due to uncertainties in both proxy- and model-based reconstructions (Liu *et al.* 2014). Although it is expected that the tropics are warmer than the subtropics, the temperature evolution in the northwest Pacific during the mid- to late-Holocene is not clear due to inconsistencies of paleoclimate proxies and model data. First, we measure linear extension, skeletal density, and calcification in fossil corals and check the relationship of these coral growth variables. While the relationships are well-established in modern corals across Indo-Pacific reef sites (Lough and Barnes 2000), no detailed report has been made if these are true for fossil corals from the northwest Pacific, at the very least. Then, we consider several factors such as temperature, water depth, turbidity, sedimentation, and light availability that may have influenced the linear extension rates of fossil corals.

This study details newly acquired growth data and radiocarbon age dates of fossil *Porites* corals collected from Holocene uplifted marine terraces in Kikaijima, southern Japan and northwest Luzon, Philippines (Figure 1). Due to the geological similarities but varying environmental conditions between the two sites, the comparison of fossil coral growth rates may provide a glimpse of past ocean conditions. Microscopic and mineralogical investigations were conducted to determine fossil preservation. AMS-^{14}C dating was done to know the absolute age dates of the fossil corals. To avoid the effect of inherent differences in growth rate among coral taxa as indicated by previous studies, we only used the

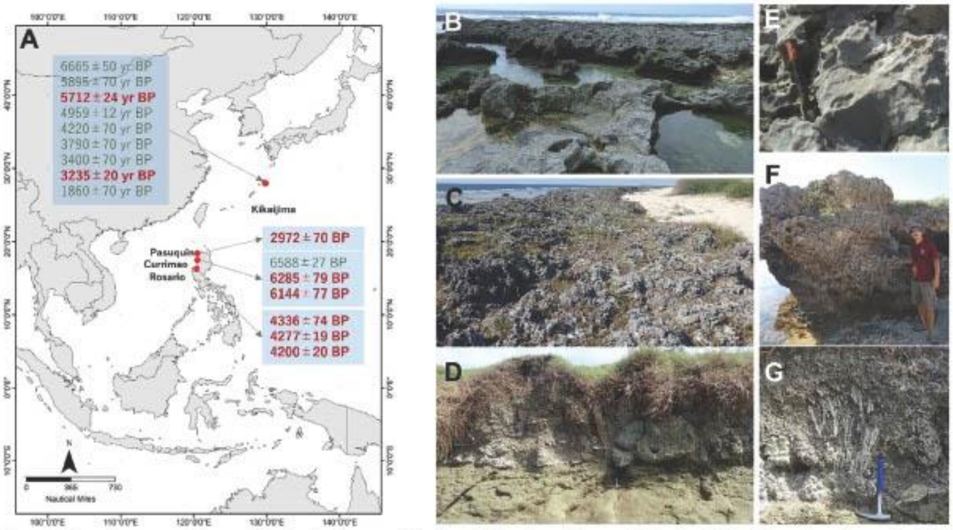

Figure 1. Location map of the sampling sites in Japan and Northern Philippines with new (red) and published (green) age dates of uplifted marine terraces. Published age dates measured from corals in Kikaijima (Abram *et al.* 2001; Morimoto *et al.* 2007) and from Currimao, Ilocos Norte (Shen *et al.* 2010). Field photos and *in situ* fossil coral photos of the uplifted marine terraces in Kikaijima (B, E); Currimao, Ilocos Norte (C, F); and Rosario, La Union (D, G).

well-studied *Porites* corals to provide a comparison with living coral data from the western Pacific. This will provide additional data to the identified gap of fossil coral growth data in the study area.

MATERIALS AND METHODS

The Study Area

Twenty-four (24) *Porites* samples were collected from the Holocene uplifted marine terraces in Kikaijima and northwest Luzon during the field surveys conducted from 2009–2018. Uplifted marine terraces are coastal geomorphic features that represent the remnants of past coral reefs. These features are formed due to sea-level fall and/or seismic events. The two sites are situated in active tectonic margins where large coseismic events formed the prominent staircase topography with horizontal abrasion platforms and terrace riser (Ota *et al.* 1978; Sugihara *et al.* 2003; Ramos and Tsutsumi 2010).

Kikaijima (28°16' to 28°22'N and 129°55' to 130°02'E) is situated in the eastern fringe of East China Sea in the northern part of Ryukyu Archipelago, Kagoshima Prefecture, Japan. The island is underlain by the Pleistocene Ryukyu Group and the Holocene marine terraces (Sasaki *et al.* 2004). The Holocene marine terraces are characterized by an offlap sequence of four marine terraces (Sugihara *et al.* 2003). These are situated up to 13 m above mean sea level, subdivided into Terrace I (10.8–11.1 and 8.5–8.9 m), Terrace II (5.0–5.3 m), Terrace III (4.0–4.3 m), and Terrace IV (1.9–2.5 m). A total of nine samples was collected from different locations in Kikaijima.

Similar to Kikaijima, the coastal stretch from La Union to Ilocos Norte in northwest Luzon is defined by the occurrence of uplifted marine terraces. Three (3) core samples were drilled from different *Porites* colonies in Rosario, La Union (N16°13'46.1" E 120°24'26.6"). The *Porites* colonies were exposed in the eroded terrace riser of a single terrace platform along Damortis Beach in the town of Rosario. Uplifted marine terraces are evident along the coastal stretch of Currimao to Burgos, Ilocos Norte. The marine terrace of Currimao (N18°1'56.7" E 120°28'25.3") is approximately 2 m high from the adjacent terrace platform and 3–4 m high above mean sea level (masl). A total of five (5) *Porites* samples were collected from the base of the highest terrace, Terrace II. An uplifted marine terrace was observed along the coast of Pasuquin, Ilocos Norte (N18°29'19.2" E 120°34'44.6"). It has a single terrace platform with a height of 2 m and covers the width of 120 m from the shoreline. Seven (7) *Porites* samples were collected from the terrace platform of this site.

The two sampling sites are different in terms of SST, salinity, and rainfall (Table 3). Because of the subtropical climate, Kikaijima has distinct SST variation from summer to winter seasons. Integrated Global Ocean Services System (Reynolds and Smith 1994, http://iridl.ldeo.columbia.edu/SOURCES/.IGOSS/.nmc/.Reyn_SmithOIv2/) SST recorded an annual average of 25.10 °C from 2000–2018. The SSTs in northwest Luzon are warmer and less varied compared to the subtropical Kikaijima. The annual mean SST in Ilocos Norte from 2000–2018 is 28.18 °C, while La Union has recorded an annual mean SST of 28.56 °C. The mean salinity in Kikaijima from 2000–2010 based on Simple Ocean Data Assimilation (Carton and Giese 2008, http://apdrc.soest.hawaii.edu/datadoc/soda_2.2.4.php) is 34.50 psu. Relative to Kikai-jima, SSS is slightly lower in Northwest Luzon with an annual mean SSS of 33.64 psu in Ilocos Norte and 33.57 psu in La Union from 2000–2010. The accumulated rainfall in Kikaijima from 2000–2018 is 2928.38 mm based on Naze Weather Station published in the Japan Meteorological Agency website (https://www.jma.go.jp/jma/indexe.html). This is higher than the recorded accumulated rainfall of 2204.95 and 2592.09 mm from Ilocos Norte and La Union, respectively. The 2000–2018 rainfall data from Laoag and Dagupan Stations were provided by the Climatology and Agrometeorology Division–Philippine Atmospheric, Geophysical, and Astronomical Services Administration (CAD-PAGASA).

Screening for Diagenesis

To reduce the uncertainty of the radiocarbon age dates, the coral samples were screened for any diagenetic alteration. The presence of secondary calcite in fossil coral skeleton was examined using an XRD Rigaku MiniFlex II at Hokkaido University and X'Pert Pro Panalytical at the Mines and Geosciences Bureau. XRD data of powdered corals were compared with the known peaks of standard aragonite and calcite. Coral samples with insignificant calcite content were analyzed using an SEM (Hitachi Miniscope TM-1000) at Hokkaido University. The SEM analysis was done to determine if the aragonite identified by XRD, is primary or secondary. Microstructures and crystal forms in a 1 cm x 1 cm coral block were observed using SEM to evaluate the recrystallization of secondary carbonate overprinting the coral skeleton.

Radiocarbon Dating Using the AMS

Pristine sections were chipped off from the top portion of the three coral cores (DMT-1, DMT-2, and DMT-3) from Rosario, La Union and analyzed using an AMS with a 0.5MV accelerator at Paleo-Labo Co., Ltd. The average error from the measurements of standard samples is less than ± 0.3% (Kobayashi *et al.* 2007). The two well-preserved corals (KIKJ-20160907-II and KIST-20160518-I) from Kikaijima were analyzed for radiocarbon age dates using an AMS with a 0.5 MV Pelletron accelerator at Yamagata University. The ^{14}C measurements of the standard samples yielded precision values that are higher than 0.3%. The $^{14}C/^{12}C$ ratio is less than 6×10^{-16} for the reagent graphite (Moriya *et al.* 2019). The three samples (PqPf-182020-4, CuPf-182018-1, CuPf-182018-4) from Ilocos Norte were analyzed at the Micro Analysis Laboratory Tandem Accelerator (MALT) of The University of Tokyo. MALT is using an ion-beam generated by a Pelletron™ 5UD tandem accelerator to conduct a highly sensitive and precise elemental and isotopic microanalysis system. At MALT, only mass 13 and 14 carbon species are injected into the AMS, limiting the transmission of ^{12}C (Matsuzaki *et al.* 2015). The ^{14}C measurements of the standard samples yielded precision values that are higher than 0.5%. Conventional radiocarbon age dates of fossil corals were converted into calendar age using the Marine20 datasets (Heaton *et al.* 2020). The radiocarbon age dates were not corrected using the regional reservoir offset (ΔR).

Two-dimensional X-ray Imaging

Coral samples were cut into 5-mm slabs along the major growth axis using a lapidary rock cutter with a diamond-tipped blade. The slabs were rinsed three times with Milli-Q water in an ultrasonic bath. The washed samples were dried in a 40 °C laboratory oven for at least 24 h.

Coral slabs were X-rayed with a cabinet radiographic unit SOFTEX M60 with direct digital imaging sensor NAOMI. The digital sensor is made up of a maximum of 192 highly sensitive monochrome CCD sensors resulting in 48.37-megapixel image quality. The X-ray unit has a maximum voltage of 60 kV and a maximum current of 3 mA. The aging of the X-ray beam was conducted before each imaging. The voltage was increased gradually by 10 kV every 3 min until it reached the desired 50 kV setting. Samples were exposed in 50 kV and 1 mA set-up for 8 s. The standard methodology of the measurement of linear extension rate, skeletal density, and calcification detailed by Sowa *et al.* (2014) was followed in this study.

Manual measurement of skeletal growth variables from the base of the sample to the topmost portion was done using ImageJ 1.50i software. The topmost (~ 20 cm) portion of some coral cores was not measured due to diagenetic alteration. Linear extension rate (cm/yr) was measured from the thickness of adjacent minima or maxima bands. An aluminum bar placed in the X and Y axes of the imaging sensor and the aragonitic step wedge from *Hippopus hippopus* (giant clam) blocks were used as the standards for analyzing skeletal density. The average skeletal density of the giant clam is 2.85 g/cm^3. This value was multiplied by the thickness of the step wedge standards. The observed density (OD) from the X-ray imaging and the actual skeletal density of the standards were plotted in the x-y graph. The generated polynomial equation from the standard aragonitic density was used to calibrate the OD data from the X-ray imaging. The average OD (the gray values of pixels from 0–255) was used to correct distance uncertainties in X-radiography. OD values for aluminum bars were used to adjust the image using the CoreCal2 software. The adjusted digital X-radiographies were used to measure the skeletal density along the maximum growth axis. The thickness of the coral slab along the growth axis was measured 10x by Vernier caliper and the OD values were averaged. The ODs were then converted to logarithmic ODs for the calculation of skeletal density (g/cm^3).

Three variables of coral growth were measured from the annual bands: 1) linear extension rate as the outward extension per year (mm/y); 2) the density of the coral skeleton being deposited each year (g/cm^3); and 3) the product of two previous variables expressed as calcification rate (g/cm^{2}y).

RESULTS

Preservation of Fossil Corals

After diagenesis screening, 10 fossil *Porites* were selected from 24 *Porites* samples from the study sites (Figure 2). Mineralogical analyses of the fossil *Porites* reveal that the selected samples have excellent to good preservation of aragonitic skeleton. Samples with predominantly aragonitic composition have diffraction peaks of a{111}, a{021}, a{012}, a{200}, a{130}, a{220}, a{221}, a{041}, a{132}, and a{113} (Figure 3a). The peak with highest intensity in calcite diffraction profile is calcite {104} at $2\theta = 29.8°$ followed by peaks at c{013}, c{018}, and c{1010} (Figure 3b). Fossil corals with $\leq 1\%$ calcite are considered to have good to excellent preservation.

The SEM images of the *Porites* samples are presented in Figure 4. Seven out of 10 coral samples have good preservation defined by intact coral microstructure and dominant primary aragonite skeleton with an isolated thin coating of secondary aragonite (Figures 4a–c and f). CuPf-180218-4, DMT-1, and DMT-2 have excellently preserved skeletons, which are completely devoid of secondary carbonate mineralization (Figures 4d, e, and g). Samples with a significant amount of abiogenic calcite and aragonite are rejected for radiocarbon dating. Calcite cement is characterized by rhombohedral crystals occupying the internal spaces of the skeleton (Figures 4h and i).

Radiocarbon Age Dates of the Uplifted Marine Terraces

Table 1 details the radiocarbon age dates of eight fossil corals from Kikaijima, Japan and northwest Luzon, Philippines. The radiocarbon ages were converted into calibrated years with 1σ and 2σ standard error using the calibration curve from Marine20 datasets.

Samples KIKJ-20160907-II and KIST-20160518-I from Keraji and Shitooke in Kikaijima were dated as 3235 ± 20 and 5712 ± 24 cal. yr BP, respectively. The ^{14}C age dates of KIKJ-20160907-II and KIST-20160518-I are consistent with the stratigraphic positions of the two samples. KIST-20160518-I was collected from Terrace II (TII) platform in Shitooke. TII is approximately 110 m wide at 4–5 masl. KIKJ-20160907-I was located from the horizontal abrasion platform of TII, while KIKJ-20160907-II was from the terrace riser wall of Terrace III (TIII) in Keraji. TII and TIII are 40 and 20 m wide, respectively. ARK05 was collected from the fossil Porites colony along a tidal inlet of Terrace IV (TIV) in Araki. TIV is around 20 m at a maximum height of 2 masl. Two samples (ARK05 and KIKJ-20160907-I) from Kikaijima were not analyzed using radiocarbon dating. Their assigned age dates were correlated based on the stratigraphic position of the samples. ARK05 was collected from TIV, which was uplifted around 1400 yr ago (Sugihara *et al.* 2003). KIKJ-20160907-I was collected from Terrace II, higher than the stratigraphic position of KIKJ-20160907-II (^{14}C age: 3235 ± 20 cal. yr BP). TII was uplifted around 4100 yr ago (Sugihara *et al.* 2003).

Samples CuPf-180218-4 and CuPf-180218-1 from Currimao, northwest Luzon yielded age dates of 6144 ± 77 and 6285 ± 79 cal. yr BP, respectively. These samples were collected from the base of Terrace II. Terrace II is 2.0 m high relative to the adjacent terrace platform and 3–4 m high relative to mean sea level. Samples DMT 1, DMT-3, and DMT-2 were obtained from a single-level marine terrace in La Union. These corals have age dates of 4200 ± 20, 4277 ± 19, and 4336 ± 21 cal. yr BP. Further north, sample PQPF-180220-4 from Pasuquin yielded an age of 2972±70 cal. yr BP. The ^{14}C age dates of CuPf-180218-4 and CuPf-180218-1 are consistent with the stratigraphic position of the two fossil corals. However, the three fossil corals (DMT 1, DMT-3, and DMT-2) from La Union are younger than the expected mid-Holocene age for the uplifted terrace. The single marine terrace from Pasuquin also yielded a relatively younger age of 2972 cal. yr BP. The geomorphic configuration of the marine terraces in La Union and Pasuquin, Ilocos Norte is different from the multi-level marine terraces observed in Currimao and Badoc Island, Ilocos Norte (Maxwell *et al.* 2018).

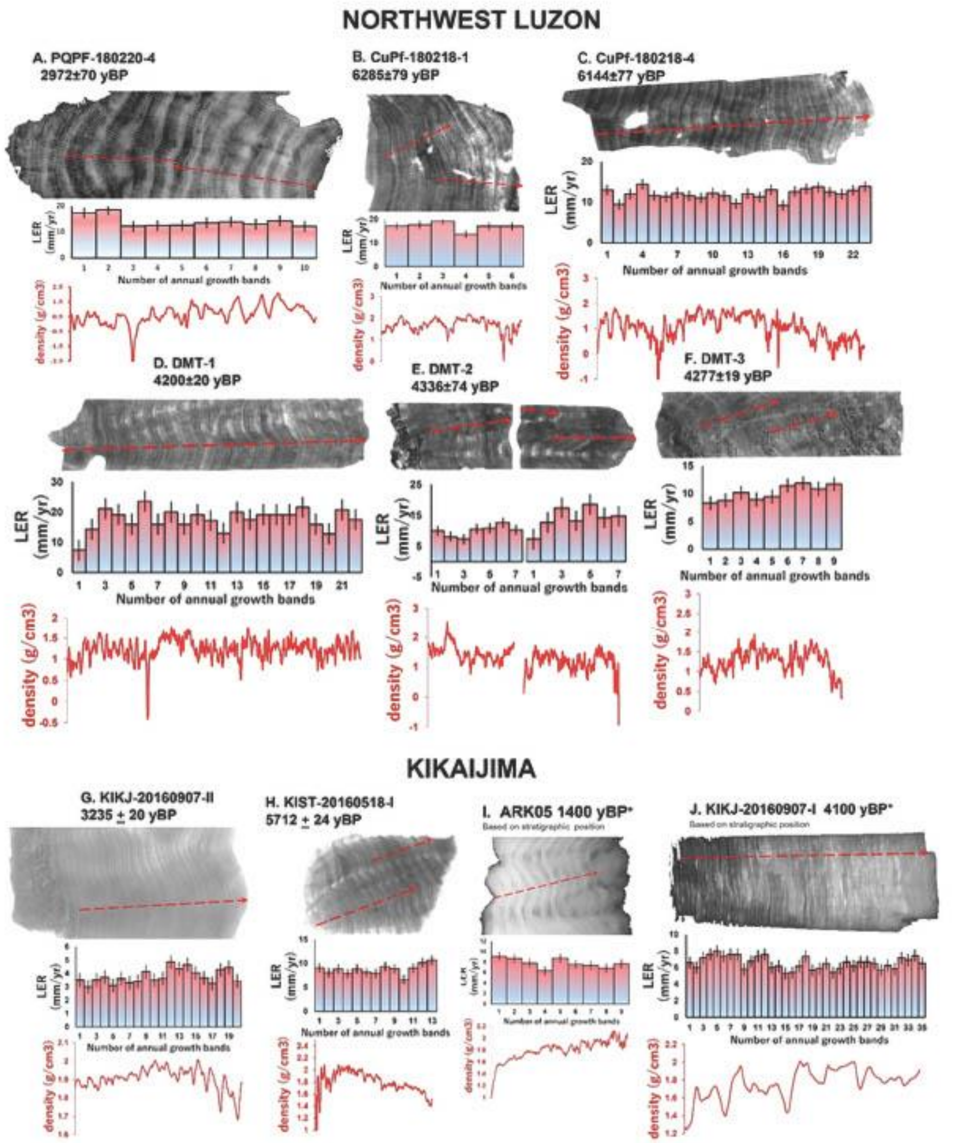

Figure 2. X-ray photographs, linear extension rate (LER), and density of the 10 fossil corals from Northwest Luzon (A, B, C, D, E, F) and Kikaijima (G, H, I, J). Sample names and corresponding ^{14}C age dates are indicated in the figure.

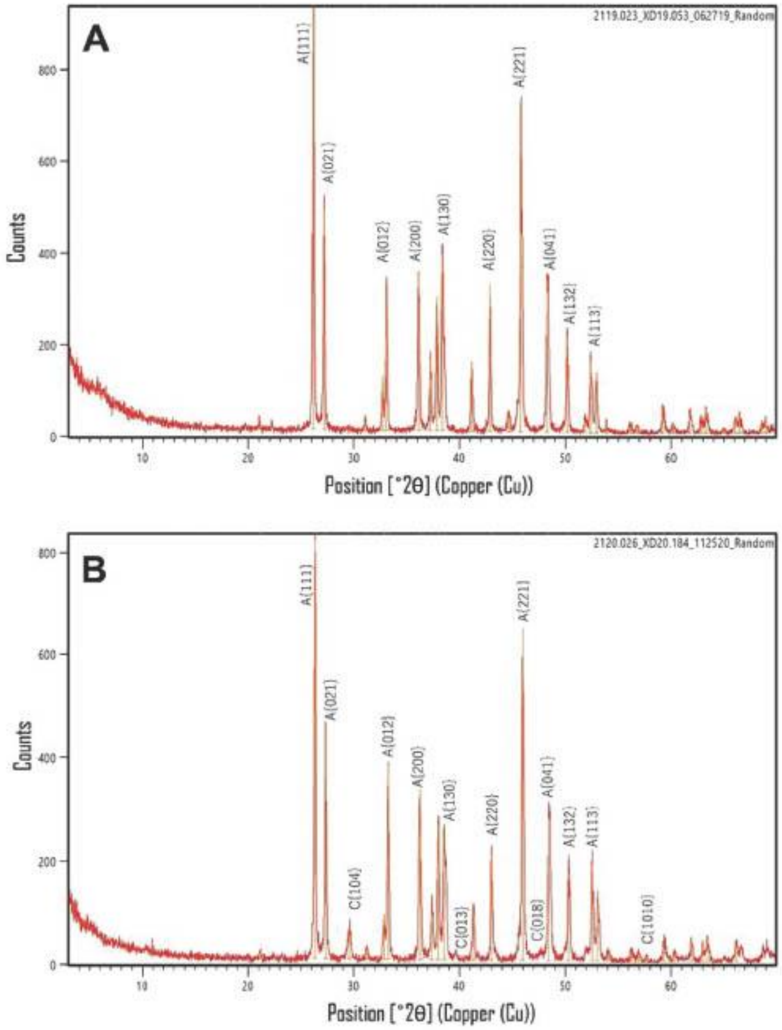

Figure 3. XRD profiles of coral skeleton with [A] 100% aragonite and [B] 95% aragonite and 5% calcite. Miller indices (notation {000}) of crystal planes were indicated for aragonite (A) and calcite (C) in coral skeleton.

Growth Patterns of Fossil Corals

Linear extension rates, skeletal density, and calcification rates were measured in 10 fossil corals from Kikaijima, Japan and northwest Luzon, Philippines (Table 2; Figure 2). Among the four fossil *Porites* from Kikaijima, KIST-20160518-I recorded the fastest growth (extension) at 0.87 cm/yr and the highest calcification rates at 1.56 g/cm^{2}yr. KIKJ-20160907-II has the slowest growth (extension) at 0.38 cm/yr and the lowest calcification rate at 0.70 g/cm^{2}yr. Skeletal densities ranging from 1.71–1.87 g/cm^3 are not largely different among the four samples.

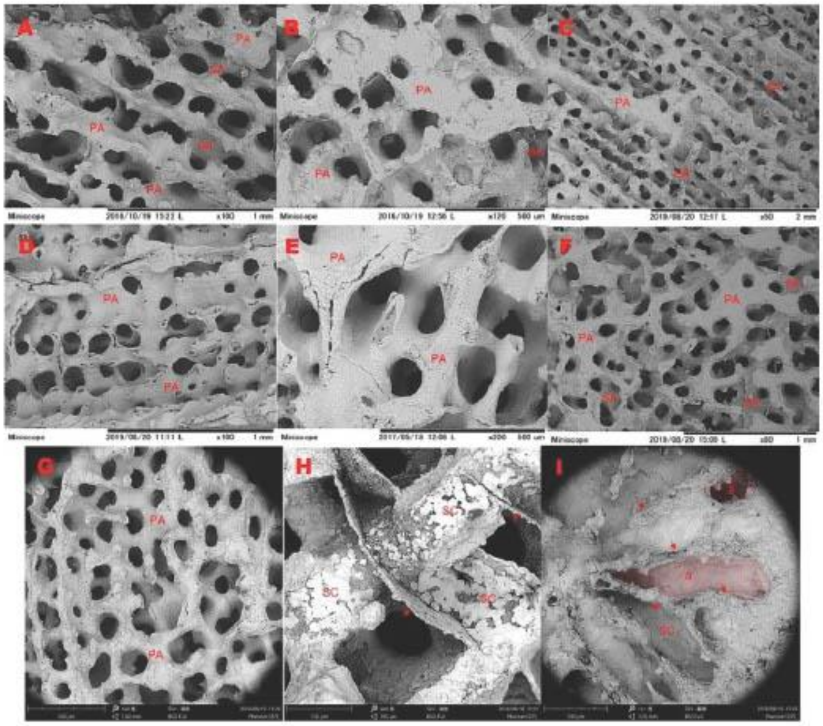

Figure 4. Backscattered electron images of fossil corals showing good preservation with occasional thin coat of fine secondary aragonite (SA) needles (A: KIST-20160518-1; B: KIKJ-20160907-II; C: CuPf-180218-I; F: PqPf-180220-4). Corals with excellent preservation have 100% primary aragonite (PA) (D: CuPf-180218-4; E. DMT-1; G: DMT-2). Corals with rhombohedral calcite cement (SC) were not included in radiocarbon dating. Preservation of coral microstructures such as dissepiment (arrow in H) and septa (arrow in I) was also considered in the screening for diagenetic imprints.

Table 1. The AMS-^{14}C age dates of fossil corals from the uplifted marine terraces in Kikaijima and Northwest Luzon. The conventional radiocarbon age was converted into calendar years using the published calibration curve data Marine20.

Sample name	Location	Conventional radio-carbon age (cal yr BP ± 1σ)	Calendar age	
			1σ calibrated year range	2σ calibrated year range
		Kikai-jima corals		
KIKJ-20160907-II	Keraji, Kikai-jima	3235 ± 20	993(68.2%)846 cal BC	1076(95.4%)793 cal BC
KIST-20160518-I	Shitooke, Kikai-jima	5712 ± 24	4047(68.2%)3890 cal BC	4141(95.4%)3801 cal BC
		Northwest Luzon corals		
PQPF-180220-4	Pasuquin, Ilocos Norte	2972 ± 70	754(68.3%)516 cal BC	822(95.4)383 cal BC
DMT-1	Rosario, La Union	4200 ± 20	2221(68.2%)2048 cal BC	2313(95.4%)1975 cal BC
DMT-3	Rosario, La Union	4277 ± 19	2335(68.2%)2164 cal BC	2432(95.4%)2094 cal BC
DMT-2	Rosario, La Union	4336 ± 21	2423(68.2%)2254 cal BC	2478(95.4%)2157 cal BC
CuPf-180218-4	Currimao, Ilocos Norte	6144 ± 77	4533(68.3%)4323 cal BC	4661(95.4)4228 cal BC
CuPf-180218-1	Currimao, Ilocos Norte	6285 ± 79	4688(68.3%)4461 cal BC	4796 (95.4)4351 cal BC

^{14}C age calculation used AD 1950 as a base point. Libby's half-life of 5568 was used as the half-life of ^{14}C.
Calib Rev 8.2 (calibration curve data: Marine20) was used to convert conventional radiocarbon age to calendar age.

Table 2. The AMS-^{14}C age dates of fossil corals from the uplifted marine terraces in Kikaijima and Northwest Luzon. The conventional radiocarbon age was converted into calendar years using the published calibration curve data Marine20.

Sample name	Location	Conventional radiocarbon age (cal. yr BP)	Number of annual bands	Extension rate (mm/yr)	Skeletal density (g/ cm^3)	Calcification rate (g/ cm^{2}yr)
			Kikai-jima corals			
ARK05	Araki, Kikai-jima	1400*	9	7.77 ± 0.86	1.81 ± 0.14	1.39 ± 0.11
KIKJ-20160907-II	Keraji, Kikai-jima	3235 ± 20	20	3.77 ± 0.51	1.87 ± 0.09	0.70 ± 0.09
KIKJ-20160907-I	Keraji, Kikai-jima	4100*	35	6.57 ± 0.74	1.71 ± 0.13	1.12 ± 0.16
KIST-20160518-I	Shitooke, Kikai-jima	5712 ± 24	13	8.72 ± 1.00	1.80 ± 0.14	1.56 ± 0.15
			Northwest Luzon corals			
PQPF-180220-4	Pasuquin, Ilocos Norte	2972 ± 70	10	14.11 ± 2.09	0.66 ± 0.50	0.91 ± 0.67
DMT-1	Rosario, La Union	4200 ± 20	22	17.6 ± 3.49	1.26 ± 0.15	2.24 ± 0.56
DMT-3	Rosario, La Union	4277 ± 19	9	10.17 ± 1.29	1.28 ± 0.18	1.30 ± 0.24
DMT-2	Rosario, La Union	4336 ± 21	26	12.35 ± 3.97	1.04 ± 0.37	1.27 ± 0.49
CuPf-180218-4	Currimao, Ilocos Norte	6144 ± 77	23	12.05 ± 1.31	1.06 ± 0.40	1.26 ± 0.46
CuPf-180218-1	Currimao, Ilocos Norte	6285 ± 79	6	16.94 ± 1.66	1.67 ± 0.16	2.81 ± 0.27

The linear extension (1.2–1.76 cm/yr) and calcification (0.91–2.81 g/cm^{2}yr) rates are higher in northwest Luzon corals compared to Kikaijima corals. DMT-1 has the fastest growth (extension) rate at 1.76 cm/yr, while DMT-3 has the slowest growth (extension) rate at 1.02 cm/yr among the six fossil *Porites* from northwest Luzon. CuPf-180218-1 has the densest skeleton (1.67 g/cm^3) and the highest calcification rate (2.81 g/cm^{2}yr). Among the six fossil corals, PQPF-180220-4 is the lightest skeleton (0.66 g/cm^3) and has the lowest calcification rate (0.91 g/cm^{2}yr).

Average linear extension rate was significantly and positively related to average calcification rate (Figure 5a, $r = 0.72$, $p = 0.019$, $n = 10$). The average skeletal density and average linear extension rates were inversely related with each other (Figure 5b, $r = -0.56$, $p = 0.09$, $n = 10$). Average calcification rate was not significantly related to the average skeletal density (Figure 5c, $r = 0.16$, $p = 0.66$, $n = 10$). These relationships show that the calcification rates were mostly influenced by linear extension rates. The changes in skeletal density did not reflect significantly in the changes in calcification rate.

In terms of interannual growth variability, the linear extension rate, skeletal density, and calcification rate of Kikaijima corals are less varied compared to the growth patterns of Northwest Luzon corals (Figure 6). This is evident in the relatively large standard deviations (1σ/S.D.) of the measured values from growth bands of the *Porites* samples of northwest Luzon. The 1σ of linear extension rates of northwest Luzon coral range from 1.29–3.97 mm/yr compared to the 0.51 to 1 mm/yr of Kikaijima corals. Skeletal densities and calcification rates of individual growth bands of northwest Luzon corals also vary within 1σ = 0.15–0.50 and 1σ = 0.24–0.67, respectively. The large deviation of these values is well-presented by the difference of maxima and minima values of growth variables in the box plots of northwest Luzon corals (Figure 6).

DISCUSSION

Paleoenvironmental Implications of Fossil Coral Growth Characteristics

Water temperature could be the dominant factor influencing coral growth. This has been documented from the linear correlation between temperature and coral extension rate among the modern coral colonies from the Great Barrier Reef, Hawaii, and Thailand (Grigg 1981; Scoffin *et al.* 1992; Lough and Barnes 2000). Growth measurements show that the linear extension is significantly and directly correlated with coral calcification ($r = 0.96$) across the 44 sites in Indo-Pacific (Lough and Barnes 2000). Skeletal density is significantly but inversely correlated with linear extension ($r = -0.80$) and calcification ($r = -0.64$) rates. Lough and Barnes (2000) concluded that linear extension and calcification rates are linked with average SST.

From this study, fossil corals from several sites in Kikaijima and Northwest Luzon show that linear extension rate is significantly correlated to calcification rate ($r = 0.72$, $p = 0.019$) and inversely correlated to skeletal density ($r = -0.56$, $p = 0.09$; Figures 5a–b). The

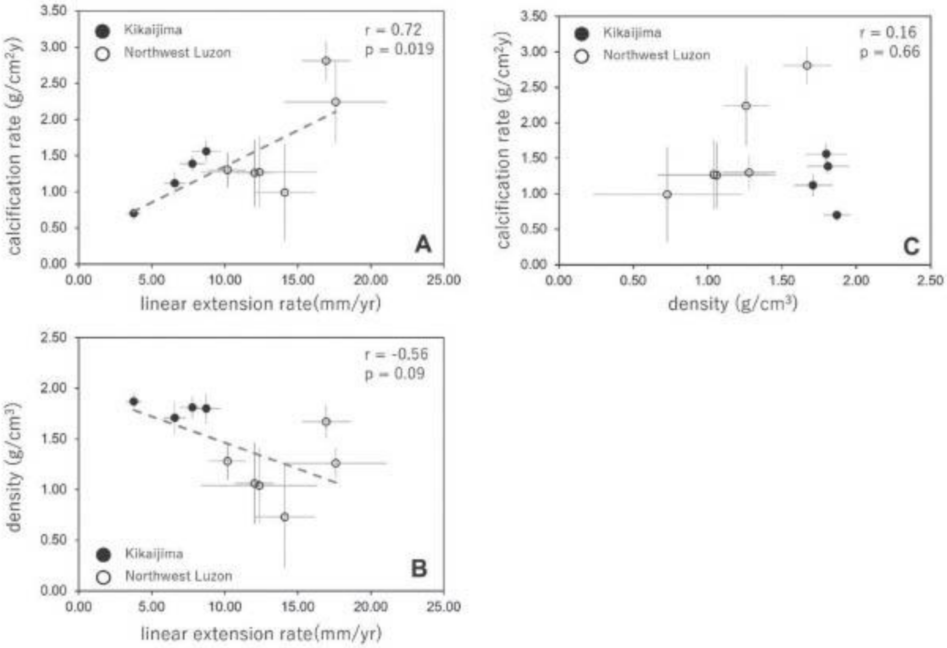

Figure 5. Relationships of fossil coral growth variables from Kikaijima and Northwest Luzon. Linear extension rate was positively (r = 0.72, $p = 0.019$) and inversely (r = –0.56, $p = 0.09$) correlated with calcification rate (A) and density (B). Density was not significantly correlated with calcification rate (C; r = 0.16; $p = 0.66$).

relationships of linear extension rate to the other two growth variables from fossil corals follow the similar trend of the modern *Porites* growth variables from the Indo-Pacific (Grigg 1981; Scoffin *et al.* 1992; Lough and Barnes 2000). However, the calcification rate of fossil corals is not significantly and weakly correlated with skeletal density (Figure 5c; r = 0.16, $p = 0.66$), which is different from the strong inverse correlation of modern *Porites* from the Indo-Pacific. This could be attributed to the limited fossil samples and geographic coverage of our sampling. Unlike the wide latitudinal coverage of the modern *Porites* data, our fossil coral data only cover the range of 16–28°N.

Linear extension rates of a few modern *Porites* corals from the Philippines measure 12.85–13.0 mm/yr (Pätzold 1984; Dizon and Yap 2005). This is higher than the linear extension rates (7.0–9.5 mm/yr) of some modern *Porites* from southern Japan (Suzuki *et al.* 2000; Mitsuguchi *et al.* 2003). These Japanese coral data are comparable with the published average linear extension rate of subtropical Indo-Pacific of 7.54 mm/yr (Brachert *et al.* 2020). Although these data are very limited, we can notice that there is a difference in linear growth rates of *Porites* from the Philippines and southern Japan, which can be attributed to different environmental conditions between the two sites, such as SST (Table 3). However, more modern coral data are needed to statistically establish the empirical relationship of linear extension rate and SST. Our fossil data show that Northwest Luzon corals have higher linear extension rates (10.2–17.6 mm/yr) compared to Kikaijima corals (3.77–8.72 mm/yr), a much larger difference compared to modern *Porites*. Following the linear extension–SST established from modern *Porites* colonies (Lough and Barnes 2000), the disparity in linear extension rate of fossil corals from the two areas is probably driven by the warmer SST in northwest Luzon relative to Kikaijima during the mid- to late-Holocene periods. Furthermore, the variations on growth patterns were possibly affected by the larger maximum-minimum SST difference in the subtropics than the tropics due to insolation (Liu *et al.* 2003). However, the quantitative sensitivity of the linear extension rate of fossil coral to paleo-SST cannot be discussed due to the absence of reconstructed SST from coral geochemical tracers.

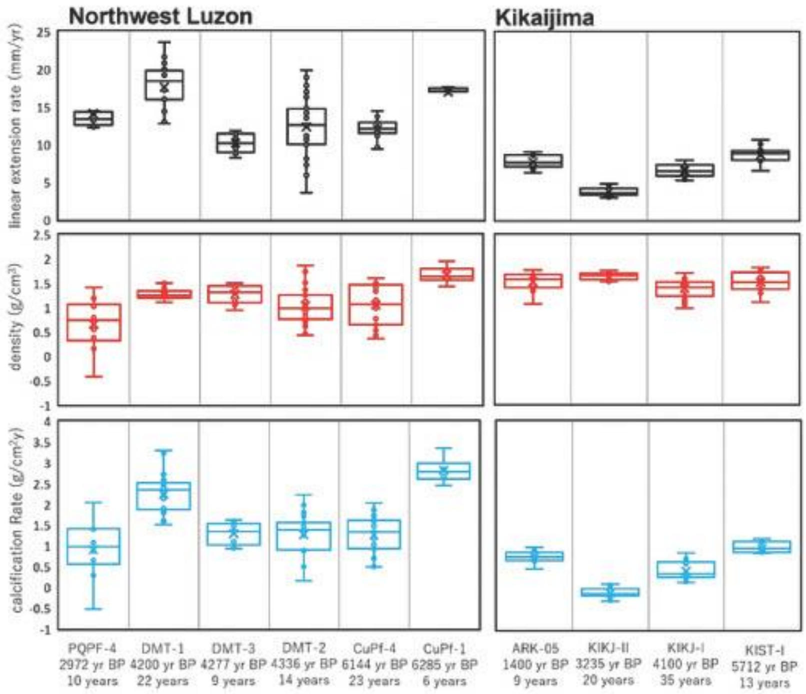

Figure 6. Box plots of the linear extension rates (black), skeletal densities (red), and calcification rates (blue) of the fossil corals from northwest Luzon and Kikaijima. The x-axis shows the sample name, number of annual bands, and radiocarbon age dates of fossil corals. Box plots show the statistical range and standard deviation of the growth variables within the internal chronology of fossil corals.

Table 3. Annual mean, maximum and minimum SST, sea surface salinity (SSS), and accumulated rainfall from Kikaijima, Japan plus Ilocos Norte and La Union, Philippines.

Location	SST (°C)*	Max-Min SST (°C)	Mean SSS** (psu)	Max-Min SSS (psu)	Annual accumulated rainfall (mm)
Kikaijima					
Mean	25.10	7.72	34.50	0.63	2928.38
Max	29.15		34.76		418.22
Min	21.43		34.13		163.83
Ilocos Norte					
Mean	28.18	4.06	33.64	0.34	2204.95
Max	29.95		33.79		600.23
Min	25.89		33.46		3.18
La Union					
Mean	28.56	3.69	33.57	0.37	2592.09
Max	30.14		33.76		636.36
Min	26.44		33.39		5.80

Light availability, together with temperature, could be a limiting factor in the growth of hermatypic corals and associated zooxanthellae (Kleypas *et al.* 1999). The linear extension rate of *Porites spp.* decreases with respect to deeper water levels due to low light conditions and photosynthesis-driven heterotrophy-autotrophy mechanism (Klein *et al.* 1993). We can estimate the paleo-depth level of the Holocene reefs in the Ryukyu Islands based on the fossil coral assemblage, as discussed by Hongo and Kayanne (2010). The most dominant coral species observed in the Holocene marine terraces of Kikaijima are *Acropora digitifera* and *Acropora robusta* with relatively fewer *Porites* sp., *Favia* sp., and *Goniopora* sp. In Northwest Luzon, fossil coral coverage includes diverse species of *Acropora digitifera*, *Acropora robusta*, *Favia sp.*, *Heliopora sp.*, *Pocillopora sp.*, *Porites sp.*, *Galaxea* sp., and *Goniastrea* sp. The presence of *Acropora digitifera* and *Acropora robusta* in all sites suggests that the paleo-reef was part of the main reef crest/edge and was deposited at 0–6 m (Cabioch *et al.* 1999; Hongo and Kayanne 2010). Considering that the estimated paleo-depth and paleo-reef settings are relatively similar in different sampling sites, we can argue that the variation of linear extension rates of the 10 fossil coral samples was not controlled by varying water depths. These colonies are situated in living positions, approximately 15–80 cm in height. Growth variables were measured from the base to the topmost portion, except for diagenetically altered areas. We can say that the growth measurements reflect the representative internal chronology of the fossil coral colony.

Sedimentation can also increase water turbidity and inhibit light penetration in shallow water. The process could affect the growth pattern and coral diversity, as shown by the dredging-related sedimentation in Bermuda around the 1940s (Dodge and Vaisnys 1977). The decrease of light penetration due to sedimentation can slow down the coral growth and calcification rates, decrease coral diversity and abundance, reduce coral net productivity, increase the abundance of branching forms, and reduce reef accretion (Rogers 1990; Crabbe and Smith 2005). The generally smaller linear extension and calcification rates of fossil *Porites* in Kikaijima were not probably driven by heavy sedimentation. No geological evidence suggests the occurrence of a large river system and high terrigenous input in Kikaijima during the mid- to late-Holocene. In the present-day, large rivers were not observed near the sampling sites. In contrast, the river systems of northwest Luzon – particularly the area surrounding Lingayen Gulf – have been supplying high amounts of sediments to the sea since the late-Holocene based on geomorphological and sedimentological investigations (Mateo and Siringan 2016). The high sedimentation in Lingayen Gulf is not indicated by the relatively large extension rates of fossil corals from Rosario, La Union (Table 2).

Coral Reef Development from Mid- to Late-Holocene

Marine terraces are important in providing morpho-stratigraphic position of the Quaternary carbonate deposition in geologic time. There are three marine terraces (TII, TIII, and TIV) observed in the sampling sites in Keraji, Shitooke and Araki, Kikaijima. Geomorphologically, TII has a wide terrace platform around 40–100 m in width at 4–5 masl. This is wider than the ~ 20 m wide terrace platforms of TIII and TIV. This is consistent with the observations of Ota *et al.* (1978) that the highest coral reef accretion in Kikaijima occurred during the formation of TII.

Aside from the shorter deposition period of TIII and TIV relative to TII, the SST-driven ecological stress possibly influenced the low reef accretion. SST estimates from coral δ^{18}O revealed cooler water conditions in Kikaijima from 3400–3790 yr ago relative to present-day – coupled with low coral coverage and species diversity, high population of macro-algae, and dominance of *Acropora* species (Abram *et al.* 2001). The low species diversity in TIII and TIV was observed in the three sampling sites in Kikaijima, dominated by branching *Acropora* species and fewer massive type corals. Cold stress decreases rates of photosynthesis, respiration, and growth – similar to the effects of high thermal stress (Higuchi *et al.* 2015). The ecological (cold) stress experienced by the reef environments in the late-Holocene was probably a major factor in the slow linear extension (3.8 mm/yr) and calcification (0.70 g/cm^{2}yr) response of KIKJ-20160907-II at 3235 cal. yr BP relative to the growth variables of other *Porites* from different time windows (Figure 6). However, additional growth data of corals from this time window should be collected to strengthen this discussion.

Compared to the Kikaijima, the uplifted marine terraces in northwest Luzon have fewer studies on coral reef evolution, tectonics, geochronology, and sea-level fluctuations (Shen *et al.* 2010; Siringan *et al.* 2016; Maxwell *et al.* 2018). Radiocarbon age dates of CuPf-180218-4 (6144 ± 77 cal. yr BP) and CuPf-180218-1 (6285 ± 79 cal. yr BP) from Currimao are in good agreement with the previously published ^{230}Th coral age dates (Shen *et al.* 2010; Maxwell *et al.* 2018). Borehole data revealed that the Currimao reef has started accumulating around 9855 yr ago until 6588 yr ago (Shen *et al.* 2010). Maxwell *et al.* (2018) further extended the reef development using younger ^{230}Th coral age dates – 6178 and 6163 yr BP. New ^{14}C ages from Currimao are consistent with published ^{230}Th coral age dates and stratigraphically correlated to the reported mid-Holocene sea-level highstand in Northwest Luzon occurred around 7000–6000 yr ago, which resulted in reef backstepping as a response to rapid sea-level rise (Shen *et al.* 2010; Maxwell *et al.* 2018).

The ^{14}C ages from Rosario, La Union and Pasuquin, Ilocos Norte are new-age dates of terrace emergence in northwest Luzon. Four new age dates represent the formation of carbonate platforms around 4200 ± 20, 4277 ± 19, 4336 ± 21 cal. yr BP, and 2972 ± 70 cal. yr BP during the late-Holocene. The 4200–4400 cal. yr BP interval is younger than the reported age (6980 yr ago) of the uplifted terrace in Rosario, La Union (Javelosa 1994). No information was provided on the nature and preservation of the material that was used in the radiocarbon dating. Both new and previously reported age dates were measured from samples collected from the coral-dominated zone at 2–3 masl. This level is composed of branching- and massive-type corals admixed with bivalve shells loosely bounded by carbonate-derived sand and silt. The 4200 yr BP event serves as the boundary between mid- and late-Holocene and is often characterized by a widespread arid condition (Walker *et al.* 2012). However, the general climate and ocean condition during the 4200-yr BP event in the northwest Pacific – including the Philippines – is yet to be established. The sedimentological and biological characteristics of younger uplifted marine terraces (4336–2972 cal. yr BP) in northwest Luzon are a good comparison to the TIII and TIV in Kikaijima. From our data, no general trend can be concluded from the variations of growth variables between mid- and late-Holocene corals from northwest Luzon. This could be an artifact of limited fossil coral sampling in the northwest Pacific. Detailed sedimentological assessment focusing on coral coverage and species diversity of the younger terraces should be done to investigate any biological response to the mid- to late-Holocene transition.

CONCLUSIONS

This study presents the variations of growth patterns of precisely dated fossil *Porites* corals from subtropical Kikaijima, Japan and tropical northwest Luzon, Philippines. The main findings are as follows:

1. Well-preserved fossil corals yielded radiocarbon age dates of 3235 ± 20 and 5712 ± 24 cal. yr BP from Kikaijima corals and 6285 ± 79, 6144 ± 77, 4336 ± 21, 4277 ± 19, 4200 ± 20, and 2972 ± 70 cal. yr BP.
2. Linear extension rate, skeletal density, and calcification rate of Kikaijima corals are 3.77–8.72 mm/yr, 1.71–1.87 g/cm^3, and 0.70–1.56 g/cm^{2}yr, respectively. Linear extension rate, skeletal density, and calcification rate of northwest Luzon corals are 10.17–17.6 mm/yr, 0.66–1.67 g/cm^3, and 0.91–2.81 g/cm^{2}yr, respectively.
3. Average linear extension rate was significantly and positively related to average calcification rate ($r = 0.72$, $p = 0.019$, $n = 10$). Skeletal density and linear extension rate were inversely related with each other ($r = -0.56$, $p = 0.09$, $n = 10$). Average calcification rate was not significantly related to average skeletal density ($r = 0.16$, $p = 0.66$, $n = 10$).
4. Following the established sensitivity of growth variables with SST in modern *Porites* in the Indo-Pacific, our data suggest that the variations of linear extension rates of fossil corals were influenced by the SST difference between our sites. The faster (slower) linear extension and calcification rates were likely driven by the warmer (cooler) SSTs in NW Luzon (Kikaijima).

This paper demonstrates the utility of fossil corals in understanding past environmental conditions driven by the latitudinal difference in SST between the tropical northwest Luzon (Philippines) and subtropical Kikaijima (Japan). While other environmental variables and stressors such as water depth, turbidity, sedimentation, and light availability were evaluated, SST is considered as the primary limiting factor to the coral growth in our two study sites during the mid- to late Holocene. However, the quantitative estimate of SST variability using linear extension rate difference was not discussed due to the scarcity of modern coral growth data and paleo-SST reconstruction from geochemical proxies. Geomorphological, sedimentological (litho- and biofacies), and geochronological (absolute dating) constraints from the uplifted marine terraces are needed to explain the coral reef development during the mid- to late Holocene, particularly around 4200 yr ago.

ACKNOWLEDGMENTS

We would like to thank K.B. Tee and M.M. Alorro of the Mines and Geosciences Bureau, as well as T.K. Watanabe, S. Ito, and W. Kobayashi of Hokkaido University–CREES for their assistance during the fieldwork in the Philippines. We thank M.L.S. Leido and H. Lacbawan of the Mines and Geosciences Bureau for their assistance in XRD analysis. We would like to acknowledge the CAD-PAGASA for providing the rainfall data from Laoag and Dagupan weather stations. We thank A. Estanislao of the Mines and Geosciences Bureau for editing the manuscript. We are deeply grateful to the anonymous reviewers for giving relevant comments, questions, and suggestions that greatly improved this manuscript. This study was supported by the Japan Society for the Promotion of Science KAKENHI Grant-in-Aid for Young Scientist 20J1425.

REFERENCES

ABRAM N, WEBSTER J, DAVIES P, DULLO W. 2001. Biological response of coral reefs to sea surface temperature variation: evidence from the raised Holocene reefs of Kikai-jima (Ryukyu Islands, Japan). Coral Reefs 20(3): 221–234. DOI:10.1007/s003380100163

BARNES DJ, LOUGH JM. 1989. The nature of skeletal density banding in scleractinian corals: fine banding and seasonal patterns. Journal of Experimental Marine Biology and Ecology 126(2): 119–134. DOI:10.1016/0022-0981(89)90084-1

BARNES DJ, LOUGH JM. 1993. On the nature and causes of density banding in massive coral skeletons. Journal of Experimental Marine Biology and Ecology 167(1): 91–108. DOI:10.1016/0022-0981(93)90186-R

BRACHERT TC, CORRÈGE T, REUTER M, WROZYNA C, LONDEIX L, SPRETER P, PERRIN C. 2020. An assessment of reef coral calcification over the late Cenozoic. Earth-Science Reviews 204: 103154. DOI: 10.1016/j.earscirev.2020.103154

BUDDEMEIER RW, MARAGOS JE, KNUTSON DW. 1974. Radiographic studies of reef coral exoskeletons: rates and patterns of coral growth. Journal of Experimental Marine Biology and Ecology 14(2): 179–199. DOI:10.1016/0022-0981(74)90024-0

CABIOCH G, MONTAGGIONI LF, FAURE G, RIBAUD-LAURENTI A. 1999. Reef coralgal assemblages as recorders of paleobathymetry and sea level changes in the Indo-Pacific province. Quaternary Science Reviews 18(14): 1681–1695. DOI: 10.1016/S0277-3791(99)00014-1

CARTON JA, GIESE BS. 2008. A reanalysis of ocean climate using Simple Ocean Data Assimilation (SODA). Monthly Weather Review 136(8): 2999–3017. DOI:

10.1175/2007MWR1978.1

CRABBE MJC, SMITH DJ. 2005. Sediment impacts on growth rates of Acropora and Porites corals from fringing reefs of Sulawesi, Indonesia. Coral Reefs 24(3): 437–441. DOI: 10.1007/s00338-005-0004-6

CUEVAS DN, SHERMAN CE, RAMÍREZ W, HUBBARD DK. 2009. Coral growth rates from the Holocene Cañada Honda fossil reef, Southwestern Dominican Republic: Comparisons with modern counterparts in high sedimentation settings. Caribbean Journal of Science 45(1): 94–109. DOI:10.18475/cjos.v45i1.a13

DIZON RM, YAP HT. 2005. Coral responses in single-and mixed-species plots to nutrient disturbance. Marine Ecology Progress Series 296: 165–172. DOI: 10.3354/meps296165

DODGE RE, VAISNYS JR. 1977. Coral populations and growth patterns: responses to sedimentation and turbidity associated with dredging. Journal of Marine Research 35(4): 715.

GOODKIN NF, SWITZER AD, MCCORRY D, DEVANTIER L, TRUE JD, HUGHEN KA, ANGELINE N, YANG TT. 2011. Coral communities of Hong Kong: long-lived corals in a marginal reef environment. Marine Ecology Progress Series 426: 185–196. DOI:10.3354/meps09019

GRIGG RW. 1981. Coral reef development at high latitudes in Hawaii. Proc 4th Int Coral Reef Symp 1: 687–693.

HEATON TJ, KÖHLER P, BUTZIN M, BARD E, REIMER RW, AUSTIN WE, RAMSEY CB, GROOTES PM, HUGHEN KA, KROMER B, REIMER PJ. 2020. Marine20—the marine radiocarbon age calibration curve (0–55,000 cal BP). Radiocarbon 62(4): 779–820. DOI: 10.1017/RDC.2020.68

HIGUCHI T, AGOSTINI S, CASARETO BE, SUZUKI Y, YUYAMA I. 2015. The northern limit of corals of the genus *Acropora* in temperate zones is determined by their resilience to cold bleaching. Scientific Reports 5(1): 1–9. DOI: 10.1038/srep18467

HONGO C, KAYANNE H. 2010. Holocene sea-level record from corals: Reliability of paleodepth indicators at Ishigaki Island, Ryukyu Islands, Japan. Palaeogeography, Palaeoclimatology, Palaeoecology 287(1–4): 143–151. DOI: 10.1016/j.palaeo.2010.01.033

JAVELOSA RS. 1994. Active Quaternary environments in the Philippine mobile belt: [unpublished Ph.D. dissertation, thesis]. International Institute for Aerospace Survey and Earth Sciences (ITC), Enschede, The Netherlands.

JOHNSON KG, PÉREZ ME. 2006. Skeletal extension rates of Cenozoic Caribbean reef corals. Palaios 21(3): 262–271. DOI:10.2110/palo.2004.p04-52

KLEIN R, PÄTZOLD J, WEFER G, LOYA Y. 1993. Depth-related timing of density band formation in *Porites* spp. corals from the Red Sea inferred from X-ray chronology and stable isotope composition. Marine Ecology Progress Series. p. 99–104. https://www.jstor.org/stable/24833602

KLEYPAS JA, MCMANUS JW, MENEZ LA. 1999. Environmental limits to coral reef development: where do we draw the line? American Zoologist 39(1): 146–159. DOI: 10.1093/icb/39.1.146

KNUTSON DW, BUDDEMEIER RW, SMITH SV. 1972. Coral chronometers: seasonal growth bands in reef corals. Science 177(4045): 270–272. DOI: 10.1126/

science.177.4045.270

KOBAYASHI K, NIU E, ITOH S, YAMAGATA H, LOMTATIDZE Z, JORJOLIANI I, NAKAMURA K, FUJINE H. 2007. The compact 14C AMS facility of Paleo Labo Co., Ltd., Japan. Nuclear Instruments and Methods in Physics Research Section B: Beam Interactions with Materials and Atoms 259(1): 31–35. DOI: 10.1016/j.nimb.2007.01.144

LIU Z, BRADY E, LYNCH-STIEGLITZ J. 2003. Global ocean response to orbital forcing in the Holocene. Paleoceanography 18(2). DOI: 10.1029/2002PA000819

LIU Z, ZHU J, ROSENTHAL Y, ZHANG X, OTTO-BLIESNER BL, TIMMERMANN A, SMITH RS, LOHMANN G, ZHENG W, TIMM OE. 2014. The Holocene temperature conundrum. Proceedings of the National Academy of Sciences 111(34): E3501–E3505. DOI: 10.1073/pnas.1407229111

LOUGH JM, BARNES DJ. 2000. Environmental controls on growth of the massive coral Porites. Journal of Experimental Marine Biology and Ecology 245(2): 225–243. DOI:10.1016/S0022-0981(99)00168-9

LOUGH JM, COOPER TF. 2011. New insights from coral growth band studies in an era of rapid environmental change. Earth-Science Reviews 108(3–4): 170–184. DOI:10.1016/j.earscirev.2011.07.001

MAEDA Y, SIRINGAN FP. 2004. Atlas of Holocene notches and the coral reef terraces of the Philippine Islands. Nature and Human Activities 8: 97–175.

MATEO ZRP, SIRINGAN FP. 2016. Morphological and Sedimentological Signatures of Late Holocene Prodelta Lobes in Lingayen Gulf, Philippines. Journal of Coastal Research 32(2): 354–364. DOI: 10.2112/JCOASTRES-D-14-00023.1

MATSUZAKI H, NAKANO C, TSUCHIYA YS, ITO S, MORITA A, KUSUNO H, MIYAKE Y, HONDA M, BAUTISTA AT, KAWAMOTO M, TOKUYAMA H. 2015. The status of the AMS system at MALT in its 20th year. Nuclear Instruments and Methods in Physics Research Section B: Beam Interactions with Materials and Atoms 361: 63–68. DOI:10.1016/j.nimb.2015.05.032

MAXWELL KV, RAMOS NT, TSUTSUMI H, CHOU YC, DUAN F, SHEN CC. 2018. Late Quaternary uplift across northwest Luzon Island, Philippines constrained from emergent coral reef terraces. Earth Surface Processes and Landforms 43(15): 3114–3132. DOI:10.1002/esp.4474

MITSUGUCHI T, MATSUMOTO E, UCHIDA T. 2003. Mg/Ca and Sr/Ca ratios of *Porites* coral skeleton: Evaluation of the effect of skeletal growth rate. Coral Reefs 22(4): 381–388. DOI: 10.1007/s00338-003-0326-1

MORIMOTO M, KAYANNE H, ABE O, MCCULLOCH MT. 2007. Intensified mid-Holocene Asian monsoon recorded in corals from Kikai Island, subtropical northwestern Pacific. Quaternary Research 67: 204–214. DOI:10.1016/j.yqres.2006.12.005

MORIYA T, TAKEYAMA M, SAKURAI H, UMEBAYASHI T, TOYOGUCHI T, SHIRAISHI T, MIYAHARA H, OHYAMA M, NOZAWA K, ITO S, ITOH S. 2019. Status of the AMS system at Yamagata University. Nuclear Instruments and Methods in Physics Research Section B: Beam Interactions with Materials and Atoms 439: 94–99. DOI:10.1016/j.nimb.2018.11.004

OTA Y, MACHIDA H, HORI N, KONISHI K, OMURA A. 1978. Holocene raised coral reefs of Kikai-jima (Ryukyu Islands). Geographical Review of Japan 51(2): 109–130. DOI: 10.4157/grj.51.109

PÄTZOLD J. 1984. Growth rhythms recorded in stable isotopes and density bands in the reef coral *Porites lobata* (Cebu, Philippines). Coral Reefs 3(2): 87–90. DOI: 10.1007/BF00263758

RAMOS NT, TSUTSUMI H. 2010. Evidence of large prehistoric offshore earthquakes deduced from uplifted Holocene marine terraces in Pangasinan Province, Luzon Island, Philippines. Tectonophysics 495(3–4): 145–158. DOI:10.1016/j.tecto.2010.08.007

REYNOLDS RW, SMITH TM. 1994. Improved global sea surface temperature analyses using optimum interpolation. Journal of Climate 7(6): 929–948. DOI: 10.1175/1520-0442(1994)007<0929:IGSSTA>2.0.CO;2

ROGERS CS. 1990. Responses of coral reefs and reef organisms to sedimentation. Marine ecology progress series. Oldendorf 62(1): 185–202.

SASAKI K, OMURA A, MURAKAMI K, SAGAWA N, NAKAMORI T. 2004. Interstadial coral reef terraces and relative sea-level changes during marine oxygen isotope stages 3–4, Kikai Island, central Ryukyus, Japan. Quaternary International 120(1): 51–64. DOI:10.1016/j.quaint.2004.01.006

SCOFFIN TP, TUDHOPE AW, BROWN BE, CHANSANG H, CHEENEY RF. 1992. Patterns and possible environmental controls of skeletogenesis of *Porites lutea*, South Thailand. Coral Reefs 11(1): 1–11. DOI:10.1007/BF00291929

SIRINGAN FP, SHEN CC, LIN K, ABIGANIA MIT, GONG SY. 2016. Coral-based Holocene sea level of Paraoir, western Luzon, Philippines. Journal of Asian Earth Sciences 123: 61–66. DOI: 10.1016/j.

jseaes.2016.03.022

SHEN CC, SIRINGAN FP, LIN K, DAI CF, GONG SY. 2010. Sea-level rise and coral-reef development of Northwestern Luzon since 9.9 ka. Palaeogeography, Palaeoclimatology, Palaeoecology 292(3–4): 465–473. DOI:10.1016/j.palaeo.2010.04.007

SOWA K, WATANABE T, KAN H, YAMANO H. 2014. Influence of land development on Holocene *Porites* coral calcification at Nagura bay, Ishigaki island, Japan. PLOS ONE 9(2): e88790. DOI:10.1371/journal.pone.0088790

SUGIHARA K, NAKAMORI T, IRYU Y, SASAKI K, BLANCHON P. 2003. Holocene sea-level change and tectonic uplift deduced from raised reef terraces, Kikai-jima, Ryukyu Islands, Japan. Sedimentary Geology 159(1–2): 5–25. DOI:10.1016/S0037-0738(03)00092-7

SUZUKI A, KAWAHATA H, TANIMOTO Y, TSUKAMOTO H, YUKINO I. 2000. Skeletal isotopic record of a *Porites* coral during the 1998 mass bleaching event. Geochemical Journal 34(4): 321–329. DOI: 10.2343/geochemj.34.321

VAN DER PLICHT J, RAMSEY CB, HEATON TJ, SCOTT EM, TALAMO S. 2020. Recent developments in calibration for archaeological and environmental samples. Radiocarbon 62(4): 1095–1117. DOI:10.1017/RDC.2020.22

WALKER MJC, BERKELHAMMER M, BJORCK S, CWYNAR LC, FISHER DA, LONG AJ, LOWE JJ, NEWHAM RM, RASUSSEN SO, WEISS H. 2012. Formal subdivision of the Holocene Series/Epoch: a Discussion Paper by a Working Group of INTIMATE (Integration of Ice-core, Marine and Terrestrial records) and the Subcommission on Quaternary Stratigraphy (International Commission on Stratigraphy). Journal of Quaternary Science 27: 649–659. DOI:10.1002/jqs.2565

APPENDIX 2: Publication

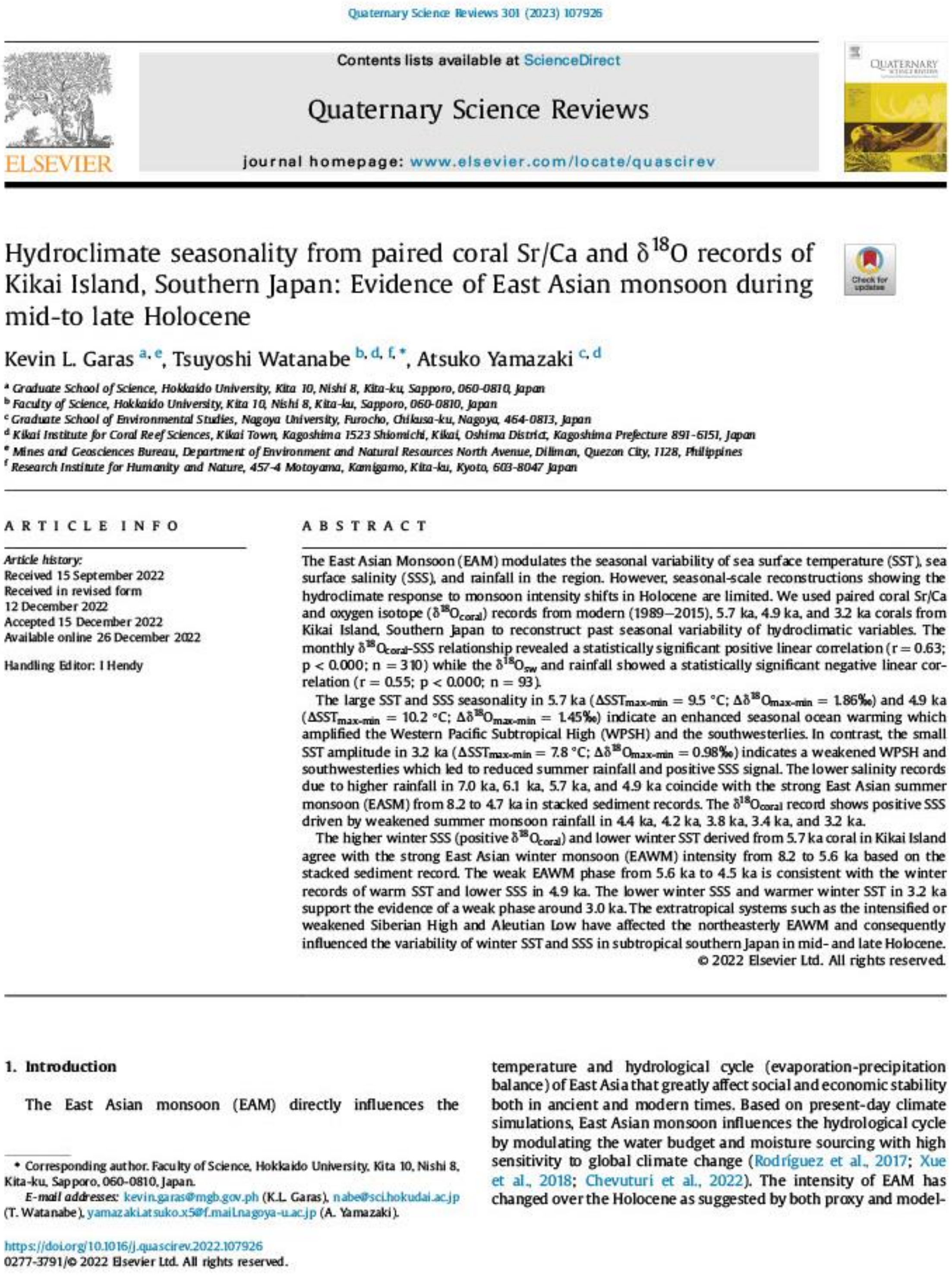

Quaternary Science Reviews 301 (2023) 107926

Contents lists available at ScienceDirect

Quaternary Science Reviews

journal homepage: www.elsevier.com/locate/quascirev

Hydroclimate seasonality from paired coral Sr/Ca and δ^{18}O records of Kikai Island, Southern Japan: Evidence of East Asian monsoon during mid-to late Holocene

Kevin L. Garas [a, e], Tsuyoshi Watanabe [b, d, f, *], Atsuko Yamazaki [c, d]

[a] *Graduate School of Science, Hokkaido University, Kita 10, Nishi 8, Kita-ku, Sapporo, 060-0810, Japan*
[b] *Faculty of Science, Hokkaido University, Kita 10, Nishi 8, Kita-ku, Sapporo, 060-0810, Japan*
[c] *Graduate School of Environmental Studies, Nagoya University, Furocho, Chikusa-ku, Nagoya, 464-0813, Japan*
[d] *Kikai Institute for Coral Reef Sciences, Kikai Town, Kagoshima 1523 Shiomichi, Kikai, Oshima District, Kagoshima Prefecture 891-6151, Japan*
[e] *Mines and Geosciences Bureau, Department of Environment and Natural Resources North Avenue, Diliman, Quezon City, 1128, Philippines*
[f] *Research Institute for Humanity and Nature, 457-4 Motoyama, Kamigamo, Kita-ku, Kyoto, 603-8047 Japan*

ARTICLE INFO

Article history:
Received 15 September 2022
Received in revised form
12 December 2022
Accepted 15 December 2022
Available online 26 December 2022

Handling Editor: I Hendy

ABSTRACT

The East Asian Monsoon (EAM) modulates the seasonal variability of sea surface temperature (SST), sea surface salinity (SSS), and rainfall in the region. However, seasonal-scale reconstructions showing the hydroclimate response to monsoon intensity shifts in Holocene are limited. We used paired coral Sr/Ca and oxygen isotope ($\delta^{18}O_{coral}$) records from modern (1989–2015), 5.7 ka, 4.9 ka, and 3.2 ka corals from Kikai Island, Southern Japan to reconstruct past seasonal variability of hydroclimatic variables. The monthly $\delta^{18}O_{coral}$-SSS relationship revealed a statistically significant positive linear correlation ($r = 0.63$; $p < 0.000$; $n = 310$) while the $\delta^{18}O_{sw}$ and rainfall showed a statistically significant negative linear correlation ($r = 0.55$; $p < 0.000$; $n = 93$).

The large SST and SSS seasonality in 5.7 ka ($\Delta SST_{max-min} = 9.5$ °C; $\Delta\delta^{18}O_{max-min} = 1.86‰$) and 4.9 ka ($\Delta SST_{max-min} = 10.2$ °C; $\Delta\delta^{18}O_{max-min} = 1.45‰$) indicate an enhanced seasonal ocean warming which amplified the Western Pacific Subtropical High (WPSH) and the southwesterlies. In contrast, the small SST amplitude in 3.2 ka ($\Delta SST_{max-min} = 7.8$ °C; $\Delta\delta^{18}O_{max-min} = 0.98‰$) indicates a weakened WPSH and southwesterlies which led to reduced summer rainfall and positive SSS signal. The lower salinity records due to higher rainfall in 7.0 ka, 6.1 ka, 5.7 ka, and 4.9 ka coincide with the strong East Asian summer monsoon (EASM) from 8.2 to 4.7 ka in stacked sediment records. The $\delta^{18}O_{coral}$ record shows positive SSS driven by weakened summer monsoon rainfall in 4.4 ka, 4.2 ka, 3.8 ka, 3.4 ka, and 3.2 ka.

The higher winter SSS (positive $\delta^{18}O_{coral}$) and lower winter SST derived from 5.7 ka coral in Kikai Island agree with the strong East Asian winter monsoon (EAWM) intensity from 8.2 to 5.6 ka based on the stacked sediment record. The weak EAWM phase from 5.6 ka to 4.5 ka is consistent with the winter records of warm SST and lower SSS in 4.9 ka. The lower winter SSS and warmer winter SST in 3.2 ka support the evidence of a weak phase around 3.0 ka. The extratropical systems such as the intensified or weakened Siberian High and Aleutian Low have affected the northeasterly EAWM and consequently influenced the variability of winter SST and SSS in subtropical southern Japan in mid- and late Holocene.

1. Introduction

The East Asian monsoon (EAM) directly influences the temperature and hydrological cycle (evaporation-precipitation balance) of East Asia that greatly affect social and economic stability both in ancient and modern times. Based on present-day climate simulations, East Asian monsoon influences the hydrological cycle by modulating the water budget and moisture sourcing with high sensitivity to global climate change (Rodríguez et al., 2017; Xue et al., 2018; Chevuturi et al., 2022). The intensity of EAM has changed over the Holocene as suggested by both proxy and model-

---

[*] Corresponding author. Faculty of Science, Hokkaido University, Kita 10, Nishi 8, Kita-ku, Sapporo, 060-0810, Japan.

E-mail addresses: kevin.garas@mgb.gov.ph (K.L. Garas), nabe@sci.hokudai.ac.jp (T. Watanabe), yamazaki.atsuko.x5@f.mail.nagoya-u.ac.jp (A. Yamazaki).

https://doi.org/10.1016/j.quascirev.2022.107926

based reconstructions (Jiang et al., 2013; Dong et al., 2018; Kaboth-Bahr et al., 2021; Zhang et al., 2021). Using seasonal-scale reconstructions, the Holocene (11,700 years ago to present) climatic shifts from warming to cooling conditions can give analogue to the present and future response of EAM. However, understanding the past and future monsoon dynamics is quite challenging given the complex forcings and the scarcity of data with intra-seasonal- to interannual resolution (Mohtadi et al., 2016).

Monsoon records from East Asia were reconstructed from paleoclimate archives in cave $\delta^{18}O$, marine sediments (Tian et al., 2010; Ujiié et al., 2003; Kajita et al., 2018), and lake sediments (Chen et al., 2015; Goldsmith et al., 2017). Speleothem $\delta^{18}O$ records show an increasing trend of isotopic values due to the enrichment of heavier ^{18}O isotope indicating a rapid retreat of EASM rainfall from 6000 years BP (Dykoski et al., 2005; Cosford et al., 2008; Dong et al., 2018). Sediment core-based paleoclimate archives do not support the rainfall interpretation of speleothem $\delta^{18}O$ arguing that it has bias to moisture source (Maher, 2008; Pausata et al., 2011; Kaboth-Bahr et al., 2021; Dayem et al., 2010). The reanalysis of atmospheric circulation and $\delta^{18}O$ of modern precipitation suggests that the speleothem $\delta^{18}O$ reflects the paleomonsoon changes driven by westerlies migration rather than variation in the precipitation amount (Chiang et al., 2020). Disagreements due to differing interpretations of paleoclimate archives lead to unresolved questions about the paleomonsoon dynamics. Furthermore, seasonally resolved paleoclimate data are scarce because of the inherent limitation of the widely-used paleoclimate materials (i.e., low sedimentation rate, low carbonate deposition rate). The input from marine-based paleoclimate records in understanding paleomonsoon is also limited.

Several climate models indicate the importance of ocean conditions (i.e., temperature, salinity) and their interaction with low-level wind circulation (Li et al., 2010; Jiang et al., 2013; Piao et al., 2020) in the study of EAM. The evaporation-precipitation balance as a function of atmosphere-ocean surface exchange is often linked to the seasonal variability of salinity (Helm et al., 2010; Bingham et al., 2012). Compared to past ocean temperature reconstructions, salinity records from Holocene are scarce. To further understand the regional climate during Holocene, hydroclimate signals such as SST, SSS, and rainfall should be reconstructed in higher temporal resolution. Seasonal-scale reconstruction can explain the summer and winter variations of East Asian monsoon. Modern and fossil coral records from Southern Japan are excellent archives of SST and SSS that are being modulated by ocean-climate systems such as Pacific Decadal Oscillation (PDO) and EASM (Morimoto et al., 2007; Kawakubo et al., 2017; Watanabe et al., 2014). Coral skeleton incorporates isotopes and trace elements that provide proxy records for past SST, salinity, and rainfall changes in seasonal to decadal resolution. Coral Sr/Ca is inversely correlated to water temperature and has been widely used to track SST changes in seasonal to decadal timescales (Beck et al., 1992). The coral oxygen isotope ($\delta^{18}O_{coral}$) is a function of water temperature (Gagan et al., 2006; Watanabe et al., 2001) and the $\delta^{18}O$ of the seawater ($\delta^{18}O_{sw}$) changes (Julliet-Leclerc and Schmidt, 2000). The $\delta^{18}O_{sw}$ is estimated using paired coral Sr/Ca and $\delta^{18}O_{coral}$ measurements by removing the SST component from the $\delta^{18}O_{coral}$ (Ren et al., 2003; Cahyarini et al., 2008; Nurhati et al., 2011).

Here we present paired coral Sr/Ca-SST and $\delta^{18}O_{coral}$ records from modern and fossil corals from Kikai Island, Southern Japan. The coral Sr/Ca was used to quantitatively estimate the mean, maximum, and minimum SSTs of the different time-windows of mid-to late Holocene. The seasonal SSS variation was reconstructed using the monthly-resolved $\delta^{18}O_{coral}$. Rainfall changes are reflected by the monthly-resolved $\delta^{18}O_{sw}$ (Morimoto et al., 2002; Gagan et al., 2006; Cahyarini et al., 2008; Nurhati et al., 2011; Thompson et al., 2022). Coral studies from Hainan Island, Southern China (Sun et al., 2005; Deng et al., 2009) and Ryukyu Archipelago, Southern Japan (Morimoto et al., 2007; Asami et al., 2020) have provided better understanding of the seasonal monsoon dynamics during mid-Holocene. Paleoclimate models are also focused on the EAM dynamics in mid-Holocene since it can be used as future analogue to recent warming climate (Jiang et al., 2013; Piao et al., 2020). Due to data gaps, the response of hydroclimate seasonality from mid-to late Holocene has yet to be understood.

2. Climate and geology of sampling site

Fossil *Porites* corals are common bioclast components of limestone of the uplifted marine terraces in Kikai Island, Kagoshima Prefecture, Southern Japan. The island (28°16′ to 28°22′N and 129°55′ to 130°02′E) is situated in the eastern fringe of East China Sea in the northern part of Ryukyu Archipelago (Fig. 1A). The island is characterized by an offlap sequence of four marine terraces. These are situated up to 13 m above mean sea level and were formed both by seismic events and sea level fall (Fig. 1B). A series of field surveys were conducted to collect modern and fossil coral samples from Holocene uplifted marine terraces in the island from 2014 to 2016. Modern and fossil coral cores were drilled in Shiomichi Bay in June 2015. In September 2016, two well-preserved fossil corals were selected from several *Porites* colonies.

SST from Advanced Very High-Resolution Radiometer (AVHRR) datasets recorded from 1981 to 2015 show maximum SST reached 28.6 °C–28.7 °C between July and August while minimum SST was 20.6 °C recorded within February to March (Fig. 1C). Gridded ocean reanalysis dataset from Simple Ocean Data Assimilation (SODA; http://apdrc.soest.hawaii.edu/dods/public_data/SODA/soda_3.3.1/) shows that monthly average SSS around Kikai Island from 1980 to 2015 varies from 34.78 psu in February to 34.31 psu in July (Fig. 1D). Accumulated monthly precipitation calculated from in-situ daily measurements (Fig. 1E) from Northern Kikai Island collected from 2007 to 2015 shows two peaks of high precipitation in June (ave. 248 mm) and September (ave. 175 mm) and lowest value in December (average of 72 mm). This rainfall pattern follows the "onset-break-revival" cycle of the East Asian summer monsoon (Chen et al., 2004). Based on Climate Prediction Center (CPC) Merged Analysis of Precipitation (CMAP) rainfall and reanalysis data, southern Japan and central China around Yangtze River Basin have generally two active rainfall peaks during the onset in early to mid-June and after the revival from August to October. The monsoon break occurs in a span of about a month from late July to August. The break is the result of seasonal march of the western Pacific tropical high. The subsequent revival is attributed to the enhancement of cyclonic circulation and intensification of the intertropical convergence zone (ITCZ). SST warming of NW Pacific sets up a necessary condition of monsoon convection and northward march of ITCZ leading to its mature stage (Ueda et al., 2009). Southwesterly EASM brings warm, humid air masses that significantly increases the precipitation while northeasterly EAWM is generally cold and dry air mass with low precipitation (Fig. 1A).

3. Materials and methods

3.1. Diagenesis screening and radiocarbon age dating

Ten (10) fossil corals were collected from Kikai Island from May 2015 to September 2016. The presence of secondary aragonite and calcite was examined using X-ray Diffraction (XRD; Rigaku MiniFlex II) and Scanning Electron Microscopy (SEM; Hitachi Miniscope TM-1000) at Hokkaido University. Three fossil corals have well-preserved aragonitic skeleton without secondary development of

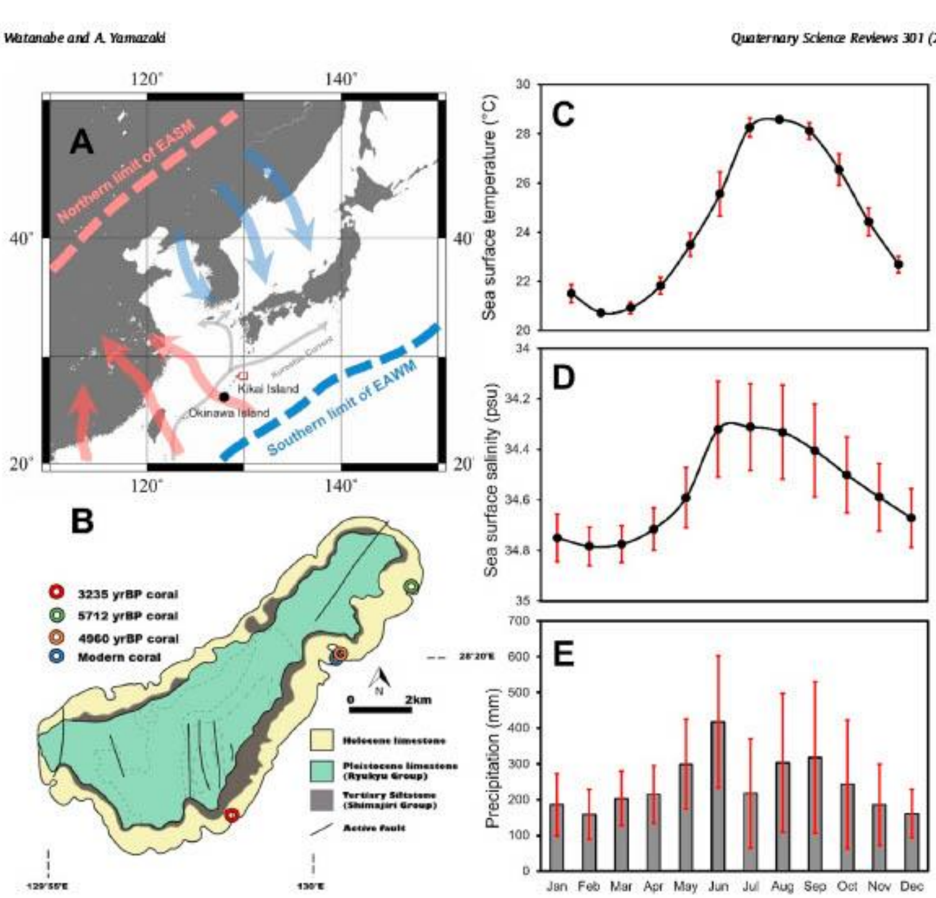

Fig. 1. Kikai Island (red box) is situated in the East Asian Monsoon region (A) that influences the seasonal variation of sea surface temperature (C), sea surface salinity (D) and precipitation (E). The island is underlain by Holocene uplifted marine terraces along its coastal zone (B). Modern and fossil corals were collected from the uplifted terraces. . (For interpretation of the references to colour in this figure legend, the reader is referred to the Web version of this article.)

abiogenic aragonite and calcite. XRD shows that well-preserved corals are predominantly composed of aragonite (Fig. S1). The SEM confirmed that skeletal microstructures are intact with well-preserved primary aragonitic composition (Fig. S1). Thus, the geochemical data will not be affected by diagenesis. Pristine portions were chipped off from the two fossil corals and analyzed using ^{14}C-accelerator mass spectrometry at Yamagata University. ^{14}C age was calibrated to calendar year using Calib 8.2 with the Marine20 dataset (Heaton et al., 2020). The radiocarbon age dates are corrected using the regional reservoir offset in Marine20 dataset. However, local reservoir effect (ΔR) was not calculated. Radiocarbon dating has yielded calibrated ages of 3235 ± 20 years BP (KIKJ-20160907-II) referred hereafter as "3.2 ka" and 5712 ± 24 years BP (KIST-20160518-I) referred hereafter as "5.7 ka".

3.2. Trace element and oxygen isotope analyses

To prepare coral slabs (Figs. S1A–B), slices measuring approximately 5 mm in thickness were cut along major growth axis using a rock saw with diamond-tipped blade. Each slab was rinsed with Milli-Q water in ultrasonicator and dried in 40 °C laboratory oven. Clean coral slabs were x-radiographed using SOFTEX M60 with a digital imaging sensor. Samples were exposed in 50 kV and 1 mA set-up for 8 s.

Fossil coral samples were milled continuously at an average interval along the corallite growth direction. A 2.0 mm thick and 3.5 mm wide ledge was prepared along the analysis line. We analyzed 18–24 subsamples/nominal year from the 5.7 ka coral (sampling interval: 0.2 mm) and 13–15 subsamples per nominal year from 3.2 ka coral (sampling interval: 0.15 mm). Approximately 12 subsamples per year were analyzed in 4960 years BP (referred hereafter as "4.9 ka") and modern coral (Kajita et al., 2017). Sr/Ca ratio was measured with an Inductively Coupled Plasma-Atomic Emission Spectrometry (iCAP 6300 ICP Spectrometer) using an automatic sample introduction set-up (CETAC ASX-260) at Hokkaido University. 90 μg (±10 μg) powder samples were dissolved with 25% HNO_3 solution and pre-calculated Milli-Q water to obtain 7 ppm Ca concentration aliquot. A reference solution of JCp-1 was measured at 5 sample intervals to correct instrumental drift. The analytical precision is ±0.07%RSD (SD of ±0.006 mmol/mol) using internal standard measurements of JCp-1 solution (Watanabe et al., 2020) Similar coral powder samples were used for oxygen and carbon isotope analysis. 30 μg (±10 μg) powder samples were reacted to 100% H_3PO_4 at 70 °C in an automated carbonate device Kiel IV. The $\delta^{18}O_{coral}$ were analyzed using Isotope Ratio Mass Spectrometer (MAT Finnigan 253) at Hokkaido University. The analytical precision for $\delta^{18}O_{coral}$ is ±0.03% RSD (SD of ±0.07‰) using replicate measurements of the NBS 19 ($n = 117$).

3.3. Calculation of $\delta^{18}O_{sw}$ and uncertainty estimation

Monthly age models for coral Sr/Ca and $\delta^{18}O_{coral}$ were developed using AnalySeries software version 2.0.8 (Paillard et al., 1996). Minima and maxima points of coral Sr/Ca were anchored respectively with maxima and minima points of SST. The same age model was used in $\delta^{18}O_{coral}$. The paired Sr/Ca and $\delta^{18}O_{coral}$ were resampled to monthly resolution using linear interpolation function.

The oxygen isotope in seawater ($\delta^{18}O_{sw}$) was isolated from the $\delta^{18}O_{coral}$ by removing the $\delta^{18}O_{SST}$ component using the Sr/Ca-SST slope (β), δ18Ocoral-SST slope (b), and the measured Sr/Ca values (Cahyarini et al., 2008) as follows:

$$\Delta\delta^{18}O_{sw-center} = \delta^{18}O_{coral} - \overline{\delta^{18}O_{coral}} - b\big/\beta \ x\,(Sr/Ca - \overline{Sr/Ca})$$

where Sr/Ca and $\delta^{18}O_{coral}$ are measured values, ($\overline{Sr/Ca}$, $\overline{\delta^{18}O_{coral}}$) are mean values, β is the Sr/Ca-SST slope, and b is the ($\delta^{18}O_{coral}$- $\delta^{18}O_{sw}$)-SST slope. The centering method was used to omit the intercept values in the regression slopes β and b from the calculation of $\delta^{18}O_{sw}$ because it could be the largest source of uncertainty in the calculation (Nurhati et al., 2011).

Watanabe and Pfeiffer (2022) combined the centering method with simple Monte Carlo simulation to propagate the analytical error and the uncertainty of regression slopes in the Sr/Ca-SST and $\delta^{18}O_{sw\text{-}center}$. We used the Sr/Ca-SST slope of −0.0643 ± 0.0026 mmol/mol/°C from modern Porites in Kikai Island (Kajita et al., 2017) and the ($\delta^{18}O_{coral}$- $\delta^{18}O_{sw}$)-SST slope of −0.20 ± 0.02‰$_{VPDB}$/°C (Julliet-Leclerc and Schmidt, 2000). The analytical errors are ±0.006 mmol/mol and ±0.07‰$_{VPDB}$ for Sr/Ca and $\delta^{18}O_{coral}$, respectively.

The error (SE) of monthly average was calculated from the year-to-year variability (1σ standard deviation/1σ SD) of uncertainties divided by the square root of number of chronological years (N) as $SE = 1\sigma SD/\sqrt{N}$.

3.4. Calculation of linear extension rate

The annual linear extension rate was calculated from the distance of two consecutive Sr/Ca maxima throughout the internal chronology of each coral colony. The linear extension rates are then compared to the annual Sr/Ca and $\delta^{18}O_{coral}$ to evaluate the effect of coral growth in geochemical records.

4. Results

4.1. Calibration of modern coral records to environmental variables

Temperature dependence of coral Sr/Ca ratio is shown by calibrating monthly-resolved Sr/Ca record from modern coral and corresponding SST data. We used the ordinary least square linear regression equation established between coral Sr/Ca and AVHRR SST data from Kikai Island within the period of 1989–2015 (Kajita et al., 2017).

$$Sr/Ca = 10.80\,(\pm 0.07) - 0.0643\,(\pm 0.0026) \text{ x SST } (^\circ C)$$

The slope of Sr/Ca-SST calibration is −0.0643 mmol/mol/°C. This slope is within the range of previously published Sr/Ca-SST slopes (−0.053 to 0.066) from Porites corals in southern Japan (Morimoto et al., 2007; Seki et al., 2012; Sowa et al., 2014; Asami et al., 2020).

Our Sr/Ca-SST largely covaries with the $\delta^{18}O_{coral}$ which suggests the temperature dependence of the oxygen isotopes in coral skeleton. Yet, it is also known that other oceanographic variables (i.e., SSS) can influence the oxygen isotopic fractionation. We regressed the monthly SSS data from SODA v3.3.1 to the monthly resolved $\delta^{18}O_{coral}$ from 1989 to 2015 (Fig. 2A). SSS and $\delta^{18}O_{coral}$ are statistically significant positive linear correlation ($r = 0.63$; $p < 0.000$; $n = 310$) wherein high and low SSS correspond to high and low $\delta^{18}O_{coral}$ (Fig. 2B). The seasonal cycle of $\delta^{18}O_{coral}$ is synchronous to the seasonal variation of SSS in Kikai Island which is consistent with published works in tropical western Pacific (Morimoto et al., 2002; Ramos et al., 2019; Reed et al., 2022). The least regression equation is as follows:

$$\delta^{18}O_{coral} = 1.49\,(\pm 0.10) \text{ x SSS} - 56.22\,(\pm 3.55)$$
$$(r = 0.634;\ p < 0.000;\ n = 310)$$

The reconstructed $\delta^{18}O_{sw}$ from 1989 to 2015 was compared to the accumulated monthly in-situ rainfall data from northern Kikai Island. The accumulated rainfall was calculated by adding up the daily rainfall record data. The 5-month running average was done for both datasets to systematically smoothen the time series profiles and to remove extremely high rainfall events. We plotted the 5-month running average of rainfall and $\delta^{18}O_{sw}$ from 2007 to 2015 as illustrated in Fig. 2C. Cross plot of the two variables has shown a statistically significant negative linear correlation ($r = 0.554$; $p < 0.000$; $n = 93$; Fig. 2D). It shows that the low (high) $\delta^{18}O_{sw}$ months occur in high (low) rainfall month.

4.2. Reconstructed Sr/Ca-SST and $\delta^{18}O_{coral}$ records from modern and fossil corals

Fig. 3A–D shows the coral Sr/Ca-SST (red) and centered $\delta^{18}O_{coral}$ (blue) records of modern and three fossil *Porites* colonies from Kikai Island. The range of Sr/Ca of modern coral is 8.86–9.59 mmol/mol (average = 9.17 mmol/mol; $n = 311$); 3.2 ka coral is 9.04–9.53 mmol/mol (average of 9.27 mmol/mol; $n = 459$); 4.9 ka coral is 8.69–9.64 mmol/mol (average of 9.08 mmol/mol; $n = 156$); and 5.7 ka coral is 8.99–9.60 mmol/mol (average of 9.22 mmol/mol; $n = 334$).

The reconstructed annual mean, maximum, and minimum Sr/Ca-SST records of modern, 3.2 ka, 4.9 ka, and 5.7 ka corals are shown in Table S1. The reconstructed SST from modern coral from 1989 to 2015 recorded a range of 20.8 °C–28.9 °C with mean SST of 25.4 °C. The confidence interval (68th percentile/1σ range) is 0.18–0.57 °C (median: 0.26 °C; Fig. S3). The summer and winter SSTs at 3.2 ka were 27.7 °C and 19.9 °C with annual mean SST of 24.1 °C. The confidence interval (68th percentile/1σ range) is 0.19–0.56 °C (median: 0.26 °C; Fig. S3). The summer at 4.9 ka was the warmest among the three Holocene time-windows with an average summer SST of 30.9 °C while winter SST was 20.7 °C (annual mean SST: 26.7). The confidence interval (68th percentile/1σ range) is 0.19–0.74 °C (median: 0.26 °C; Fig. S3). The 5.7 ka recorded the coldest winter among the three Holocene time-windows with an average winter SST of 18.5 °C. The summer and annual mean SSTs at 5.7 ka were 28.0 °C and 24.5 °C, respectively. The confidence interval (68th percentile/1σ range) is 0.62–0.82 °C (median: 0.66 °C; Fig. S3). The seasonality of SST was computed as the difference between maximum and minimum values. The Sr/Ca-

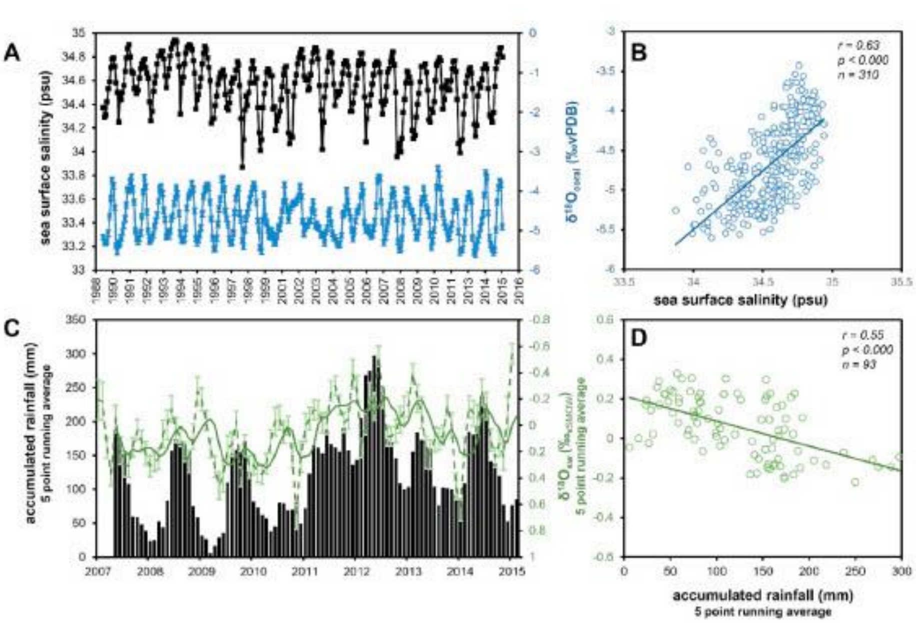

Fig. 2. Salinity records (black) from 1989 to 2015 around Kikai Island based on SODA v3.3.1 compared to monthly-resolved $\delta^{18}O$ (blue) of modern coral from Kikai Island (A). X-y plot (B) of the two datasets shows statistically significant positive linear correlation ($r = 0.634$, $p < 0.000$, $n = 310$). The regression equation is $\delta^{18}O_{coral} = 1.49\ (\pm 0.10) \times SSS - 56.22\ (\pm 3.55)$. Seawater $\delta^{18}O$ (green; dashed line = original data, solid line = 5 point running average) calculated from the coral Sr/Ca-SST and $\delta^{18}O$ records compared to the local precipitation data from Kikai Island covering 2007–2015(C). X-y plot (D) of the 5-point running average of both $\delta^{18}O_{sw}$ and rainfall shows a statistically significant negative linear correlation ($r = 0.554$; $p < 0.000$; $n = 93$). The regression equation is $\delta^{18}O_{sw} = -0.001\ (\pm 0.0002) \times \text{rainfall} + 0.20\ (\pm 0.03)$. . (For interpretation of the references to colour in this figure legend, the reader is referred to the Web version of this article.)

SST seasonal difference ($\Delta SST_{max-min}$) of modern, 3.2 ka, 4.9 ka, and 5.7 ka are 8.1 °C, 7.8 °C, 10.2 °C, and 9.5 °C. The mid-Holocene corals dated 5.7 ka and 4.9 ka recorded the largest $\Delta SST_{max-min}$ between summer and winter values. The late Holocene coral (3.2 ka) has relatively smaller $\Delta SST_{max-min}$ relative to mid-Holocene corals (Table S1).

The $\delta^{18}O_{coral}$ ranges (Table S2) from −5.09‰ to −3.23‰ (average of −4.44‰, $n = 334$) in 5.7 ka, −4.25‰ to −3.27‰ (average of −3.79‰, $n = 459$) in 3.2 ka, −4.77‰ and −3.32‰ (average of −4.16‰, $n = 156$) in 4.9 ka, and −5.18‰ and −4.02‰ (average of −4.66‰, $n = 311$) in modern coral (1989–2015). The centered $\delta^{18}O_{coral}$ (Fig. 3) was calculated by removing the mean $\delta^{18}O_{coral}$ from the measured values. Modern, 3.2 ka, 4.9 ka, and 5.7 ka corals have seasonal amplitude of 1.16 ± 0.06‰, 0.98 ± 0.07‰, 1.45 ± 0.14‰, and 1.86 ± 0.06‰ respectively. Similarly, the mid-Holocene corals, 5.7 ka and 4.9 ka, reveal a larger seasonal range while the late Holocene (3.2 ka) coral shows the smallest seasonal range (Table S1).

4.3. $\delta^{18}O$ of seawater

Fig. 3E–H shows the centered $\delta^{18}O_{sw}$ records (green) from modern (1989–2015), 3.2 ka, 4.9 ka, and 5.7 ka corals estimated from paired coral Sr/Ca and $\delta^{18}O_{coral}$. Relative seasonality change was calculated by subtracting the mean monthly $\delta^{18}O_{sw}$ of modern coral (Fig. 4H) from the mean monthly $\delta^{18}O_{sw}$ of three fossil corals (Fig. 4E–G). A significant increase or decrease in the past seasonality was based on the exceedance to the 1σ standard deviation of the whole dataset. At 5.7 ka and 4.9 ka, there was a positive shift in $\delta^{18}O_{sw}$ in winter associated with reduced rainfall and/or higher SSS (higher $\delta^{18}O_{coral}$; Fig. 4A–B). This is opposite to the 3.2 ka record of negative change in $\delta^{18}O_{sw}$ due to enhanced rainfall and/or lower salinity (lower $\delta^{18}O_{coral}$; Fig. 4C). The $\delta^{18}O_{sw}$ shifted negatively in June to July at 5.7 ka and in September to November at 4.9 ka relating to the more rainfall during these months. The 3.2 ka coral recorded a reduced rainfall (positive $\delta^{18}O_{sw}$ changes) and higher SSS (higher summer $\delta^{18}O_{coral}$; Fig. 4C). The changes in coral-based SST, SSS, and rainfall records in different time-windows in mid-to late Holocene were possibly driven by the changes in the monsoon intensity.

4.4. Growth rate and coral geochemical records

Linear extension rates of modern, 3.2 ka, 4.9 ka, and 5.7 ka corals are 11.0 mm/year, 3.93 mm/year, 5.6 mm/year, and 8.7 mm/year respectively. Annual linear extensions of each *Porites* colony were compared to the annual Sr/Ca and $\delta^{18}O_{coral}$ calculated from the monthly resolved data of each year. Fig. S2A shows that plot of annual Sr/Ca and annual linear extension is highly scattered. It indicates that the extension rate does not strongly affect the variation of Sr/Ca in coral skeleton and vice versa. Cross plot (Fig. S2B) of annual $\delta^{18}O_{coral}$ and linear extension shows negative correlation as shown by the equation $\delta^{18}O_{coral} = 0.0105(\text{linear ext.})^2 - 0.266(\text{linear ext.}) - 3.0114$ ($r^2 = 0.7426$). The difference in the comparison of annual extension rate versus annual Sr/Ca and $\delta^{18}O_{coral}$ suggests that the linear extension is not solely affected by SST (Lough and

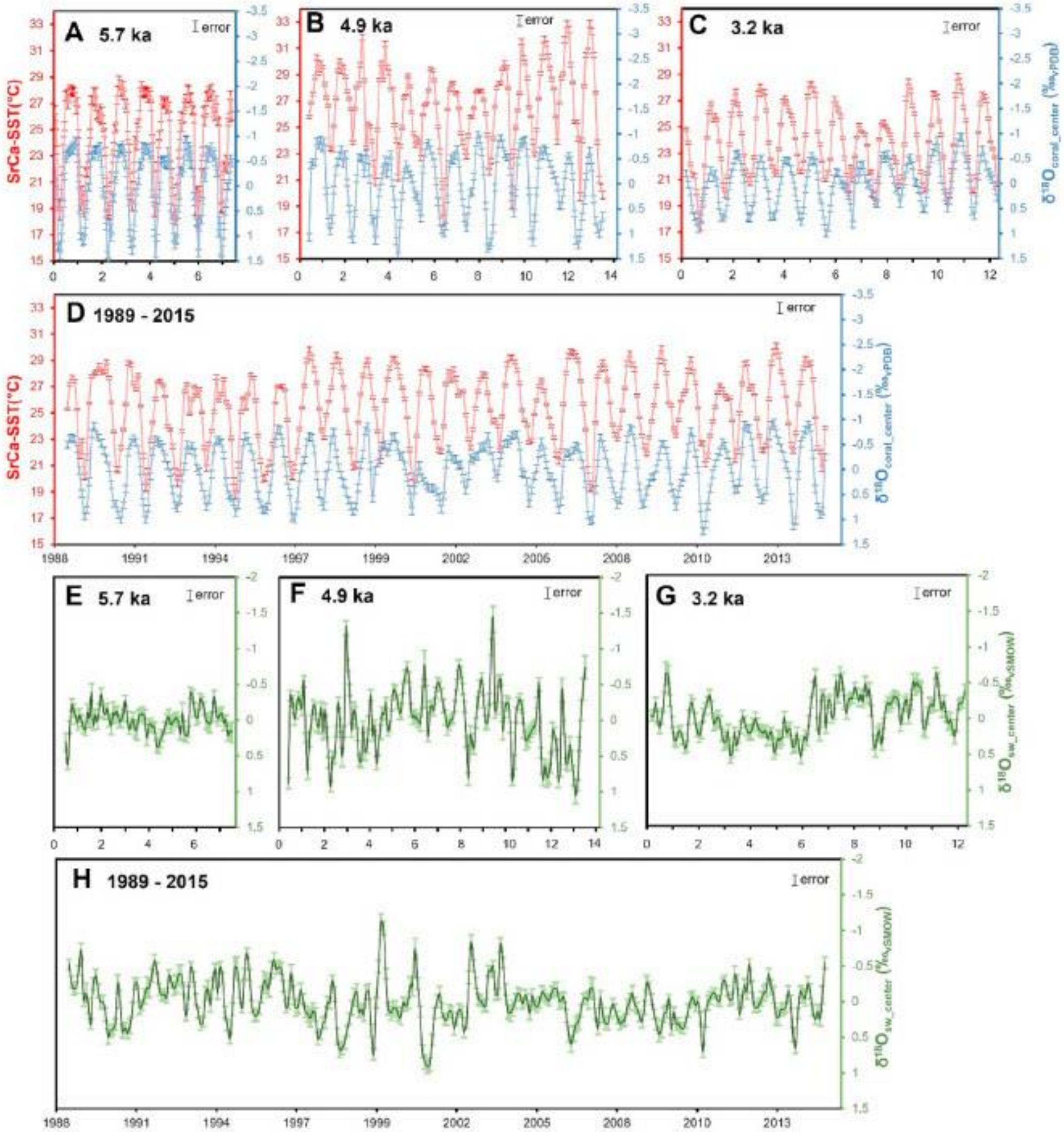

Fig. 3. Centered Sr/Ca-SST anomaly (red), $\delta^{18}O_{coral}$ (blue), and estimated $\delta^{18}O_{seawater}$ (green) of the modern (n = 26), 3.2 ka (n = 12), 4.9 ka (n = 13), and 5.7 ka (n = 7) corals from Kikai Island (n = no. of reconstructed years). Error bar represents the 1σ standard deviation (68% confidence interval) which shows the uncertainty estimates from analytical and calibration errors of Sr/Ca-SST and $\delta^{18}O_{coral}$ following the Monte Carlo simulation method (Watanabe and Pfeiffer, 2022). . (For interpretation of the references to colour in this figure legend, the reader is referred to the Web version of this article.)

Cooper, 2011). If the linear extension is solely influenced by SST, the two variables should be directly correlated. The negative correlation of $\delta^{18}O_{coral}$ and linear extension also supports that the $\delta^{18}O_{coral}$ variation is not only affected by SST but multiple variables (e.g. SSS, $\delta^{18}O_{sw}$).

5. Discussion

5.1. *Weakening of EASM in late Holocene recorded in fossil corals*

To investigate the seasonal SSS change in Holocene, we compiled the minimum, maximum, and annual mean $\delta^{18}O_{coral}$

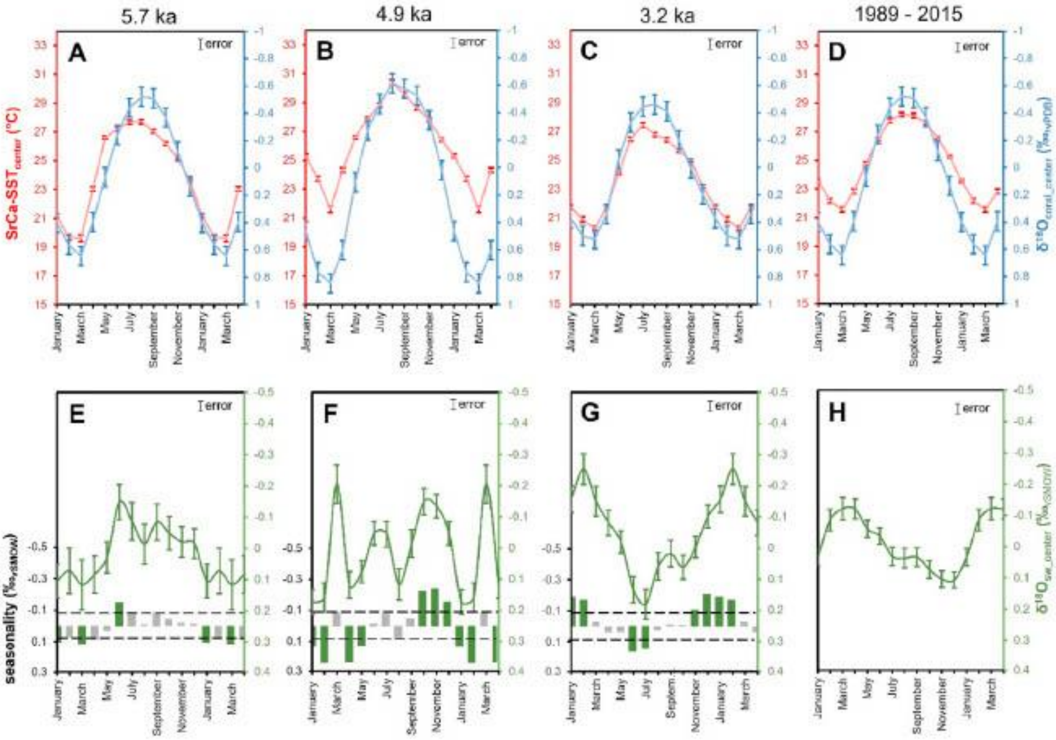

Fig. 4. Mean seasonal cycles of coral Sr/Ca-SST (red), δ^{18}O (blue), and estimated δ^{18}O of seawater (green) of modern and fossil corals from Kikai Island. Relative change in $\delta^{18}O_{sw}$ seasonality is represented by the green and gray bars. Green bars show anomalous increase/decrease exceeding the ± 1σ standard deviation of the modern coral seasonal cycle. Uncertainties of the monthly climatology is presented in the error bar calculated from the analytical error, calibration error, and year-to-year variability of the internal coral chronology. . (For interpretation of the references to colour in this figure legend, the reader is referred to the Web version of this article.)

records from fossil *Porites* in Kikai Island and Okinawa Island in Southern Japan (Fig. 5A; Kiyama et al., 2000; Abram et al., 2001; Morimoto et al., 2007; Asami et al., 2020). A steady decrease (~1.1‰) is observed in minimum (summer) and annual mean $\delta^{18}O_{coral}$ values from ~5.7 ka to ~3.4 ka. Following the $\delta^{18}O_{coral}$-SSS relationship (Fig. 3B) in Kikai, this trend suggests increasing SSS from ~5.7 ka to ~3.2 ka. The coral Sr/Ca-based SST reconstruction from 5.7 ka and 4.9 ka revealed that the annual mean SSTs were 24.5 °C and 26.7 °C respectively. The average summer SSTs at 5.7 ka and 4.9 ka were 28.0 °C and 30.9 °C. The summer SST at 4.9 ka was warmer by 2 °C relative to the present-day and represents a period of warmer and less saline water in the northern Ryukyu Archipelago of southern Japan. On the other hand, the 5.7 ka was cooler by 0.9 °C relative present-day and the SST record is comparable to the Sr/Ca-based SST records at 6.1 and 7.0 ka from Kikai Island (Morimoto et al., 2007). The surface water became cooler by 1.2 °C around 3.2 ka and summer SSS increased relative to 4.9 ka and 5.7 ka.

Aside from the summer rainfall, the freshwater discharge of the Changjiang river basin in China modulates the SSS variability (Siswanto et al., 2008) as reflected by the δ^{18}Ocoral from Koshiki Island in northern East China Sea (Watanabe et al., 2014). However, the Changjiang River discharge does not influence the SSS and $\delta^{18}O_{sw}$ in the Ryukyu Archipelago because of the strong Kuroshio current along the Okinawa Trough (Horikawa et al. , 2015). The pathway of Kuroshio current is located west of Amami Island Group which acts as a barrier from the freshwater discharge. Thus, the $\delta^{18}O_{sw}$ in corals from Kikai Island could not reflect large scale freshwater discharge from the Asian continent. The negative linear correlation between the coral-derived $\delta^{18}O_{sw}$ and local instrumental rainfall (Fig. 2D) suggests that monsoon-driven rainfall affects the oxygen isotope fractionation in Kikai corals. Using the coral-derived $\delta^{18}O_{sw}$-rainfall correlation, we explained the relative seasonal change in rainfall in 5.7 ka, 4.9 ka, and 3.2 ka by subtracting the mean monthly average of modern coral record from the monthly average of fossil coral records. The negative $\delta^{18}O_{sw}$ change in June to August and in September to November at 5.7 ka and 4.9 ka respectively corresponds to higher rainfall relative to the present-day (Fig. 4E–F). It also shows the positive shift in $\delta^{18}O_{sw}$ interpreted as decrease of rainfall at 3.2 ka (late Holocene) (Fig. 4G). The positive shift of $\delta^{18}O_{coral}$ (Fig. 4C) and $\delta^{18}O_{sw}$ (Fig. 4G) in summer months at 3.2 ka indicating a decrease in rainfall. The coral records revealed an enhanced summer monsoon rainfall in 5.7 ka and 4.9 ka then a reduced summer rainfall condition towards the late Holocene as shown by 3.2 ka.

Climate simulations have shown that the strengthening and weakening of Western Pacific Subtropical High (WPSH) are influenced by the meridional movement of heat and moisture from

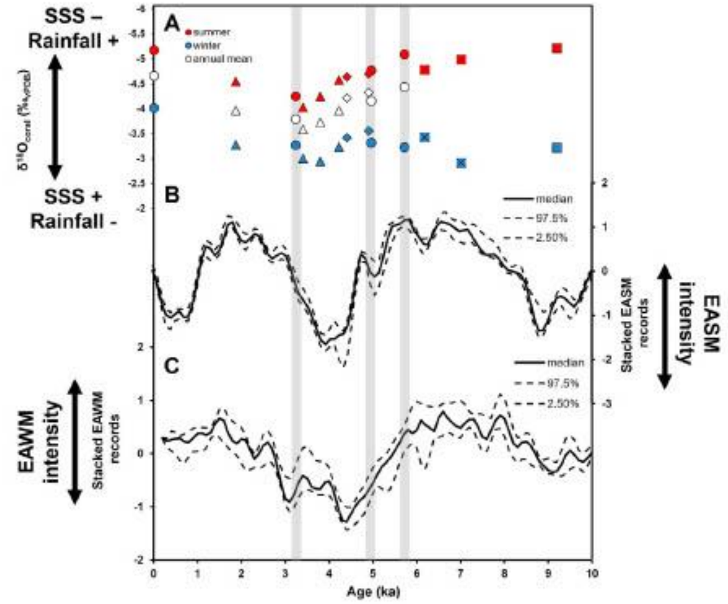

Fig. 5. Average maximum, minimum, and mean annual values of $\delta^{18}O_{coral}$ records (A) from Kikai Island (this study – circle; Abram et al., 2001 – triangle; Morimoto et al., 2007 – cross; Kiyama et al., 2001 – square) and Okinawa Island (Asami et al., 2020 – diamond) compared to the stacked EASM-sensitive marine and lake sediment records (B) and stacked EAWM-sensitive marine and lake sediment records (C). The position of the three fossil corals relative to other paleoclimate records is indicated by the gray bars.

tropics to subtropics and the zonal gradient between North Pacific and East Asian continent (Jiang et al., 2013; Piao et al., 2020). The seasonal-scale coral Sr/Ca-SST and $\delta^{18}O_{coral}$ records from 5.7 ka ($\Delta SST_{max-min} = 9.5$ °C; $\Delta\delta^{18}O_{max-min} = 1.86$‰) and 4.9 ka ($\Delta SST_{max-min} = 10.2$ °C; $\Delta\delta^{18}O_{max-min} = 1.45$‰) both have larger summer-winter difference which relates to seasonal SST and SSS amplitude. The large SST amplitude indicates an enhanced surface ocean warming from early spring to summer of 5.7 ka and 4.9 ka. This resulted in intensified WPSH and in turn, enhanced southwesterlies. The stronger southwesterlies carried more rainfall in subtropical southern Japan. This is evident in the more negative SSS signal from summer $\delta^{18}O_{coral}$ record. Conversely, the 3.2 ka coral ($\Delta SST_{max-min} = 7.8$ °C; $\Delta\delta^{18}O_{max-min} = 0.98$‰) has smaller seasonal SST and SSS amplitude. The small SST amplitude indicates a reduction in surface ocean warming from early spring to summer of 3.2 ka. This resulted in weakened WPSH and southwesterlies. This condition led to the reduced summer rainfall and positive SSS signal from summer $\delta^{18}O_{coral}$ record in 3.2 ka.

Our evidence from compiled $\delta^{18}O_{coral}$ from southern Japan supports the widely reported EASM intensification during mid-Holocene followed by EASM weakening towards the late Holocene. The compiled $\delta^{18}O_{coral}$ from southern Japan was compared to the stacked EASM records from marine and terrestrial sediments (Fig. 5B). The timing of the high and low rainfall in the reconstructed records is slightly different in the individual records. Linear resampling and low-pass filtering were done to address the issue on differing sampling resolutions of marine and terrestrial records used in the stacking (Kaboth-Bahr et al., 2021). The stacked sediment records show that the EASM was strong from 8.2 to 4.7 ka. The compiled $\delta^{18}O_{coral}$ recorded a relatively lower SSS and higher rainfall in 7.0 ka, 6.1 ka, 5.7 ka, and 4.9 ka, which occurred within the duration of intensified EASM from 8.2 to 4.7 ka. The annual mean and summer $\delta^{18}O_{coral}$ record shows higher SSS in 4.4 ka, 4.2 ka, 3.8 ka, 3.4 ka, and 3.2 ka. The seasonal $\delta^{18}O_{sw}$ trend of 3.2 ka coral indicated that positive SSS was accompanied by reduced summer rainfall (Fig. 4G). The stacked sediment records also indicated a weakened EASM intensity around 4.0 ka. Furthermore, marine sediment records from Japan Sea and Northern East China Sea included in the stacked EASM record both show positive SSS and negative rainfall signals around 3.3 ka which is consistent with the coral record (Kubota et al., 2015; Nagashima et al., 2013). The stacked records show intensified monsoon after ~3.0 ka until 1.0 ka then weakened again around 0.6 ka (Fig. 5B). This is the major disagreement between the stacked sediment records and published speleothem $\delta^{18}O$ records (Dong et al., 2018; Cosford et al., 2008; Dykoski et al., 2005). The source of offset in the timing and amplitude of speleothem $\delta^{18}O$ is probably the moisture source bias. The paleoclimate interpretation of speleothem $\delta^{18}O$ is subject to debate since this archive is often linked to moisture sourcing rather than amount-weighted $\delta^{18}O$ of precipitation (Maher, 2008; Dayem et al., 2010; Pausata et al., 2011). The $\delta^{18}O_{coral}$ record favors the stacked EASM sediment records rather than the speleothem $\delta^{18}O$. The 1.8 ka coral indicates a lower salinity which correlates to the intensified EASM and accompanying higher summer rainfall at 1.0–3.0 ka from the stacked sediment records (Fig. 5B). However, additional high resolution $\delta^{18}O_{coral}$ data are needed to confirm this trend since coral record after 3.2 ka is scarce.

5.2. Evidence of EAWM variability from fossil corals

The present-day winter SST, SSS, and rainfall in East Asia are primarily controlled by the intensity of winter monsoon. Reanalysis data and climate model simulation attributed the variation of winter monsoon intensity and winter temperature in East Asia with the changes of high latitude low-level tropospheric circulation (i.e. polar jet stream, Siberian high and Aleutian low) in boreal winter (Jhun and Lee, 2004). The compiled winter $\delta^{18}O_{coral}$ could reflect the variation of SSS during winter as a function of evaporation-precipitation balance. We also considered both winter SST and SSS as signals of the EAWM intensity. The cold winter temperature surge in eastern China, Korea, and Japan is an indicator of strong winter monsoon intensity (Jhun and Lee, 2004). In the coral-derived Sr/Ca-SST, the 5.7 ka coral recorded a drop of -2.3 °C in the winter SST relative to the present-day (Fig. 4A, D). This is cooler compared to the reconstructed winter SST at 3.2 ka and 4.9 ka. The higher winter SSS (positive $\delta^{18}O_{coral}$) and lower winter SST indicate that the cold and dry northeasterlies of the winter monsoon intensified in 5.7 ka. The strong EAWM enhanced the evaporation during 5.7 ka which resulted in higher SSS accompanied with increased surface ocean cooling. Relative to 5.7 ka, the 3.2 ka and 4.9 ka corals both recorded warmer winter SST and lower winter SSS. This evidence would indicate that the northeasterly-driven winter monsoon weakened in these time-windows.

We compared our compiled winter (maximum) $\delta^{18}O_{coral}$ from Kikai and Okinawa islands, Southern Japan (Fig. 5A) to the stacked EAWM records (Fig. 5C). The stacked EAWM record was generated from several lacustrine sediment recordss from China (Kaboth-Bahr et al., 2021). Similar to the stacked EASM sediment records, linear resampling and low-pass filtering were done to address the issue of differing temporal resolution. However, winter records from the Asian continent show spatiotemporal variation in the EAWM intensity in northwestern and southeastern China (Zhang et al., 2015). This might have affected the timing and/or amplitude of the stack EAWM record (Fig. 5C). The stacked record has revealed strong winter monsoon (more positive values) from 8.2 to 5.6 ka. This is a good agreement with the strong winter monsoon signals derived from 5.7 ka coral in Kikai Island. The weak EAWM phase started after 5.6 ka until around 4.5 ka. The winter records of warm SST and lower SSS in 4.9 ka showed the surface ocean response to weaker EAWM in southern Japan. The more positive SSS at 3.8 ka and 3.4 ka signals a drier winter condition during enhanced winter monsoon. The stacked sediment records from -4.4 ka to 3.2 ka show relatively wider uncertainty envelope due to wide range of values derived from individual records. This time interval could be an intensified EAWM phase that was abruptly punctuated by a shorter weakened EAWM phase around 3.0 ka. The 3.2 ka coral recorded negative winter $\delta^{18}O_{coral}$ indicating lower winter SSS accompanied by warmer winter SST relative to 5.7 ka. However, the winter SST in 3.2 ka was cooler than the winter SST in 4.9 ka, thus, we can conclude that 4.9 ka was a period of weaker EAWM relative to both 5.7 ka and 3.2 ka.

The intense cooling in high latitude Northern Hemisphere strengthens and expands the Siberian high which amplifies the winter variability mode (Li et al., 2018). Previous studies show that the intensity of Siberian high and Aleutian low directly influences the wind circulation and winter climate variation over East Asia (Wu and Wang, 2002; Jhun and Lee, 2004). The intensification of the EAWM based on the compiled paleoclimate records suggests that these extratropical climate systems were well-developed in mid-Holocene. On the other hand, the weakening of EAWM could be attributed to the higher solar irradiance measured from sunspot records (Kaboth-Bahr et al., 2021). The higher solar irradiance could have possibly reduced the sea-ice cover affecting the development of Siberian high and Aleutian low in the extratropics.

6. Conclusions

The EASM and EAWM affect the seasonal SST, SSS, and rainfall of East Asia. Coral-derived geochemical proxies from Kikai Island, Southern Japan are effective in tracking hydroclimatic changes driven by shifting monsoon intensities during the mid-to late Holocene. The covariation of Sr/Ca-SST and $\delta^{18}O_{coral}$ indicates the water temperature dependence of these two geochemical proxies. The coral Sr/Ca was used to estimate the seasonal SST variation in 5.7 ka, 4.9 ka, and 3.2 ka relative to present-day (1989–2015). The $\delta^{18}O_{coral}$ fractionation is both influenced by temperature and variations in $\delta^{18}O_{sw}$. We used the Sr/Ca-SST to isolate the $\delta^{18}O_{sw}$ from $\delta^{18}O_{coral}$. The monthly $\delta^{18}O_{coral}$-SSS relationship from 1989 to 2015 revealed a statistically significant positive linear correlation ($r = 0.634$; $p < 0.000$; $n = 310$) with high and low SSS corresponding to high and low $\delta^{18}O_{coral}$. The reconstructed $\delta^{18}O_{sw}$ was then compared to the variation of accumulated rainfall from the northern Kikai Island. The comparison showed a statistically significant negative linear correlation ($r = 0.554$; $p < 0.000$; $n = 93$) with low (high) $\delta^{18}O_{sw}$ months are related to high (low) rainfall month. The relative $\delta^{18}O_{sw}$ seasonality change calculated by subtracting the mean monthly $\delta^{18}O_{sw}$ of modern coral from three fossil corals, shows the positive or negative shift of rainfall at 5.7 ka, 4.9 ka, and 3.2 ka relative to the modern (1989–2015) record.

The mid-Holocene corals dated 5.7 ka ($\Delta SST_{max-min} = 9.5$ °C) and 4.9 ka ($\Delta SST_{max-min} = 10.2$ °C) recorded the largest seasonal SST difference ($\Delta SST_{max-min}$). The enhanced seasonality in mid-Holocene is also reflected by the higher seasonal $\delta^{18}O_{coral}$ difference in 5.7 ka (1.86 ± 0.06‰) and 4.9 ka (1.45 ± 0.14‰) as compared to 3.2 ka (0.98 ± 0.07‰). The enhanced SST and SSS seasonality indicate an enhanced surface ocean warming from early spring to summer of 5.7 ka and 4.9 ka. The stronger ocean heating amplified the WPSH and in turn, enhanced the southwesterlies. The stronger southwesterlies carried more rainfall in subtropical southern Japan as supported by more negative SSS signal from summer $\delta^{18}O_{coral}$ values. In contrast, the 3.2 ka coral ($\Delta SST_{max-min} = 7.8$ °C; $\Delta\delta^{18}O_{max-min} = 0.98$‰) has smaller SST and SSS seasonality. The small SST amplitude indicates a reduction in surface ocean warming from early spring to summer of 3.2 ka which could have weakened the WPSH and southwesterlies. The weakened southwesterlies led to the decrease of summer rainfall and positive SSS signal in 3.2 ka. The compiled $\delta^{18}O_{coral}$ from southern Japan was compared to the stacked EASM records from marine and terrestrial sediments. The lower salinity and higher rainfall in 7.0 ka, 6.1 ka, 5.7 ka, and 4.9 ka stacked sediment records coincided with the strong EASM from 8.2 to 4.7 ka in stacked sediment records. The $\delta^{18}O_{coral}$ record shows positive SSS driven by weakened summer monsoon rainfall in 4.4 ka, 4.2 ka, 3.8 ka, 3.4 ka, and 3.2 ka.

For the winter monsoon intensity, we considered both winter SST and SSS signals from coral records. The higher winter SSS (positive $\delta^{18}O_{coral}$) and lower winter SST indicate that the cold and dry northeasterlies of the winter monsoon intensified in 5.7 ka. The strong winter monsoon signals derived from 5.7 ka coral in Kikai Island agree with the strong winter monsoon (more positive values) from 8.2 to 5.6 ka based on the stacked sediment record. The 3.2 ka and 4.9 ka corals both recorded warmer winter SST and lower winter SSS compared to 5.7 ka. The weak EAWM phase started after 5.6 ka until around 4.5 ka which is consistent with the winter records of warm SST and lower SSS in 4.9 ka showed the surface ocean response to weaker EAWM in southern Japan. The more positive SSS at 3.8 ka and 3.4 ka signals a drier winter condition during enhanced winter monsoon from 4.4 ka to 3.2 ka in the stacked sediment records. The intensified EAWM phase from 4.4 ka to 3.2 ka was abruptly punctuated by a shorter weakened EAWM phase around 3.0 ka represented by the lower winter SSS and warmer winter SST in 3.2 ka relative to 5.7 ka. However, the winter SST in 3.2 ka was cooler than the winter SST in 4.9 ka, thus, we can conclude that 4.9 ka was a period of weaker EAWM than 5.7 ka and 3.2 ka.

Credit author statement

Kevin L. Garas: Conceptualization, Investigation, Formal analysis, Writing-Original draft, Visualization, Tsuyoshi Watanabe: Conceptualization, Writing-Review & Editing, Supervision, Atsuko Yamazaki: Conceptualization, Investigation, Writing-Review & Editing.

Declaration of competing interest

The authors declare that they have no known competing financial interests or personal relationships that could have appeared to influence the work reported in this paper.

Data availability

The research data is available in data repository at KIKAI Institute for coral reef sciences (https://coralogy.kikaireefs.org/C-1%20Scientific%20data.html).

Acknowledgements

We would like to thank members of Coral Reef Earth Environmental Sciences/Carbonate Research for Earth Evolution Systems (CREES) at Hokkaido University for their help in the geochemical analysis of the samples. We acknowledge T. Irino for managing the MAT 253 and Kiel-IV device at Hokkaido University. This study was supported by Japan Society for the Promotion of Science (JSPS) KAKENHI Grants JP 25257207, 15H03742, 15KK0145, 13J07017, and 17H04708.

Appendix A. Supplementary data

Supplementary data to this article can be found online at https://doi.org/10.1016/j.quascirev.2022.107926.

References

Abram, N., Webster, J., Davies, P., Dullo, W., 2001. Biological response of coral reefs to sea surface temperature variation: evidence from the raised Holocene reefs of Kikai-jima (Ryukyu Islands, Japan). Coral Reefs 20 (3), 221–234.

Asami, R., Yoshimura, N., Toriyabe, H., Minei, S., Shinjo, R., Hongo, C., et al., 2020. High-resolution evidence for middle Holocene East Asian winter and summer monsoon variations: snapshots of fossil coral records. Geophys. Res. Lett. 47 (16), e2020GL088509.

Beck, J.W., Edwards, R.L., Ito, E., Taylor, F.W., Recy, J., Rougerie, F., Joanot, P., Henin, C., 1992. sea surface temperature from coral strontium/calcium ratios. Science 257, 644–647.

Bingham, F.M., Foltz, G.R., McPhaden, M.J., 2012. Characteristics of the seasonal cycle of surface layer salinity in the global ocean. Ocean Sci. 8 (5), 915–929.

Cahyarini, S.Y., Pfeiffer, M., Timm, O., Dullo, W.C., Schönberg, D.G., 2008. Reconstructing seawater δ18O from paired coral δ18O and Sr/Ca ratios: methods, error analysis and problems, with examples from Tahiti (French Polynesia) and Timor (Indonesia). Geochem. Cosmochim. Acta 72 (12), 2841–2853.

Chen, T.C., Wang, S.Y., Huang, W.R., Yen, M.C., 2004. Variation of the East Asian summer monsoon rainfall. J. Clim. 17, 744–762.

Chen, F., Xu, Q., Chen, J., Birks, H.J.B., Liu, J., Zhang, S., Jin, L., An, C., Telford, R.J., Cao, X., Wang, Z., 2015. East Asian summer monsoon precipitation variability since the last deglaciation. Sci. Rep. 5, 11186. https://doi.org/10.1038/srep11186.

Chevuturi, A., Klingaman, N.P., Turner, A.G., Guo, L., Vidale, P.L., 2022. Projected changes in the East Asian hydrological cycle for different levels of future global warming. Atmosphere 13 (3), 405.

Chiang, J.C., Herman, M.J., Yoshimura, K., Fung, I.Y., 2020. Enriched East Asian oxygen isotope of precipitation indicates reduced summer seasonality in regional climate and westerlies. Proc. Natl. Acad. Sci. USA 117 (26), 14745–14750.

Cosford, J., Qing, H., Eglington, B., Mattey, D., Yuan, D., Zhang, M., Cheng, H., 2008. East Asian monsoon variability since the Mid-Holocene recorded in a high-resolution, absolute-dated aragonite speleothem from eastern China. Earth Planet Sci. Lett. 275 (3–4), 296–307.

Dayem, K.E., Molnar, P., Battisti, D.S., Roe, G.H., 2010. Lessons learned from oxygen isotopes in modern precipitation applied to interpretation of speleothem records of paleoclimate from eastern Asia. Earth Planet Sci. Lett. 295 (1–2), 219–230.

Deng, W.F., Wei, G.J., Li, X.H., Yu, K.F., Zhao, J.X., Sun, W.D., Liu, Y., 2009. Paleo-precipitation record from coral Sr/Ca and δ18O during the mid Holocene in the northern South China Sea. Holocene 19 (6), 811–821.

Dong, J., Shen, C.C., Kong, X., Wu, C.C., Hu, H.M., Ren, H., Wang, Y., 2018. Rapid retreat of the East Asian summer monsoon in the middle Holocene and a millennial weak monsoon interval at 9 ka in northern China. J. Asian Earth Sci. 151, 31–39.

Dykoski, C.A., Edwards, R.L., Cheng, H., Yuan, D., Cai, Y., Zhang, M., et al., 2005. A high-resolution, absolute-dated Holocene and deglacial Asian monsoon record from Dongge Cave, China. Earth Planet Sci. Lett. 233 (1–2), 71–86.

Gagan, M.K., Ayliffe, L.K., Hopley, D., Cali, J.A., Mortimer, G.E., Chappell, J., McCulloch, M.T., Head, M.J., 2006. Temperature and surface-ocean water balance of the mid-holocene tropical western pacific. Science 279, 1014–1018.

Goldsmith, Y., Broecker, W.S., Xu, H., Polissar, P.J., Demenocal, P.B., Porat, N., Lan, J., Cheng, P., Zhou, W., An, Z., 2017. Northward extent of East Asian monsoon covaries with intensity on orbital and millennial timescales. Proc. Natl. Acad. Sci. USA 114 (8), 1817–1821. https://doi.org/10.1073/pnas.1616708114.

Heaton, T.J., Köhler, P., Butzin, M., Bard, E., Reimer, R.W., Austin, W.E., Ramsey, C.B., Grootes, P.M., Hughen, K.A., Kromer, B., Reimer, P.J., 2020. Marine20—the marine radiocarbon age calibration curve (0–55,000 cal BP). Radiocarbon 62 (4), 779–820.

Helm, K.P., Bindoff, N.L., Church, J.A., 2010. Changes in the global hydrological-cycle inferred from ocean salinity. Geophys. Res. Lett. 37 (18).

Jhun, J.G., Lee, E.J., 2004. A new East Asian winter monsoon index and associated characteristics of the winter monsoon. J. Clim. 17 (4), 711–726.

Jiang, D., Lang, X., Tian, Z., Ju, L., 2013. Mid-holocene East Asian summer monsoon strengthening: insights from paleoclimate modeling intercomparison project (PMIP) simulations. Palaeogeogr. Palaeoclimatol. Palaeoecol. 369, 422–429.

Julliet-Leclerc, A., Schmidt, G., 2000. A calibration of the oxygen isotope paleothermometer of coral aragonite from Porites. Geophys. Res. Lett. 28 (21), 4135–4138.

Kaboth-Bahr, S., Bahr, A., Zeeden, C., Yamoah, K.A., Lone, M.A., Chuang, C.K., et al., 2021. A tale of shifting relations: East Asian summer and winter monsoon variability during the Holocene. Sci. Rep. 11 (1), 1–10.

Kajita, H., Yamazaki, A., Watanabe, T., Wu, C.C., Shen, C.C., Watanabe, T., 2017. Holocene sea surface temperature variations recorded in corals from Kikai Island, Japan. Geochem. J. 51 (4), e9–e14.

Kajita, H., Kawahata, H., Wang, K., Zheng, H., Yang, S., Ohkouchi, N., et al., 2018. Extraordinary cold episodes during the mid-Holocene in the Yangtze delta: interruption of the earliest rice cultivating civilization. Quat. Sci. Rev. 201, 418–428.

Kawakubo, Y., Alibert, C., Yokoyama, Y., 2017. A reconstruction of subtropical western North Pacific SST variability back to 1578, based on a Porites Coral Sr/Ca record from the northern Ryukyus, Japan. Paleoceanography 32 (12), 1352–1370.

Kiyama, O., Yamada, T., Nakamori, T., Iryu, Y., 2000. Early Holocene coral δ18O-based sea surface temperature. Quat. Res. (Daiyonki-Kenkyu) 39 (1), 69–80.

Kubota, Y., Tada, R., Kimoto, K., 2015. Changes in East Asian summer monsoon precipitation during the Holocene deduced from a freshwater flux reconstruction of the Changjiang (Yangtze River) based on the oxygen isotope mass balance in the northern East China Sea. Clim. Past 11 (2), 265–281.

Li, H., Dai, A., Zhou, T., Lu, J., 2010. Responses of East Asian summer monsoon to historical SST and atmospheric forcing during 1950–2000. Clim. Dynam. 34 (4), 501–514.

Li, D., Li, T., Jiang, H., Björck, S., Seidenkrantz, M.S., Zhao, M., et al., 2018. East Asian winter monsoon variations and their links to Arctic sea ice during the last millennium, inferred from sea surface temperatures in the Okinawa Trough. Paleoceanogr. Paleoclimatol. 33 (1), 61–75.

Lough, J.M., Cooper, T.F., 2011. New insights from coral growth band studies in an era of rapid environmental change. Earth Sci. Rev. 108 (3–4), 170–184.

Maher, B.A., 2008. Holocene variability of the East Asian summer monsoon from Chinese cave records: a re-assessment. Holocene 18 (6), 861–866.

Mohtadi, M., Prange, M., Steinke, S., 2016. Paleoclimatic insights into forcing and response of monsoon rainfall. Nature 533, 191–199.

Morimoto, M., Abe, O., Kayanne, H., Kurita, N., Matsumoto, F., Yoshida, N., 2002. Salinity records for the 1997–98 el Niño from western pacific corals. Geophys. Res. Lett. 29, 11.

Morimoto, M., Kayanne, H., Abe, O., McCulloch, M.T., 2007. Intensified mid-Holocene Asian monsoon recorded in corals from Kikai Island, subtropical northwestern Pacific. Quat. Res. 67, 204–214.

Nagashima, K., Tada, R., Toyoda, S., 2013. Westerly jet-East Asian summer monsoon connection during the Holocene. G-cubed 14 (12), 5041–5053.

Nurhati, I.S., Cobb, K.M., Di Lorenzo, E., 2011. Decadal-scale SST and salinity variations in the central tropical Pacific: signatures of natural and anthropogenic climate change. J. Clim. 24 (13), 3294–3308.

Paillard, D., Labeyrie, L.D., Yiou, P., 1996. AnalySeries 1.0: a Macintosh software for the analysis of geophysical time-series. Eos 77, 379.

Pausata, F.S., Battisti, D.S., Nisancioglu, K.H., Bitz, C.M., 2011. Chinese stalagmite δ18 O controlled by changes in the Indian monsoon during a simulated Heinrich event. Nat. Geosci. 4 (7), 474.

Piao, J., Chen, W., Wang, L., Pausata, F.S., Zhang, Q., 2020. Northward extension of the East Asian summer monsoon during the mid-Holocene. Global Planet. Change 184, 103046.

Ramos, R.D., Goodkin, N.F., Siringan, F.P., Hughen, K.A., 2019. Coral records of temperature and salinity in the Tropical Western Pacific reveal influence of the

Pacific Decadal Oscillation since the late nineteenth century. Paleoceanogr. Paleoclimatol. 34 (8), 1344–1358.

Reed, E.V., Thompson, D.M., Anchukaitis, K.J., 2022. Coral-based sea surface salinity reconstructions and the role of observational uncertainties in inferred variability and trends. Paleoceanogr. Paleoclimatol. 37 (6), e2021PA004371.

Ren, L., Linsley, B.K., Wellington, G.M., Schrag, D.P., Hoegh-Guldberg, O., 2003. Deconvolving the δ18O seawater component from subseasonal coral δ18O and Sr/Ca at Rarotonga in the southwestern subtropical Pacific for the period 1726 to 1997. Geochem. Cosmochim. Acta 67 (9), 1609–1621.

Rodríguez, J.M., Milton, S.F., Marzin, C., 2017. The East Asian atmospheric water cycle and monsoon circulation in the met office unified model. J. Geophys. Res. Atmos. 122 (19), 10–246.

Siswanto, E., Nakata, H., Matsuoka, Y., Tanaka, K., Kiyomoto, Y., Okamura, K., Zhu, J., Ishizaka, J., 2008. The long-term freshening and nutrient increases in summer surface water in the northern East China Sea in relation to Changjiang discharge variation. J. Geophys. Res.: Oceans 113 (C10).

Sowa, K., Watanabe, T., Kan, H., Yamano, H., 2014. Influence of land development on Holocene Porites coral calcification at Nagura bay, Ishigaki island, Japan. PLoS One 9 (2), e88790.

Sun, D., Gagan, M.K., Cheng, H., Scott-Gagan, H., Dykoski, C.A., Edwards, R.L., Su, R., 2005. Seasonal and interannual variability of the Mid-Holocene East Asian monsoon in coral d18O records from the South China Sea. Earth Planet Sci. Lett. 237, 69–84.

Tian, J., Huang, E., Pak, D.K., 2010. East Asian winter monsoon variability over the last glacial cycle: insights from a latitudinal sea-surface temperature gradient across the South China Sea. Palaeogeogr. Palaeoclimatol. Palaeoecol. 292 (1–2), 319–324.

Thompson, D.M., Conroy, J.L., Konecky, B.L., Stevenson, S., DeLong, K.L., McKay, N., Reed, E., Jonkers, L., Carré, M., 2022. Identifying hydro-sensitive coral δ18O records for improved high-resolution temperature and salinity reconstructions. Geophys. Res. Lett., e2021GL096153

Ueda, H., Ohba, M., Xie, S.P., 2009. Important factors for the development of the Asian–Northwest Pacific summer monsoon. J. Clim. 22, 649–669. https://doi.org/10.1175/2008JCLI2341.1.

Ujiié, Y., Ujiié, H., Taira, A., Nakamura, T., Oguri, K., 2003. Spatial and temporal variability of surface water in the Kuroshio source region, Pacific Ocean, over the past 21,000 years: evidence from planktonic foraminifera. Mar. Micropaleontol. 49 (4), 335–364.

Watanabe, T.K., Watanabe, T., Ohmori, K., Yamazaki, A., 2020. Improving analytical method of Sr/Ca ratios in coral skeletons for paleo-SST reconstructions using ICP-OES. Limnol Oceanogr. Methods 18 (6), 297–310.

Watanabe, T., Winter, A., Oba, T., 2001. Seasonal changes in sea surface temperature and salinity during the Little Ice Age in the Caribbean Sea deduced from Mg/Ca and $^{18}O/^{16}O$ ratios in corals. Mar. Geol. 173, 21–35.

Watanabe, T., Kawamura, T., Yamazaki, A., Murayama, M., Yamano, H., 2014. A 106 year monthly coral record reveals that the East Asian summer monsoon modulates winter PDO variability. Geophys. Res. Lett. 41 (10), 3609–3614.

Watanabe, T.K., Pfeiffer, M., 2022. A simple Monte Carlo approach to estimate the uncertainties of SST and δ18Osw inferred from coral proxies. G-cubed 23 (3), e2021GC009813.

Wu, B., Wang, J., 2002. Winter Arctic oscillation, siberian high and East Asian winter monsoon. Geophys. Res. Lett. 29 (19), 3, 1.

Xue, D., Lu, J., Leung, L.R., Zhang, Y., 2018. Response of the hydrological cycle in Asian monsoon systems to global warming through the lens of water vapor wave activity analysis. Geophys. Res. Lett. 45 (21), 11–904.

Zhang, H., Zhang, X., Cai, Y., Sinha, A., Spötl, C., Baker, J., et al., 2021. A data-model comparison pinpoints Holocene spatiotemporal pattern of East Asian summer monsoon. Quat. Sci. Rev. 261, 106911.

Zhang, X., Jin, L., Li, N., 2015. Asynchronous variation in the East Asian winter monsoon during the Holocene. J. Geophys. Res. Atmos. 120 (11), 5357–5370.

LIST OF FIGURES

Figure 1. Paleoclimate archives and external climate forcings. A. Oxygen isotope of speleothem from Northern and Southern China (Dong et al. 2018; Cosford et al. 2008; Dykoski et al. 2005) B. Bulk Titanium* % of marine sediment core from Cariaco Basin, Venezuela (Haug et al. 2001) C. Event per 100yr based on the frequency of clastic laminae from Lake Pallacocha, Ecuador (Moy et al. 2002) D. Bond events from the record of ocean ice rift debris of Northern Altantic Ocean (Bond et al. 2001) E. Total Solar Irradiance (ΔTSI) record in Holocene (Steinhilber et al. 2009) F. Summer solar insolation in the tropics (Berger and Loutre 1991)

Figure 2. Composite sea-level pressure map (A) and 1000 mb vector wind map (B) from June to August (1982 – 2020) derived from NCEP/NCAR reanalysis data. The anticyclonic wind circulation around the Western Pacific Subtropical high (WPSH) is the dominant atmospheric circulation in boreal summer. Composite sea-level pressure map (C) and 1000 mb vector wind map (D) from December to February (1982 – 2020) derived from NCEP/NCAR reanalysis data. The well-developed Siberian high and Aleutian low dominate the winter variability mode in the Northern Hemisphere. Composite maps were generated in the National Ocean and Atmospheric Administration - Physical Sciences Laboratory (NOAA-PSL) Climate Plotting and Analysis Tools (https://psl.noaa.gov/data/getpage/).

Figure 3. Composite SST map (A) and rainfall map (B) from June to August (1982 – 2020) derived from NOAA OISST and GPCP data. Composite SST map (C) and rainfall map (D) from December to February (1982 – 2020) derived from NOAA OISST and GPCP data. The seasonal shift between summer and winter monsoon corresponds to the expansion and contraction of the Indo-Pacific Warm Pool (IPWP) and the intertropical convergence zone (ITCZ) rainbelt. Black box represents the NW Pacific area. Composite maps were generated in the National Ocean and Atmospheric Administration - Physical Sciences Laboratory (NOAA-PSL) Climate Plotting and Analysis Tools (https://psl.noaa.gov/data/getpage/).

Figure 4. A. Correlation map illustrates the warm phase of ENSO when the central and eastern equatorial Pacific are warmer than the western equatorial Pacific (160°E to 120°E). The SSTs of South China Sea and East China Sea shows weak to moderate positive correlation (r = 0.2 to 0.7) to the Niño-3.4 SSTA. **B.** Correlation map of the Niño-3.4 SSTA and GPCP precipitation (September to April) from 1948 to 2012 shows weak to moderate positive correlation (r = 0.2 – 0.6) in China and Southern Japan and strong negative correlation (r = -0.2 to -0.8) in mainland Southeast Asia, the Philippines, and Indonesia**.** Correlation maps were generated in the National Ocean and Atmospheric Administration - Physical Sciences Laboratory (NOAA-PSL) Climate Plotting and Analysis Tools (https://psl.noaa.gov/data/getpage/).

Figure 5. Growth parameters in annually banded *Porites* corals. A. The alternating light and dark bands represent seasonal cycles in annual coral growth. B. Linear extension rate is measured from the outward growth per year. C. The light and dark bands correspond to the high- and low-density bands, respectively.

Figure 6. Coral geochemical proxies in annually banded *Porites* corals. Coral Sr/Ca is used to track changes in SST. $\delta^{18}O_{coral}$ is a function of both changes in SST and $\delta^{18}O_{sw}$ and can track changes in both SST and SSS. $\delta^{18}O_{sw}$ can potentially reconstruct changes in the hydrological processes such as evaporation and precipitation.

Figure 7. Geologic map and cross-section of Kikai Island. The Pleistocene Ryukyu Group (green) is distributed in the interior part of the island while the Holocene uplifted terraces (yellow) are distributed along the coastal zones. The clastic-dominated Shimajiri Group is the basement unit of Kikai Island.

Figure 8. Carbonate sedimentological composition of the Holocene limestone in Kikai Island. A. Panoramic view of the three-level uplifted marine terraces in Kikai Island. The island is predominantly composed of reef-building hermatypic coral genera such as *Favites* (B), *Acropora* (C,D), and *Porites* (E,F).

Figure 9. Hydroclimate of Kikai Island. A. Advanced Very High-Resolution Radiometer (AVHRR) SST in Kikai Island from 1981 to 2015. B. Simple Ocean Data Assimilation (SODA) reanalysis SSS in Kikai Island from 1981 to 2015. C. Monthly accumulated rainfall from in-situ daily rainfall gauge data from northern Kikai Island from 2007 to 2017. D. Mean monthly SST from AVHRR SST. E. Mean monthly SODA SSS and in-situ rainfall

Figure 10. Geologic Map of Santo Tomas, La Union showing the Holocene uplifted marine terrace (blue) along Damortis beach. The red circle represents the sampling site. *Source: Updated MGB Geologic Map by Cenozoic Stratigraphy of the Philippines Project (2020)*

Figure 11. Geologic Map of Batac Quadrangle, Ilocos Norte where the town of Currimao is in the southwesternmost portion. The red circle represents the sampling site. *Source: MGB Region 1 (2021)*

Figure 12. Carbonate sedimentological composition of the Holocene limestone in NW Luzon Island. A. Terrace I of the Holocene uplifted marine terraces in Currimao where fossil *Porites* (B) were observed. C. Photo of the single marine terrace in Damortis Beach, La Union. D. Photo of fossil microatoll in Balaoan, La Union. E. Fossil corals in Damortis Beach bounded by calcareous silt and mud.

Figure 13. Hydroclimate in NW Luzon, Philippines. A. Monthly SST of Ilocos Norte and La Union from 2000 to 2021 B. Monthly SSS of Ilocos Norte (2000 to 2015) and La Union (1991 to 2015) C. The 1991 – 2019 rainfall data from Laoag (Ilocos Norte) and Dagupan (La Union) stations

Figure 14. A. Mean seasonal change of SST in La Union and Ilocos Norte; B. Mean seasonal change of SSS in La Union and Ilocos Norte C. Mean monthly rainfall during neutral and warm (El Niño) phases of ENSO in La Union D. Mean monthly rainfall during neutral and warm (El Niño) phases of ENSO in Ilocos Norte E. Linear correlation of SST in La Union and Ilocos F. Linear correlation of SSS in La Union and Ilocos

Figure 15. Selected X-ray photographs of fossil corals from Kikai Island. KINM-20160908-I and NGM03 were collected from Nakaguma; KISK-20160907-III was collected from Sateku; KIST-20160518-I was collected from Shitooke; KIKJ-20160907-I, KIKJ-20160907-II, and KKEJ-1702_I were collected from Keraji

Figure 16. Selected X-ray photographs of fossil and modern corals from NW Luzon Island. CuPf-180218-1 and CuPf-180218-4 were collected from Currimao, Ilocos Norte; PQPF-180220-4 was collected from Pasuquin, Ilocos Norte; DMT-1, DMT-2, and DMT-3 were drilled from Damortis, La Union; and BDC1 and BC2 are modern corals collected from Badoc Island, Ilocos Norte

Figure 17. Fieldwork photos in Kikai Island and NW Luzon Island. A. Coral sampling in Sateku, Kikai Island. B. Measurement of fossil microatoll in Paraoir (Balaoan), La Union. C. Fossil coral sampling in Pasuquin, Ilocos Norte. D. Terrace measurement in Bacnotan, La Union

Figure 18. Thin Section Analysis. A. Cutting samples into coral blocks. B. Preparing thin sections from coral blocks. C. Petrographic analysis of corals using polarizing microscope

Figure 19. Xray diffraction (XRD) Analysis. Pulverized coral samples were analyzed in X'Pert PRO PANalytical XRD.

Figure 20. Scanning Electron Microscope (SEM) Analysis. Miniblocks/fragments (~1cm x 1cm) from different parts of the fossil coral colonies were analyzed using Hitachi TM-1000 Miniscope.

Figure 21. Cutting of coral samples using lapidary rock saw with diamond-tipped blade

Figure 22. A. Coral slabs were X-rayed using a 2D cabinet-type radiographic unit. B. Calibration of gray values using aluminum bar and giant clam mini blocks as thickness standards

Figure 23. A. Preparation of the ledge B. Schematic diagram of the coral subsampling/micro sampling procedure C. Subsampling procedure was done using diamond-tipped drill bit with a constant rotation speed of 1 mm/min mounted in CNC MM-250 S3 milling machine

Figure 24. The ThermoScientific iCAP 6200 Inductively-coupled Plasma-Optical Emission Spectrometer (ICP-OES) at the Hokkaido University was used to measure the Sr and Ca concentrations in coral skeleton

Figure 25. The Finnigan MAT 253plus stable isotope ratio mass spectrometer with the Kiel IV automated carbonate device was used to measure oxygen ($\delta^{18}O$) and carbon ($\delta^{13}C$) isotopes in coral skeleton.

Figure 26. Flowchart of the error propagation using the simple Monte Carlo simulation in R software. The flowchart published by Watanabe and Pfeiffer (2022) was adapted.

Figure 27. Diagenetic texture under thin section. A. Well-preserved coral skeleton with clear centers of calcification and no observed deposition of secondary carbonate mineral. B. The primary aragonite is still preserved but precipitation of aragonite cement is now evident. C. Aragonite cement has fine acicular fabric. D. The coral skeleton is now completely replaced by calcite.

Figure 28. XRD profile from 25°θ to 35°θ showing the main aragonite and calcite peaks of A. KIST-20160518-I, B. KIKJ-20160907-II, C. KSOM141006, D. ARK05, E. KIKJ-20160907-I, F. KINM-I, G. KISK-III, H. NGM03

Figure 29. XRD profile from 25°θ to 50°θ showing the aragonite peaks of A. DMT1, B. DMT2, C. CUPF3, D. PQPF7, E. BLN-PAR-4, F. SLN-URB-1, G. BAPF-1, H. BAPF-2-1, I. BAPF-9. These samples have 0% calcite content.

Figure 30. XRD profile from 25°θ to 50°θ showing the aragonite peaks of A. CUPF4, B. CUPF1, C. PQPF4, D. BAPF-5, E. BAPF-3, F. BAPF-9-2, G. PQPF-3, H. CUPF0, I. CUPF5, J. BAPF-6, L. BAPF7. Samples A-J have 2-7% calcite content while samples K-L have 100% calcite content.

Figure 31. SEM images of A. KIST-20160518-I, B. KSOM141006, C. KIKJ-20160907-II, D. ARK05, E. KIKJ-20160907-I, F. KINM-I, G. NGM03, H. KISK-III. Samples A-C have relatively good to excellent preservation. Samples D, E, H have typical early marine phreatic diagenetic imprints while sample F-G are typical of subaerial vadose diagenesis.

Figure 32. SEM images of A. DMT1, B. DMT2, C. CUPF-4, D. CUPF3. These samples from NW Luzon Island have good to excellent preservation of the aragonitic coral skeleton.

Figure 33. SEM images of A. CUPF1, B. CUPF5, C. PQPF3, D. PQPF4, E. PQPF7, F. BAPF6, G. CUPF1, H. BAPF3, I. BAPF9, J. BAPF-5, K. BAPF7, and L. ROS-DAM-1.

Figure 34. The Xray photo of the coral DMT-1d from Damortis Beach, La Union shows irregular, anomalously high-density sections D and E. XRD analysis shows that sections A and C have 0% calcite, section B has 9% calcite and 91% aragonite, section D has 55% calcite and section E has 70% calcite. SEM images revealed the well-preserved coral aragonite in sections A and C. Some intraskeletal spaces have been occupied by cement in section B. Rhombohedral calcite cement and minor dissolution are evident in the SEM image of Section D. In Section E, powdery unstable aragonite is formed due to the advanced dissolution and calcite crystals have been precipitated simultaneously.

Figure 35. Cross-plots of (A) δ^{18}O-%calcite, (B) δ^{13}C-%calcite, (C) Sr/Ca-%calcite, and (D) Mg/Ca-%calcite. Each bulk sample from sections A, B, C, D, and E were analyzed. The δ^{18}O, δ^{13}C, and Sr/Ca are significantly decreased with increasing %calcite as shown by the trendline (solid black line) of the weighted mean from the 5 replicate bulk analysis for each sample. The black dashed line is the proxy-%calcite trend relationship published by McGregor and Gagan et al. 2003. The Mg/Ca is significantly increased as a function of increasing %calcite content.

Figure 36. Ten-year record of (A) δ^{18}O, (B) δ^{13}C, (C) Sr/Ca, and (D) Mg/Ca of DMT-1d. The red-shaded sections indicate the parts where coral is diagenetically altered. The incorporation of secondary calcite significantly changes the geochemistry of the fossil coral.

Figure 37. X-ray photographs, linear extension rate (LER) and density of the 4 fossil corals from Kikai Island: A. ARK05, B. KIKJ-20160907-II, C. KIKJ-20160907-I, D. KIST-20160518-I. Sample names and corresponding ^{14}C age dates are indicated in the figure.

Figure 38. X-ray photographs, linear extension rate (LER) and density of the 6 fossil corals from NW Luzon Island: A. PQPF-180220-4, B. CuPf-180218-4 C. DMT-1, D. CuPf-180218-1, E. DMT-2, F. DMT-3. Sample names and corresponding ^{14}C age dates are indicated in the figure.

Figure 39. Relationships of coral growth variables from Kikai Island and Northwest Luzon Island. Linear extension rate was directly ($r = 0.72$, $p = 0.019$) and inversely ($r = -0.56$, $p = 0.09$) correlated with calcification rate (A) and density (B). Density was not significantly correlated with calcification rate (C; $r = 0.16$; $p = 0.66$)

Figure 40. Box plots of the linear extension rates (black), skeletal densities (red) and calcification rates (blue) of the fossil corals from Northwest Luzon and Kikaijima. The x-axis shows the sample name, number of annual bands and radiocarbon age dates of fossil corals. Box plots show the statistical range and standard deviation of the growth variables within the internal chronology of fossil corals

Figure 41. Scatter plots of (A) annual Sr/Ca vs linear extension and (B) $\delta^{18}O_{coral}$ vs linear extension of the modern (black), 3.2 ka (blue), 4.9 ka (green), and 5.7 ka (red) corals from Kikai Island. Fitting line of δ18Ocoral-linear extension curve is δ18Ocoral = 0.0105(linear ext.)2 - 0.266(linear ext.) - 3.0114 (R2= 0.7426). Scatter plots of (C) annual Sr/Ca vs linear extension and (D) $\delta^{18}O_{coral}$ vs linear extension of the 4.2 ka (blue), 4.3 ka (orange), and 6.1 ka (gray) corals from NW Luzon Island.

Figure 42. A. Comparison of monthly-resolved Sr/Ca (red) from Kikai Island, Japan and AVHRR SST (gray) data from 1989 to 2015. B. Comparison of monthly-resolved Sr/Ca-SST (red) from Badoc Island, NW Luzon, Philippines, and Optimum Interpolation SST (gray) data from 2011 to 2017.

Figure 43. A. Bivariate regression analysis using the minimum and maximum Sr/Ca from Kikai Island plotted against the summer and winter SST from 1989 to 2015. B. Bivariate regression analysis using the minimum and maximum Sr/Ca from NW Luzon plotted against the summer and winter SST from 2011 to 2017. The pair of green lines indicate the 95% bootstrap confidence interval of the linear model.

Figure 44. Plots of previously published Sr/Ca-SST slopes from several locations around South China Sea (Leizhou Peninsula, China (Yu et al. 2005); Xisha Island (Sun et al. 2005); Hainan Island, China (Wei et al. 2007); Con Dao Island, Vietnam (Mitsuguchi et al. 2008); Bicol, Philippines (Liu et al. 2013); Hon Tre Island, Vietnam (Bolton et al. 2014); Palaui Island, Philippines (Ramos et al. 2017); Con Dao Island, Vietnam (Phan et al. 2019)). These slopes were compared to the newly established Sr/Ca-SST slope from Badoc Island, NW Luzon, Philippines (red).

Figure 45. A. Comparison of monthly-resolved $\delta^{18}O_{coral}$ (blue) from Kikai Island, Japan and SODA v3.3.1 SSS (black) data from 1989 to 2015. B. Comparison of monthly-resolved $\delta^{18}O_{coral}$ (blue) from Badoc Island, NW Luzon, Philippines, and SODA v3.3.1 SSS from 2011 to 2015.

Figure 46. A. Bivariate regression analysis using the minimum and maximum $\delta^{18}O_{coral}$ from Kikai Island plotted against the minimum and maximum SSS from 1989 to 2015. B. Bivariate regression analysis using the minimum and maximum $\delta^{18}O_{coral}$ from NW Luzon plotted against the minimum and maximum SSS from 2011 to 2017. The pair of green lines indicate the 95% bootstrap confidence interval of the linear model.

Figure 47. A. Comparison of the 5-point moving average monthly-resolved $\delta^{18}O_{sw}$ (green) and accumulated monthly rainfall data (black) from Kikai Island, Japan from 2007 to 2015. B. Comparison of monthly-resolved $\delta^{18}O_{sw}$ (green) from Badoc Island, NW Luzon, Philippines, and SODA v3.3.1 SSS from 2011 to 2015.

Figure 48. A. Bivariate regression analysis using the 5-point moving average monthly-resolved $\delta^{18}O_{sw}$ and accumulated monthly rainfall data from Kikai Island. B. Bivariate regression analysis using the minimum and maximum $\delta^{18}O_{sw}$ from NW Luzon plotted against the minimum and maximum SSS from 2011 to 2017. The pair of green lines indicate the 95% bootstrap confidence interval of the linear model.

Figure 49. Centered Sr/Ca-SST anomaly (red), δ18Ocoral (blue), and estimated δ18Oseawater (green) of the modern (n = 26), 3.2 ka (n = 13), 4.9 ka (n = 13), and 5.7 ka (n = 7) corals from Kikai Island (n = no. of reconstructed years). Error bar represents the 1σ standard deviation (68% confidence interval) which shows the uncertainty estimates from analytical and calibration errors of Sr/Ca-SST and δ18Ocoral following the Monte Carlo simulation method (Watanabe and Pfeiffer 2022).

Figure 50. Mean seasonal cycles of coral Sr/Ca-SST (red) and $\delta^{18}O$ (blue) of modern (A), 3.2 ka (B), 4.9 ka (C), and 5.7 ka (D) corals from Kikai Island. Uncertainties of the monthly climatology are presented in the error bar calculated from the analytical error, calibration error, and year-to-year variability of the internal coral chronology.

Figure 51. Centered Sr/Ca-SST anomaly (red), δ18Ocoral (blue), and estimated δ18Oseawater (green) of the modern (n = 7), 4.2 ka (n = 44), 4.3 ka (n = 20), and 6.1 ka (n = 20) corals from NW Luzon Island (n = no. of reconstructed years). Error bar represents the 1σ standard deviation (68% confidence interval) which shows the uncertainty estimates from analytical and calibration errors of Sr/Ca-SST and $\delta^{18}O_{coral}$ following the simple Monte Carlo method (Watanabe and Pfeiffer 2022).

Figure 52. Mean seasonal cycles of coral Sr/Ca-SST (red) and $\delta^{18}O$ (blue) of modern (A), 4.2 ka (B), 4.3 ka (C), and 6.1 ka (D) corals from NW Luzon Island. Uncertainties of the monthly climatology are presented in the error bar calculated from the analytical error, calibration error, and year-to-year variability of the internal coral chronology.

Figure 53. A. The minimum, maximum, and annual mean δ18Ocoral records from fossil Porites in Kikai Island and Okinawa Island in Southern Japan. B. Compiled summer SSTA and C. winter SSTA from Kikai

Island (Morimoto et.al. 2007; Garas et al. 2023), Okinawa Island (Mitsuguchi et.al. 1998), Ishigaki Island (Sowa et.al. 2014) and Kume Island (Seki et.al. 2012).

Figure 54. A. The minimum, maximum, and annual mean δ18Ocoral records from fossil Porites of NW Luzon Island, Philippines (This study; Yokoyama et al. 2011), Hainan Island (Wei et al. 2007; Su et al. 2010; Guo et al. 2016) and Leizhou Peninsula, China (Yu et al. 2005), and Taiwan (Shen et al. 2005). B. Compiled summer SSTA and C. winter SSTA from NW Luzon Island, Philippines (This study), Hainan Island (Wei et al. 2007) and Leizhou Peninsula, China (Yu et al. 2005)

Figure 55. A. The low saline (wet) waters in Ryukyu Archipelago and high saline (dry) waters in northern SCS as indicated by low $\delta^{18}O_{coral}$ and high $\delta^{18}O_{coral}$ respectively are supported by the northerly shift of the ITCZ. B. The cooling of the subtropical and tropical NW Pacific triggered the southward migration of the ITCZ resulted in increased SSS (dry) in Ryukyu Archipelago and decreased SSS (wet) in northern SCS

Figure 56. A. The higher winter SSS (positive $\delta^{18}O_{coral}$) and cooler winter SST indicate an intensified cold and dry northeasterlies of the winter monsoon. The lower winter SSS (positive $\delta^{18}O_{coral}$) and warmer winter SST indicate a weakened cold and dry northeasterlies of the winter monsoon. B. Winter in tropical northern SCS was characterized by dry and warm conditions from 6.7 ka to 4.4 ka and wet and cool conditions from 4.3 ka to 4.2 ka

Figure 57. A. Comparison of the 2–8-year bandpass filtered $\delta^{18}O_{sw}$ data from 1954 to 2012 (black) and the ERSST v4 NINO 3.4 SSTA from 1982 to 2012 (red) B. Comparison of the 2–8-year bandpass filtered $\delta^{18}O_{sw}$ data from 2011 to 2017 (black) and the ERSST v4 NINO 3.4 SSTA from 2011 to 2017 (red)

Figure 58. $\delta^{18}O_{sw}$ threshold values were obtained from the OLS bivariate regression analysis of the 2–8-year bandpass filtered $\delta^{18}O_{sw}$ data of NE Luzon coral and the ERSST v4 NINO 3.4 SSTA

Figure 59. The bandpass filtered $\delta^{18}O_{sw}$ of 4.2 ka coral shows 8 very strong and strong (red circles), and 3 moderate (orange circles) El Niño events and 15 very strong and strong La Niña events (green circles)
Figure 60. The bandpass filtered $\delta^{18}O_{sw}$ of 4.3 ka coral shows 5 very strong and strong (red circles), and 1 moderate (orange circles) El Niño events and 6 very strong and strong La Niña events (green circles)

Figure 61. The bandpass filtered $\delta^{18}O_{sw}$ of 6.1 ka coral shows 4 very strong and strong (red circles), and 3 moderate (orange circles) El Niño events and 4 very strong and strong La Niña events (green circles)

Figure 62. Spectral analysis using REDFIT method of the $\delta^{18}O_{sw}$ of (a) NE Luzon modern coral, (b) NW Luzon modern coral, (c) 4.2 ka coral, (d) 4.3 ka coral, and (e) 6.1 ka coral. The red noise spectra were tested for statistical significance of the 90%, 95%, and 99% percentiles in Monte Carlo simulation

Figure 63. The mean seasonal climatology of neutral (black) and El Niño (blue) years from the 2 – 8-year bandpass filtered $\delta^{18}O_{sw}$ of (a) NE Luzon coral 1952-2012, (b) NW Luzon coral 2011-2017, (c) 4.2 ka, (d) 4.3 ka, and (e) 6.1 ka

Figure 64. Comparison of the 2–8-year bandpass filtered $\delta^{18}O_{sw}$ data of Kikai modern coral from 1989 to 2015 (black) and the ERSST v4 NINO 3.4 SSTA from 1989 to 2022 (red)

Figure 65. The bandpass filtered $\delta^{18}O_{sw}$ of 3.2 ka coral shows 2 very strong and strong (red circles), and 1 moderate (orange circles) El Niño events and 2 very strong and strong La Niña events (green circles)

Figure 66. The bandpass filtered $\delta^{18}O_{sw}$ of 4.9 ka coral shows 2 very strong and strong (red circles), and 2 moderate (orange circles) El Niño events and 2 very strong and strong La Niña events (green circles)

Figure 67. The bandpass filtered $\delta^{18}O_{sw}$ of 5.7 ka coral shows 1 moderate (orange circles) El Niño event and 2 very strong and strong La Niña events (green circles)

Figure 68. Spectral analysis using REDFIT method of the $\delta^{18}O_{sw}$ of (a) modern coral, (b) 3.2 ka coral, (c) 4.9 ka coral, and (d) 5.7 ka coral. The red noise spectra were tested for statistical significance of the 90%, 95%, and 99% percentiles in Monte Carlo simulations

Figure 69. The mean seasonal climatology of neutral (black) and El Niño (blue) years from the 2 – 8-year bandpass filtered $\delta^{18}O_{sw}$ of (a) Kikai modern coral 1989-2015, (b) 3.2 ka, (c) 4.9 ka, and (d) 5.7 ka

Figure 70. The rainfall anomaly map of 1997-1998 El Niño relative to the 1995-1996 neutral phase showing distinct variation in rainfall response in subtropical and tropical NW Pacific.

Figure 71. A. Minimum $\delta^{18}O_{coral}$ from fossil Porites in Kikai Island and Okinawa Island in Southern Japan B. Minimum $\delta^{18}O_{coral}$ from fossil Porites in NW Luzon Island, Philippines, Hainan Island and Leizhou Peninsula, China, and Taiwan C. Speleothem $\delta^{18}O$ from several stalagmite deposits from northern and southern China D. Stacked sediment records from marine and terrestrial cores showing the variation of EASM intensity in Holocene E. Speleothem $\delta^{18}O$ from northen Borneo

Figure 72. The strong WPSH increased the eastward flow of Pacific equatorial trade winds resulted in wide meridional scale of ENSO/NINO region, weakened the thermocline, and then reduced ENSO amplitude. This condition defines a weak El Niño phase during the mid-Holocene.

LIST OF TABLES

TABLE OF CORAL GEOCHEMICAL DATA

Kikai modern coral (1989-2015)

Date	Sr/Ca	SrCa-SST	1 σ SD	$\delta^{18}O_{coral}$	$\delta^{18}O_{sw\_centered}$	1 σ SD
01/04/2015	9.2642087	23.88477974	0.11225	-4.904161894	-0.5448	-0.120261538
01/03/2015	9.4640393	20.77699313	0.20975	-3.833799534	-0.0971	-0.121538462
01/02/2015	9.3826014	22.04352376	0.1623	-3.756189776	0.235	-0.085811538
01/01/2015	9.3633612	22.34275025	0.15495	-3.911963897	0.1384	0.033492308
01/12/2014	9.2121099	24.6950249	0.09725	-4.276354564	0.2454	0.106657692
01/11/2014	9.0296719	27.53231882	0.1286	-4.976350419	0.1121	0.103911538
01/10/2014	8.9471909	28.81507151	0.16435	-5.491836929	-0.1461	0.072607692
01/09/2014	8.9590087	28.63127922	0.15965	-5.560325662	-0.2499	0.033569231
01/08/2014	8.9285182	29.10547123	0.17635	-5.452749013	-0.0494	0.036580769
01/07/2014	8.9721338	28.42715731	0.1542	-5.361716684	-0.0924	0.030553846
01/06/2014	9.0457799	27.28180546	0.1202	-5.180065639	-0.1404	-0.033707692
01/05/2014	9.1504953	25.65326148	0.0947	-4.550559338	0.1628	-0.05734
01/04/2014	9.2907257	23.47238487	0.1221	-3.635964239	0.6405	-0.120261538
01/03/2014	9.3797878	22.08728165	0.16185	-3.536708998	0.4627	-0.121538462
01/02/2014	9.3475664	22.58839226	0.14865	-4.098692603	9.00E-04	-0.085811538
01/01/2014	9.2452156	24.18016196	0.106	-4.567708318	-0.1504	0.033492308
01/12/2013	9.1107397	26.27154398	0.0991	-4.758427253	0.0786	0.106657692
01/11/2013	9.0450114	27.29375706	0.1205	-4.936263146	0.1044	0.103911538
01/10/2013	8.9891538	28.16246019	0.14635	-5.104912574	0.1105	0.072607692
01/09/2013	8.9108392	29.38041683	0.1863	-5.236504184	0.2225	0.033569231
01/08/2013	8.8652896	30.08880886	0.21145	-5.394466705	0.2044	0.036580769
01/07/2013	8.8932355	29.65419135	0.19445	-5.605612422	-0.0939	0.030553846
01/06/2013	8.9474567	28.81093726	0.16675	-5.547292715	-0.2035	-0.033707692
01/05/2013	9.1251844	26.04689843	0.09685	-5.186930532	-0.3943	-0.05734
01/04/2013	9.3495603	22.55738241	0.1482	-4.251515143	-0.1592	-0.120261538
01/03/2013	9.3786137	22.10554124	0.16285	-4.120238022	-0.1168	-0.121538462
01/02/2013	9.3741949	22.17426227	0.16055	-4.061380952	-0.0436	-0.085811538
01/01/2013	9.3059018	23.23636344	0.12925	-4.185517072	0.0446	0.033492308
01/12/2012	9.2199882	24.57250061	0.0994	-4.412579658	0.0839	0.106657692
01/11/2012	9.1047244	26.36509526	0.102	-4.775277196	0.08	0.103911538
01/10/2012	9.0594158	27.06973855	0.114	-5.205288527	-0.2103	0.072607692
01/09/2012	9.0757116	26.81630544	0.1094	-5.470259518	-0.524	0.033569231
01/08/2012	8.9463975	28.82740991	0.1663	-5.490774695	-0.1425	0.036580769
01/07/2012	8.9521466	28.73800009	0.164	-5.551477153	-0.223	0.030553846
01/06/2012	9.0504138	27.20973837	0.118	-5.033574366	-0.0093	-0.033707692
01/05/2012	9.1934238	24.98563348	0.09495	-4.409658639	0.1702	-0.05734
01/04/2012	9.3816363	22.05853303	0.1634	-4.272188689	-0.276	-0.120261538
01/03/2012	9.4221291	21.42878591	0.18415	-4.257138199	-0.3894	-0.121538462

01/02/2012	9.2289071	24.43379255	0.10165	-4.517357397	-0.0484	-0.085811538
01/01/2012	9.1181438	26.1563946	0.09755	-4.834790955	-0.0222	0.033492308
01/12/2011	9.1222927	26.09187149	0.09775	-4.955441184	-0.1546	0.106657692
01/11/2011	9.1066005	26.33591781	0.1006	-5.149264358	-0.2994	0.103911538
01/10/2011	9.0764567	26.80471705	0.1105	-5.201846714	-0.2589	0.072607692
01/09/2011	9.0568035	27.11036538	0.1158	-5.019796207	-0.0149	0.033569231
01/08/2011	9.0932001	26.54432233	0.10275	-4.909089301	-0.0187	0.036580769
01/07/2011	9.1633449	25.4534237	0.09255	-4.789186074	-0.1167	0.030553846
01/06/2011	9.2331325	24.36807922	0.1028	-4.575171244	-0.1186	-0.033707692
01/05/2011	9.3060318	23.23434227	0.12785	-4.280810632	-0.0512	-0.05734
01/04/2011	9.3990187	21.78820137	0.1748	-3.923895736	0.0151	-0.120261538
01/03/2011	9.4438959	21.0902654	0.1989	-3.561131413	0.2383	-0.121538462
01/02/2011	9.3406177	22.69645891	0.1453	-3.427975866	0.693	-0.085811538
01/01/2011	9.338099	22.73562932	0.14345	-3.897085283	0.2326	0.033492308
01/12/2010	9.1670112	25.39640453	0.0938	-4.660880223	0.0016	0.106657692
01/11/2010	9.0457027	27.28300641	0.1216	-4.986360105	0.0527	0.103911538
01/10/2010	8.9918509	28.12051495	0.14435	-5.265284943	-0.0583	0.072607692
01/09/2010	8.9300524	29.08161154	0.1762	-5.426483822	-0.0288	0.033569231
01/08/2010	8.9870238	28.19558675	0.14535	-5.098737248	0.1235	0.036580769
01/07/2010	9.0833149	26.69805798	0.1058	-4.631446013	0.29	0.030553846
01/06/2010	9.1008965	26.42462616	0.1033	-4.495869836	0.3722	-0.033707692
01/05/2010	9.1351068	25.89258439	0.09525	-4.401494681	0.3601	-0.05734
01/04/2010	9.2272026	24.46030107	0.10145	-4.173528204	0.3008	-0.120261538
01/03/2010	9.3025029	23.28922435	0.12505	-3.92270251	0.3167	-0.121538462
01/02/2010	9.2679773	23.82616877	0.11355	-4.194800801	0.1535	-0.085811538
01/01/2010	9.1574285	25.54543622	0.0929	-4.302976925	0.3893	0.033492308
01/12/2009	9.1432823	25.76543834	0.0955	-4.769928655	-0.0349	0.106657692
01/11/2009	8.9984485	28.01790796	0.1408	-5.042714574	0.1424	0.103911538
01/10/2009	8.9421177	28.89397121	0.1685	-5.182473016	0.1797	0.072607692
01/09/2009	8.8778193	29.89394493	0.20585	-5.175496497	0.3862	0.033569231
01/08/2009	8.9379349	28.95902188	0.17155	-4.917675831	0.4564	0.036580769
01/07/2009	9.0599772	27.06100719	0.1146	-4.680873589	0.3137	0.030553846
01/06/2009	9.1540978	25.59723484	0.0941	-4.52947907	0.1736	-0.033707692
01/05/2009	9.2315787	24.39224407	0.1007	-4.498128246	-0.0362	-0.05734
01/04/2009	9.3123449	23.13615998	0.12985	-4.404613451	-0.1947	-0.120261538
01/03/2009	9.3928064	21.88481457	0.1717	-4.220405003	-0.261	-0.121538462
01/02/2009	9.3539728	22.4887589	0.15105	-3.997002108	0.0834	-0.085811538
01/01/2009	9.302797	23.28464935	0.1277	-3.962664749	0.2759	0.033492308
01/12/2008	9.2133951	24.6750368	0.09785	-4.316509556	0.2008	0.106657692
01/11/2008	9.1061951	26.34222165	0.1006	-4.765888364	0.0848	0.103911538
01/10/2008	8.9803851	28.29883148	0.1499	-5.207653338	0.035	0.072607692
01/09/2008	8.9559755	28.6784533	0.1611	-5.443539044	-0.1255	0.033569231
01/08/2008	8.9031997	29.49922712	0.18905	-5.484855313	-0.003	0.036580769

01/07/2008	8.9494429	28.78004858	0.16725	-5.274282302	0.0647	0.030553846
01/06/2008	9.0716043	26.88018257	0.11155	-4.704745977	0.2543	-0.033707692
01/05/2008	9.1797098	25.19891515	0.09395	-4.34623781	0.2764	-0.05734
01/04/2008	9.2642535	23.88408193	0.11225	-4.049574378	0.3091	-0.120261538
01/03/2008	9.3215257	22.99337904	0.1351	-3.966184458	0.214	-0.121538462
01/02/2008	9.2983632	23.35360518	0.12625	-4.132950021	0.1193	-0.085811538
01/01/2008	9.2507188	24.0945754	0.10795	-4.364184223	0.0364	0.033492308
01/12/2007	9.1429559	25.77051501	0.0953	-4.571009271	0.1653	0.106657692
01/11/2007	9.0329572	27.48122582	0.12485	-4.768973027	0.3109	0.103911538
01/10/2007	8.9736607	28.40341075	0.15225	-4.968879373	0.2941	0.072607692
01/09/2007	8.9428251	28.88296829	0.16805	-5.167792924	0.1928	0.033569231
01/08/2007	8.9777692	28.33951507	0.14955	-5.306634565	-0.0557	0.036580769
01/07/2007	9.0113006	27.81803036	0.13325	-4.779116192	0.3681	0.030553846
01/06/2007	9.2408143	24.24861121	0.1048	-4.263097978	0.1701	-0.033707692
01/05/2007	9.5432313	19.54539229	0.25695	-3.671297531	-0.1808	-0.05734
01/04/2007	9.5580772	19.31450726	0.2678	-3.638954293	-0.1951	-0.120261538
01/03/2007	9.4694428	20.69295764	0.2106	-3.747380872	-0.0272	-0.121538462
01/02/2007	9.2772863	23.68139502	0.1163	-4.363631919	-0.0451	-0.085811538
01/01/2007	9.1476724	25.69716317	0.0953	-4.762181117	-0.0405	0.033492308
01/12/2006	9.0356049	27.44004802	0.12555	-4.943707399	0.1285	0.106657692
01/11/2006	8.9337788	29.02365798	0.1737	-5.103064427	0.284	0.103911538
01/10/2006	8.914412	29.3248525	0.1833	-5.13527769	0.3131	0.072607692
01/09/2006	8.899095	29.56306387	0.1912	-5.048577006	0.4471	0.033569231
01/08/2006	8.8927919	29.66109009	0.19575	-4.927512235	0.5885	0.036580769
01/07/2006	8.9131769	29.34406	0.1853	-4.997829216	0.4538	0.030553846
01/06/2006	8.9976939	28.02964379	0.14185	-4.992274435	0.1961	-0.033707692
01/05/2006	9.1480292	25.6916139	0.0949	-4.785499145	-0.0641	-0.05734
01/04/2006	9.3782734	22.11083305	0.16395	-4.02538289	-0.0204	-0.120261538
01/03/2006	9.4287236	21.32622781	0.1905	-3.857230706	-0.0095	-0.121538462
01/02/2006	9.3949555	21.85139264	0.17095	-4.129555168	-0.177	-0.085811538
01/01/2006	9.3127858	23.12930322	0.1333	-4.394777188	-0.1864	0.033492308
01/12/2005	9.2594373	23.95898449	0.11095	-4.510034145	-0.1357	0.106657692
01/11/2005	9.2138791	24.66750978	0.0983	-4.532403626	-0.0183	0.103911538
01/10/2005	9.1509484	25.64621425	0.0935	-4.755021702	-0.0436	0.072607692
01/09/2005	9.0838563	26.68963701	0.10785	-5.012914587	-0.0926	0.033569231
01/08/2005	9.032447	27.48916058	0.12755	-5.215496992	-0.1362	0.036580769
01/07/2005	9.0611204	27.04322925	0.1146	-4.979217559	0.0119	0.030553846
01/06/2005	9.1343093	25.9049879	0.09575	-4.689899891	0.0738	-0.033707692
01/05/2005	9.1986134	24.9049233	0.0963	-4.524621733	0.0382	-0.05734
01/04/2005	9.3279356	22.89369263	0.13845	-4.251419891	-0.0906	-0.120261538
01/03/2005	9.3341781	22.79660768	0.14065	-3.9797888	0.1608	-0.121538462
01/02/2005	9.2533136	24.05422117	0.10765	-4.421648836	-0.0289	-0.085811538
01/01/2005	9.2288573	24.43456737	0.1014	-4.560608318	-0.0913	0.033492308

01/12/2004	9.1788834	25.21176645	0.09485	-4.601200652	0.024	0.106657692
01/11/2004	9.0470663	27.261799	0.1194	-5.130292236	-0.0946	0.103911538
01/10/2004	8.9812076	28.28604008	0.1498	-5.351273146	-0.1115	0.072607692
01/09/2004	8.9429296	28.88134364	0.168	-5.366624357	-0.0079	0.033569231
01/08/2004	8.9195542	29.24487963	0.1816	-5.338645528	0.0933	0.036580769
01/07/2004	8.9211086	29.22070675	0.182	-5.262920088	0.1624	0.030553846
01/06/2004	8.9548334	28.69621495	0.16465	-5.182958875	0.1392	-0.033707692
01/05/2004	9.0571463	27.10503362	0.11625	-5.173796043	-0.1701	-0.05734
01/04/2004	9.2106515	24.71770639	0.09635	-5.07166016	-0.5461	-0.120261538
01/03/2004	9.3755183	22.15368142	0.16375	-4.809854891	-0.7973	-0.121538462
01/02/2004	9.2571605	23.99439365	0.1095	-4.49255096	-0.1116	-0.085811538
01/01/2004	9.2258698	24.48102981	0.1001	-4.575675411	-0.0967	0.033492308
01/12/2003	9.2370127	24.30773415	0.1023	-4.9406758	-0.4963	0.106657692
01/11/2003	9.1804588	25.18726619	0.09455	-5.040233623	-0.4199	0.103911538
01/10/2003	9.0952838	26.51191652	0.1048	-5.317944883	-0.4324	0.072607692
01/09/2003	9.0096596	27.84355219	0.13715	-5.096664848	0.0537	0.033569231
01/08/2003	9.0005454	27.98529726	0.13995	-5.123727325	0.0556	0.036580769
01/07/2003	9.0307374	27.51574795	0.1268	-5.101517053	-0.0173	0.030553846
01/06/2003	9.0871322	26.63869087	0.10595	-4.942050577	-0.0321	-0.033707692
01/05/2003	9.1694514	25.35845432	0.0945	-4.917924164	-0.2643	-0.05734
01/04/2003	9.2724652	23.7563728	0.11565	-4.84194528	-0.5076	-0.120261538
01/03/2003	9.362152	22.36155512	0.15285	-4.892957371	-0.8381	-0.121538462
01/02/2003	9.3186444	23.03818991	0.135	-4.531878978	-0.343	-0.085811538
01/01/2003	9.2011263	24.86584261	0.0974	-4.253982643	0.3019	0.033492308
01/12/2002	9.0877652	26.62884667	0.1068	-4.482514503	0.4265	0.106657692
01/11/2002	9.0879733	26.62561022	0.1053	-4.760572244	0.1466	0.103911538
01/10/2002	9.1062016	26.34212157	0.1003	-4.741725591	0.1083	0.072607692
01/09/2002	9.0244052	27.6142267	0.12935	-4.868151482	0.2381	0.033569231
01/08/2002	8.977985	28.33615795	0.14975	-4.877041404	0.372	0.036580769
01/07/2002	9.0332053	27.47736653	0.1262	-4.931652183	0.1463	0.030553846
01/06/2002	8.9901056	28.14765862	0.1447	-5.079212975	0.1327	-0.033707692
01/05/2002	9.050911	27.20200591	0.11885	-4.771728472	0.2518	-0.05734
01/04/2002	9.2554954	24.02028863	0.1098	-4.141500376	0.2449	-0.120261538
01/03/2002	9.3820407	22.05224387	0.1662	-3.87050541	0.1219	-0.121538462
01/02/2002	9.3747479	22.16566243	0.16135	-4.12592404	-0.1121	-0.085811538
01/01/2002	9.3142811	23.10604879	0.1321	-4.212574083	-0.0086	0.033492308
01/12/2001	9.2381943	24.28935743	0.1047	-4.279871938	0.1617	0.106657692
01/11/2001	9.1150719	26.20417019	0.09895	-4.290406699	0.5327	0.103911538
01/10/2001	9.000293	27.9892224	0.1396	-4.295648804	0.885	0.072607692
01/09/2001	8.9765887	28.35787477	0.1508	-4.347961044	0.9058	0.033569231
01/08/2001	8.9733418	28.40836949	0.15205	-4.416650694	0.8481	0.036580769
01/07/2001	8.9945938	28.07785641	0.1411	-4.500711871	0.6974	0.030553846
01/06/2001	9.0966957	26.48995773	0.1023	-4.742959758	0.137	-0.033707692

01/05/2001	9.3079202	23.20497327	0.1292	-4.474682739	-0.252	-0.05734
01/04/2001	9.5358581	19.66006104	0.24965	-4.256220818	-0.7424	-0.120261538
01/03/2001	9.5019631	20.18719946	0.2314	-3.835011237	-0.2151	-0.121538462
01/02/2001	9.3711664	22.22136258	0.15815	-4.267341024	-0.241	-0.085811538
01/01/2001	9.2136144	24.67162653	0.0979	-4.496207216	0.0208	0.033492308
01/12/2000	9.1241852	26.06243925	0.0977	-4.735916416	0.0584	0.106657692
01/11/2000	9.0704439	26.89822874	0.1117	-4.945860306	0.0166	0.103911538
01/10/2000	9.0154613	27.75332356	0.1338	-4.905702693	0.2276	0.072607692
01/09/2000	8.9612764	28.59601258	0.15995	-5.129399469	0.1719	0.033569231
01/08/2000	8.9279239	29.11471356	0.17675	-5.316191121	0.0902	0.036580769
01/07/2000	8.9268684	29.1311289	0.17935	-5.309756167	0.0996	0.030553846
01/06/2000	8.9716379	28.43486882	0.15405	-5.109099648	0.1603	-0.033707692
01/05/2000	9.0283764	27.5524661	0.12855	-4.995205745	0.0969	-0.05734
01/04/2000	9.1307174	25.96084891	0.09605	-5.164132804	-0.3903	-0.120261538
01/03/2000	9.3474735	22.58983711	0.1458	-5.136999793	-1.036	-0.121538462
01/02/2000	9.4259499	21.36936417	0.19065	-4.974504075	-1.1189	-0.085811538
01/01/2000	9.2821715	23.60541967	0.11945	-4.792652483	-0.4899	0.033492308
01/12/1999	9.1701811	25.34710594	0.09305	-4.638823971	0.0123	0.106657692
01/11/1999	9.1170548	26.17333101	0.09865	-4.077766692	0.7389	0.103911538
01/10/1999	9.0138911	27.77774353	0.13405	-4.739662221	0.3997	0.072607692
01/09/1999	8.9351025	29.0030718	0.1733	-5.52452009	-0.1428	0.033569231
01/08/1999	8.9598904	28.61756841	0.1601	-5.435659494	-0.1293	0.036580769
01/07/1999	9.0086671	27.85898796	0.13545	-4.973551392	0.1813	0.030553846
01/06/1999	9.1034597	26.3847639	0.1005	-4.752677641	0.1076	-0.033707692
01/05/1999	9.2387728	24.28036145	0.10475	-4.292049536	0.1465	-0.05734
01/04/1999	9.4471383	21.03983907	0.1995	-3.92387535	-0.1335	-0.120261538
01/03/1999	9.4568294	20.88912309	0.20555	-3.829387851	-0.0682	-0.121538462
01/02/1999	9.3758525	22.14848412	0.16275	-3.925370617	0.0854	-0.085811538
01/01/1999	9.2871897	23.52737659	0.11985	-4.045410971	0.241	0.033492308
01/12/1998	9.1788809	25.21180561	0.0943	-4.212880989	0.4109	0.106657692
01/11/1998	9.0662391	26.9636226	0.11265	-4.397939816	0.5774	0.103911538
01/10/1998	8.9904555	28.1422158	0.1442	-4.560237421	0.6503	0.072607692
01/09/1998	8.9359307	28.9901912	0.17105	-4.703194487	0.6758	0.033569231
01/08/1998	8.9095624	29.40027358	0.1857	-4.98058708	0.4839	0.036580769
01/07/1998	8.962005	28.58468151	0.15815	-5.405903227	-0.107	0.030553846
01/06/1998	9.0693468	26.91529123	0.1119	-5.259037055	-0.2931	-0.033707692
01/05/1998	9.1375412	25.85472398	0.0949	-4.731572664	0.0218	-0.05734
01/04/1998	9.2023002	24.84758555	0.0966	-4.551781628	4.00E-04	-0.120261538
01/03/1998	9.3141812	23.10760173	0.13155	-3.926370059	0.2773	-0.121538462
01/02/1998	9.2786435	23.66028729	0.1153	-4.011437059	0.3026	-0.085811538
01/01/1998	9.1735288	25.29504244	0.09415	-4.185321165	0.4564	0.033492308
01/12/1997	9.0411155	27.35434747	0.1223	-4.539562915	0.5142	0.106657692
01/11/1997	8.9806363	28.29492529	0.1495	-5.065783008	0.1778	0.103911538

01/10/1997	8.9202213	29.23450512	0.1828	-5.296724743	0.1317	0.072607692
01/09/1997	8.8831888	29.8104382	0.19995	-5.317015151	0.228	0.033569231
01/08/1997	8.9354024	28.99840726	0.1726	-5.207553773	0.1755	0.036580769
01/07/1997	9.0591328	27.07414061	0.1145	-4.852707566	0.1451	0.030553846
01/06/1997	9.1658682	25.41418107	0.0939	-4.705495169	-0.0401	-0.033707692
01/05/1997	9.2702237	23.79123372	0.11425	-4.513135371	-0.1727	-0.05734
01/04/1997	9.3785219	22.10696897	0.1634	-3.944399856	0.0602	-0.120261538
01/03/1997	9.4570105	20.88630586	0.2048	-3.675374221	0.0834	-0.121538462
01/02/1997	9.5024622	20.17943663	0.2353	-3.709546878	-0.0913	-0.085811538
01/01/1997	9.4452307	21.06950673	0.19925	-4.200885094	-0.4043	0.033492308
01/12/1996	9.2278753	24.4498391	0.10155	-4.444319966	0.0282	0.106657692
01/11/1996	9.0817947	26.72169986	0.1069	-4.845356686	0.0811	0.103911538
01/10/1996	9.0604951	27.05295407	0.11515	-5.210668726	-0.2176	0.072607692
01/09/1996	9.0651922	26.97990336	0.1109	-5.445614407	-0.4664	0.033569231
01/08/1996	9.063152	27.01163327	0.11375	-5.474329512	-0.4897	0.036580769
01/07/1996	9.1441467	25.75199589	0.0933	-5.194020008	-0.4603	0.030553846
01/06/1996	9.3437891	22.64713621	0.14545	-4.706169037	-0.5945	-0.033707692
01/05/1996	9.4334314	21.25301096	0.19255	-4.276941833	-0.4452	-0.05734
01/04/1996	9.4668777	20.73285009	0.213	-3.921137223	-0.1913	-0.120261538
01/03/1996	9.5099285	20.06332039	0.23475	-3.849826678	-0.2536	-0.121538462
01/02/1996	9.5147331	19.98859913	0.23845	-3.87167048	-0.2915	-0.085811538
01/01/1996	9.4239172	21.40097691	0.1874	-3.960338181	-0.0977	0.033492308
01/12/1995	9.3030541	23.28065168	0.12625	-4.148738717	0.0898	0.106657692
01/11/1995	9.1313593	25.95086594	0.096	-4.577337015	0.1957	0.103911538
01/10/1995	9.0219898	27.65179131	0.12895	-4.925352897	0.1867	0.072607692
01/09/1995	9.0035765	27.93815683	0.13795	-5.103021468	0.0667	0.033569231
01/08/1995	9.1042067	26.37314586	0.10185	-5.236757842	-0.3788	0.036580769
01/07/1995	9.174263	25.28362442	0.09425	-5.3169726	-0.6772	0.030553846
01/06/1995	9.1192431	26.13929885	0.09785	-5.200399187	-0.3905	-0.033707692
01/05/1995	9.1872782	25.0812097	0.09425	-4.515710036	0.0841	-0.05734
01/04/1995	9.448146	21.02416751	0.2011	-3.955501618	-0.1685	-0.120261538
01/03/1995	9.5929163	18.77268622	0.2831	-3.803394243	-0.4679	-0.121538462
01/02/1995	9.5272175	19.79443988	0.24655	-4.025069139	-0.4843	-0.085811538
01/01/1995	9.3152992	23.09021501	0.13325	-4.095089867	0.1042	0.033492308
01/12/1994	9.1641256	25.44128089	0.0934	-4.15641926	0.515	0.106657692
01/11/1994	9.1384538	25.84053201	0.0954	-4.419268102	0.3296	0.103911538
01/10/1994	9.0274684	27.56658796	0.128	-4.947343959	0.1476	0.072607692
01/09/1994	9.1014317	26.41630322	0.10175	-5.200289782	-0.3347	0.033569231
01/08/1994	9.1311477	25.95415678	0.09635	-5.2580114	-0.4861	0.036580769
01/07/1994	9.0172216	27.72594757	0.13165	-5.250718994	-0.1227	0.030553846
01/06/1994	9.1852136	25.11331922	0.09375	-5.06354249	-0.4591	-0.033707692
01/05/1994	9.2789673	23.6552523	0.1178	-4.568882573	-0.2556	-0.05734
01/04/1994	9.3437539	22.64768362	0.14545	-4.060702431	0.0514	-0.120261538

01/03/1994	9.4629959	20.79322031	0.2081	-3.919728759	-0.1786	-0.121538462
01/02/1994	9.3616756	22.36896386	0.15415	-4.169508455	-0.1131	-0.085811538
01/01/1994	9.189207	25.05121345	0.0943	-4.312497401	0.2795	0.033492308
01/12/1993	9.0765578	26.8031446	0.10855	-4.622036847	0.3226	0.106657692
01/11/1993	9.1064307	26.3385579	0.1	-4.697321941	0.1529	0.103911538
01/10/1993	9.0642497	26.99456156	0.1141	-5.012341565	-0.0303	0.072607692
01/09/1993	9.1274298	26.01197863	0.0968	-5.134531605	-0.35	0.033569231
01/08/1993	9.1966858	24.93490205	0.09595	-5.052759057	-0.4842	0.036580769
01/07/1993	9.0516199	27.19098205	0.11765	-5.155596025	-0.1344	0.030553846
01/06/1993	9.0870897	26.63935084	0.10635	-4.720130864	0.1904	-0.033707692
01/05/1993	9.2802559	23.63521176	0.118	-4.493957878	-0.1848	-0.05734
01/04/1993	9.487675	20.40940826	0.2221	-4.054319405	-0.3898	-0.120261538
01/03/1993	9.5356456	19.66336583	0.2527	-3.885799609	-0.3689	-0.121538462
01/02/1993	9.47808	20.55863146	0.21675	-3.949193841	-0.2569	-0.085811538
01/01/1993	9.3561979	22.45415412	0.15255	-4.258549395	-0.1856	0.033492308
01/12/1992	9.2766858	23.69073465	0.1161	-4.599522007	-0.2792	0.106657692
01/11/1992	9.2591597	23.96330201	0.11	-4.742444215	-0.3668	0.103911538
01/10/1992	9.1124293	26.24526823	0.09925	-4.889920583	-0.0577	0.072607692
01/09/1992	9.0568287	27.10997291	0.11575	-5.107167416	-0.1027	0.033569231
01/08/1992	9.0332329	27.47693743	0.1262	-5.177046772	-0.0989	0.036580769
01/07/1992	9.0404017	27.36544798	0.1224	-5.223064246	-0.1668	0.030553846
01/06/1992	9.1232914	26.07633877	0.0973	-5.27120304	-0.4738	-0.033707692
01/05/1992	9.239254	24.27287725	0.10375	-5.019773032	-0.5827	-0.05734
01/04/1992	9.3267835	22.91160919	0.13845	-4.532499021	-0.3676	-0.120261538
01/03/1992	9.4778302	20.56251579	0.21485	-3.886203867	-0.1885	-0.121538462
01/02/1992	9.5583224	19.31069295	0.2625	-3.648102418	-0.2019	-0.085811538
01/01/1992	9.4009627	21.75796689	0.1741	-4.01305814	-0.0781	0.033492308
01/12/1991	9.1591545	25.51859325	0.09205	-4.639239091	0.0472	0.106657692
01/11/1991	9.0088169	27.85665756	0.13755	-5.069102558	0.0859	0.103911538
01/10/1991	9.0776888	26.78555593	0.10855	-5.20183491	-0.2619	0.072607692
01/09/1991	9.0470726	27.2617017	0.12065	-5.285522134	-0.25	0.033569231
01/08/1991	8.9580552	28.64610919	0.16015	-5.202592448	0.11	0.036580769
01/07/1991	8.9472472	28.81419546	0.16675	-5.001266075	0.3442	0.030553846
01/06/1991	9.1492848	25.6720867	0.09405	-4.275411117	0.442	-0.033707692
01/05/1991	9.2767456	23.68980373	0.1161	-3.949883171	0.3699	-0.05734
01/04/1991	9.3607006	22.38412812	0.15315	-3.643999449	0.4158	-0.120261538
01/03/1991	9.4698551	20.68654649	0.2131	-3.756535286	-0.0371	-0.121538462
01/02/1991	9.467769	20.71898908	0.2144	-3.978441193	-0.2528	-0.085811538
01/01/1991	9.2838819	23.57881994	0.11935	-3.973141842	0.3247	0.033492308
01/12/1990	9.1411668	25.79833852	0.09455	-4.358221279	0.3837	0.106657692
01/11/1990	9.02279	27.63934622	0.13155	-4.702231696	0.4081	0.103911538
01/10/1990	8.9434661	28.87300044	0.1687	-4.872590809	0.486	0.072607692
01/09/1990	8.9885633	28.17164384	0.14625	-5.042207183	0.1754	0.033569231

01/08/1990	8.9952067	28.06832496	0.143	-5.191143299	0.0052	0.036580769
01/07/1990	8.9608674	28.60237348	0.16045	-5.30189658	0.0015	0.030553846
01/06/1990	8.9940109	28.08692165	0.14175	-5.350772717	-0.1496	-0.033707692
01/05/1990	9.0012038	27.97505832	0.14015	-5.533773021	-0.3582	-0.05734
01/04/1990	9.0132904	27.78708569	0.13335	-5.388029863	-0.2471	-0.120261538
01/03/1990	9.1446085	25.74481295	0.0941	-4.415950563	0.3152	-0.121538462
01/02/1990	9.4068489	21.66642386	0.1778	-3.858667054	0.0572	-0.085811538
01/01/1990	9.5048228	20.14272487	0.2317	-3.732858158	-0.1232	0.033492308
01/12/1989	9.3296268	22.86739067	0.14075	-4.179992965	-0.0248	0.106657692
01/11/1989	9.4026613	21.73155072	0.17455	-4.641786468	-0.7139	0.103911538
01/10/1989	9.1761707	25.25395496	0.0938	-5.0737411	-0.4389	0.072607692
01/09/1989	9.0374109	27.41196076	0.1238	-5.266227114	-0.201	0.033569231
01/08/1989	9.0185846	27.70475033	0.13155	-5.306013824	-0.183	0.036580769
01/07/1989	9.0543181	27.14901939	0.11625	-5.284954489	-0.2739	0.030553846
01/06/1989	9.1729512	25.30402418	0.0932	-5.164766649	-0.5211	-0.033707692

Kikai 3.2 ka

Date	Sr/Ca	SrCa-SST	1 σ SD	$\delta^{18}O_{coral}$	$\delta^{18}O_{sw\_centered}$	1 σ SD
Jul	9.203707	24.8257	0.09885	-3.99003	-0.0377	0.07535
Aug	9.271566	23.77036	0.0943	-3.77592	-0.0348	0.0731
Sep	9.374705	22.16633	0.11725	-3.63457	-0.2133	0.0816
Oct	9.424133	21.39761	0.13505	-3.27463	-0.0077	0.0903
Nov	9.431017	21.29056	0.13935	-3.12094	0.1235	0.09185
Dec	9.511648	20.03657	0.183	-3.01866	-0.0243	0.11045
Jan	9.621022	18.33558	0.24385	-2.88515	-0.2295	0.13865
Feb	9.679438	17.42709	0.27855	-3.10217	-0.6307	0.15775
Mar	9.56746	19.16859	0.21265	-3.44	-0.6201	0.12535
Apr	9.383555	22.0287	0.11985	-3.64635	-0.2534	0.08255
May	9.245095	24.18204	0.0946	-3.77564	0.0483	0.07295
Jun	9.122262	26.09235	0.13075	-3.91475	0.2932	0.08665
Jul	9.076619	26.80219	0.15055	-4.04773	0.2989	0.097
Aug	9.15909	25.51959	0.11415	-3.90205	0.1901	0.07985
Sep	9.134304	25.90507	0.12665	-3.98495	0.1835	0.08375
Oct	9.157945	25.53741	0.11365	-3.80982	0.2845	0.07935
Nov	9.264574	23.8791	0.09305	-3.35234	0.4113	0.07215
Dec	9.348	22.58165	0.1074	-3.11241	0.3903	0.0779
Jan	9.479947	20.52959	0.1662	-3.11319	-0.0199	0.10385
Feb	9.523797	19.84763	0.1883	-3.17555	-0.218	0.11385
Mar	9.43435	21.23872	0.1416	-3.41484	-0.1806	0.0913
Apr	9.277221	23.6824	0.09345	-3.73309	-0.0093	0.0728
May	9.131318	25.95151	0.1265	-4.0016	0.1768	0.08485
Jun	9.072435	26.86727	0.1517	-4.12586	0.2359	0.0979

Jul	9.018683	27.70322	0.17995	-4.36105	0.1678	0.10975
Aug	9.081655	26.72387	0.14855	-4.38649	-0.053	0.0954
Sep	9.13019	25.96905	0.12525	-4.31481	-0.1345	0.08505
Oct	9.223826	24.51282	0.0964	-4.12024	-0.2301	0.07305
Nov	9.330796	22.8492	0.10255	-3.88631	-0.3284	0.0764
Dec	9.409126	21.63101	0.13145	-3.47669	-0.164	0.0878
Jan	9.44892	21.01213	0.1497	-3.1175	0.0718	0.0957
Feb	9.468631	20.70558	0.1567	-3.09751	0.0309	0.1005
Mar	9.427516	21.34501	0.1393	-3.27613	-0.0191	0.0922
Apr	9.340765	22.69417	0.10395	-3.48884	0.0358	0.07705
May	9.148014	25.69185	0.1185	-3.89782	0.2269	0.08265
Jun	9.02982	27.53002	0.1746	-4.15614	0.337	0.107
Jul	8.995498	28.06379	0.19475	-4.29431	0.3066	0.1164
Aug	9.035155	27.44705	0.1716	-4.29093	0.1869	0.1056
Sep	9.020929	27.66829	0.17815	-4.01067	0.5103	0.1098
Oct	9.110313	26.27819	0.13435	-3.78433	0.4591	0.08735
Nov	9.268368	23.82009	0.09245	-3.55693	0.1946	0.07155
Dec	9.350501	22.54276	0.1073	-3.12328	0.372	0.0773
Jan	9.385597	21.99693	0.12005	-3.12209	0.2646	0.0833
Feb	9.42498	21.38445	0.13765	-3.14069	0.1221	0.0902
Mar	9.412727	21.575	0.1329	-3.3276	-0.0263	0.08805
Apr	9.301376	23.30675	0.0959	-3.59531	0.0527	0.0737
May	9.181225	25.17535	0.1064	-3.85495	0.1682	0.07745
Jun	9.065169	26.98026	0.15455	-4.18432	0.1998	0.0999
Jul	9.047666	27.25247	0.1646	-4.25147	0.1867	0.10465
Aug	9.07825	26.77683	0.1498	-4.25305	0.0892	0.09575
Sep	9.114218	26.21746	0.1327	-4.23199	1.00E-04	0.08865
Oct	9.137521	25.85504	0.12245	-4.07878	0.08	0.08485
Nov	9.175931	25.25768	0.10845	-3.88377	0.1547	0.07775
Dec	9.249175	24.11858	0.0937	-3.62358	0.1879	0.07285
Jan	9.327112	22.9065	0.1007	-3.37188	0.1973	0.076
Feb	9.409182	21.63014	0.1306	-3.13456	0.1798	0.08715
Mar	9.411617	21.59227	0.1322	-3.01566	0.2892	0.0878
Apr	9.359039	22.40998	0.11095	-3.24974	0.2194	0.07915
May	9.231339	24.39598	0.09495	-3.67612	0.1904	0.0733
Jun	9.043622	27.31536	0.16705	-3.98407	0.4654	0.1037
Jul	8.984362	28.23699	0.2012	-4.2385	0.3963	0.11905
Aug	8.987312	28.19111	0.19765	-4.33798	0.2879	0.119
Sep	9.008742	27.85782	0.1846	-4.26165	0.2969	0.11225
Oct	9.035478	27.44202	0.1731	-4.21528	0.2614	0.1057
Nov	9.214763	24.65376	0.0975	-3.93999	-0.0219	0.07435
Dec	9.277881	23.67214	0.0939	-3.53033	0.1915	0.0735
Jan	9.358613	22.41659	0.1109	-3.32888	0.1415	0.07935

Feb	9.44978	20.99876	0.15045	-3.03963	0.1457	0.09445
Mar	9.449143	21.00866	0.15035	-2.79937	0.3893	0.09555
Apr	9.416323	21.51908	0.1361	-2.90221	0.3876	0.08875
May	9.352062	22.51848	0.10835	-3.29318	0.1973	0.0779
Jun	9.17409	25.28632	0.1103	-3.66109	0.3826	0.07885
Jul	9.056505	27.115	0.16195	-3.87929	0.5306	0.09995
Aug	9.077577	26.7873	0.15185	-4.01155	0.3341	0.09645
Sep	9.108242	26.31039	0.1354	-3.9946	0.2545	0.0894
Oct	9.139422	25.82547	0.12165	-3.85587	0.2984	0.0837
Nov	9.24866	24.12659	0.09395	-3.77853	0.0342	0.0729
Dec	9.345192	22.62532	0.1071	-3.73418	-0.2222	0.07675
Jan	9.425213	21.38082	0.13655	-3.68779	-0.4246	0.09025
Feb	9.520017	19.90642	0.18585	-3.54129	-0.574	0.11325
Mar	9.386443	21.98378	0.1206	-3.31093	0.0736	0.083
Apr	9.449038	21.0103	0.149	-2.97548	0.2141	0.09465
May	9.335611	22.77432	0.10305	-3.86203	-0.3202	0.07685
Jun	9.242626	24.22044	0.0943	-4.16818	-0.3364	0.0723
Jul	9.184034	25.13167	0.1055	-3.88495	0.1285	0.0775
Aug	9.212852	24.68348	0.09875	-4.15124	-0.227	0.07365
Sep	9.219883	24.57414	0.09715	-4.16678	-0.2646	0.0746
Oct	9.230221	24.41335	0.09625	-3.87961	-0.0098	0.0738
Nov	9.283287	23.58808	0.0944	-3.7659	-0.0609	0.07215
Dec	9.415266	21.53552	0.1323	-3.80966	-0.516	0.0893
Jan	9.411101	21.60029	0.1307	-3.60596	-0.3001	0.0872
Feb	9.525523	19.8208	0.19145	-3.56413	-0.6127	0.11325
Mar	9.557236	19.32758	0.20515	-3.37506	-0.5245	0.1221
Apr	9.459333	20.85018	0.1544	-3.38368	-0.2257	0.09705
May	9.252653	24.06449	0.0926	-3.86547	-0.0652	0.07265
Jun	9.180761	25.18257	0.1075	-4.27978	-0.2562	0.0774
Jul	9.166956	25.39727	0.111	-4.35664	-0.2897	0.07965
Aug	9.187316	25.08063	0.1047	-4.28983	-0.2867	0.07705
Sep	9.207934	24.75996	0.10015	-4.37205	-0.4322	0.0745
Oct	9.231959	24.38633	0.0966	-4.21831	-0.3543	0.07365
Nov	9.263235	23.89991	0.0937	-4.01042	-0.2434	0.0731
Dec	9.338633	22.72733	0.1035	-3.8677	-0.3342	0.0768
Jan	9.364315	22.32791	0.1129	-3.68623	-0.2332	0.0793
Feb	9.459534	20.84706	0.154	-3.64582	-0.4907	0.0972
Mar	9.482224	20.49418	0.1665	-3.39588	-0.3104	0.1025
Apr	9.438443	21.17507	0.1435	-3.63043	-0.4094	0.09245
May	9.277572	23.67695	0.0935	-3.83162	-0.1083	0.07255
Jun	9.054159	27.15149	0.1621	-4.08404	0.3342	0.10155
Jul	8.971558	28.43611	0.20705	-4.25752	0.4157	0.12205
Aug	9.016496	27.73723	0.1803	-4.3069	0.2268	0.1099

Sep	9.08696	26.64137	0.14425	-4.14628	0.1687	0.09375
Oct	9.129586	25.97845	0.12695	-3.82206	0.3612	0.0854
Nov	9.232426	24.37907	0.0958	-3.79962	0.064	0.0738
Dec	9.344521	22.63576	0.10545	-3.68026	-0.165	0.0771
Jan	9.41197	21.58678	0.12985	-3.52026	-0.2175	0.08845
Feb	9.477093	20.57398	0.16485	-3.29493	-0.1944	0.10235
Mar	9.499792	20.22097	0.1737	-3.27476	-0.2452	0.1072
Apr	9.42021	21.45863	0.1349	-3.58358	-0.3041	0.0896
May	9.266965	23.84191	0.0938	-4.04902	-0.2927	0.073
Jun	9.184312	25.12735	0.1074	-4.27146	-0.2581	0.0765
Jul	9.029836	27.52976	0.17515	-4.41469	0.077	0.1057
Aug	9.032317	27.49118	0.17245	-4.51578	-0.0287	0.1074
Sep	9.045341	27.28863	0.16545	-4.65043	-0.2065	0.1041
Oct	9.164478	25.43581	0.11195	-4.33702	-0.2618	0.07995
Nov	9.230987	24.40144	0.09505	-3.86692	3.00E-04	0.07335
Dec	9.337884	22.73898	0.1034	-3.72595	-0.1912	0.0767
Jan	9.506704	20.11346	0.17605	-3.52214	-0.5128	0.1078
Feb	9.555712	19.35129	0.2059	-3.30205	-0.447	0.12245
Mar	9.528498	19.77452	0.19235	-3.44851	-0.5058	0.116
Apr	9.407941	21.64944	0.1292	-3.76321	-0.4481	0.08645
May	9.280079	23.63797	0.0932	-4.15343	-0.4379	0.0728
Jun	9.036573	27.42499	0.17065	-4.33862	0.1342	0.10535
Jul	8.945157	28.8467	0.2236	-4.612	0.1423	0.12945
Aug	8.969317	28.47097	0.2066	-4.71988	-0.0366	0.12265
Sep	9.017991	27.71399	0.18345	-4.71278	-0.1836	0.1092
Oct	9.095775	26.50427	0.14265	-4.47628	-0.186	0.0928
Nov	9.160411	25.49906	0.115	-4.2737	-0.1862	0.08
Dec	9.341266	22.68638	0.10615	-4.15559	-0.6314	0.07655
Jan	9.439187	21.1635	0.1448	-3.76978	-0.5515	0.09335
Feb	9.503745	20.15949	0.17985	-3.2423	-0.2233	0.10805
Mar	9.503559	20.16238	0.1778	-3.14569	-0.1264	0.10805
Apr	9.435175	21.2259	0.1427	-3.46739	-0.2355	0.0924
May	9.219252	24.58395	0.09715	-3.93018	-0.0257	0.0749
Jun	9.076999	26.79628	0.15135	-4.27771	0.0681	0.09645
Jul	9.033335	27.47535	0.17225	-4.46204	0.0186	0.1053
Aug	9.044739	27.29799	0.16815	-4.32604	0.1211	0.10525
Sep	9.063501	27.0062	0.1569	-4.13428	0.2546	0.0986
Oct	9.152883	25.61613	0.1158	-4.01124	0.0988	0.08135
Nov	9.266552	23.84834	0.09365	-3.94744	-0.1911	0.0719
Dec	9.297976	23.35963	0.09645	-3.87359	-0.216	0.0734
Jan	9.337888	22.73891	0.10515	-3.75844	-0.2246	0.07615
Feb	9.47254	20.64479	0.15925	-3.50062	-0.3844	0.10065

Kikai 4.9 ka

Date	Sr/Ca	SrCa-SST	1 σ SD	$\delta^{18}O_{coral}$	$\delta^{18}O_{sw\_centered}$	1 σ SD
Mar	9.52197471	19.8759766	0.2934	-3.51880867	-0.7341	0.1651
Feb	9.48740359	20.4136301	0.273	-3.33164232	-0.4389	0.1563
Jan	9.44717979	21.0391946	0.2486	-3.16125643	-0.1443	0.1432
Dec	9.26555256	23.8638793	0.1519	-3.25113357	0.3321	0.0971
Nov	9.02263048	27.6418277	0.1018	-3.43021511	0.9099	0.0754
Oct	8.83923211	30.4940574	0.1767	-3.85655514	1.053	0.1083
Sep	8.7238424	32.2886096	0.2451	-4.50000542	0.7688	0.1385
Aug	8.68761649	32.8519986	0.2658	-4.81806938	0.5633	0.1499
Jul	8.81950168	30.800907	0.1882	-4.62815383	0.3424	0.1134
Jun	8.83827135	30.5089992	0.1794	-4.30896581	0.6036	0.1094
May	8.99041192	28.1428939	0.1092	-3.83596609	0.6028	0.0786
Apr	9.25750852	23.9889811	0.1464	-3.50636488	0.1006	0.0942
Mar	9.53141739	19.7291231	0.2995	-3.18055577	-0.4226	0.1666
Feb	9.24825685	24.132864	0.1413	-2.9376028	0.6985	0.0912
Jan	9.16553168	25.4194141	0.1071	-3.03021354	0.8638	0.0784
Dec	9.16343864	25.4519651	0.1068	-3.56500375	0.3362	0.0785
Nov	8.97187399	28.4311977	0.1157	-4.31335779	0.1827	0.0808
Oct	8.88674806	29.7550846	0.1526	-4.6321747	0.1292	0.0972
Sep	8.71230639	32.4680188	0.2475	-4.71437767	0.5904	0.1424
Aug	8.68873866	32.8345465	0.2657	-4.63463701	0.7435	0.1494
Jul	8.76528555	31.6440817	0.2187	-4.33620068	0.8027	0.1305
Jun	8.93189396	29.052971	0.1312	-3.98743045	0.6343	0.087
May	8.95210238	28.7386878	0.123	-3.72531649	0.8327	0.0848
Apr	9.0720596	26.8731011	0.094	-3.73108071	0.4538	0.0725
Mar	9.26389983	23.8895828	0.1471	-4.09143294	-0.5034	0.0955
Feb	9.13822023	25.8441644	0.0993	-4.23107216	-0.253	0.0749
Jan	9.00372186	27.9358965	0.1056	-4.33690582	0.0605	0.0774
Dec	8.9567046	28.6671136	0.1206	-4.44295064	0.1	0.0827
Nov	8.90356246	29.4935854	0.1451	-4.56227931	0.1481	0.0936
Oct	8.84446409	30.4126891	0.1758	-4.68951281	0.2022	0.1075
Sep	8.78536573	31.3317928	0.2066	-4.81674631	0.2585	0.1229
Aug	8.76225939	31.6911447	0.2212	-4.8658419	0.2846	0.1293
Jul	8.84884508	30.3445555	0.173	-4.73350361	0.147	0.1052
Jun	8.92844024	29.1066837	0.1341	-4.82815073	-0.1956	0.0879
May	9.05048674	27.2086043	0.0953	-4.54887029	-0.2978	0.073
Apr	9.20408526	24.8198249	0.1216	-4.01260843	-0.2384	0.0841
Mar	9.32523585	22.9356789	0.1812	-3.47579753	-0.0787	0.1077
Feb	9.26405826	23.8871188	0.1491	-3.00453674	0.5818	0.0961
Jan	9.13808862	25.8462112	0.0993	-3.14128776	0.8384	0.0757
Dec	9.09483049	26.5189659	0.0937	-4.0153291	0.0986	0.0726

Nov	8.95098887	28.7560051	0.1226	-4.78208219	-0.2205	0.0839
Oct	8.87398009	29.9536533	0.1601	-5.04065711	-0.2388	0.1006
Sep	8.85238202	30.2895488	0.1704	-5.00788106	-0.1398	0.1052
Aug	8.77319112	31.5211335	0.2132	-4.97221977	0.1427	0.1266
Jul	9.02563901	27.5950387	0.0985	-4.89950679	-0.5705	0.0741
Jun	9.10842423	26.3075547	0.0946	-4.61674769	-0.545	0.0724
May	9.19246608	25.0005275	0.1151	-3.98291254	-0.1737	0.0824
Apr	9.31059718	23.1633409	0.1746	-3.57657312	-0.1342	0.1063
Mar	9.57164608	19.1034824	0.3242	-4.04589761	-1.4146	0.1811
Feb	9.32982231	22.8643498	0.1832	-4.40287671	-1.0208	0.1111
Jan	9.00171074	27.9671735	0.1062	-4.70073614	-0.2956	0.077
Dec	8.8999386	29.5499441	0.1469	-4.68483014	0.0364	0.0937
Nov	8.87763158	29.8968651	0.159	-4.75634135	0.0325	0.098
Oct	8.90821376	29.4212479	0.1427	-4.96049973	-0.2656	0.0926
Sep	8.97514921	28.3802612	0.1146	-5.0692867	-0.5824	0.0802
Aug	8.9762632	28.3629363	0.1144	-4.95834824	-0.4751	0.0803
Jul	8.99977044	27.9973494	0.1068	-4.66891117	-0.2586	0.0773
Jun	9.0911155	26.5767419	0.0942	-4.08679779	0.0385	0.0722
May	9.24704252	24.1517493	0.141	-3.26121166	0.3803	0.0924
Apr	9.3579754	22.4265101	0.1969	-2.9935859	0.3032	0.1183
Mar	9.41047735	21.6099946	0.2273	-2.92198422	0.2091	0.1343
Feb	9.23168424	24.3906028	0.1332	-2.86943672	0.8194	0.0876
Jan	9.12620334	26.0310522	0.0968	-3.71607919	0.3006	0.0745
Dec	9.05786751	27.0938179	0.0952	-4.41818381	-0.1895	0.0725
Nov	9.01702837	27.7289523	0.1005	-4.79497312	-0.438	0.0757
Oct	9.01019381	27.835244	0.1037	-5.05561233	-0.6781	0.0764
Sep	9.01242439	27.8005539	0.1019	-5.14123107	-0.7709	0.0753
Aug	9.02016345	27.6801952	0.1005	-4.84456296	-0.4987	0.076
Jul	9.09697106	26.4856757	0.0949	-4.31077676	-0.2023	0.0729
Jun	9.13854419	25.8391262	0.0999	-4.01345846	-0.0346	0.0749
May	9.14247979	25.7779193	0.1008	-3.97115224	-0.0058	0.0753
Apr	9.23367977	24.3595681	0.1345	-3.63026314	0.0523	0.0885
Mar	9.33641158	22.7618728	0.1885	-3.26906069	0.0931	0.1112
Feb	9.31129363	23.1525096	0.1728	-3.47967646	-0.0396	0.1066
Jan	9.26592655	23.8580629	0.1489	-3.78328435	-0.2015	0.0953
Dec	9.21979356	24.5755278	0.1276	-4.08847799	-0.3632	0.0863
Nov	9.10051459	26.4305663	0.0951	-4.57468653	-0.4788	0.0729
Oct	9.0281529	27.5559424	0.0993	-4.84785631	-0.5264	0.0737
Sep	9.02267224	27.6411782	0.099	-4.72744708	-0.3901	0.0751
Aug	8.97362886	28.4039058	0.1152	-4.63284403	-0.1406	0.0806
Jul	8.9817448	28.2776859	0.1128	-4.67261686	-0.205	0.0795
Jun	9.0088488	27.8561618	0.1049	-4.56255625	-0.1813	0.0771
May	9.10438969	26.3703003	0.0947	-3.85900871	0.2248	0.0735

Apr	9.45952056	20.8472698	0.2577	-3.31429617	-0.3357	0.1491
Mar	9.64542177	17.9561156	0.3683	-3.17857048	-0.7762	0.2018
Feb	9.47545562	20.599446	0.2667	-3.2442454	-0.316	0.1525
Jan	9.30726532	23.2151583	0.1684	-3.40516017	0.0496	0.1057
Dec	9.18957888	25.0454295	0.1154	-3.80499871	0.0147	0.0814
Nov	9.07276737	26.8620939	0.0946	-4.21014835	-0.0274	0.0732
Oct	8.96378677	28.5569709	0.12	-4.58540109	-0.0627	0.082
Sep	8.91207733	29.3611614	0.1393	-4.71640937	-0.0332	0.0925
Aug	8.90660492	29.4462688	0.1427	-4.84109737	-0.1436	0.0934
Jul	9.01258012	27.7981319	0.103	-4.97448439	-0.6044	0.076
Jun	9.07497478	26.8277639	0.0939	-4.92179331	-0.7462	0.073
May	9.0829123	26.7043188	0.094	-4.77797636	-0.6271	0.0722
Apr	9.13098333	25.9567133	0.0993	-4.45026116	-0.449	0.0732
Mar	9.34373551	22.6479703	0.1927	-3.46512684	-0.1258	0.1139
Feb	9.2620174	23.9188585	0.1494	-3.70009188	-0.1056	0.0953
Jan	9.24929057	24.1167875	0.1419	-3.89401168	-0.2611	0.0917
Dec	9.27853947	23.6619056	0.1558	-3.93629214	-0.394	0.0973
Nov	9.22210412	24.5395938	0.1299	-4.14069251	-0.4239	0.0862
Oct	9.11562338	26.1955929	0.0955	-4.25713564	-0.2078	0.0738
Sep	8.99317974	28.0998485	0.1081	-4.34811284	0.0817	0.0776
Aug	8.94118659	28.9084512	0.1282	-4.45593225	0.1361	0.0861
Jul	9.03651949	27.4258244	0.0976	-4.54268378	-0.2483	0.0742
Jun	9.04708413	27.2615221	0.0953	-4.33947652	-0.0776	0.0738
May	9.1927801	24.9956439	0.1183	-3.91707311	-0.1089	0.0816
Apr	9.2844251	23.5703718	0.1596	-3.36085079	0.1625	0.1
Mar	9.43756542	21.1887182	0.2437	-2.7045021	0.3441	0.1403
Feb	9.2572087	23.9936439	0.1456	-3.01823841	0.5923	0.0938
Jan	9.18046224	25.1872124	0.1123	-3.77439923	0.0733	0.0799
Dec	9.00423165	27.9279681	0.1061	-4.17786686	0.2183	0.0773
Nov	9.00403305	27.9310568	0.1042	-4.7459692	-0.3498	0.077
Oct	8.92483432	29.1627633	0.136	-4.61190063	0.0308	0.0893
Sep	8.89739633	29.5894817	0.1487	-4.36276781	0.3658	0.0953
Aug	8.78616017	31.3194375	0.2065	-4.63576642	0.4368	0.1217
Jul	8.95953855	28.6230397	0.1211	-4.44565131	0.0893	0.0838
Jun	8.8795045	29.8677372	0.1589	-4.21750573	0.5651	0.099
May	8.9596804	28.6208336	0.1211	-3.97169611	0.5627	0.0834
Apr	9.20578119	24.7934497	0.1213	-3.57262749	0.1973	0.0835
Mar	9.46110238	20.822669	0.2553	-3.02927299	-0.0547	0.1464
Feb	9.3677944	22.273804	0.205	-3.39680398	-0.133	0.121
Jan	9.26027679	23.9459286	0.1469	-3.45670789	0.1429	0.0939
Dec	9.18688475	25.0873289	0.1155	-4.25024618	-0.4217	0.0813
Nov	9.17636433	25.2509436	0.111	-4.63084185	-0.7715	0.0791
Oct	9.29460396	23.4120691	0.1631	-4.78360117	-1.2911	0.1012

Sep	8.96378255	28.5570365	0.1196	-4.36347519	0.1587	0.0813
Aug	8.75409464	31.8181238	0.2262	-4.65723786	0.5165	0.131
Jul	8.88747759	29.7437389	0.1525	-4.69210974	0.0682	0.0962
Jun	8.98265004	28.2636074	0.1102	-4.70600841	-0.2426	0.0789
May	8.99647607	28.0485837	0.1079	-4.26852525	0.1514	0.0779
Apr	9.10144724	26.4160615	0.0943	-3.56981451	0.5237	0.0729
Mar	9.26826244	23.8217351	0.1517	-3.05083291	0.5224	0.0947
Feb	9.10391451	26.3776904	0.0945	-3.16246429	0.9232	0.0724
Jan	9.05135353	27.195124	0.0956	-3.66077186	0.589	0.0735
Dec	9.01669701	27.7341056	0.1017	-4.18883267	0.1689	0.0756
Nov	8.94232639	28.8907249	0.1278	-4.73804059	-0.1499	0.0852
Oct	8.89722324	29.5921736	0.1494	-4.55436831	0.174	0.0947
Sep	8.91796008	29.2696721	0.1382	-4.84102621	-0.176	0.0905
Aug	8.86910653	30.0294475	0.1617	-4.73410084	0.0822	0.1015
Jul	8.91430088	29.3265804	0.1401	-4.60369348	0.0725	0.091
Jun	9.05008031	27.2149253	0.095	-4.41808798	-0.1634	0.0734
May	9.18473775	25.1207193	0.1149	-4.04210998	-0.2075	0.0814
Apr	9.29949394	23.3360197	0.1665	-3.45325565	0.0246	0.1035
Mar	9.29705166	23.3740022	0.1655	-3.21497031	0.2691	0.1027
Feb	9.08595313	26.6570276	0.0938	-3.3918907	0.7498	0.0732
Jan	9.04725721	27.2588303	0.0955	-4.01990656	0.2428	0.072
Dec	8.98283576	28.2607191	0.1119	-5.00527951	-0.5437	0.0801
Nov	8.90035222	29.5435114	0.146	-4.88287301	-0.1648	0.0955
Oct	8.87934807	29.87017	0.1573	-5.0393083	-0.2537	0.0968
Sep	8.9300631	29.0814447	0.1326	-4.94144521	-0.3143	0.0872
Aug	8.8497032	30.33121	0.1735	-5.00701951	-0.1307	0.1057
Jul	8.948116	28.8006844	0.1263	-4.58972508	-0.0187	0.0848
Jun	9.02775426	27.5621421	0.0992	-4.59334347	-0.2709	0.0741
May	9.07214978	26.8716985	0.0937	-4.53429092	-0.3488	0.0721
Apr	9.14169555	25.7901159	0.1009	-3.08712061	0.8815	0.0757

Kikai 5.7 ka

Sample Number	Sr/Ca	SrCa-SST	1 σ SD	$\delta^{18}O_{coral}$	$\delta^{18}O_{sw\_centered}$
1	9.096076	26.499595	0.32065	-5.014293	-0.1904
3	9.170481	25.342442	0.3149	-4.489897	0.1032
5	9.2935087	23.429103	0.31505	-4.088702	0.1211
8	9.5601859	19.281713	0.3776	-3.190801	0.1885
9	9.5623271	19.248412	0.3789	-3.218813	0.1564
11	9.6103405	18.501704	0.3989	-3.042039	0.1803
13	9.507489	20.10126	0.35975	-3.400242	0.1439
15	9.3966357	21.825261	0.33035	-3.733191	0.155
17	9.2484374	24.130056	0.3132	-4.070345	0.2791

19	9.175277	25.267854	0.31305	-4.622247	-0.0447
21	9.0271811	27.571057	0.34005	-5.043237	-0.0047
23	9.0179647	27.714391	0.34165	-4.955525	0.1116
25	9.0686984	26.925374	0.3234	-5.081437	-0.1734
27	9.0403721	27.365909	0.33665	-5.087981	-0.0909
29	9.0059414	27.901377	0.339	-5.126219	-0.0211
31	8.9952567	28.067548	0.343	-5.163135	-0.0245
33	9.006673	27.89	0.3395	-5.205421	-0.1025
35	9.0026385	27.952745	0.33985	-5.13878	-0.0255
37	9.0102542	27.834305	0.33625	-5.238247	-0.1473
39	9.0322863	27.491659	0.33275	-5.306817	-0.2834
41	9.095167	26.513733	0.32115	-5.335446	-0.5088
43	9.0599027	27.062166	0.32795	-4.982897	-0.0471
45	9.2135381	24.672814	0.3112	-4.458352	-1.00E-04
47	9.3962102	21.831878	0.32635	-3.952133	-0.0609
49	9.5607657	19.272695	0.3767	-3.423089	-0.0436
51	9.4925858	20.333036	0.35465	-3.413142	0.1763
53	9.5309218	19.736831	0.368	-3.284208	0.1861
55	9.590706	18.807061	0.38455	-3.337781	-0.0532
57	9.5170345	19.952807	0.36185	-3.520457	-0.0069
59	9.4008635	21.759511	0.33155	-3.822374	0.0529
61	9.4048501	21.697511	0.32705	-4.050936	-0.1873
63	9.332111	22.828756	0.31545	-4.403495	-0.3142
65	9.2919218	23.453783	0.321	-4.391094	-0.1767
67	9.2113332	24.707104	0.31335	-4.879401	-0.4147
69	9.0484383	27.240462	0.33035	-5.020053	-0.0477
71	9.045171	27.291275	0.3327	-5.032784	-0.0494
73	9.0087172	27.858209	0.3389	-5.07304	0.0233
75	9.0567083	27.111845	0.3312	-5.129414	-0.183
77	9.0090172	27.853543	0.3381	-5.168764	-0.0741
79	9.1224156	26.08996	0.3163	-5.154342	-0.412
81	9.1149737	26.205696	0.31765	-5.014404	-0.2507
83	9.134482	25.902301	0.31745	-5.177799	-0.4738
85	9.0902797	26.589741	0.32375	-5.232258	-0.3884
87	9.1447911	25.741973	0.31385	-5.086782	-0.4151
89	9.1042956	26.371763	0.3213	-4.721921	0.0768
91	9.1829719	25.148181	0.3136	-4.313427	0.2401
93	9.208735	24.747511	0.3098	-4.244593	0.2294
95	9.3008497	23.314934	0.3123	-3.867407	0.3191
97	9.4490553	21.010026	0.34085	-3.619336	0.107
99	9.5742833	19.062468	0.38305	-3.042617	0.2939
101	9.6095031	18.514726	0.3951	-2.92221	0.3059
104	9.5881725	18.846463	0.3886	-3.696299	-0.404

105	9.4765528	20.582383	0.34625	-3.591353	0.0483
107	9.4245754	21.390741	0.33715	-3.399443	0.4012
109	9.3352639	22.779722	0.3193	-4.190825	-0.1105
111	9.2747219	23.721277	0.3147	-4.180332	0.0884
113	9.1872081	25.082301	0.3112	-4.556935	-0.0155
115	9.1770037	25.241001	0.3095	-4.627892	-0.0555
119	9.045619	27.284308	0.3272	-4.957618	0.0244
121	9.0031063	27.94547	0.34215	-5.074959	0.0388
125	8.9534293	28.718051	0.3564	-5.195958	0.0708
127	8.9737886	28.401421	0.35195	-5.144595	0.0599
129	9.0106419	27.828275	0.3392	-5.166028	-0.075
131	9.0110179	27.822427	0.33305	-5.246247	-0.1569
133	8.9795718	28.311481	0.3478	-5.181495	0.0062
136	9.0224918	27.643984	0.33855	-4.958194	0.0953
137	9.0663156	26.962432	0.32995	-4.890769	0.0263
139	9.0854902	26.664227	0.3279	-4.690559	0.1664
141	9.2243703	24.50435	0.30925	-4.308747	0.1157
143	9.2814326	23.616911	0.31155	-4.091953	0.1552
145	9.426877	21.354945	0.33825	-3.487994	0.3071
147	9.529601	19.757371	0.36505	-3.253376	0.2224
149	9.5628766	19.239866	0.38155	-3.127879	0.2433
151	9.4655231	20.753917	0.3501	-3.299923	0.3752
153	9.377019	22.130343	0.3275	-3.585958	0.3646
155	9.2459199	24.169209	0.3119	-3.987559	0.3696
157	9.2717536	23.76744	0.3095	-4.31757	-0.0405
159	9.1812574	25.174847	0.31135	-4.423683	0.1353
161	9.1627505	25.462667	0.31035	-4.525594	0.0905
163	9.120591	26.118336	0.31875	-4.819223	-0.0721
165	9.0104307	27.83156	0.33705	-4.82975	0.259
167	8.9804351	28.298054	0.3478	-4.90088	0.2823
169	9.0061664	27.897879	0.3445	-5.236979	-0.1334
171	9.0181124	27.712093	0.3349	-5.026351	0.0407
173	9.002756	27.950918	0.3417	-5.197396	-0.0833
175	9.0122511	27.803249	0.34065	-5.126562	-0.0406
177	9.0073151	27.880014	0.3392	-5.212748	-0.1125
179	9.0350861	27.448116	0.33475	-5.135662	-0.1222
181	9.0075093	27.876993	0.3334	-5.204635	-0.103
183	9.0251656	27.602401	0.33465	-5.04975	-0.0049
185	9.0806868	26.73893	0.31965	-4.956063	-0.0838
187	9.2381796	24.289586	0.3103	-4.266377	0.1144
189	9.3759281	22.147308	0.32585	-4.170907	-0.219
191	9.591256	18.798507	0.3822	-3.488259	-0.2069
193	9.5967461	18.713124	0.3923	-2.931271	0.3341

195	9.5359031	19.65936	0.3711	-3.391371	0.0645
197	9.3724261	22.201771	0.3237	-4.016154	-0.0518
199	9.260914	23.936019	0.31125	-4.12751	0.1835
201	9.2245376	24.501748	0.31225	-4.431797	-0.0073
203	9.1740881	25.286344	0.3132	-4.927274	-0.3452
205	9.0464407	27.271529	0.33185	-4.935648	0.0437
207	9.0659683	26.967834	0.32585	-4.956428	-0.0404
209	9.0598585	27.062854	0.3295	-4.874309	0.064
211	9.0670288	26.951341	0.32705	-4.936139	-0.0221
213	9.090915	26.57986	0.3251	-4.857393	-0.0186
215	9.0541181	27.152129	0.3312	-4.831108	0.1231
217	9.0784081	26.774369	0.3227	-5.120732	-0.2415
219	9.1293421	25.982238	0.3122	-4.836282	-0.1163
221	9.3641167	22.331	0.32135	-4.000045	-0.0095
223	9.406158	21.67717	0.3348	-3.822711	0.0356
225	9.4981707	20.246179	0.36075	-3.756752	-0.1836
227	9.5917425	18.790941	0.3876	-3.403074	-0.1212
230	9.6357674	18.106261	0.4039	-3.236814	-0.0906
231	9.6091884	18.519621	0.3921	-3.333533	-0.1047
233	9.486987	20.420109	0.3532	-3.36723	0.2412
235	9.435037	21.22804	0.3412	-3.842289	-0.0721
237	9.3115998	23.147748	0.31355	-4.098126	0.0552
240	9.2233786	24.519774	0.3106	-4.724454	-0.2965
241	9.1263431	26.028879	0.31805	-4.741858	-0.0127
243	9.1825629	25.154543	0.31375	-4.692874	-0.1384
245	9.1351095	25.892543	0.31695	-4.79094	-0.0883
247	9.074605	26.833515	0.32945	-5.082377	-0.1909
250	9.0618762	27.031474	0.32755	-5.367173	-0.4377
251	9.0416762	27.345627	0.33095	-5.349547	-0.3566
253	8.9970544	28.039589	0.341	-5.000513	0.132
255	8.998325	28.019829	0.34135	-5.234991	-0.1072
257	9.0389939	27.387343	0.33145	-4.846849	0.1545
259	9.0334565	27.473461	0.335	-5.161297	-0.1424
261	9.0950581	26.515426	0.3191	-4.868827	-0.0419
264	9.1006026	26.429197	0.3205	-4.693157	0.1172
265	9.1386868	25.836908	0.3131	-4.218612	0.4706
267	9.5874085	18.858344	0.3881	-4.218366	-0.9226
269	9.5033347	20.165868	0.35895	-3.720279	-0.1621
271	9.4929372	20.327571	0.3519	-3.685309	-0.097
273	9.6514292	17.862687	0.41085	-3.082662	0.0115
275	9.5178858	19.939568	0.36015	-3.578692	-0.0666
277	9.4942835	20.306633	0.3554	-3.762053	-0.1754
279	9.3653377	22.31201	0.3214	-3.761635	0.2238

281	9.298016	23.359005	0.3142	-4.120379	0.0762
284	9.1006329	26.428726	0.3175	-4.669357	0.1398
285	9.153088	25.612939	0.3151	-4.594739	0.0519
287	9.09593	26.501867	0.32035	-4.855667	-0.0306
289	9.0318036	27.499167	0.33385	-5.166517	-0.1429
291	9.0279037	27.559818	0.3367	-4.977825	0.0584
293	9.0041098	27.929864	0.33825	-5.083852	0.0247
295	9.0144472	27.769095	0.3367	-5.113722	-0.0348
297	8.99232	28.113219	0.3409	-5.215934	-0.0686
299	9.0268638	27.575991	0.33365	-5.121182	-0.0839
301	9.1072615	26.325637	0.3179	-4.986472	-0.1983
303	9.1284884	25.995515	0.31675	-5.069051	-0.3466
305	9.085682	26.661244	0.32665	-4.902598	-0.0461
307	9.0445791	27.300481	0.33505	-4.679907	0.3046
309	9.147834	25.69465	0.31595	-4.821467	-0.1591
312	9.1540464	25.598034	0.313	-3.480486	1.1639
313	9.3895577	21.93534	0.32865	-3.744303	0.1669
315	9.5783972	18.998488	0.3804	-2.971076	0.3537
317	9.570634	19.119222	0.3844	-2.949945	0.3968
319	9.4609491	20.825053	0.34385	-3.303359	0.3849
321	9.3765455	22.137706	0.3252	-3.62557	0.3255
323	9.3692281	22.251507	0.32305	-3.923083	0.051
325	9.3388014	22.724706	0.3216	-4.081595	-0.012
327	9.3843822	22.015829	0.32755	-4.408487	-0.4806
329	9.1543308	25.59361	0.313	-4.428187	0.2149
330	9.132387	25.934884	0.3135	-4.624715	0.0865
332	9.0245817	27.611482	0.33425	-4.971252	0.0755
334	9.1254492	26.042781	0.3118	-4.894453	-0.163

TABLE OF CORAL GEOCHEMICAL DATA

NW Luzon 2011-2017

Date	Sr/Ca	SrCa-SST	1 σ SD	$\delta^{18}O_{coral}$	$\delta^{18}O_{sw\_centered}$	1 σ SD
22/08/2010	8.70472	30.45143	0.173	-6.37424751	-0.30899	0.08365
20/09/2010	8.671494	31.04475	0.21875	-6.6779171	-0.494	0.0926
19/10/2010	8.645418	31.51039	0.2556	-6.76330263	-0.48625	0.1021
17/11/2010	8.672551	31.02587	0.21705	-6.28311542	-0.10297	0.0922
16/12/2010	8.612774	32.09332	0.3	-5.807952	0.585682	0.1142
14/01/2011	8.8673	27.54822	0.16795	-4.91237769	0.572237	0.08425
11/02/2011	8.898308	26.99449	0.2065	-4.86064602	0.513224	0.0909
12/03/2011	8.752901	29.59105	0.12085	-5.17361484	0.719565	0.07575
10/04/2011	8.714365	30.2792	0.1616	-5.49328012	0.537532	0.0815
09/05/2011	8.720671	30.1666	0.15275	-5.83679405	0.171497	0.08055
07/06/2011	8.703136	30.47971	0.17455	-6.27887899	-0.20797	0.0838
06/07/2011	8.668223	31.10315	0.22235	-6.57895994	-0.38336	0.0932
04/08/2011	8.673607	31.00702	0.2146	-6.3518989	-0.17552	0.09055
30/09/2011	8.823824	28.32457	0.1204	-5.44176542	0.198121	0.07435
29/10/2011	8.84405	27.96339	0.1388	-5.42924701	0.138402	0.0781
27/11/2011	8.943073	26.19512	0.27175	-5.32364799	-0.10965	0.10515
26/12/2011	9.025372	24.72551	0.39155	-5.28775062	-0.36768	0.13545
24/01/2012	8.855684	27.75564	0.15105	-5.11042896	0.415671	0.08075
22/02/2012	8.757035	29.51723	0.11815	-6.12198043	-0.24356	0.0747
21/03/2012	8.797426	28.79597	0.10845	-5.89101718	-0.15685	0.074
19/04/2012	8.799968	28.75058	0.10875	-6.07327943	-0.34819	0.07355
18/05/2012	8.704431	30.45659	0.1743	-6.14813032	-0.08184	0.0835
16/06/2012	8.72258	30.1325	0.14905	-6.61389	-0.61242	0.0798
15/07/2012	8.710288	30.35201	0.167	-6.80313669	-0.75776	0.0825
13/08/2012	8.704871	30.44873	0.1726	-6.83288132	-0.76816	0.08315
10/09/2012	8.702197	30.49649	0.17635	-6.66267278	-0.5884	0.0848
09/10/2012	8.750574	29.63261	0.12295	-5.85311515	0.048378	0.07525
07/11/2012	8.820483	28.38423	0.11855	-5.96514896	-0.31333	0.0744
06/12/2012	8.873486	27.43775	0.17395	-5.56717959	-0.10466	0.08525
04/01/2013	8.89222	27.10322	0.19995	-5.31500741	0.080608	0.0886
02/02/2013	8.898378	26.99326	0.2093	-5.59111866	-0.2175	0.0906
31/03/2013	8.758948	29.48307	0.11735	-5.81011548	0.06147	0.07465
29/04/2013	8.714832	30.27086	0.16045	-5.66381321	0.36533	0.08165
28/05/2013	8.66537	31.1541	0.22615	-5.92089861	0.284893	0.09515
26/06/2013	8.721158	30.15789	0.1528	-6.38720352	-0.38065	0.08065
25/07/2013	8.749303	29.6553	0.1228	-6.57583379	-0.6698	0.07585
23/08/2013	8.788895	28.94831	0.1067	-6.62074015	-0.85611	0.0743
21/09/2013	8.671106	31.05169	0.2154	-7.07357086	-0.88826	0.09415

19/10/2013	8.675834	30.96725	0.21065	-6.80323444	-0.63481	0.091
17/11/2013	8.801092	28.73049	0.10825	-5.86068763	-0.13962	0.0728
16/12/2013	8.81104	28.55285	0.1139	-5.37499482	0.310547	0.0751
14/01/2014	8.869823	27.50316	0.1676	-5.16280837	0.312796	0.0835
12/02/2014	8.941667	26.22022	0.26905	-4.81765656	0.401359	0.1039
13/03/2014	8.89835	26.99375	0.20725	-4.95043471	0.423287	0.09125
11/04/2014	8.809003	28.58923	0.11235	-5.25678138	0.436037	0.0746
09/05/2014	8.702425	30.49242	0.1749	-5.7625756	0.310879	0.08405
07/06/2014	8.732149	29.96162	0.1404	-6.24365172	-0.27636	0.07865
06/07/2014	8.741787	29.78953	0.13185	-6.43221915	-0.49934	0.07635
04/08/2014	8.865167	27.5863	0.16555	-6.42932952	-0.9371	0.08225
02/09/2014	8.826257	28.28112	0.12265	-6.59645103	-0.96526	0.0748
30/10/2014	8.757383	29.51102	0.11705	-6.42300132	-0.54583	0.07465
27/11/2014	8.846418	27.9211	0.1428	-6.05078745	-0.4916	0.07825
26/12/2014	8.898944	26.98315	0.20975	-5.61670388	-0.2451	0.09085
24/01/2015	8.992322	25.31567	0.3454	-4.98308504	0.055021	0.1225
22/02/2015	8.933148	26.37236	0.25565	-4.48117493	0.768269	0.10155
23/03/2015	8.885802	27.21782	0.1895	-4.79903792	0.619498	0.0863
21/04/2015	8.833992	28.143	0.12915	-5.19865107	0.404921	0.07595
19/05/2015	8.705949	30.42948	0.1688	-6.17785008	-0.11698	0.08415
17/06/2015	8.604469	32.24163	0.3206	-5.80860927	0.614687	0.11535
16/07/2015	8.645338	31.51182	0.2552	-5.51256816	0.764766	0.0994
14/08/2015	8.782121	29.06926	0.108	-5.02528631	0.763537	0.07425
12/09/2015	8.773655	29.22045	0.11115	-5.09456459	0.724496	0.07325
11/10/2015	8.833645	28.1492	0.12945	-5.09850287	0.506308	0.07675
09/11/2015	8.908658	26.80968	0.22225	-4.83914238	0.497764	0.09285
07/12/2015	8.937125	26.30135	0.261	-4.85675694	0.378483	0.1016
05/01/2016	8.95731	25.94089	0.2912	-4.91050369	0.252646	0.1108
03/02/2016	8.915927	26.67987	0.2291	-4.98674359	0.324201	0.0961
03/03/2016	8.874545	27.41884	0.1739	-5.06298349	0.395756	0.0844
30/04/2016	8.842211	27.99623	0.1378	-4.83329217	0.740926	0.0781
29/05/2016	8.717082	30.23067	0.1549	-5.06035813	0.960747	0.08015
26/06/2016	8.759342	29.47603	0.11705	-5.87086958	-0.00069	0.07425
25/07/2016	8.665716	31.14793	0.22405	-6.10487109	0.099686	0.0945
23/08/2016	8.69136	30.69	0.1899	-6.30565683	-0.19269	0.0867
21/09/2016	8.74277	29.77196	0.12935	-6.33886418	-0.4095	0.07695
20/10/2016	8.855618	27.75683	0.15095	-6.0820995	-0.55576	0.08065
18/11/2016	8.868665	27.52384	0.16825	-5.57916699	-0.09943	0.0825
17/12/2016	8.873471	27.43801	0.17425	-5.34872153	0.113852	0.08325
14/01/2017	8.946709	26.13019	0.27555	-5.08363827	0.117371	0.1051
12/02/2017	8.970792	25.70014	0.3117	-4.87207056	0.242928	0.1151
13/03/2017	8.9096	26.79285	0.22445	-4.9590543	0.374487	0.09455
11/04/2017	8.810229	28.56734	0.11315	-5.0319395	0.656501	0.07395

10/05/2017	8.679645	30.89919	0.20625	-6.36829119	-0.21348	0.0896
08/06/2017	8.68143	30.86732	0.20485	-6.12762894	0.020807	0.0896
07/07/2017	8.696863	30.59173	0.18195	-6.54282488	-0.44951	0.0853
04/08/2017	8.690708	30.70165	0.1909	-6.75938227	-0.64408	0.08815
02/09/2017	8.683073	30.83799	0.20325	-6.38164638	-0.23908	0.0907
30/10/2017	8.680094	30.89118	0.2045	-6.13241737	0.02079	0.09065
28/11/2017	8.771374	29.26119	0.11095	-5.9015614	-0.07435	0.07445
27/12/2017	8.803843	28.68138	0.11085	-5.77872858	-0.06748	0.07385
25/01/2018	8.852918	27.80503	0.1511	-5.41999068	0.115987	0.07885

NW Luzon 4.2 ka

Date	Sr/Ca	SrCa-SST	1 σ SD	$\delta^{18}O_{coral}$	$\delta^{18}O_{sw\_centered}$	1 σ SD
Dec	8.789029	28.94591	0.17775	-5.7244	0.653319644	0.08425
Jan	8.857217	27.72826	0.1118	-5.885	0.249267747	0.07415
Feb	8.907242	26.83497	0.11845	-6.0162	-0.060673655	0.0748
Mar	8.823626	28.32811	0.1378	-6.2174	0.036752736	0.0775
Apr	8.746466	29.70596	0.2348	-6.5023	0.027518035	0.0954
May	8.65734	31.29749	0.36265	-6.8935	-0.045451656	0.1283
Jun	8.605732	32.21907	0.4469	-7.2856	-0.253247399	0.1498
Jul	8.678793	30.91441	0.3351	-7.216	-0.444528599	0.1207
Aug	8.744522	29.74069	0.23935	-7.2235	-0.6867538	0.097
Sep	8.757361	29.5114	0.2188	-6.7516	-0.260731466	0.09345
Oct	8.838857	28.05612	0.12255	-6.3582	-0.158430565	0.07545
Nov	8.78809	28.96267	0.1759	-5.9853	0.39586316	0.0842
Dec	8.916224	26.67458	0.1262	-5.7211	0.202389005	0.0763
Jan	8.959516	25.90151	0.1722	-5.6415	0.127352016	0.08405
Feb	8.946812	26.12836	0.1565	-5.6495	0.164739827	0.0816
Mar	8.810772	28.55764	0.15225	-6.0393	0.260826905	0.07885
Apr	8.739662	29.82746	0.24325	-6.723	-0.168916762	0.09855
May	8.788312	28.95871	0.1783	-7.07	-0.689676067	0.0839
Jun	8.695367	30.61844	0.31295	-6.5631	0.149170536	0.1148
Jul	8.800056	28.74901	0.16215	-6.1145	0.2238634	0.08225
Aug	8.867976	27.53615	0.10805	-5.8293	0.266482949	0.07325
Sep	8.888169	27.17556	0.10945	-5.7229	0.300745444	0.07275
Oct	8.92869	26.45197	0.136	-5.6585	0.220451525	0.07795
Nov	8.924026	26.53524	0.1322	-5.5965	0.299115059	0.07645
Dec	8.953769	26.00412	0.16725	-5.5852	0.204234083	0.0832
Jan	8.967594	25.75724	0.1821	-5.5798	0.160195355	0.0845
Feb	8.824809	28.30698	0.13485	-5.6893	0.560684873	0.0778
Mar	8.798243	28.78137	0.16545	-6.0209	0.323947708	0.0822

Apr	8.825745	28.29027	0.13475	-6.583	-0.336393986	0.07755
May	8.760411	29.45694	0.2126	-7.1171	-0.637116313	0.0926
Jun	8.703198	30.4786	0.2962	-7.4978	-0.813488937	0.11025
Jul	8.712788	30.30736	0.2804	-7.0264	-0.376337736	0.1081
Aug	8.745696	29.71971	0.23685	-7.05	-0.517428258	0.09645
Sep	8.768335	29.31545	0.2039	-6.7771	-0.32547312	0.0904
Oct	8.802785	28.70027	0.1605	-6.4877	-0.159063839	0.081
Nov	8.876973	27.37548	0.10875	-6.3341	-0.27041131	0.0738
Dec	8.97436	25.63643	0.19175	-6.1805	-0.464609383	0.08645
Jan	9.027437	24.68863	0.2651	-5.9704	-0.444092414	0.1036
Feb	8.987796	25.3965	0.2104	-5.6865	-0.018604357	0.09155
Mar	8.877561	27.36499	0.107	-5.571	0.490559524	0.0731
Apr	8.82625	28.28125	0.1343	-5.6226	0.622231041	0.07645
May	8.761604	29.43564	0.21065	-5.5532	0.922556777	0.0912
Jun	8.695559	30.61502	0.31105	-5.6427	1.068838938	0.11375
Jul	8.721107	30.15881	0.2697	-5.8611	0.759209193	0.104
Aug	8.739874	29.82368	0.24565	-6.2608	0.292523133	0.0985
Sep	8.723401	30.11784	0.2695	-6.6166	-0.004467377	0.1034
Oct	8.743582	29.75746	0.23915	-6.7787	-0.238661393	0.09755
Nov	8.746366	29.70775	0.2326	-6.8979	-0.367731452	0.0962
Dec	8.805719	28.64788	0.15655	-6.7366	-0.418400258	0.08075
Jan	9.078736	23.77256	0.346	-6.348	-1.004899367	0.12185
Feb	9.006853	25.05619	0.2395	-5.6079	-0.008126427	0.09705
Mar	8.85748	27.72356	0.11125	-5.5586	0.57467543	0.07395
Apr	8.808466	28.59882	0.15145	-6.0742	0.234168255	0.0804
May	8.83461	28.13197	0.12685	-6.6756	-0.46066128	0.0757
Jun	8.739586	29.82882	0.2427	-6.7173	-0.162905937	0.0975
Jul	8.718457	30.20612	0.27405	-6.624	0.005782417	0.1041
Aug	8.755359	29.54716	0.2193	-6.5273	-0.029301848	0.0943
Sep	8.797874	28.78796	0.1643	-6.3944	-0.048238809	0.0819
Oct	8.828358	28.24361	0.1314	-6.2505	-0.013220615	0.07795
Nov	8.876259	27.38824	0.10815	-6.0432	0.023002007	0.07275
Dec	8.936054	26.32047	0.14435	-5.7878	0.064893255	0.0788
Jan	8.942412	26.20693	0.15335	-5.6251	0.20489652	0.07985
Feb	8.953135	26.01545	0.166	-5.5677	0.223979112	0.082
Mar	8.908639	26.81001	0.1194	-5.5934	0.357199663	0.0754
Apr	8.800613	28.73905	0.1629	-5.514	0.822413552	0.0829
May	8.779312	29.11943	0.1863	-5.7022	0.710251696	0.08685
Jun	8.778701	29.13034	0.187	-5.8596	0.555082212	0.0864
Jul	8.775854	29.18118	0.19245	-6.0975	0.327359227	0.0882

Aug	8.772953	29.23298	0.19955	-6.5238	-0.088645715	0.08845
Sep	8.758089	29.49842	0.2187	-6.9462	-0.45795565	0.0924
Oct	8.744509	29.74091	0.236	-6.8103	-0.273501463	0.0971
Nov	8.783198	29.05003	0.18555	-6.5371	-0.138464925	0.0862
Dec	8.930437	26.42076	0.1393	-6.0863	-0.213578536	0.07735
Jan	9.007757	25.04005	0.23555	-5.7055	-0.108894603	0.09705
Feb	8.990957	25.34005	0.214	-5.5088	0.147780996	0.09215
Mar	8.837806	28.0749	0.1246	-5.5856	0.618009002	0.0756
Apr	8.810159	28.56859	0.15105	-5.8936	0.4087059	0.07965
May	8.801857	28.71684	0.16125	-6.1419	0.190084861	0.08225
Jun	8.695785	30.61099	0.3081	-7.0263	-0.315531693	0.11335
Jul	8.741567	29.79344	0.24055	-6.9817	-0.434425339	0.09825
Aug	8.806853	28.62763	0.1536	-6.9756	-0.661492339	0.0803
Sep	8.756623	29.52459	0.2207	-6.9682	-0.474669744	0.09405
Oct	8.850727	27.84415	0.11465	-6.4103	-0.252882817	0.07465
Nov	8.88064	27.30999	0.10805	-6.2152	-0.164609896	0.0734
Dec	8.916805	26.66419	0.1263	-5.8612	0.060261979	0.0762
Jan	8.932051	26.39194	0.14015	-5.8024	0.064541601	0.07895
Feb	8.92852	26.45501	0.1353	-5.9129	-0.033363599	0.07755
Mar	8.900221	26.96033	0.11525	-5.8135	0.167108378	0.0746
Apr	8.82709	28.26625	0.1325	-5.6903	0.551518942	0.07725
May	8.772776	29.23614	0.19705	-6.187	0.248800055	0.08785
Jun	8.73663	29.8816	0.24545	-6.5637	0.001175435	0.1
Jul	8.791312	28.90514	0.1717	-6.5237	-0.154110024	0.08415
Aug	8.740759	29.80787	0.2399	-6.6903	-0.140156868	0.09985
Sep	8.750886	29.62704	0.22885	-6.493	0.020981815	0.09575
Oct	8.761861	29.43105	0.21415	-6.3711	0.103684646	0.0923
Nov	8.777684	29.1485	0.19055	-6.4142	0.004084855	0.0881
Dec	8.912264	26.74528	0.1231	-6.2067	-0.269051318	0.0745
Jan	8.957702	25.9339	0.1697	-5.8368	-0.061422562	0.08295
Feb	8.922856	26.55614	0.13125	-5.9112	-0.011354296	0.0762
Mar	8.843002	27.98211	0.12085	-5.8553	0.329664961	0.0752
Apr	8.790805	28.9142	0.1767	-6.5345	-0.163097254	0.0841
May	8.796695	28.80901	0.16605	-6.7995	-0.449099373	0.0829
Jun	8.752802	29.59283	0.22335	-6.914	-0.406897832	0.0938
Jul	8.812401	28.52856	0.14805	-6.57	-0.275731488	0.07985
Aug	8.825514	28.29439	0.1349	-6.4412	-0.193706678	0.0773
Sep	8.8669	27.55536	0.1072	-6.3146	-0.214932542	0.07285
Oct	8.894457	27.06327	0.1127	-6.1707	-0.169487008	0.07365
Nov	8.954968	25.98272	0.16725	-5.9957	-0.210541117	0.0831

Dec	8.939127	26.26559	0.14675	-5.6835	0.158246341	0.0794
Jan	8.963539	25.82966	0.17765	-5.5979	0.156611683	0.0843
Feb	8.898894	26.98404	0.11465	-5.6092	0.37623376	0.0741
Mar	8.809616	28.57828	0.15135	-5.9244	0.379805309	0.0807
Apr	8.77242	29.24251	0.198	-6.3376	0.09948332	0.08745
May	8.753761	29.5757	0.22465	-6.8266	-0.322909733	0.0945
Jun	8.702497	30.49112	0.2985	-7.0074	-0.320548838	0.11115
Jul	8.762309	29.42305	0.21095	-6.8984	-0.425183281	0.0918
Aug	8.844493	27.95549	0.1185	-6.5826	-0.402911376	0.0753
Sep	8.826681	28.27355	0.1324	-6.3016	-0.058288497	0.07725
Oct	8.877472	27.36657	0.10725	-6.0728	-0.010879267	0.07315
Nov	8.942241	26.20998	0.15135	-5.8451	-0.014556367	0.08
Dec	8.976405	25.5999	0.1935	-5.7463	-0.037743214	0.0879
Jan	8.989094	25.37333	0.21325	-5.6509	0.012313434	0.0919
Feb	8.944459	26.17038	0.15295	-5.5749	0.247742179	0.0806
Mar	8.851572	27.82907	0.1148	-5.7539	0.400462641	0.0735
Apr	8.823899	28.32324	0.1349	-5.8541	0.39914236	0.07815
May	8.791886	28.8949	0.17435	-6.3842	-0.016626444	0.08445
Jun	8.720987	30.16094	0.27065	-6.9282	-0.307400327	0.10595
Jul	8.771051	29.26695	0.19965	-6.6964	-0.254468844	0.09
Aug	8.826212	28.28192	0.13395	-6.4272	-0.182267245	0.07655
Sep	8.87725	27.37053	0.10705	-6.1661	-0.103384936	0.0732
Oct	8.909332	26.79764	0.12005	-6.1156	-0.167481849	0.07495
Nov	8.972976	25.66114	0.19105	-5.9865	-0.265732047	0.0873
Dec	8.945814	26.14617	0.1547	-5.8596	-0.041753852	0.08015
Jan	8.990053	25.35619	0.21245	-5.7327	-0.07291652	0.0916
Feb	8.967526	25.75846	0.18165	-5.5945	0.145792632	0.0863
Mar	8.919231	26.62088	0.12765	-5.5637	0.349073578	0.0774
Apr	8.825978	28.28611	0.13305	-5.6577	0.588081687	0.0777
May	8.802664	28.70242	0.15865	-5.8592	0.469900176	0.08125
Jun	8.758429	29.49234	0.21585	-6.4109	0.076122865	0.09355
Jul	8.7979	28.78751	0.1633	-6.4535	-0.107376371	0.0831
Aug	8.758014	29.49975	0.21795	-6.6406	-0.152067107	0.0922
Sep	8.768941	29.30463	0.2001	-6.4887	-0.039222201	0.08895
Oct	8.840036	28.03507	0.1208	-6.3264	-0.130781013	0.07455
Nov	8.935084	26.33778	0.1438	-6.0504	-0.19422512	0.07935
Dec	8.924707	26.52309	0.1318	-5.6252	0.267976149	0.0767
Jan	8.930542	26.4189	0.13845	-5.4964	0.37591569	0.07725
Feb	8.85002	27.85678	0.116	-5.6311	0.528881524	0.07425
Mar	8.782882	29.05568	0.18295	-5.5788	0.820867477	0.0853

Apr	8.799681	28.7557	0.16325	-5.9561	0.383664923	0.082
May	8.75714	29.51535	0.2164	-6.1409	0.350731018	0.09365
Jun	8.695804	30.61064	0.3095	-6.5401	0.170601661	0.11345
Jul	8.712788	30.30736	0.2812	-6.5698	0.08026583	0.107
Aug	8.753945	29.57241	0.22315	-6.2514	0.251641146	0.09405
Sep	8.751451	29.61694	0.22855	-6.1599	0.352081233	0.09515
Oct	8.777043	29.15995	0.19115	-6.1112	0.309340905	0.08775
Nov	8.857345	27.72598	0.1107	-6.0127	0.121045187	0.0734
Dec	8.902265	26.92384	0.1152	-5.8785	0.094877928	0.0743
Jan	8.959714	25.89796	0.17185	-5.7421	0.026115184	0.0834
Feb	8.902065	26.9274	0.1146	-5.6134	0.360612168	0.0737
Mar	8.803238	28.69218	0.1599	-5.7532	0.573794725	0.0808
Apr	8.773859	29.21681	0.1992	-5.8246	0.607349753	0.0886
May	8.772773	29.23619	0.19585	-6.3831	0.052752907	0.0886
Jun	8.706199	30.42502	0.2944	-6.5113	0.162241104	0.111
Jul	8.728848	30.02057	0.25765	-6.5193	0.073399597	0.1013
Aug	8.760378	29.45754	0.21525	-6.5255	-0.045456329	0.09225
Sep	8.780975	29.08973	0.1886	-6.5146	-0.108047496	0.08655
Oct	8.786488	28.99128	0.1773	-6.3529	0.033916595	0.08415
Nov	8.819494	28.40189	0.14145	-6.1562	0.112797924	0.07795
Dec	8.895152	27.05085	0.11295	-5.9439	0.05486681	0.0741
Jan	8.958391	25.92159	0.1718	-5.6869	0.086017253	0.08425
Feb	8.925886	26.50204	0.13515	-5.6511	0.237861336	0.07705
Mar	8.850049	27.85627	0.11565	-5.6	0.559866073	0.0741
Apr	8.819616	28.39971	0.13965	-5.6491	0.619429131	0.07845
May	8.775471	29.18803	0.19235	-6.3734	0.052805524	0.0879
Jun	8.702501	30.49106	0.29495	-6.8943	-0.207500225	0.1104
Jul	8.703046	30.48131	0.29745	-6.98	-0.295192056	0.11225
Aug	8.726863	30.05603	0.2645	-6.8289	-0.229119471	0.1035
Sep	8.75988	29.46643	0.21635	-6.6993	-0.217454228	0.0921
Oct	8.825312	28.298	0.1346	-6.5234	-0.27518688	0.0773
Nov	8.879292	27.33407	0.1085	-6.1446	-0.089249265	0.0735
Dec	8.955438	25.97431	0.1659	-5.8511	-0.067693557	0.0823
Jan	8.990143	25.35458	0.21035	-5.7361	-0.0766206	0.0909
Feb	9.009858	25.00254	0.241	-5.6829	-0.093769833	0.09925
Mar	8.889889	27.14485	0.1102	-5.6527	0.364827739	0.073
Apr	8.804307	28.6731	0.15675	-5.722	0.601168515	0.08215
May	8.75489	29.55554	0.22195	-6.3672	0.132504627	0.09225
Jun	8.669529	31.07984	0.34875	-6.8023	0.002283714	0.1231
Jul	8.684547	30.81166	0.3265	-6.9132	-0.162291972	0.1197

Aug	8.706464	30.42029	0.294	-7.1293	-0.456683764	0.10835
Sep	8.687305	30.7624	0.3189	-7.1808	-0.439729102	0.11585
Oct	8.706845	30.41349	0.2908	-6.7509	-0.079592836	0.10925
Nov	8.821148	28.37235	0.1387	-6.4835	-0.220435157	0.077
Dec	8.898118	26.99788	0.11435	-6.1986	-0.210474207	0.07445
Jan	8.98911	25.37304	0.21105	-5.8691	-0.205916079	0.09155
Feb	8.991669	25.32734	0.21345	-5.5407	0.113349411	0.09235
Mar	8.865418	27.58183	0.1103	-5.5577	0.547284684	0.0738
Apr	8.83924	28.04928	0.1218	-5.9358	0.262625993	0.07545
May	8.782028	29.07093	0.18655	-6.2297	0.173097786	0.08565
Jun	8.731512	29.973	0.2548	-6.7105	-0.127359612	0.09985
Jul	8.746564	29.70422	0.23535	-6.6175	-0.088080657	0.0955
Aug	8.806888	28.627	0.156	-6.421	-0.106996331	0.08015
Sep	8.844018	27.96397	0.1186	-6.2042	-0.022852267	0.0745
Oct	8.89694	27.01893	0.1106	-6.2005	-0.208148552	0.0748
Nov	8.971714	25.68369	0.18765	-5.9346	-0.209283936	0.08805
Dec	9.011285	24.97705	0.24095	-5.6116	-0.027563879	0.0992
Jan	9.027809	24.68198	0.26715	-5.5453	-0.020356337	0.1047
Feb	8.955916	25.96578	0.1671	-5.6445	0.137243233	0.0828
Mar	8.910168	26.78271	0.12105	-5.8335	0.11159424	0.07505
Apr	8.854802	27.77139	0.11305	-6.2351	-0.092240173	0.07395
May	8.745288	29.727	0.2333	-6.7562	-0.222234743	0.097
Jun	8.68948	30.72357	0.31895	-7.1124	-0.379134561	0.11645
Jul	8.721492	30.15193	0.2696	-7.0368	-0.417868071	0.1044
Aug	8.771152	29.26514	0.1997	-6.7661	-0.324487296	0.08995
Sep	8.805473	28.65227	0.15285	-6.4954	-0.176322415	0.0807
Oct	8.85085	27.84196	0.11595	-6.2551	-0.098161086	0.07365
Nov	8.88385	27.25269	0.10625	-6.084	-0.044890411	0.07405
Dec	8.932567	26.38274	0.1405	-5.9155	-0.050400831	0.07805
Jan	8.967665	25.75599	0.18205	-5.7408	-0.00106522	0.08635
Feb	8.910614	26.77475	0.12235	-5.8318	0.111736348	0.07445
Mar	8.872793	27.45012	0.1069	-6.4914	-0.41277317	0.07365
Apr	8.881216	27.29971	0.1068	-5.9128	0.135762013	0.0744
May	8.835513	28.11585	0.126	-5.982	0.22975895	0.07665
Jun	8.754063	29.57031	0.22395	-6.5314	-0.028770196	0.09445
Jul	8.789517	28.9372	0.17595	-6.2722	0.103798014	0.08475
Aug	8.833579	28.15038	0.1269	-6.1363	0.082399175	0.07575
Sep	8.853134	27.80119	0.11325	-6.0093	0.139510877	0.07375
Oct	8.931383	26.40388	0.1387	-5.8824	-0.013000828	0.07745
Nov	8.961256	25.87043	0.1746	-5.7632	-0.000509828	0.0845

Dec	8.946726	26.12989	0.15725	-5.6539	0.160659363	0.0808
Jan	8.937743	26.2903	0.14555	-5.606	0.240644959	0.07985
Feb	8.926066	26.49882	0.1331	-5.8706	0.017721034	0.07735
Mar	8.879134	27.3369	0.1069	-6.5925	-0.536498568	0.0724
Apr	8.830953	28.19726	0.1294	-6.2584	-0.030346454	0.0762
May	8.909008	26.80343	0.1209	-5.4185	0.530721246	0.0756
Jun	8.770799	29.27145	0.1965	-5.6463	0.796571221	0.0882
Jul	8.768463	29.31317	0.20295	-5.8227	0.628465661	0.08965
Aug	8.826102	28.2839	0.13485	-6.0363	0.209088773	0.07725
Sep	8.816612	28.45335	0.14445	-6.2152	0.06409245	0.078
Oct						
Nov						
Dec						
Jan						
Feb						
Mar						
Apr						
May						
Jun						
Jul						
Aug						
Sep						
Oct						
Nov						
Dec						
Jan						
Feb						
Mar						
Apr						
May						
Jun						
Jul						
Aug						
Sep						
Oct						
Nov						
Dec						
Jan						
Feb						
Mar						

Apr						
May						
Jun						
Jul	8.809514	28.5801	0.1519	-6.2927	0.011933135	0.08055
Aug	8.928299	26.45895	0.1356	-6.0187	-0.13830618	0.07815
Sep	8.989508	25.36592	0.2148	-5.7447	-0.082921894	0.0924
Oct	9.010028	24.9995	0.24045	-5.536	0.052489622	0.0981
Nov	9.010432	24.99228	0.24325	-5.5197	0.067308298	0.09745
Dec	9.010026	24.99953	0.2402	-5.5095	0.079035178	0.09805
Jan	9.005965	25.07205	0.23305	-5.485	0.117957429	0.09735
Feb	8.92244	26.56357	0.13025	-5.4828	0.418462984	0.07685
Mar	8.897584	27.00743	0.11305	-5.7698	0.220309672	0.07355
Apr	8.846323	27.92281	0.11705	-6.486	-0.312815064	0.07505
May	8.7854	29.01072	0.1806	-6.7399	-0.349174919	0.085
Jun	8.772285	29.24491	0.19745	-6.5811	-0.143564996	0.0883
Jul	8.782465	29.06313	0.18455	-6.5823	-0.181064422	0.085
Aug	8.801545	28.7224	0.159	-6.5498	-0.21674185	0.0811
Sep	8.86368	27.61285	0.1079	-6.3976	-0.286464587	0.073
Oct	8.927848	26.46701	0.13595	-6.1374	-0.255433187	0.07745
Nov	8.991198	25.33575	0.21375	-5.8613	-0.205558229	0.09335
Dec	8.961358	25.86862	0.17425	-5.6906	0.071697884	0.0846
Jan	9.008893	25.01977	0.2392	-5.6174	-0.024883918	0.0964
Feb	8.959927	25.89415	0.1729	-5.4053	0.362106928	0.0836
Mar	8.87907	27.33804	0.1078	-5.6426	0.413572979	0.07255
Apr	8.78355	29.04375	0.1819	-6.1642	0.233126566	0.08565
May	8.786924	28.9835	0.1772	-6.2894	0.095866926	0.08485
Jun	8.748534	29.66904	0.22955	-6.7828	-0.260461004	0.09545
Jul	8.810973	28.55405	0.15045	-6.6555	-0.356146117	0.07995
Aug	8.859002	27.69639	0.1119	-6.424	-0.296117512	0.0739
Sep	8.84579	27.93232	0.1174	-5.9929	0.18214138	0.07455
Oct	8.937656	26.29186	0.14485	-5.5641	0.282852648	0.079
Nov	8.880524	27.31207	0.1085	-5.4073	0.643665873	0.07335
Dec	8.889191	27.1573	0.1101	-5.3149	0.705156476	0.07335
Jan	8.957073	25.94513	0.1715	-5.1681	0.609552336	0.0829
Feb	8.920724	26.59422	0.1296	-5.1875	0.719916546	0.07625
Mar	8.87292	27.44786	0.1077	-5.7404	0.337797172	0.0733
Apr	8.822379	28.35038	0.1374	-6.743	-0.484369449	0.0778
May	8.762952	29.41157	0.2107	-7.0461	-0.575247085	0.09045
Jun	8.715954	30.25082	0.277	-7.0259	-0.3871111	0.10745
Jul	8.758219	29.49609	0.21975	-6.8533	-0.365454962	0.09255

Aug	8.814099	28.49823	0.1468	-6.6682	-0.379970997	0.07945
Sep	8.867147	27.55094	0.1093	-6.479	-0.380195836	0.0724
Oct	8.874514	27.41939	0.10695	-6.2628	-0.19037667	0.07375
Nov	8.879493	27.33049	0.10825	-6.0419	0.012775699	0.07365
Dec	8.894481	27.06285	0.11255	-5.8327	0.168470716	0.07445
Jan	8.934903	26.34102	0.1441	-5.7459	0.11083529	0.0784
Feb	8.908029	26.82092	0.1203	-5.624	0.328779902	0.0748
Mar	8.870751	27.48659	0.10665	-5.6437	0.442199788	0.0734
Apr	8.748512	29.66944	0.22905	-6.4753	0.047173906	0.0944
May	8.740243	29.81709	0.2446	-7.0663	-0.51433294	0.099
Jun	8.698865	30.55599	0.30845	-7.2766	-0.576856618	0.11245
Jul	8.847308	27.90522	0.1171	-6.464	-0.294386755	0.07515
Aug	8.827959	28.25073	0.1315	-6.2236	0.015128742	0.07695
Sep	8.867298	27.54825	0.10885	-6.0999	-0.001667446	0.073
Oct	8.906443	26.84924	0.11795	-6.0154	-0.056974605	0.07435
Nov	8.930291	26.42338	0.13895	-5.9386	-0.065389929	0.0782
Dec	8.923139	26.5511	0.13205	-5.7775	0.121260415	0.07685
Jan	8.937277	26.29863	0.14545	-5.6688	0.179547751	0.07895
Feb	8.930825	26.41385	0.13845	-5.6061	0.26529947	0.0793
Mar	8.896915	27.01937	0.11325	-5.5336	0.458841065	0.0734
Apr	8.833132	28.15835	0.1264	-5.5423	0.677902164	0.0761
May	8.787332	28.97622	0.17845	-5.7562	0.627644249	0.0851
Jun	8.726623	30.0603	0.26095	-6.1745	0.426184794	0.10195
Jul	8.81664	28.45286	0.1428	-6.6733	-0.394162848	0.0778
Aug	8.782024	29.07099	0.18395	-6.8301	-0.427355032	0.0869
Sep	8.823969	28.32198	0.1362	-6.9543	-0.701313385	0.0765
Oct	8.822764	28.34351	0.13725	-7.115	-0.857681318	0.0781
Nov	8.817	28.44643	0.14245	-7.135	-0.857089976	0.07825
Dec	8.854569	27.77555	0.1124	-6.8445	-0.700766881	0.0744
Jan	8.922299	26.56608	0.1308	-6.4189	-0.517109052	0.0766
Feb	8.926108	26.49808	0.13365	-5.8841	0.00412802	0.0771
Mar	8.922194	26.56796	0.13275	-5.6377	0.264455501	0.07735
Apr	8.833323	28.15494	0.1266	-5.5848	0.634783869	0.07525
May	8.785146	29.01525	0.18145	-5.7672	0.624480548	0.0849
Jun	8.686674	30.77368	0.32145	-6.1199	0.623414708	0.11755
Jul	8.776372	29.17194	0.1932	-6.4661	-0.043172767	0.08725
Aug	8.843101	27.98034	0.1186	-6.7777	-0.59300956	0.075
Sep	8.914982	26.69674	0.1232	-6.5242	-0.596242053	0.07535
Oct	8.955411	25.9748	0.1671	-6.07	-0.286425441	0.0826
Nov	8.967423	25.7603	0.18095	-5.7356	0.005044769	0.08575

Dec	8.991066	25.3381	0.2144	-5.7127	-0.056519505	0.09225
Jan	9.012903	24.94816	0.2438	-5.7059	-0.127711045	0.09835
Feb	8.969805	25.71777	0.18785	-5.6765	0.055655034	0.08615
Mar	8.941387	26.22524	0.14995	-5.5485	0.285118483	0.07935
Apr	8.85821	27.71053	0.1118	-5.6268	0.503890211	0.0737
May	8.798044	28.78492	0.16635	-5.8565	0.489022708	0.08265
Jun	8.752032	29.60656	0.2265	-6.4015	0.108428456	0.09365
Jul	8.781724	29.07636	0.18445	-6.6691	-0.265255998	0.0864
Aug	8.816479	28.45573	0.1452	-6.5486	-0.268870868	0.0792
Sep	8.8721	27.4625	0.10645	-6.3942	-0.313160494	0.0731
Oct	8.923855	26.53831	0.1339	-6.1996	-0.303342086	0.0768
Nov	9.002009	25.14269	0.23055	-5.9992	-0.382085643	0.09585
Dec	9.004126	25.1049	0.23135	-5.7892	-0.179680497	0.09425
Jan	9.031252	24.62049	0.27275	-5.5948	-0.082162354	0.10545
Feb	8.998218	25.21039	0.2232	-5.5218	0.108869214	0.095
Mar	8.887333	27.19048	0.1101	-5.4741	0.552533773	0.0737
Apr	8.920351	26.60088	0.1275	-5.6443	0.264466058	0.0756
May	8.817471	28.43803	0.14275	-5.9707	0.305526298	0.07865
Jun	8.744442	29.7421	0.23555	-6.3833	0.153745673	0.0964
Jul	8.792166	28.88989	0.1731	-6.771	-0.404410978	0.08305
Aug	8.853063	27.80245	0.11405	-6.8751	-0.726002851	0.07475
Sep	8.918247	26.63845	0.1277	-6.8003	-0.88402225	0.07605
Oct	8.979339	25.54752	0.2001	-6.5643	-0.86616592	0.0891
Nov	9.016238	24.8886	0.25225	-6.2348	-0.668478583	0.0986
Dec	9.016735	24.87974	0.2523	-5.9085	-0.344016847	0.09865
Jan	9.014462	24.92031	0.2485	-5.6929	-0.12029407	0.0987
Feb	8.937608	26.29272	0.14805	-6.435	-0.5878386	0.07875
Mar	8.920246	26.60274	0.1294	-6.0633	-0.154140682	0.0771
Apr	8.966375	25.77902	0.18065	-5.6087	0.135675482	0.08525
May	8.829873	28.21655	0.1311	-5.8888	0.343063008	0.0771
Jun	8.7514	29.61786	0.22885	-6.4672	0.044918484	0.0948
Jul	8.781684	29.07707	0.1861	-6.6807	-0.276708971	0.0869
Aug	8.786174	28.99689	0.178	-6.5334	-0.145483594	0.08465
Sep	8.818713	28.41583	0.14195	-6.3269	-0.055118348	0.0782
Oct	8.888437	27.17077	0.1098	-6.1183	-0.095535481	0.07335
Nov	8.98269	25.48769	0.20185	-5.8974	-0.211329706	0.0899
Dec	9.075889	23.82341	0.3382	-5.6746	-0.321305517	0.1197
Jan	9.139204	22.69279	0.4357	-5.455	-0.327870133	0.14475
Feb	9.096765	23.45062	0.37035	-5.2755	0.003161205	0.1293
Mar	9.048691	24.30909	0.295	-5.3734	0.076970618	0.1113

Apr	8.987789	25.39663	0.20885	-5.7728	-0.104929585	0.0921
May	8.851359	27.83287	0.11505	-6.3072	-0.152093847	0.0744
Jun	8.787152	28.97942	0.1791	-6.622	-0.237485729	0.0855
Jul	8.880874	27.30582	0.10835	-6.4676	-0.417850178	0.0733
Aug	8.997112	25.23015	0.2237	-6.2112	-0.57656498	0.0952
Sep	9.086952	23.62586	0.35415	-5.9548	-0.641001047	0.1254
Oct	9.170554	22.13297	0.485	-5.7594	-0.74422356	0.1598
Nov	9.247278	20.76289	0.6043	-5.6735	-0.932320057	0.19175
Dec	9.31079	19.62874	0.7073	-5.5897	-1.075410935	0.2218
Jan	9.357951	18.78658	0.77515	-5.5043	-1.158358511	0.24365
Feb	9.242968	20.83986	0.60505	-5.3828	-0.626272377	0.19305
Mar	8.998971	25.19695	0.22645	-5.4044	0.223533222	0.09465
Apr	8.920855	26.59187	0.13085	-5.6826	0.224339706	0.07685
May	8.874137	27.42612	0.10695	-6.1643	-0.090528183	0.0732
Jun	8.77196	29.25071	0.20025	-6.5405	-0.101767999	0.08875
Jul	8.787495	28.9733	0.17895	-6.4747	-0.091420311	0.08355
Aug	8.851228	27.83521	0.1153	-6.3909	-0.235300155	0.0738
Sep	8.926514	26.49082	0.1338	-6.2365	-0.349799588	0.0776
Oct	8.994381	25.27892	0.2193	-6.0178	-0.373402845	0.09415
Nov	8.977102	25.58747	0.1955	-5.799	-0.092915665	0.08855
Dec	8.996262	25.24531	0.22175	-5.6247	0.012973691	0.0937
Jan	9.074702	23.84461	0.33375	-5.5076	-0.150110591	0.11965
Feb	9.053429	24.22449	0.30865	-5.4097	0.023741902	0.11405
Mar	8.959671	25.89874	0.1716	-5.5651	0.203238579	0.0826
Apr	8.898795	26.9858	0.1147	-5.9609	0.024817136	0.07395
May	8.848172	27.88978	0.11685	-6.0922	0.074359999	0.07515
Jun	8.805427	28.6531	0.15565	-6.2333	0.085943954	0.08105
Jul	8.858154	27.71154	0.11165	-6.2594	-0.128521785	0.0736
Aug	8.93494	26.34036	0.1436	-6.1205	-0.263856107	0.0783
Sep	8.934523	26.3478	0.14255	-5.9443	-0.086176045	0.0784
Oct	8.933012	26.37478	0.14025	-5.7779	0.085660632	0.0786
Nov	9.06308	24.05215	0.318	-5.6359	-0.236931383	0.1169
Dec	9.06203	24.07089	0.3168	-5.4954	-0.092673116	0.1149
Jan	9.093939	23.50109	0.3632	-5.4228	-0.133953691	0.12815
Feb	9.000874	25.16296	0.23	-5.4046	0.216602285	0.0954
Mar	8.951399	26.04645	0.1639	-5.3831	0.414797897	0.0821
Apr	8.909096	26.80186	0.12135	-5.8012	0.147705118	0.07465
May	8.837718	28.07646	0.12405	-6.9696	-0.765725794	0.075
Jun	8.734215	29.92474	0.2521	-7.1064	-0.532826964	0.101
Jul	8.829436	28.22435	0.13145	-6.6563	-0.422825272	0.07625

Aug	8.899932	26.9655	0.1153	-6.2348	-0.253080458	0.07405
Sep	9.014967	24.9113	0.2462	-5.9065	-0.335671336	0.09855
Oct	9.052466	24.24168	0.30255	-5.6813	-0.244391118	0.1124
Nov	9.036089	24.53413	0.27985	-5.5525	-0.057068994	0.10675
Dec	9.048901	24.30535	0.29325	-5.4616	-0.011920472	0.11155
Jan	9.05293	24.2334	0.30535	-5.3832	0.052011002	0.1137
Feb	9.046705	24.34455	0.2948	-5.4458	0.011643292	0.11115
Mar	8.99923	25.19232	0.2256	-6.1539	-0.526862097	0.0949
Apr	8.861377	27.65397	0.11035	-6.574	-0.454647844	0.07235
May	8.773325	29.22634	0.1968	-6.953	-0.519156224	0.08785
Jun	8.728292	30.03049	0.26095	-7.0892	-0.494503166	0.102
Jul	8.795175	28.83616	0.1683	-7.0565	-0.700693597	0.08305
Aug	8.833785	28.14669	0.1287	-6.9091	-0.691179248	0.0753
Sep	8.836672	28.09515	0.1238	-6.7144	-0.506800251	0.0762
Oct	8.83431	28.13732	0.12495	-6.4746	-0.258562654	0.0759
Nov	8.862176	27.63972	0.1089	-6.1406	-0.024092201	0.07315
Dec	8.931872	26.39514	0.1422	-5.8101	0.05747555	0.0778
Jan	9.010277	24.99506	0.24195	-5.5583	0.029281017	0.0969
Feb	8.933232	26.37086	0.1415	-5.3757	0.48706313	0.07805
Mar	8.874787	27.41452	0.10815	-5.4661	0.605397879	0.073
Apr	8.830097	28.21255	0.13165	-5.6311	0.599969823	0.07625
May	8.788673	28.95227	0.1767	-5.9834	0.395619735	0.08465
Jun	8.733404	29.93922	0.2532	-6.6343	-0.057900535	0.09985
Jul	8.786881	28.98427	0.17745	-6.4094	-0.023932156	0.08405
Aug	8.837786	28.07526	0.12405	-6.1174	0.086185769	0.0751
Sep	8.956283	25.95924	0.16805	-5.9858	-0.205368885	0.08425
Oct	8.989116	25.37293	0.21085	-5.9094	-0.246263591	0.0916
Nov	8.985633	25.43513	0.2064	-5.8028	-0.127145903	0.09085
Dec	9.027466	24.68811	0.267	-5.6591	-0.132937732	0.10505
Jan	9.074948	23.84022	0.3403	-5.516	-0.159345745	0.1206
Feb	9.008891	25.01981	0.2364	-5.434	0.158591304	0.09785
Mar	8.885782	27.21818	0.10905	-5.7077	0.324549208	0.0726
Apr	8.883066	27.26668	0.1069	-6.2379	-0.195956668	0.07275
May	8.84555	27.9366	0.11795	-6.5007	-0.324834433	0.0754
Jun	8.74744	29.68857	0.23225	-6.5013	0.025025755	0.09535
Jul	8.780002	29.1071	0.1854	-6.5436	-0.133609931	0.08505
Aug	8.80256	28.70428	0.1581	-6.5557	-0.226244847	0.08205
Sep	8.894775	27.05758	0.1121	-6.4288	-0.428705439	0.07415
Oct	8.957138	25.94397	0.1676	-6.2781	-0.500740908	0.08375
Nov	8.954445	25.99206	0.1637	-6.0882	-0.301222706	0.0829

Dec	8.965062	25.80247	0.17865	-5.8992	-0.150103301	0.08545
Jan	9.002578	25.13253	0.232	-5.7693	-0.154169486	0.0957
Feb	9.017298	24.86968	0.25055	-5.6703	-0.107799191	0.10005
Mar	8.978112	25.56942	0.19525	-5.643	0.059480824	0.08785
Apr	8.959781	25.89676	0.1732	-5.6471	0.120838923	0.08305
May	8.886295	27.20902	0.10955	-5.8655	0.16483702	0.0731
Jun	8.815328	28.47629	0.1449	-6.0381	0.245690187	0.07805
Jul	8.887653	27.18476	0.10995	-5.9994	0.026089997	0.07415
Aug	8.860673	27.66656	0.10975	-6.1529	-0.030999208	0.0741
Sep	8.860169	27.67555	0.11	-6.2736	-0.14989369	0.07385
Oct	8.841866	28.00239	0.12005	-6.3223	-0.133192995	0.07595
Nov	8.853769	27.78984	0.11415	-6.4829	-0.336347135	0.0754
Dec	8.923597	26.54291	0.13165	-6.2992	-0.402002369	0.07675
Jan	9.037597	24.5072	0.28305	-5.9216	-0.431544717	0.10655
Feb	9.019927	24.82274	0.25755	-5.5053	0.047792314	0.1016
Mar	8.963951	25.82231	0.1769	-5.3509	0.402108117	0.08515
Apr	8.890593	27.13227	0.10975	-5.7172	0.297870344	0.07375
May	8.856223	27.74602	0.1109	-6.1784	-0.040608594	0.07355
Jun	8.790987	28.91094	0.1751	-6.6564	-0.285609726	0.0828
Jul	8.8243	28.31608	0.1353	-6.8654	-0.613648146	0.0778
Aug	8.891768	27.11129	0.11025	-6.671	-0.660179792	0.07345
Sep	8.942895	26.1983	0.1534	-6.4144	-0.586137467	0.0802
Oct	8.997481	25.22355	0.2251	-6.1185	-0.485252972	0.09375
Nov	9.000801	25.16427	0.22745	-5.8176	-0.196157927	0.09445
Dec	8.994766	25.27204	0.22005	-5.5151	0.127923979	0.09295
Jan	9.0641	24.03393	0.32295	-5.3823	0.013045975	0.11765
Feb	9.041366	24.4399	0.28725	-5.3502	0.126351785	0.10805
Mar	8.986873	25.41298	0.20805	-5.3883	0.282832179	0.09125
Apr	8.929867	26.43095	0.13735	-5.8248	0.050005041	0.0774
May	8.82636	28.27929	0.1347	-6.5109	-0.26645576	0.0778
Jun	8.738175	29.85401	0.24485	-6.8054	-0.245967705	0.09955
Jul	8.81831	28.42304	0.14075	-6.5659	-0.292675864	0.0778
Aug	8.83223	28.17447	0.12905	-6.1032	0.120252303	0.07595
Sep	8.884005	27.24992	0.10725	-5.7393	0.299274804	0.0733
Oct	8.974553	25.63298	0.19325	-5.5993	0.115909016	0.0877
Nov	8.953282	26.01282	0.16585	-5.5203	0.270839416	0.08225
Dec	8.966526	25.77632	0.1806	-5.5025	0.241295929	0.0847
Jan	9.067859	23.9668	0.3271	-5.5117	-0.129754825	0.1177
Feb	9.039499	24.47322	0.2843	-5.5951	-0.11191916	0.1078
Mar	8.977527	25.57988	0.19435	-5.7154	-0.010847226	0.08735

Apr	8.900973	26.9469	0.1135	-5.9236	0.054378032	0.0752
May	8.856768	27.73628	0.11175	-6.4895	-0.353621047	0.07355
Jun	8.833988	28.14308	0.1267	-6.729	-0.511774394	0.0758
Jul	8.863033	27.62441	0.10935	-6.6597	-0.546258816	0.07305
Aug	8.909574	26.79332	0.12205	-6.5606	-0.613313684	0.07465
Sep	8.952093	26.03405	0.16265	-6.4642	-0.668811757	0.08255
Oct	8.948255	26.10259	0.15695	-6.3759	-0.566782317	0.08215
Nov	8.938918	26.26932	0.1494	-6.2598	-0.417349039	0.07945
Dec	8.976279	25.60216	0.1932	-6.0375	-0.328472635	0.0875
Jan	9.009509	25.00876	0.242	-5.8139	-0.223589412	0.0972
Feb	8.973002	25.66068	0.188	-5.6454	0.075325537	0.0868
Mar	8.952495	26.02687	0.1648	-5.5611	0.232903925	0.0819
Apr	8.902958	26.91147	0.1152	-5.5663	0.404589414	0.0745
May	8.902513	26.91941	0.1165	-5.9582	0.014295459	0.07525
Jun	8.825366	28.29704	0.13435	-6.2439	0.004104182	0.07755
Jul	8.887483	27.1878	0.1083	-6.3701	-0.343967559	0.07375
Aug	8.877632	27.36372	0.1073	-6.5993	-0.537933352	0.0737
Sep	8.856648	27.73844	0.1118	-6.83	-0.69370759	0.0736
Oct	8.854013	27.78548	0.1125	-6.7767	-0.631033385	0.0739
Nov	8.86733	27.54768	0.10895	-6.6097	-0.511593968	0.07345
Dec	8.926543	26.49031	0.13385	-6.3417	-0.455094947	0.07805
Jan	9.066921	23.98356	0.32715	-5.9649	-0.579574279	0.11745
Feb	9.170532	22.13336	0.48645	-5.5979	-0.582681982	0.15865
Mar	9.112688	23.16628	0.39885	-5.5554	-0.333548176	0.13525
Apr	8.94949	26.08054	0.1613	-5.8768	-0.072139312	0.081
May	8.837739	28.07609	0.12455	-6.6053	-0.401514769	0.07625
Jun	8.753188	29.58593	0.2237	-6.9592	-0.453478827	0.09395
Jul	8.779847	29.10987	0.18735	-6.8888	-0.478286871	0.0879
Aug	8.809436	28.5815	0.15175	-6.7732	-0.468293148	0.07955
Sep	8.849175	27.87187	0.1159	-6.5409	-0.377958752	0.0741
Oct	8.889355	27.15438	0.11065	-6.2592	-0.239773722	0.0743
Nov	8.932912	26.37657	0.14205	-6.0115	-0.147651473	0.07835
Dec	9.004682	25.09496	0.23115	-5.8756	-0.268033104	0.09685
Jan	9.068137	23.96183	0.3267	-5.7481	-0.367196449	0.11945
Feb	9.024969	24.7327	0.2667	-5.5839	-0.048742153	0.10155
Mar	9.002799	25.1286	0.2302	-5.5476	0.066740133	0.09525
Apr	8.941876	26.21649	0.14865	-5.8741	-0.042220663	0.0805
May	8.851996	27.8215	0.11475	-6.3091	-0.156260975	0.0745

NW Luzon 4.3 ka

Date	Sr/Ca	SrCa-SST	1 σ SD	$\delta^{18}O_{coral}$	$\delta^{18}O_{sw\_centered}$	1 σ SD
Apr	8.89125	27.12054	0.11475	-6.00807	0.059418	0.0741
May	8.823215	28.33545	0.1309	-6.67194	-0.33869	0.0773
Jun	8.812042	28.53497	0.141	-6.84471	-0.46782	0.07855
Jul	8.839433	28.04584	0.1176	-6.71924	-0.44934	0.0748
Aug	8.852706	27.80881	0.1116	-6.49533	-0.27728	0.07315
Sep	8.849926	27.85846	0.1131	-6.1431	0.085812	0.07425
Oct	8.930498	26.41968	0.1447	-6.09943	-0.18526	0.07965
Nov	8.911335	26.76188	0.1276	-5.82929	0.159744	0.076
Dec	8.906256	26.85257	0.1237	-5.61627	0.392604	0.075
Jan	8.933791	26.36087	0.1479	-5.63608	0.265231	0.07965
Feb	8.984269	25.45948	0.2135	-5.61967	0.084467	0.0911
Mar	8.822485	28.34848	0.13095	-5.97493	0.361168	0.0763
Apr	8.852343	27.8153	0.1113	-6.20575	0.013718	0.07345
May	8.750329	29.63698	0.21955	-6.71842	-0.10046	0.09335
Jun	8.667669	31.11305	0.34045	-6.91349	0.027367	0.1229
Jul	8.764626	29.38167	0.19915	-6.54782	0.014296	0.08985
Aug	8.815945	28.46526	0.13875	-6.3598	0.001851	0.07855
Sep	8.85201	27.82124	0.11135	-6.24573	-0.02496	0.07345
Oct	8.905114	26.87297	0.121	-6.09962	-0.08629	0.0765
Nov	8.910503	26.77673	0.12455	-5.95352	0.038765	0.07645
Dec	8.892815	27.0926	0.11355	-5.88027	0.181106	0.074
Jan	8.901394	26.93939	0.11935	-5.84079	0.18707	0.074
Feb	8.970428	25.70664	0.19315	-5.79044	-0.03224	0.0885
Mar	8.932391	26.38588	0.14805	-5.58729	0.319493	0.07865
Apr	8.844128	27.962	0.1142	-5.96128	0.290281	0.07395
May	8.798238	28.78147	0.1571	-6.12936	0.301459	0.08085
Jun	8.737443	29.86709	0.23775	-6.20595	0.462348	0.09705
Jul	8.870611	27.48908	0.1073	-6.61994	-0.47183	0.0723
Aug	8.816265	28.45955	0.1377	-6.81029	-0.44989	0.078
Sep	8.895014	27.05332	0.11625	-6.60946	-0.55668	0.0747
Oct	8.92875	26.45089	0.1432	-6.36204	-0.44104	0.0787
Nov	8.942345	26.20813	0.15955	-6.08001	-0.21211	0.08165
Dec	8.915785	26.68241	0.12945	-5.7701	0.201546	0.0771
Jan	8.960319	25.88716	0.17925	-5.62952	0.168165	0.0854
Feb	9.039778	24.46825	0.29145	-5.47127	0.016033	0.11035
Mar	8.997901	25.21605	0.23215	-5.39189	0.258989	0.09575
Apr	8.951594	26.04296	0.1696	-5.56423	0.267539	0.0834
May	8.882727	27.27273	0.11055	-5.63937	0.461417	0.0736
Jun	8.81466	28.48822	0.1377	-5.80425	0.562422	0.07805
Jul	8.824239	28.31717	0.12945	-6.07605	0.253207	0.0764

Aug	8.8266	28.275	0.12875	-5.99343	0.326596	0.07565
Sep	8.828438	28.24218	0.1263	-6.2839	0.028949	0.0761
Oct	8.936437	26.31362	0.15325	-6.50314	-0.61217	0.0796
Nov	8.886411	27.20695	0.1104	-6.19567	-0.10927	0.0736
Dec	8.852014	27.82118	0.11185	-5.94019	0.280567	0.0735
Jan	8.971086	25.6949	0.19375	-5.66604	0.089594	0.08875
Feb	8.980925	25.5192	0.2067	-5.60778	0.109421	0.0906
Mar	8.939974	26.25046	0.15515	-5.50996	0.367203	0.0818
Apr	8.841574	28.0076	0.1175	-5.7107	0.550836	0.07405
May	8.825243	28.29924	0.129	-6.14126	0.184073	0.07685
Jun	8.719072	30.19514	0.2645	-7.4142	-0.67414	0.1034
Jul	8.762159	29.42574	0.203	-7.18866	-0.61691	0.0892
Aug	8.868264	27.53099	0.1073	-6.65163	-0.49435	0.07345
Sep	8.83737	28.08268	0.1195	-6.30252	-0.02456	0.0746
Oct	8.890803	27.12852	0.11325	-6.15424	-0.085	0.0734
Nov	8.963048	25.83843	0.18565	-6.04045	-0.25342	0.0863
Dec	8.980324	25.52992	0.2081	-5.9411	-0.22156	0.0921
Dec	8.953288	26.01271	0.1734	-5.90662	-0.08147	0.0836
Jan	8.97168	25.68429	0.19535	-5.8884	-0.13509	0.0885
Mar	8.95556	25.97215	0.17515	-5.82116	-0.00488	0.0842
Mar	8.948818	26.09254	0.1662	-5.6017	0.240916	0.08295
Apr	8.866561	27.56141	0.1085	-5.75656	0.40737	0.07305
May	8.834955	28.12581	0.1211	-6.96909	-0.6817	0.07495
Jun	8.712758	30.30789	0.27285	-7.17571	-0.41099	0.10485
Jul	8.783869	29.03806	0.1748	-7.07128	-0.58433	0.0841
Aug	8.816669	28.45233	0.1375	-6.99336	-0.63454	0.078
Sep	8.806311	28.6373	0.1484	-6.85857	-0.45929	0.07985
Oct	8.807356	28.61865	0.1469	-6.71768	-0.32248	0.0799
Nov	8.896139	27.03324	0.1163	-6.43831	-0.38992	0.075
Dec	8.993852	25.28836	0.22665	-6.19213	-0.52543	0.0956
Jan	9.008053	25.03477	0.2464	-5.98787	-0.37664	0.0997
Feb	8.991364	25.33278	0.22275	-5.61937	0.057053	0.09345
Mar	8.843207	27.97845	0.1175	-5.56379	0.691364	0.07405
Apr	8.920536	26.59757	0.13755	-5.96491	-0.01182	0.0771
May	8.775683	29.18423	0.1853	-6.37392	0.145004	0.086
Jun	8.702896	30.48401	0.28965	-6.85084	-0.04759	0.10835
Jul	8.742098	29.78396	0.2318	-6.62081	0.029301	0.0961
Aug	8.790687	28.9163	0.16545	-6.39079	0.069522	0.08225
Sep	8.740073	29.82013	0.2339	-6.14249	0.515534	0.0974
Oct	8.833522	28.15139	0.12195	-5.97921	0.313777	0.07525
Nov	8.910018	26.7854	0.1248	-5.8514	0.142781	0.0761
Dec	8.924633	26.52441	0.1388	-5.74775	0.18934	0.0776
Jan	8.953329	26.01197	0.174	-5.65741	0.167587	0.08395

Feb	9.002055	25.14187	0.24075	-5.55441	0.08025	0.09805
Mar	8.953362	26.01139	0.17275	-5.60739	0.21747	0.08435
Apr	8.869496	27.509	0.1088	-5.6732	0.479267	0.07355
May	8.835326	28.11918	0.12115	-5.65151	0.634434	0.0763
Jun	8.82033	28.38696	0.1316	-5.78606	0.558458	0.07735
Jul	8.883117	27.26577	0.1102	-5.80968	0.289575	0.0739
Aug	8.871861	27.46677	0.1078	-6.00773	0.135495	0.07295
Sep	8.808476	28.59864	0.1472	-6.38907	0.001756	0.07965
Oct	8.831675	28.18437	0.12445	-6.58802	-0.28782	0.07565
Nov	8.74939	29.65376	0.22165	-6.39885	0.222779	0.0927
Dec	8.872566	27.45417	0.1075	-5.99171	0.148765	0.0736
Jan	8.877767	27.3613	0.1092	-5.78158	0.338575	0.0739
Feb	8.987803	25.39637	0.21905	-5.69179	-0.00146	0.09305
Mar	8.920452	26.59907	0.13555	-5.69344	0.259976	0.07695
Apr	8.876283	27.38781	0.1081	-5.68834	0.437619	0.0745
May	8.863	27.62499	0.10865	-5.78525	0.392588	0.07375
Jun	8.858852	27.69907	0.1091	-6.18781	0.006237	0.0747
Jul	8.862606	27.63204	0.10805	-6.43376	-0.25438	0.07395
Aug	8.852864	27.806	0.11025	-6.55829	-0.34085	0.0746
Sep	8.860218	27.67467	0.10815	-6.70406	-0.51535	0.0733
Oct	8.862026	27.6424	0.1078	-7.01366	-0.83201	0.0737
Nov	8.780759	29.09359	0.1796	-6.93129	-0.4322	0.08515
Dec	8.757212	29.51408	0.21225	-6.36169	0.229392	0.0916
Jan	8.872191	27.46087	0.1084	-6.15468	-0.01274	0.0726
Feb	8.934471	26.34873	0.14955	-5.94564	-0.04698	0.07955
Mar	8.862389	27.63591	0.10945	-5.76514	0.415091	0.07305
Apr	8.888799	27.16429	0.1114	-5.95915	0.117914	0.0742
May	8.846178	27.92539	0.11475	-5.77324	0.470309	0.0744
Jun	8.785713	29.00512	0.1718	-5.73792	0.741821	0.0842
Jul	8.80899	28.58947	0.1457	-5.78764	0.601179	0.07925
Aug	8.814601	28.48927	0.1387	-5.95908	0.40782	0.07795
Sep	8.644892	31.51979	0.37435	-6.8684	0.161424	0.13035
Oct	8.716651	30.23837	0.26685	-6.91381	-0.1643	0.1034
Nov	8.61834	31.99393	0.4174	-6.65317	0.480381	0.1423
Dec	8.749247	29.6563	0.223	-6.17888	0.443304	0.0936
Jan	8.897596	27.00722	0.11745	-5.7682	0.274499	0.0734
Feb	8.928076	26.46293	0.14385	-5.61695	0.306688	0.07765
Mar	8.930396	26.42151	0.1436	-5.62978	0.2848	0.07785
Apr	8.89195	27.10804	0.113	-5.71727	0.347491	0.07385
May	8.908228	26.81735	0.12505	-5.81943	0.181741	0.0756
Jun	8.846623	27.91744	0.11355	-5.7874	0.454409	0.07475
Jul	8.826331	28.27981	0.1281	-5.95339	0.367687	0.0766
Aug	8.873614	27.43546	0.10875	-6.15993	-0.02355	0.07285

Sep	8.77777	29.14696	0.1829	-6.92975	-0.41898	0.0865
Oct	8.708185	30.38955	0.2807	-7.43026	-0.64768	0.10695
Oct	8.762644	29.41707	0.203	-7.81051	-1.24065	0.0895
Nov	8.851555	27.82938	0.112	-6.96765	-0.7451	0.07315
Dec	8.907446	26.83132	0.1233	-6.32326	-0.31904	0.0762
Jan	8.893795	27.07509	0.1132	-6.0802	-0.02265	0.075
Feb	8.890689	27.13056	0.11395	-5.78676	0.282925	0.07395
Mar	8.774004	29.21422	0.1876	-5.76545	0.76003	0.0871
Apr	8.845187	27.94308	0.11495	-5.95946	0.287963	0.07435
May	8.868927	27.51916	0.10785	-6.22253	-0.06784	0.0737
Jun	8.736962	29.87569	0.2397	-6.45976	0.210416	0.0981
Jul	8.756919	29.5193	0.208	-6.68348	-0.09126	0.09145
Aug	8.711414	30.33189	0.2794	-6.53338	0.236593	0.1059
Sep	8.777499	29.15181	0.1801	-6.35724	0.154588	0.086
Oct	8.800762	28.73639	0.1534	-6.00905	0.41191	0.0806
Nov	8.891412	27.11763	0.11335	-6.0344	0.032457	0.0739
Dec	8.821227	28.37094	0.1324	-5.7611	0.579917	0.07705
Jan	8.98951	25.36589	0.22215	-5.88233	-0.19867	0.0931
Feb	8.935559	26.3293	0.14815	-6.16994	-0.27553	0.07985
Mar	8.792297	28.88755	0.166	-6.61115	-0.15713	0.08255
Apr	8.847648	27.89915	0.1133	-6.89363	-0.65582	0.07485
May	8.838931	28.05481	0.11865	-6.80325	-0.53139	0.07515
Jun	8.661927	31.2156	0.3525	-6.88897	0.074318	0.1231
Jul	8.737869	29.85949	0.2401	-6.62165	0.044986	0.0976
Aug	8.764941	29.37606	0.1985	-6.55391	0.006972	0.08805
Sep	8.782827	29.05666	0.1767	-6.50041	-0.0094	0.0839
Oct	8.805749	28.64733	0.1496	-6.3606	0.040874	0.0786
Nov	8.73635	29.88661	0.23645	-6.22079	0.451776	0.0977
Dec	8.745329	29.72627	0.2275	-5.82594	0.811556	0.09465
Jan	8.780709	29.09449	0.1781	-5.59101	0.908283	0.0853
Feb	8.81029	28.56626	0.14295	-5.69433	0.689408	0.07875
Mar	8.816667	28.45237	0.13675	-5.80159	0.557239	0.07725
Apr	8.754641	29.55998	0.21155	-6.00634	0.594775	0.09235
May	8.703134	30.47974	0.2873	-6.68371	0.118606	0.11105
Jun	8.689411	30.72481	0.30465	-6.96632	-0.11039	0.11345
Jul	8.866602	27.56069	0.1094	-6.66428	-0.5005	0.0735
Aug	8.906865	26.84169	0.12365	-6.28173	-0.27524	0.07635
Sep	8.846332	27.92265	0.1141	-5.88691	0.356045	0.0746
Oct	8.847394	27.90367	0.11355	-5.65102	0.587778	0.07395
Nov	8.844369	27.9577	0.11445	-5.57669	0.673933	0.0749
Dec	8.919409	26.61769	0.1346	-5.51833	0.439167	0.0776
Jan	9.019721	24.82641	0.26305	-5.48733	0.078321	0.1037
Feb	9.029316	24.65507	0.2729	-5.53699	-0.00882	0.1056

Mar	8.721676	30.14864	0.26255	-5.64644	1.083452	0.1025
Apr	8.76563	29.36375	0.1992	-5.928	0.630198	0.08925
May	8.688749	30.73663	0.3101	-6.85503	0.003483	0.1133
Jun	8.606316	32.20865	0.43445	-6.72353	0.45699	0.1452
Jul	8.692997	30.66076	0.3047	-6.66844	0.173473	0.11205
Aug	8.762479	29.42001	0.20295	-6.4529	0.117602	0.0906
Sep	8.727803	30.03922	0.25005	-6.16039	0.545566	0.09995
Oct	8.801424	28.72457	0.15355	-5.91979	0.498582	0.08
Nov	8.874742	27.41532	0.1076	-5.67919	0.45278	0.0732
Dec	8.912328	26.74415	0.1283	-5.57448	0.410678	0.0767
Jan	8.906416	26.84971	0.1229	-5.65563	0.352612	0.07615
Feb	8.967758	25.75432	0.1899	-5.69086	0.07777	0.0887
Mar	8.954189	25.99662	0.17385	-5.736	0.085637	0.08355
Apr	8.961921	25.85856	0.1827	-5.82179	-0.03036	0.0857
May	8.828212	28.24621	0.12625	-6.00052	0.313211	0.0762
Jun	8.851468	27.83093	0.11215	-6.40876	-0.18587	0.074
Jul	8.951854	26.03833	0.1688	-6.78041	-0.94965	0.08375
Aug	8.849165	27.87206	0.11245	-6.79867	-0.56679	0.0742
Sep	8.829169	28.22912	0.1246	-6.73635	-0.42636	0.07615
Oct	8.809174	28.58617	0.1454	-6.67404	-0.28594	0.0792
Nov	8.789179	28.94323	0.1692	-6.61172	-0.14551	0.08285
Dec	8.769184	29.30029	0.1954	-6.5494	-0.00509	0.08755
Jan	8.820563	28.38281	0.1351	-6.32556	0.018054	0.07715
Feb	9.006118	25.06933	0.24435	-5.86707	-0.24828	0.0988
Mar	8.959001	25.9107	0.18075	-5.72277	0.080073	0.0857
Apr	8.948916	26.09078	0.1679	-5.85097	-0.00874	0.0828
May	8.956668	25.95236	0.17475	-6.11563	-0.30368	0.0848
Jun	8.876112	27.39085	0.10805	-6.95371	-0.82709	0.07315
Jul	8.858821	27.69962	0.108	-7.13832	-0.94416	0.0734
Jul	8.972381	25.67177	0.19905	-6.93504	-1.18447	0.0884
Aug	9.009058	25.01683	0.2494	-6.87491	-1.2676	0.0991
Sep	9.022771	24.77194	0.2708	-6.33796	-0.78422	0.1052
Oct	9.022804	24.77136	0.2717	-5.88375	-0.33014	0.1041
Nov	8.944174	26.17547	0.16185	-5.59088	0.269877	0.0817
Dec	9.04872	24.30857	0.30715	-5.50281	-0.05044	0.11295
Jan	9.087611	23.61409	0.36935	-5.4992	-0.19874	0.1272
Feb	8.98592	25.42999	0.2181	-5.50283	0.194855	0.09225
Mar	8.896433	27.02797	0.1154	-5.51913	0.528109	0.0753
Apr	8.947747	26.11167	0.16435	-5.88636	-0.03956	0.0825
May	8.90022	26.96035	0.11885	-6.32728	-0.29483	0.0751
Jun	8.824469	28.31306	0.12815	-7.01304	-0.68469	0.07625
Jul	8.850841	27.84212	0.1112	-6.98338	-0.75804	0.074
Aug	8.892107	27.10524	0.11415	-6.98085	-0.91671	0.07415

Sep	8.942772	26.20049	0.16015	-6.99551	-1.12928	0.08155
Oct	8.91463	26.70303	0.12995	-6.87594	-0.89978	0.07635
Nov	8.903485	26.90206	0.1198	-6.6575	-0.6378	0.07495
Dec	8.916464	26.67029	0.13215	-6.29874	-0.32974	0.0769
Jan	8.995817	25.25328	0.23035	-6.03282	-0.3738	0.09525
Feb	9.049754	24.2901	0.31115	-5.89991	-0.45158	0.1132
Mar	9.001726	25.14774	0.2388	-5.44749	0.188447	0.0977
Apr	9.016968	24.87557	0.26145	-5.37357	0.202837	0.10075
May	9.018381	24.85034	0.2634	-5.55548	0.015404	0.10305
Jun	8.722277	30.13791	0.25875	-6.06747	0.66007	0.1018
Jul	8.89091	27.1266	0.11175	-6.04221	0.026608	0.0739
Aug	8.942726	26.20133	0.16185	-6.14988	-0.28347	0.0827
Sep	9.014021	24.9282	0.25345	-6.27398	-0.68607	0.1013
Oct	8.987952	25.39372	0.217	-6.23546	-0.54571	0.09425
Nov	8.942329	26.20841	0.15765	-6.2351	-0.36713	0.0807
Dec	8.972564	25.6685	0.198	-6.0877	-0.33784	0.08845
Jan	9.054082	24.21282	0.3143	-5.47499	-0.04356	0.11585
Feb	9.151463	22.47388	0.4655	-5.39059	-0.33956	0.15545
Mar	9.016737	24.87969	0.26185	-5.06496	0.512349	0.10265
Apr	9.034307	24.56594	0.28545	-5.62859	-0.11991	0.10815
May	9.006294	25.06617	0.2481	-6.15653	-0.53843	0.09995
Jun	8.75135	29.61875	0.21925	-6.98541	-0.37144	0.0932
Jul	8.817922	28.42997	0.1364	-6.91306	-0.55913	0.0766
Aug	8.848415	27.88545	0.11355	-6.73424	-0.49943	0.0737
Sep	8.83457	28.13268	0.121	-6.44824	-0.15935	0.0752
Oct	8.875537	27.40112	0.10895	-6.32957	-0.2007	0.07315
Nov	8.872178	27.46111	0.10665	-6.12567	0.016318	0.0722
Dec	8.917248	26.65628	0.13275	-5.86626	0.099672	0.07625
Jan	9.006825	25.0567	0.243	-5.57682	0.039207	0.0992
Feb	9.095619	23.4711	0.38025	-5.30714	-0.03797	0.1323
Mar	8.971552	25.68657	0.196	-5.59888	0.154934	0.0877
Apr	8.960197	25.88935	0.17965	-5.40678	0.391384	0.085
May	8.885325	27.22634	0.1112	-6.32956	-0.23893	0.07415
Jun	8.764084	29.39136	0.20285	-6.52692	0.037315	0.08995
Jul	8.835375	28.11831	0.12015	-6.47953	-0.19377	0.0757
Aug	8.874877	27.4129	0.10725	-6.00116	0.13029	0.0737
Sep	8.760147	29.46166	0.20755	-5.61534	0.964267	0.0913
Oct	8.916526	26.66918	0.13205	-5.34074	0.628019	0.0763
Nov	8.767543	29.3296	0.19595	-5.31273		0.0891

NW Luzon 6.1 ka

Date	Sr/Ca	SrCa-SST	1 σ SD	$\delta^{18}O_{coral}$	$\delta^{18}O_{sw\_centered}$	1 σ SD
Jan	9.003914	25.10868	0.1209	-5.18435	0.585937	0.0754
Feb	9.143848	22.60986	0.2016	-5.13124	0.139279	0.08995
Mar	9.064004	24.03565	0.11595	-5.31199	0.24369	0.0745
Apr	9.067797	23.96791	0.12015	-5.78199	-0.23986	0.0745
May	9.007349	25.04734	0.11765	-6.00525	-0.24723	0.0742
Jun	8.95056	26.06143	0.1755	-6.0808	-0.11996	0.08475
Jul	8.9671	25.76607	0.1556	-6.1658	-0.26403	0.0809
Aug	8.977858	25.57397	0.14465	-6.07133	-0.20798	0.0779
Sep	9.027492	24.68765	0.1088	-5.87987	-0.19378	0.0725
Oct	9.013605	24.93563	0.113	-5.97602	-0.24034	0.074
Nov	8.996997	25.23219	0.1249	-5.74743	0.047565	0.075
Dec	9.011232	24.978	0.1161	-5.30112	0.443035	0.074
Jan	9.077488	23.79486	0.1262	-5.11512	0.392407	0.0763
Feb	9.154184	22.42528	0.2161	-4.78878	0.444832	0.09275
Mar	9.180731	21.95124	0.2562	-4.73262	0.40618	0.1006
Apr	9.125116	22.94436	0.179	-4.91622	0.421206	0.0834
May	9.020672	24.80943	0.11025	-5.29427	0.416172	0.0739
Jun	8.911478	26.75933	0.2278	-5.91688	0.18354	0.09485
Jul	8.879317	27.33363	0.274	-6.01324	0.202037	0.1058
Jul	8.867549	27.54376	0.2934	-5.93164	0.325668	0.10965
Aug	8.829269	28.22733	0.35595	-5.72829	0.665725	0.1248
Sep	8.92204	26.57071	0.21305	-5.47941	0.583287	0.09265
Oct	9.017513	24.86583	0.1127	-5.31483	0.406884	0.0743
Nov	9.071029	23.91019	0.12075	-5.28945	0.241139	0.07535
Dec	9.132423	22.81388	0.1878	-5.1788	0.132525	0.0869
Jan	9.111796	23.18221	0.1606	-5.09026	0.294733	0.08135
Feb	9.085969	23.64342	0.13165	-5.13122	0.346014	0.07745
Mar	9.068086	23.96274	0.11845	-5.36789	0.173206	0.0747
Apr	8.982333	25.49405	0.1376	-5.66143	0.185928	0.0778
May	8.947339	26.11895	0.1793	-5.91762	0.054721	0.08525
Jun	8.978209	25.5677	0.14355	-6.02001	-0.15792	0.0788
Jul	8.991412	25.33194	0.12765	-5.94671	-0.13177	0.0768
Aug	8.933539	26.36537	0.19935	-5.95084	0.070789	0.0891
Sep	8.979076	25.55222	0.14245	-5.84175	0.017242	0.07805
Oct	9.210598	21.4179	0.30005	-5.59783	-0.5657	0.1122
Nov	9.218976	21.26828	0.3114	-5.42974	-0.42754	0.11285
Dec	9.227543	21.1153	0.3253	-5.34155	-0.36994	0.11555
Jan	9.207654	21.47046	0.29295	-5.28776	-0.24512	0.10925
Feb	9.004432	25.09942	0.1191	-5.23576	0.532681	0.0743
Mar	9.016015	24.89258	0.1127	-5.51211	0.214958	0.0742

Apr	9.007123	25.05138	0.11605	-5.77585	-0.01702	0.0735
May	8.977924	25.57279	0.14485	-6.08247	-0.21936	0.07795
Jun	8.946034	26.14225	0.1841	-6.23167	-0.25466	0.0848
Jul	8.984093	25.46263	0.1379	-5.80131	0.039772	0.07745
Aug	9.042774	24.41475	0.1085	-5.68296	-0.05146	0.0727
Sep	9.133963	22.78638	0.18975	-5.53925	-0.23342	0.0872
Oct	9.232586	21.02524	0.3334	-5.3721	-0.41849	0.119
Nov	9.207741	21.4689	0.2932	-5.31081	-0.26847	0.1089
Dec	9.306342	19.70817	0.44535	-5.35284	-0.66266	0.1486
Jan	9.203524	21.54421	0.2882	-5.26044	-0.20305	0.10905
Feb	9.207366	21.4756	0.29525	-5.24074	-0.19707	0.1102
Mar	9.126752	22.91514	0.1793	-5.32531	0.006267	0.0857
Apr	9.041822	24.43175	0.10855	-5.65266	-0.01775	0.0738
May	8.971308	25.69094	0.1506	-5.90666	-0.01992	0.07935
Jun	8.927397	26.47505	0.2054	-6.02848	0.015083	0.0914
Jul	8.914519	26.70503	0.2242	-5.90932	0.180233	0.09325
Aug	8.964579	25.8111	0.15805	-6.00274	-0.09197	0.08145
Sep	9.014239	24.92431	0.11385	-5.91972	-0.1863	0.07375
Oct	9.155758	22.39717	0.21695	-5.61984	-0.39186	0.09255
Nov	9.117326	23.08347	0.16725	-5.53132	-0.16608	0.08215
Dec	9.133942	22.78674	0.1888	-5.44287	-0.13697	0.087
Jan	9.14034	22.67249	0.1961	-5.33325	-0.0502	0.0897
Feb	9.071843	23.89566	0.1215	-5.22962	0.298065	0.0741
Mar	9.052403	24.2428	0.10895	-5.28655	0.310566	0.0732
Apr	9.050993	24.26798	0.11015	-5.40419	0.197961	0.073
May	9.038976	24.48257	0.10625	-5.56374	0.081325	0.07335
Jun	8.98002	25.53535	0.1422	-5.93612	-0.0805	0.07855
Jul	8.961339	25.86894	0.16195	-5.94156	-0.01922	0.0818
Aug	8.993708	25.29093	0.12855	-5.89147	-0.08473	0.0757
Sep	9.004933	25.09048	0.11895	-5.85176	-0.08511	0.07525
Oct	9.025571	24.72195	0.11015	-5.65331	0.039634	0.0739
Nov	9.032689	24.59484	0.1078	-5.65893	0.008588	0.073
Dec	9.042622	24.41747	0.10915	-5.48648	0.145561	0.0727
Jan	9.073188	23.87165	0.1202	-5.34935	0.173535	0.0755
Feb	9.083415	23.68902	0.1299	-5.31089	0.175463	0.07725
Mar	9.138608	22.70343	0.19535	-5.37871	-0.08947	0.08865
Apr	9.147339	22.54751	0.2086	-5.45426	-0.19621	0.0909
May	9.075985	23.82171	0.12405	-5.54698	-0.03408	0.0755
Jun	8.996462	25.24175	0.12515	-5.94048	-0.14358	0.07485
Jul	8.94052	26.24071	0.18855	-6.1865	-0.1898	0.08685
Aug	8.927204	26.4785	0.2077	-6.12021	-0.07595	0.0906
Aug	8.908268	26.81665	0.2347	-6.03589	0.075988	0.09625
Sep	8.894621	27.06034	0.25265	-5.77712	0.3835	0.1011

Oct	8.910284	26.78065	0.2312	-5.4067	0.697979	0.09465
Nov	8.957934	25.92974	0.167	-5.21378	0.720718	0.0823
Dec	9.026596	24.70364	0.10915	-5.04373	0.645552	0.0736
Jan	9.126062	22.92746	0.17985	-5.01206	0.321983	0.0847
Feb	9.137376	22.72542	0.1912	-5.22421	0.069428	0.0868
Mar	9.066163	23.99709	0.1184	-5.63198	-0.08401	0.0751
Apr	9.044333	24.3869	0.1073	-5.86689	-0.24095	0.0733
May	8.975651	25.61337	0.1473	-6.20344	-0.33221	0.08025
Jun	9.009774	25.00403	0.1152	-6.24857	-0.49921	0.07515
Jul	9.035436	24.54579	0.1073	-6.00519	-0.34748	0.07295
Aug	9.076744	23.80815	0.12645	-5.81273	-0.30255	0.0772
Sep	9.236753	20.95083	0.33945	-5.64806	-0.70934	0.1217
Oct	9.147488	22.54486	0.206	-5.36226	-0.10473	0.09005
Nov	9.339413	19.11762	0.49365	-5.37096	-0.79888	0.1631
Dec	9.290624	19.98886	0.4235	-5.37031	-0.62398	0.14175
Jan	9.176779	22.0218	0.2467	-5.2661	-0.11319	0.0985
Feb	9.208017	21.46398	0.294	-5.27592	-0.23457	0.11075
Mar	9.011697	24.96969	0.1144	-5.52331	0.219182	0.0744
Apr	8.946383	26.13601	0.1819	-5.73526	0.240498	0.0855
May	8.970507	25.70524	0.15245	-5.88578	0.003821	0.07955
Jun	8.960057	25.89184	0.1661	-6.11058	-0.18366	0.08215
Jul	8.963562	25.82925	0.15975	-6.07782	-0.16342	0.08195
Aug	8.909955	26.78651	0.23075	-5.92578	0.180077	0.0963
Sep	8.967971	25.75052	0.1546	-5.86089	0.037766	0.0809
Oct	9.001138	25.15826	0.1224	-5.68695	0.093252	0.0757
Nov	8.949965	26.07205	0.1763	-5.39186	0.571103	0.08525
Dec	9.025058	24.73111	0.11	-5.4346	0.260169	0.0739
Jan	9.08202	23.71393	0.12995	-5.38234	0.109003	0.0759
Feb	9.1042	23.31786	0.1513	-5.29971	0.112411	0.07975
Mar	9.030243	24.63852	0.1084	-5.66318	0.013077	0.0734
Apr	8.958151	25.92587	0.166	-5.81882	0.114909	0.08275
May	8.888732	27.1655	0.263	-5.91511	0.266541	0.10225
Jun	8.946713	26.13013	0.1821	-5.9166	0.057982	0.0856
Jul	8.991227	25.33523	0.1296	-5.67139	0.14421	0.0774
Aug	9.038686	24.48775	0.10775	-5.41437	0.231729	0.07345
Sep	9.145151	22.58658	0.2038	-5.39042	-0.12455	0.09065
Oct	9.143293	22.61978	0.2028	-5.37668	-0.10417	0.0889
Nov	9.075984	23.82171	0.1244	-5.35745	0.155448	0.0759
Dec	9.099113	23.40869	0.1478	-5.33013	0.100159	0.08
Jan	9.141202	22.65711	0.1995	-5.18835	0.091624	0.08835
Feb	9.181164	21.9435	0.2562	-4.93301	0.204244	0.10055
Mar	9.118301	23.06606	0.16505	-5.29065	0.071118	0.083
Apr	9.041027	24.44594	0.10875	-5.61239	0.025352	0.07295

May	8.898439	26.99215	0.2475	-6.06734	0.079641	0.0983
Jun	8.864778	27.59325	0.2986	-6.37958	-0.11238	0.11085
Jul	8.910643	26.77424	0.23165	-6.32188	-0.21848	0.09605
Aug	8.980012	25.5355	0.14505	-6.06666	-0.211	0.0786
Sep	9.007491	25.0448	0.1178	-5.99738	-0.23987	0.07415
Oct	8.977977	25.57185	0.14375	-6.00793	-0.14501	0.0787
Nov	9.02188	24.78786	0.1103	-5.23332	0.472802	0.0731
Dec	9.04401	24.39268	0.10815	-5.00396	0.623131	0.07415
Jan	9.10254	23.3475	0.152	-4.8191	0.598948	0.07935
Feb	9.170008	22.14271	0.2397	-4.62843	0.548665	0.0977
Mar	9.114958	23.12575	0.1645	-4.96138	0.41232	0.08285
Apr	9.067215	23.97829	0.11805	-5.24012	0.304087	0.07455
May	9.060921	24.0907	0.1136	-5.34374	0.222953	0.07425
Jun	8.978858	25.5561	0.1416	-6.03317	-0.1734	0.07915
Jul	8.9184	26.63571	0.2198	-6.57445	-0.49876	0.0931
Aug	8.920551	26.5973	0.216	-6.47652	-0.40851	0.09285
Sep	8.95962	25.89964	0.1666	-6.41649	-0.48801	0.08215
Sep	8.991104	25.33743	0.13125	-6.1868	-0.37077	0.0757
Oct	9.017546	24.86526	0.11285	-5.91205	-0.19044	0.0742
Nov	9.059709	24.11235	0.1142	-5.62329	-0.05227	0.0738
Dec	9.128884	22.87707	0.18135	-5.34721	-0.02325	0.0846
Jan	9.151553	22.47227	0.2125	-5.22008	0.022929	0.0909
Feb	9.202308	21.56592	0.28965	-5.24431	-0.18257	0.10885
Mar	9.138428	22.70665	0.19465	-5.39841	-0.10853	0.08805
Apr	9.125827	22.93165	0.17915	-5.43739	-0.10251	0.0844
May	9.03331	24.58375	0.10815	-6.04085	-0.37555	0.07355
Jun	8.949631	26.07802	0.1776	-6.40505	-0.4409	0.08505
Jul	8.886603	27.20352	0.2646	-6.41233	-0.22308	0.1033
Aug	8.921507	26.58024	0.21535	-6.25911	-0.19451	0.09325
Sep	8.988373	25.3862	0.1324	-6.05242	-0.22663	0.07675
Oct	8.989973	25.35762	0.1325	-5.86337	-0.0433	0.07675
Nov	9.00278	25.12893	0.1222	-5.71615	0.058185	0.0752
Dec	9.062427	24.06381	0.11575	-5.6886	-0.12728	0.07315
Jan	9.115034	23.12439	0.16355	-5.55246	-0.17903	0.0818
Feb	9.134463	22.77744	0.1905	-5.20339	0.100653	0.08685
Mar	9.132843	22.80638	0.1889	-5.24889	0.060938	0.0866
Apr	9.102359	23.35073	0.14915	-5.45475	-0.03605	0.0795
May	8.988546	25.3831	0.1326	-5.81841	0.006764	0.0775
Jun	8.886713	27.20156	0.2654	-6.38245	-0.19359	0.10265
Jul	8.886496	27.20543	0.2665	-6.39736	-0.20772	0.10295
Aug	8.870557	27.49005	0.28745	-6.21259	0.03397	0.1087
Sep	8.861078	27.65932	0.3001	-6.08471	0.195701	0.11155
Oct	8.881874	27.28796	0.268	-6.09988	0.106261	0.1042

Nov	8.903184	26.90743	0.2389	-6.11324	0.016799	0.0978
Dec	8.918102	26.64104	0.21935	-5.9169	0.159856	0.09325
Jan	8.929636	26.43507	0.2064	-5.60959	0.425981	0.08995
Feb	8.963415	25.83188	0.15705	-5.36239	0.552536	0.0824
Mar	9.014034	24.92796	0.1133	-5.44652	0.287625	0.07385
Apr	9.008561	25.0257	0.1158	-5.67169	0.082008	0.0752
May	8.933046	26.37417	0.1978	-5.93223	0.09116	0.0884
Jun	8.977741	25.57606	0.14495	-6.09715	-0.23339	0.07895
Jul	8.969395	25.72508	0.15345	-6.07885	-0.18528	0.0797
Aug	8.948003	26.10709	0.17775	-5.95217	0.017801	0.08495
Sep	8.957004	25.94635	0.1669	-5.7488	0.189019	0.084
Oct	8.986755	25.4151	0.1344	-5.56118	0.270395	0.07705
Nov	9.018309	24.85163	0.1104	-5.37492	0.343958	0.0745
Dec	9.034188	24.56807	0.1073	-5.27475	0.387419	0.07275
Jan	9.033481	24.5807	0.10795	-5.26567	0.399026	0.07345
Feb	9.032896	24.59113	0.1086	-5.27128	0.395498	0.0742
Mar	9.126588	22.91807	0.1794	-5.40304	-0.07088	0.08415
Apr	9.165791	22.21801	0.23275	-5.3578	-0.16565	0.09535
May	9.014404	24.92136	0.1136	-5.4994	0.233423	0.07355
Jun	8.991158	25.33647	0.12915	-5.91232	-0.09647	0.07635
Jul	8.999946	25.17954	0.1236	-6.12814	-0.34369	0.07535
Aug	9.008788	25.02164	0.1168	-6.10082	-0.34794	0.0742
Sep	9.01763	24.86374	0.11235	-5.97867	-0.25737	0.07405
Oct	9.006693	25.05906	0.11755	-6.10196	-0.3416	0.0752
Nov	8.974292	25.63763	0.1487	-6.4843	-0.60822	0.07975
Dec	8.996598	25.23933	0.12435	-5.83031	-0.03389	0.0759
Jan	9.005197	25.08576	0.12055	-5.45178	0.313921	0.0747
Feb	9.072514	23.88368	0.12235	-4.92166	0.603632	0.0743
Mar	9.154164	22.42564	0.2172	-4.84493	0.388754	0.09185
Apr	9.205196	21.51435	0.29065	-4.9206	0.130825	0.10835
May	9.152652	22.45264	0.2124	-5.17957	0.059507	0.09235
Jun	8.985489	25.4377	0.1355	-5.98978	-0.15369	0.0767
Jul	8.904593	26.88226	0.24025	-6.23196	-0.10696	0.0977
Aug	8.895385	27.0467	0.24845	-6.06652	0.091372	0.1003
Aug	8.914528	26.70486	0.22595	-5.91549	0.174036	0.0935
Sep	8.995785	25.25384	0.12665	-5.93037	-0.13105	0.07645
Oct	9.003909	25.10877	0.12135	-5.80826	-0.03796	0.07455
Nov	8.995732	25.25479	0.12545	-5.61916	0.180353	0.07595
Dec	9.013571	24.93623	0.11305	-5.41669	0.319112	0.07455
Jan	9.032302	24.60174	0.10715	-5.29177	0.377134	0.07365
Feb	9.043619	24.39965	0.10735	-5.26333	0.365155	0.0736
Mar	9.09711	23.44446	0.14505	-5.39699	0.040456	0.0786
Apr	9.137662	22.72032	0.195	-5.38414	-0.09152	0.08715

May	9.093947	23.50095	0.1394	-5.63746	-0.18871	0.078
Jun	8.950301	26.06605	0.1765	-6.15604	-0.19428	0.0839
Jul	9.047063	24.33816	0.1082	-6.15518	-0.539	0.07365
Aug	9.178912	21.98371	0.2499	-6.08646	-0.94117	0.1009
Sep	9.060236	24.10293	0.1131	-6.02302	-0.45388	0.0744
Oct	9.106606	23.27489	0.15615	-5.99697	-0.59344	0.08135
Nov	9.085204	23.65706	0.12975	-5.78296	-0.30299	0.07685
Dec	9.063822	24.03889	0.1157	-5.6074	-0.05107	0.07455
Jan	9.080499	23.7411	0.12785	-5.51345	-0.01668	0.0764
Feb	9.086738	23.62968	0.13245	-5.5064	-0.03191	0.0766
Mar	9.11674	23.09393	0.16485	-5.5008	-0.13347	0.0834
Apr	9.055026	24.19596	0.11165	-5.73179	-0.14404	0.07335
May	8.973633	25.6494	0.14845	-6.06757	-0.18914	0.07885
Jun	8.957403	25.93923	0.16645	-6.30975	-0.37335	0.08325
Jul	9.034271	24.5666	0.1072	-6.16674	-0.50487	0.07305
Aug	9.079967	23.75059	0.12765	-5.84658	-0.34791	0.0762
Sep	9.105512	23.29442	0.155	-5.52501	-0.11757	0.0812
Oct	9.098909	23.41233	0.14575	-5.30978	0.121234	0.0782
Nov	9.113645	23.14919	0.1629	-5.29492	0.083474	0.08135
Dec	9.125834	22.93154	0.1804	-5.30074	0.034123	0.085
Jan	9.132529	22.81199	0.1869	-5.32557	-0.01462	0.08715
Feb	9.156301	22.38749	0.21955	-5.23793	-0.01188	0.09375
Mar	9.13106	22.83822	0.18625	-5.32292	-0.00673	0.08685
Apr	9.031112	24.62301	0.10785	-5.43747	0.235681	0.07345
May	8.959647	25.89917	0.1652	-5.66077	0.267612	0.0828
Jun	8.889563	27.15066	0.26425	-6.167	0.011682	0.10325
Jul	8.919133	26.62263	0.2174	-6.25117	-0.17809	0.094
Aug	8.981845	25.50277	0.1418	-6.13266	-0.28355	0.0781
Sep	9.004485	25.09848	0.1197	-6.01042	-0.24218	0.07455
Oct	8.993823	25.28888	0.12795	-5.88509	-0.07876	0.0767
Nov	8.992488	25.31271	0.1292	-5.67745	0.133639	0.0758
Dec	9.016705	24.88027	0.1111	-5.36327	0.36134	0.07445
Jan	9.056758	24.16504	0.1111	-5.35125	0.230312	0.07395
Feb	9.096579	23.45395	0.14285	-5.37295	0.06639	0.0785
Mar	9.116629	23.09591	0.1677	-5.44941	-0.08167	0.08215
Apr	9.13088	22.84142	0.18625	-5.54131	-0.22447	0.0859
May	9.14303	22.62447	0.20115	-5.48438	-0.21093	0.0896
Jun	9.128343	22.88673	0.18075	-5.4309	-0.105	0.0849
Jul	9.080473	23.74155	0.12755	-5.53374	-0.03687	0.077
Aug	9.037116	24.51579	0.10725	-5.62807	0.023643	0.0731
Sep	9.009979	25.00038	0.11765	-5.69035	0.058276	0.07425
Oct	8.984228	25.46021	0.13765	-5.7499	0.090698	0.0779